Ion Velocity Distributions in Inhomogeneous and Time-dependent Auroral Situations

A Thesis Submitted to the
College of Graduate Studies and Research
in Partial Fulfillment of the Requirements
for the degree of Doctor of Philosophy
in the Department of Physics and Engineering Physics
University of Saskatchewan
Saskatoon

By
John Zhen Guo Ma

Permission to Use

In presenting this thesis in partial fulfilment of the requirements for a Postgraduate degree from the University of Saskatchewan, I agree that the Libraries of this University may make it freely available for inspection. I further agree that permission for copying of this thesis in any manner, in whole or in part, for scholarly purposes may be granted by the professor or professors who supervised my thesis work or, in their absence, by the Head of the Department or the Dean of the College in which my thesis work was done. It is understood that any copying or publication or use of this thesis or parts thereof for financial gain shall not be allowed without my written permission. It is also understood that due recognition shall be given to me and to the University of Saskatchewan in any scholarly use which may be made of any material in my thesis.

Requests for permission to copy or to make other use of material in this thesis in whole or part should be addressed to:

Head of the Department of Physics and Engineering Physics
161 Physics Building
116 Science Place
University of Saskatchewan
Saskatoon, Saskatchewan
Canada
S7N 5E2

Abstract

Aurorae often break down into elongated filaments parallel to the geomagnetic field lines ($\mathbf{B}$) with cylindrically symmetric structures. The object of this thesis is to study the ion distribution function and transport properties in response to the sudden introduction of a radial electric field ($\mathbf{E}$) in such a cylindrical geometry. Both collision-free and collisional situations are considered.

The thesis starts by solving a collision-free problem where the electric field is constant in time but increases linearly with radius, while the initial ion density is uniform in space. The attendant Boltzmann equation is solved by tracking the ions back in time, thereby using the temporal link between the initial position and velocity of an ion and its position and velocity at an arbitrary time and place. Complete analytical solutions show that the ion distribution function is a pulsating Maxwellian in time, and all transport parameters (e.g., bulk speed, temperature, etc.) oscillate in time but independent of radius. If the ion-neutral collisions are taken into account by employing a simple relaxation model, analytical solutions are also obtained. In this case, the ion distribution function can be driven to horseshoe shapes which are symmetric with respect to the $\mathbf{E} \times \mathbf{B}$ direction. The bulk parameters evolve in a transition period of the order of one collision time as they go from oscillating to the non-oscillating steady state.

In more realistic electric field structures which are spatially inhomogeneous but still constant in time, a generalized semi-numerical code is developed under collision-free conditions. This code uses a backmapping approach to calculate the ion velocity distribution and bulk parameters. With arbitrarily selected electric field profiles, calculations reveal various shapes of ion velocity distribution functions (e.g., tear-drop, core-halo, ear-donut, etc). The associated transport properties are also obtained and discussed.

Under both collision-free and collisional conditions, the effect of the density in-

homogeneities at the initial time is studied in an electric field which is proportional to radius and constant in time. With two profiles of the initial ion density for the collision-free case, and one profile for the collisional case, complete analytical solutions are obtained. The results reveal that the distribution function and the bulk properties are now strongly dependent on radial position.

If the radial electric field is unable to stay constant with time but modulated by incoming charged particles, a fluid formalism is used to study the excitation of several plasma waves under different kinds of initial conditions. These identified waves include the ion cyclotron oscillation, the ion and electron upper-hybrid oscillations, and the lower-hybrid oscillation.

The results of this thesis are expected to be applicable to high-resolution observations. Future work should also include the mirror effect and the formation of conics in velocity space. Finally, the velocity distributions obtained in this thesis could trigger various plasma instabilities, and this topic should also be looked at in the future.

Acknowledgements

First and foremost, I would like to express my sincere thanks to my advisor, Professor *Jean-Pierre St.-Maurice*, for providing me with an opportunity to switch from an engineering-oriented plasma research field to a theory-oriented one by the completion of my second PhD work at the University of Saskatchewan, Saskatoon, Canada. I especially want to thank him for a resourceful guidance and a full support in last three and a half years. He has always been active and available in my study for supervision, even either on holidays and weekends, or in travels abroad. His fruitful achievements, extraordinary patience, and everlasting enthusiasm have made him a great mentor in my life. Especially, he and his wife, Monique, have helped me a lot to overcome difficulties my family encountered during my study. I do not know how to thank them.

Many thanks to Professor *Sasha Koustov*. In the first talk with him, I found him sharp, frank, and with a great sense of cold humor. In my study, he has often guided me with fundamental questions and new considerations. For example, in a group talk, he asked me a question about what is going to happen when the constant electric field is modified by the incoming ions. This lead me to pay attention to the wave excitation mechanism as given in Chapter 6. He read my thesis in details and gave many valuable advices.

Particular thanks to Professor *Akira Hirose*. I have known him since the first time I attended his class, *Plasma Wave* (I), at the beginning of 2007. He has an immense knowledge in fusion plasma theory and experiment. I have learnt from him about plasma instabilities, waves, and soliton physics. Though I am not in his group, he has always introduced me to most recent developments in plasma research via a meeting in his laboratory, private communications, and paper readings. Even two papers have been accepted for publication after reading one of his important papers and following his kind guidance.

I thank Professor Chijin Xiao for his help in the application of the waiver of two mandatory courses. I also want to say that his lectures on Classical Mechanics

were very important for me to deal with the characteristics of particles: I used the Hamiltonian formulation to describe the ion motion in Appendix C.

I would also like to thank past and present members in my group. Dr. *Raj Kumar Choudhary* shared his experiences about Fortran programming, Linux operation system, lecture presentation, etc. *Megan Gillies* has been like an angel to me: she has often told me many things I did not know about the culture shocks; she has often helped my family with private matters; she has often corrected my pronunciations... She is gentle, sincere, and warm-hearted, bringing sunshine into our office.

I also hope to give my heartfelt thanks to Ms. *Marj Granrude*, *Debbie Parker*, *Michelle Bedier*, *Angelika Ortlepp*, *Cindy Jelinski*, and *Debbie Kowaliuk*. They have helped me complete various administrative and teaching-assistant tasks. Many thanks also to other ISAS professors, staffs, and students for their helps and chats, and for providing a good environment.

I express my sincere gratitude to Professor *D. J. Knudsen*, University of Calgary. He was the first scientist my advisor mentioned to me during my study. He offered me helpful suggestions and discussions about rocket measurement. His JGR (2004) paper, suggesting a challenging and insightful mechanism for transverse ion heating, became a good reference for my thesis orientation. He carefully examined the thesis, and commented on it with many suggestive ideas.

Finally, I offer my love and thanks to my wife, *Cui Wei Yang*, my daughter, *Hélène Ma-Yang*, and my son, *Richard Ma-Yang*. Their presence in this world has definitely brought me a lot of happiness, hope, strength, and motivation in my life.

In Appreciation to the Beauty of the Universe

Contents

List of Tables

List of Figures

List of Abbreviations

AE-C	Atmospheric Explorer C
ARCS	Argon Release Controlled Studies
BGK	Bhatnagar-Gross-Krook
EISCAT	European Incoherent Scatter
e-POP	Enhanced Polar Outflow Probe
GC	Guiding Center
GEODESIC	Geoelectrodynamics and Electro-Optical Detection of Electron and Suprathermal Ion Currents
FFT	Fast Fourier Transformation
IMF	Interplanetary Magnetic Field
INT	Integer
LH	Lower-Hybrid
LHS	Left-Hand-Side
LTE	Local Thermal Equilibrium
MHD	Magneto-Hydro-Dynamic
MLat	magnetic latitude
OEDIPUS	Observations of Electric-field Distributions in the Ionospheric Plasma - a Unique Strategy
RHS	Right-Hand-Side
RM	Relaxation Model
SMI	Solar-wind–Magnetosphere–Ionosphere
SOHO	Solar and Heliospheric Observatory
SuperDARN	Super Dual Auroral Radar Network
UH	Upper-Hybrid
VLF	Very Low Frequency
WPI	Wave-Particle Interaction

List of Symbols

$\mathbf{A}$	vector potential
a_0	distribution coefficient
a_1, a_2	components of a_0
A_0	back-mapping coefficient
b_1, b_2, b_3	intermediate parameters
B	magnitude of $\mathbf{B}$
B_1, B_2	back-mapping coefficients
B_y	Y-component of IMF
B_{sw}	magnitude of $\mathbf{B}_{sw}$
$\mathbf{B}$	Auroral F-region geomagnetic field
$\mathbf{B}_I$	ionospheric magnetic field
$\mathbf{B}_{sw}$	solar-wind magnetic field
c_0	back-mapping coefficient
c_d	dimensionless coefficient related to E_c/B
c_k	dimensionless coefficient related to K
C	constant
$C_{1\sim3}$	coefficients in η
C^*	coefficient less than 1
D'	ion Mach number
e	elementary charge
$\hat{\mathbf{e}}_{r,\phi,z}$	cylindrical unit vectors
E	magnitude of $\mathbf{E}$
E_0	E at $y = 0$
$E_\parallel$	E component along $\mathbf{B}$
E_c	radially linear -E_r at R_c
E_r	magnitude of $\mathbf{E_r}$
E_x	x-component of E
$\mathbf{E}$	electric field
$\mathbf{E}_I$	ionospheric electric field
$\mathbf{E_r}$	radial electric field
$\mathbf{E}_{sw}$	solar-wind convection electric field
F	equivalent function of f_i
$\mathbf{F}$	arbitrary vector
$f(r)$	electric field function
f_i	O^+ distribution function
f_{i1}	time-free part of f_{iCfree}
f_{i2}	time-free part of f_{iCnal}
f_{iCfree}	collision-free part of f_i
f_{iCnal}	collisional part of f_i
f_n	O distribution function
g	relative velocity magnitude
g_i	1-D ion distribution function
$\mathbf{g}$	gravitational acceleration
h	altitude
$h_{2\pi}$	ratio of ω and Ω
$h(\alpha)$	integral related to a_0
H	Hamiltonian
$I(\alpha)$	integral related to a_0^2
I_0	zeroth-order modified Bessel function
$I_{1\sim6}$	velocity moment parameters
$I_{001\sim016}$	distribution integrals
$I'_{001\sim016}$	
$J_\parallel$	magnitude of $\mathbf{J}_\parallel$
$\mathbf{J}$	total current
$\mathbf{J}_\parallel$	"Region 1" field-alighed current
$\mathbf{J}_\perp$	solar-wind driven perpendicular current
$\mathbf{J}_{I\perp}$	solar-wind driven perpendicular current at ionospheric heights
k_b	Boltzmann constant
l	integer
K	angular momentum
L	characteristic length in $\hat{\mathbf{y}}$; Lagrangian
m	particle mass
m_e	electron mass
m_i	O^+ mass
m_n	O mass
n_0	Nonuniform initial O^+ density at maximum
n_{0r}	modified background O^+ density
n_e	electron density

δn_e	electron space-charge density	t	time
		t_0	initial time E_r is turned on
n_i	O^+ density	$t_{1,2,\cdots}$	pulsating moments of f_i
δn_i	ion space-charge density	T	O^+ cyclotron period; ion kinetic energy
n_{e0}	initial electron density		
n_{i0}	uniform O^+ density at equilibrium	$T_\parallel$	O^+ parallel temperature
		T_0	O^+ equilibrium temperature
n'_{i0}	initial O^+ density after a transition time	T_i	O^+ temperature
		T_n	O temperature
n_n	O density	T_r, T_ϕ	T_i components
N_i	intermediate parameter for n_i	T_Ω	O^+ gyro-period
p	solar wind plasma pressure	u_r, u_ϕ	components of $\mathbf{u}_i$
$\mathbf{p}$	canonical momentum	$\mathbf{u}_i$	O^+ bulk velocity
p_0	O^+ equilibrium pressure	$v_\perp, v_\parallel$	$\mathbf{v}_i$ components
$p_{r,\phi,z}$	components of generalized momentum	v_0	ion initial speed
		$v_{\mathrm{d}r}, v_{\mathrm{d}\phi}$	$\mathbf{v}_\mathrm{d}$ components
$p_{rr}, p_{r\phi}$	components of $\mathbb{P}$	v_i	magnitude of $\mathbf{v}_i$
$p_{rz}, p_{\phi r}$		v_r, v_ϕ, v_z	cylindrical $\mathbf{v}_i$ components
$p_{\phi\phi}, p_{\phi z}$		$v_{r0}, v_{\phi 0}$	initial v_r, v_ϕ
$p_{zr}, p_{z\phi}$		v_{th}	ion thermal speed at equilibrium
p_{zz}			
P	potential energy	v_{Te}	electron thermal speed at equilibrium
P_r	potential energy at r		
P_{r0}	potential energy at r_0	v_{x0}, v_{y0}	x, y-components of v_0
P_{rr0}	potential energy difference from r_0 to r	$\mathbf{v}_\mathrm{d}$	ion drift (GC) velocity
		$\mathbf{v}_i$	ion velocity
q_0	O^+ equilibrium $m_i v_{th}^3$	$\mathbf{v}_n$	neutral velocity
q_r, q_ϕ	components of $\mathbf{q}_i$	V	complex variable
$\mathbf{q}_i$	heat flow	V_r, V_ϕ	u_r, u_ϕ independent of r
r, ϕ, z	cylindrical coordinates	$\mathbf{V}_{sw}$	solar-wind velocity
r_0	initial radial position	x_0	intermediate parameter
r_T	O^+ thermal gyroradius	x, y, z	Cartesian coordinates
R_E	Earth radius	Z	complex variable
R_c	cylindrical radius at which $E_r = -E_c$	Z'	comoving Z
		$\hat{\mathbf{z}}$	axial unit vector
$R_\mathbf{v}$	velocity radius		
$\hat{\mathbf{r}}$	radial unit vector		
$\mathbf{r}, \mathbf{v}$	phase-space vectors	α	phase angle variable
$\mathbf{r}_0, \mathbf{v}_0$	initial $\mathbf{r}, \mathbf{v}$	α_{0c}	distribution coefficient related to $n_{i0}(r_0)$
s	field-aligned distance		

$\beta_{1\sim3}$	distribution coefficients related to $n_{i0}(r_0)$	Ψ	gravitational potential
		φ	scalar potential
γ	ratio of specific heats	χ	extra parameter in f_i related to $n_{i0}(r_0)$
Γ	intermediate parameter		
Δf_i	leading-order correction of f_i	ω	O^+ cyclotron frequency in radially linear electric fields
$\Delta\langle v_r\rangle$	leading-order correction of $\langle v_r\rangle$	ω_p	plasma frequency
		ω_r	comoving angular speed
ϵ_0	permittivity of space	ω_{pe}	electron plasma frequency
ε	phase-angle residual	ω_{pi}	ion plasma frequency
ε_0	back-mapping coefficient	ω_{LH}	lower-hybrid frequency
η	integration coefficient	ω_{UH}	ion or electron upper-hybrid frequency
θ	phase angle; center-of-mass scattering angle	Ω	solid angle
		Ω_i	O^+ gyrofrequency
ι	degrees of freedom	Ω_e	electron gyrofrequency
κ	coefficient in $n_{i0}(r_0)$	Ω_r	Ω_i caused by B_r
λ	characteristic speed related to ω_{pi}	Ω_z	Ω_i caused by B_z
ν_{in}	ion-neutral collision frequency		
Ξ	total energy	∇	spatial gradient
ρ	solar-wind mass density	$\nabla_\perp$	spatial gradient perpendicular to magnetic field lines
ρ_i	O^+ mass density		
σ_{in}	differential scattering cross section	$\nabla_{\mathbf{v}}$	velocity gradient
		$\langle\cdots\rangle$	average of $\cdots$
$\mathbf{\Sigma}_\perp$	ionospheric height-integrated conductivity	$\mathcal{E}$	time dependent E_c/B
		$\mathcal{E}_\perp$	perpendicular energy gain due to WPI
$\vec{\sigma}$	ionospheric conductivity		
ϕ_0	back-mapping coefficient	$\mathbb{P}$	pressure tensor

Chapter 1

Introduction

1.1 Background

1.1.1 Ion velocity distributions in space

In local thermal equilibrium (LTE), the ion distribution function is described by a Maxwellian distribution. However, in the solar-terrestrial system, numerous non-Maxwellian distributions have been found with non-equilibrium characteristics such as beams, temperature or pitch-angle anisotropies. For example, the SOHO spacecraft measured the distribution function of the coronal base and the extended solar-wind acceleration region between 2 and 10 solar radii. Coupled with interplanetary particle measurements going back several decades, the observations strongly suggest that collisionless particles exhibit non-Maxwellian velocity distributions with anisotropic ion temperatures and differential outflows (*Cranmer* 2002).

Another example of large distortions from equilibrium is the Io plasma torus (*Steffl* 2005). The tidal heating of Io's interior produces volcanos which expel neutrals (mostly O and S atoms) outward. Through electron impact and charge exchange reactions, the neutrals convert to ions (very intense emissions are seen for O^+, O^{2+}, S^+, S^{2+}, and S^{3+}). Voyager observations demonstrate that at 65 km/s the S^+ velocity distribution has a peak and that of O^+ has a sharp shoulder, while other ions could be more Maxwellian-like (*Banaszkiewicz* & *Ip* 1993). For electrons, Voyager and Galileo spacecrafts suggest that they may actually be non-thermal or at least have a non-thermal, high-energy tail (*Frank* & *Paterson* 2000).

In addition, in both the upstream and downstream regions of the Earth's bow shock, the Interball/Tail-probe satellite detected that the upstream ion population

has a ring-like (or, halo) distribution, while in the downstream, the distribution has a hot bell-like core and a flat tail (*Yermolaev et al.* 1997). Specifically on field-aligned beams upstream of the bow shock, Cluster observations reported that: (1) parallel to the magnetic field, the distribution is Maxwellian, and (2) perpendicular to the magnetic field, it has a non-thermal, high-energy tail, bringing about a ratio of $\sim$3 between the perpendicular and parallel temperatures (*Meziane et al.* 2006).

Moreover, at altitudes ranging from 1000 km up through one Earth radius and beyond, there is another kind of non-Maxwellian distribution, ion conics (*Yau et al.* 1984). Rocket and satellite measurements showed that ions are concentrated into cones in velocity space under different conditions, and the distribution peaks at specific pitch angles, respectively.

Even below 1000 km, many direct observations have also shown the ion velocity distributions to depart from the Maxwellian shape over wide areas. In particular, the retarding potential analyser onboard AE-C satellite has produced convincing evidence for ion velocity distributions with flat-top shapes compared to Maxwellians (*St-Maurice et al.* 1976). The EISCAT incoherent scatter radar also detected the flat-top-shaped distributions in poleward ion flow bursts in the dayside auroral ionosphere (*Lockwood et al.* 1987). The distributions were observed whenever the ion drift exceeded the neutral thermal speed.

Another type of low-altitude non-Maxwellian ion velocity distribution has been found in high-resolution GEODESIC rocket experiments (*Burchill et al.* 2004). It is crescent-shaped in velocity space with a ring pattern, and was found in lower-hybrid (LH) cavities. At 980 km altitude, 12 sequenced images were produced as the payload flew through one cavity, displaying non-thermal distributions of transversely-heated ions (*Bock* 2005). Some of the distributions revealed tails associated with the energization of the ion population (*Knudsen et al.* 2004).

Artificial plasma disturbances can also produce non-Maxwellian distributions. For instance, two dedicated burns of the space shuttle engines were implemented over the Millstone Hill incoherent scatter radar (*Bernhardt et al.* 2005). The radar recorded ionospheric density depressions resulting from recombination of the molec-

ular ions with electrons. At the same time, radar spectra revealed unusual signatures that may have been produced by ion ring-beam distributions.

1.1.2 Goal of the present research

From the above we can see clearly that non-Maxwellian distributions are frequently present in different regions in geospace. Several possible causes have been proposed for the deviation of the distribution from the Maxwellian equilibrium configuration (*St.-Maurice & Schunk* 1979):

(1) it can be a consequence of the collisionless nature of the medium, particularly in the presence of large or rapidly varying forces acting on the medium, (2) it can occur when a minor constituent of a gas mixture experiences a force (say, $\mathbf{E}\times\mathbf{B}$ drift, where $\mathbf{E}$ and $\mathbf{B}$ represent electric and magnetic fields, respectively) that differs from the forces acting on the major constituent, (3) it can be the result of ion and neutral species chemistry, producing kinetic energies which are substantially different from thermal energies.

For the research related to this thesis, we will study how the interplay between the auroral ionospheric plasma and the $\mathbf{E} \times \mathbf{B}$ drift affects the ion velocity distribution with and without collisions with neutrals, in the presence of transverse electric fields that change spatially and temporally. As shown below in Section 1.3, there are many geophysical situations in auroral regions where the localized electric fields vary quickly in space and time.

1.1.3 Importance of the problem

The importance of gaining a deep understanding of ion velocity distributions in the ionosphere cannot be understated. First, this is simply a case of making sense of the observations. For instance, when we observe conics, or horseshoe distributions, it would be highly desirable to understand how they form, and to test the data against particular theories.

Secondly, a large departure from an equilibrium Maxwellian distribution goes hand in hand with important modifications to transport properties. For exam-

ple, conics are very efficient at 'expelling' ionospheric ions into the magnetosphere through a mirror effect. Likewise, a strong temperature anisotropy will modify the vertical transport, and strong skewness will create heat flow, etc.

Furthermore, a proper interpretation of ionospheric measurements (satellites, rockets, radars) often depends on a knowledge of the velocity distribution. In the data inversion process of the satellite measurements, for example, *St-Maurice et al.* (1976) found that, if the temperature is above 2000 K, the interpretation can be seriously affected when the normally assumed ion Maxwellian distribution is used. For example, the atomic to ion molecular ion density ratios can be affected by a factor of 2 or more, and for the very high temperature data (> 3000 K) the ion temperature can be underestimated by as much as 2700 K.

Similar problems also exist in the spectral analysis of the radar waves scattered incoherently from the ionosphere above 150 km. At these altitudes, the ion-neutral collision frequency is small compared to the ion gyrofrequency. *Raman* (1980) and *Raman et al.* (1981) found that electric fields larger than 45 mV/m could cause a serious underestimation of the electron-ion temperature ratio, sometimes by as much as a factor of 2. This results in an error of several hundred degrees Kelvin in the interpreted electron and ion temperatures.

Last but not least, large departures from Maxwellian may play a role in the excitation of plasma micro-instabilities. In the auroral F region, for example, if the perpendicular electric field exceeds $\sim$50 mV/m, the non-Maxwellian distribution may excite short wavelength instabilities of $\sim$10-20 cm (*Ott* & *Farley* 1975; *St.-Maurice* 1978).

1.1.4 Focus and organization

The thesis focuses on the high-latitude ionospheric ion velocity distributions, in various inhomogeneous electric field configurations, with and without time dependence, and under collision-free and collisional conditions. The problem is studied in cylindrical geometries.

For the remainder of this chapter, we start with a brief discussion of different

scales of electric fields that are formed in the high-latitude ionosphere. Then, we give a review of earlier work on non-Maxwellian distributions produced by the introduction of strong electric fields in the ionosphere. We finish the chapter with a description of the work presented in subsequent chapters.

1.2 Large scale convective electric fields

In auroral regions, the ionosphere is permeated by strong electric fields which can be as high as several hundred mV/m. Contrary to those at other latitudes, these electric fields are not produced by neutral wind dynamos, but rather by processes that go back to the solar-wind–magnetosphere–ionosphere (SMI) electrodynamic coupling processes. Fig.1.1 shows a cartoon of the SMI system (*Curtis* 2005). Every part is labeled for the geospace (left panel) and the magnetosphere (right panel). The electrodynamics in the SMI system is described in great detail by, e.g., *Akasofu* (1977,1981a,b); *Kan & Akasofu* (1989); *Lyon* (2000), and *Oulu Space Physics Group* (2006).

The boundary between the solar wind and the magnetosphere is the magnetopause. Roughly, it has the shape of a bullet immersed into the solar wind. On the dayside (upstream) of the Earth, the dynamic pressure of the solar wind compresses the magnetosphere. A bow shock is thus formed which separates the solar wind and the magnetopause at about 10-12 Earth radii (R_E) away from the Earth. The region between the bow shock and the magnetopause is called the magnetosheath. The reconnection between the interplanetary magnetic field (IMF) and the geomagnetic field on the dayside leads to funnel-shaped areas, called the polar cusps. Through the cusp, the magnetosheath plasma directly enters into the magnetosphere. On the nightside (downstream), the magnetopause is highly elongated with a radius of 20-25R_E and stretches well past 200R_E, forming the magnetotail. The night-side magnetosphere consists of lower density tail lobes and a higher density plasma sheet.

The solar wind interacts with the magnetosphere in two ways. One is the quasi-viscous interaction (*Ratcliffe* 1972), as shown in the upper panel of Fig.1.2, and the other is the magnetic merging and reconnection (*Dungey* 1961), as shown in the lower

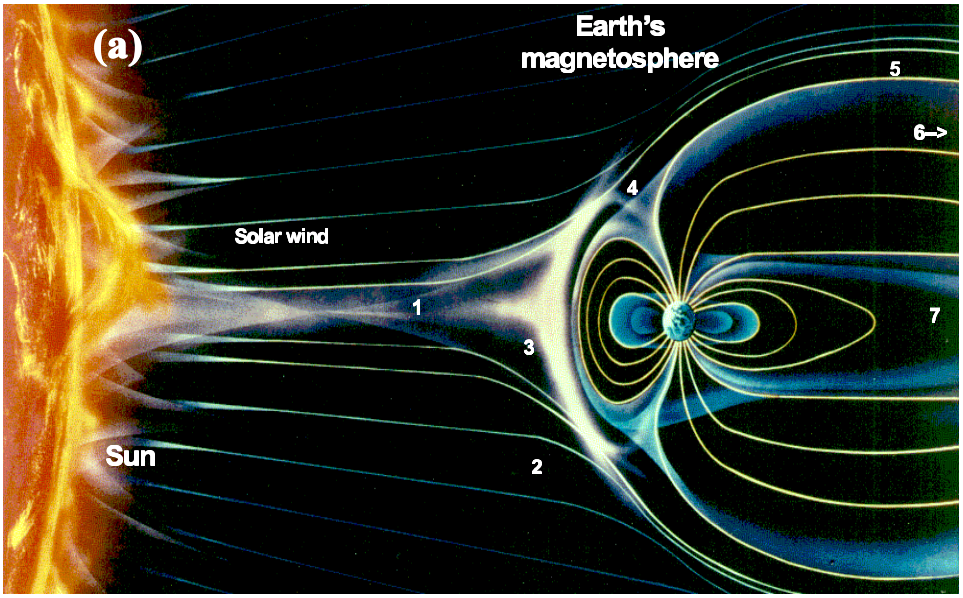

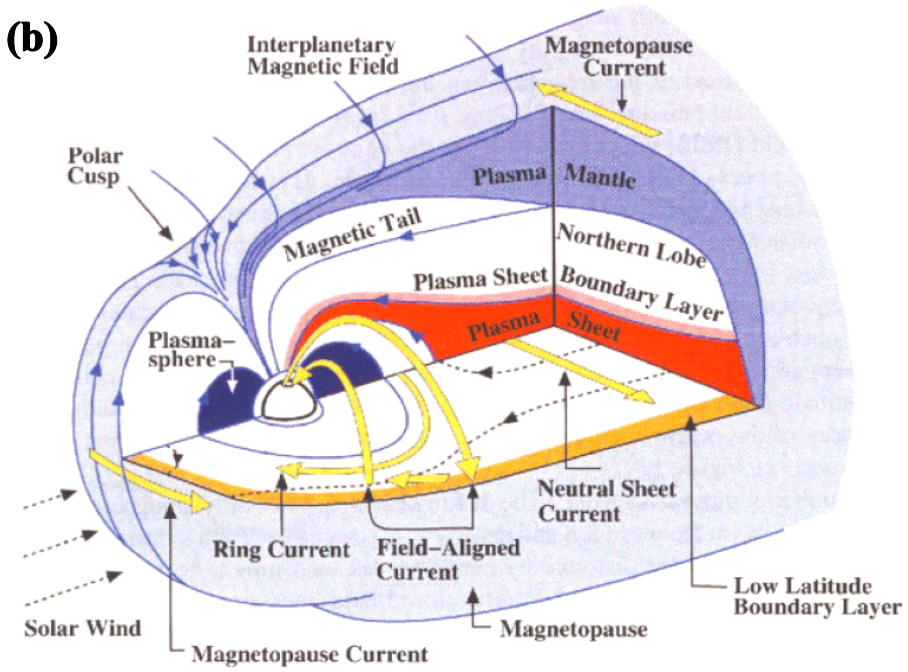

Figure 1.1: Solar-wind–Magnetosphere–Ionosphere (SMI) system (*Curtis* 2005). (a) Geospace; (b) Magnetosphere.

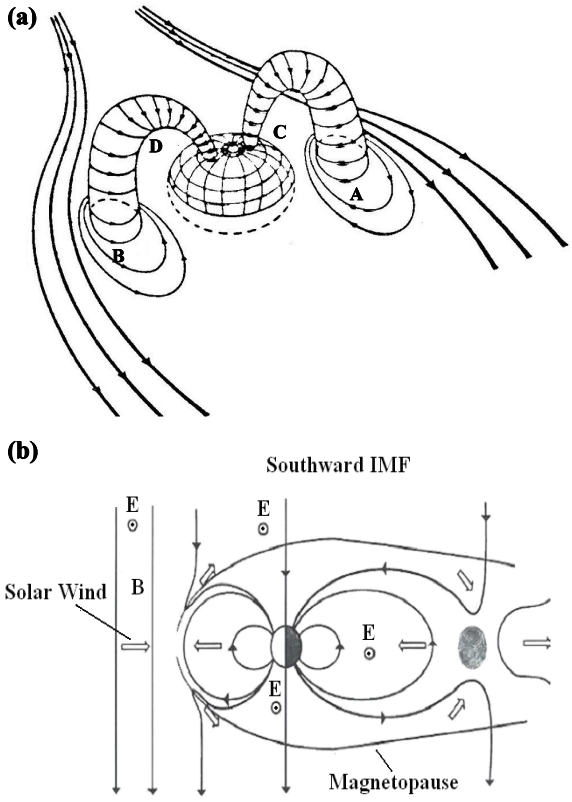

Figure 1.2: Two types of the solar wind-magnetosphere interaction. (a) Quasi-viscous processes (*Ratcliffe* 1972); (b) Magnetic merging and reconnection (*Dungey* 1961).

panel of Fig.1.2. In the quasi-viscous mode, the solar wind produces circulatory shear flow of plasma which creates a drag at A and B. The drag is carried by magnetic field lines on the tubes AC and BD to enter the low ionosphere at C and D. At the ionospheric footprint of this pattern, a two-cell pattern is formed, as shown in Fig.1.3(a). In the figure, the green and grey shading in both diagrams indicate the auroral oval and polar cap.

For the magnetic merging and reconnection mode, *Dungey* (1961) described a cyclical motion driven by the magnetic reconnection with the solar wind. This is believed to be the major process that transports mass, momentum, and energy from the solar wind into the magnetosphere. Fig.1.2(b) illustrates a large-scale convection

cycle when the IMF and geomagnetic field lines are antiparallel to each other in the dayside magnetosphere. This pattern is now commonly referred to as the "Dungey cycle". When the southward IMF line in the solar wind reaches the magnetopause to merge with a closed northward geomagnetic field line (i.e., both ends attached to the Earth), an open field line (that is, one end attached to the Earth, and the other end in the IMF) is produced to stretch out into the interplanetary space. The solar wind sweeps the open lines over poles and stretches them into a long magnetic tail downstream of the Earth, forming the northern and southern "lobes". In the tail, the field lines sink towards the tail center. As the oppositely directed lines anchored in the northern and southern lobes meet with each other, magnetic reconnection happens in the tail current sheet. After reconnection, disconnected field lines are formed on the downstream side and flow away with the solar wind. On the upstream side, closed field lines convect back towards the Earth and return to the dayside magnetosphere. There, they participate in the convection cycle again. Similar to the viscous process (but much more effective), this cycle also gives rise to a two-cell pattern at the ionospheric footprint, as shown in Fig.1.3(a).

However, the convection pattern is different if the IMF changes. Fig.1.3(b) shows a case when the IMF is northward. In this case, the pattern becomes four cells. Moreover, the IMF B_y is important for the symmetry of the convection patterns relative to the noon-midnight magnetic meridian. For the two-cell pattern, at $B_y = 0$, the cells are symmetric. For $B_y > 0$, the dusk cell dominates, and for $B_y < 0$, the dawn cell dominates. For the four-cell pattern, at $B_y > 0$, the inner morning cell dominates; at $B_y < 0$, the inner dusk cell dominates [see, e.g., *Drayton* (2006) for more details, and *Rich & Hairston* (1994), *Hesse et al.* (1997) for much more complicated patterns]. In any case, *Reiff & Burch* (1985), *Ruohoniemi & Greenwald* (1996), and the *Oulu Space Physics Group* (2006) have provided the following basic convection features: (1) the streamlines are equipotential lines, and no two streamlines cross one another; (2) the total convection pattern has contributions jointly from both the quasi-viscous interaction and the magnetic merging process. Even when the IMF is around zero, the former can still produce a two-cell pattern; and (3) for a southward

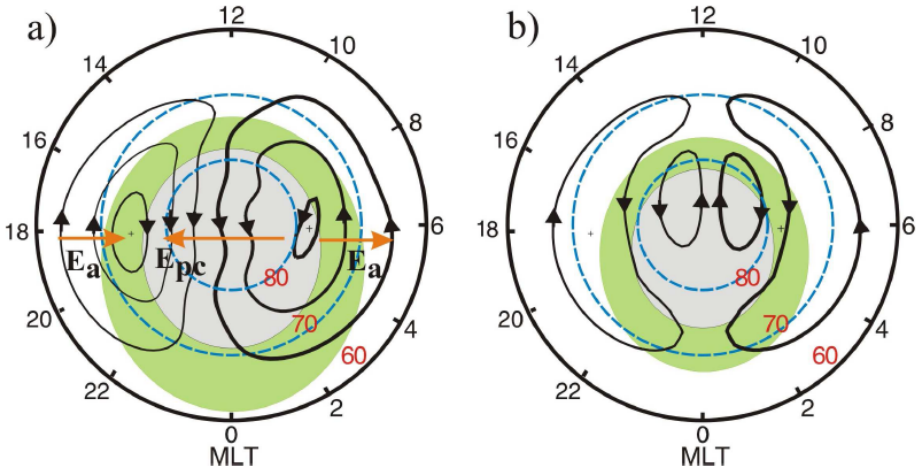

Figure 1.3: Convection patterns of the high latitude ionospheric plasma: (a) Ionospheric electric fields and typical two-cell convection pattern for a southward IMF and $B_y = 0$. (b) Four-cell convection pattern for a strongly northward IMF and $B_y = 0$. The green and grey shading in both diagrams indicate the auroral oval and polar cap, respectively. Selected from *Drayton* (2006).

IMF, the convection pattern is usually made of two cells, and for a northward IMF, the convection patterns may consist of several cells.

The large-scale solar wind (velocity $\mathbf{V}_{sw}$) flowing in open field lines (magnetic field $\mathbf{B}_{sw}$) plays two roles following the merging process (*Kelley & Heelis* 1989). On one hand, it produces a convection electric field $\mathbf{E}_{sw} = -\mathbf{V}_{sw} \times \mathbf{B}_{sw}$ (upper left panel, Fig.1.4). This field is partially shorted by the polar cap ionosphere. As a result, electrons are deposited at the duskside, and ions on the dawnside of the Earth at $70° - 80°$ magnetic latitude (MLat). Another contribution comes from the perpendicular current, $\mathbf{J}_\perp$, driven by the solar wind, which is given by

$$\mathbf{J}_\perp = \frac{1}{B_{sw}^2}\left(\rho \mathbf{B}_{sw} \times \frac{\mathrm{d}\mathbf{V}_{sw}}{\mathrm{d}t} + \rho \mathbf{g} \times \mathbf{B}_{sw} + \mathbf{B}_{sw} \times \nabla p\right) \tag{1.1}$$

where ρ is the plasma density, $\mathbf{g}$ the gravitational acceleration, and p the plasma

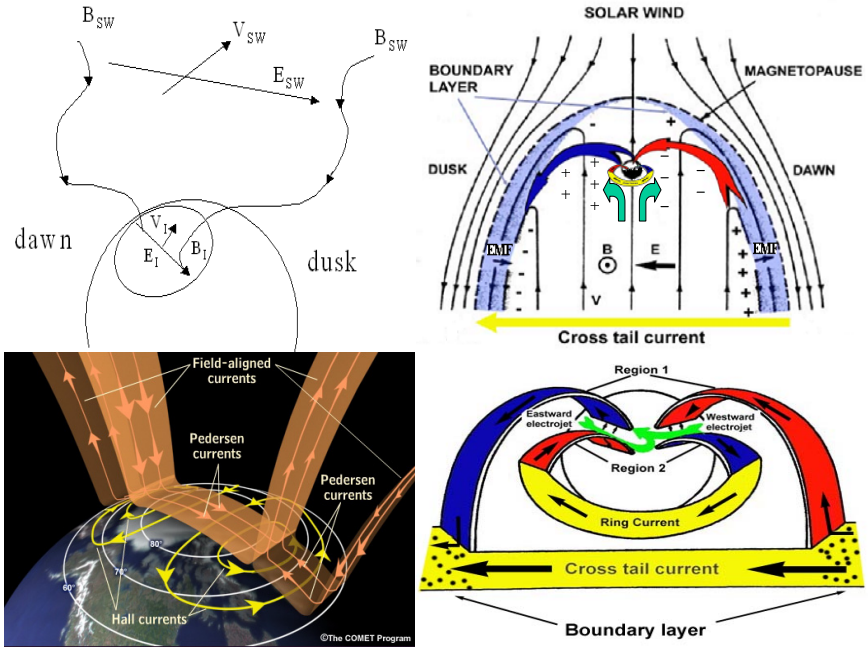

Figure 1.4: Schematic electrodynamic process in the system of solar wind, magnetosphere, and ionosphere. Adapted from *Kelley & Heelis* (1989) (upper left), *Israelevich* (2006) (upper right, lower right), and UCLR http://meted.ucar.edu/hao/aurora/txt (lower left).

pressure.

There are three terms which contribute to $\mathbf{J}_\perp$: the total time derivative, $\mathrm{d}\mathbf{V}_{sw}/\mathrm{d}t$, of the plasma flow, the gravitation, $\mathbf{g}$, and the pressure gradient ∇p. For a a negligible gravitational term and a small pressure gradient, $\mathbf{J}_\perp$ is only determined by the first term. Clearly, $\mathbf{J}_\perp$ is not controlled by $\mathbf{E}_{sw}$ but, rather, by the rate of change in the solar wind momentum through the interaction between the solar wind and the magnetosphere/ionosphere.

The ionospheric field $\mathbf{E}_I$ serves two basic functions (*Kelley & Heelis* 1989). It drives not only a plasma convection in the ionospheric F-region plasma at a speed $\mathbf{V}_I = \mathbf{E}_I \times \mathbf{B}_I / B_I^2$ (where $\mathbf{B}_I$ is the ionospheric magnetic field), but a perpendicular current $\mathbf{J}_{I\perp} = \mathbf{J}_\perp$ at ionospheric heights by $\mathbf{J}_{I\perp} = \vec{\sigma} \cdot \mathbf{E}_I$ (where $\vec{\sigma}$ is the ionospheric conductivity) as well. "Region 1" field-aligned current $\mathbf{J}_\parallel$ (also called Birkeland currents; upper right and two lower panels, Fig.1.4) can thus be obtained by the

zero divergence of the total current $\mathbf{J} = \mathbf{J}_\perp + \mathbf{J}_\parallel$: $\nabla \cdot \mathbf{J} = 0$. This means that $\nabla_\perp \cdot \mathbf{J}_\perp + \partial J_\parallel / \partial s = 0$, or, $\Delta J_\parallel = J_\parallel^{top} - J_\parallel^{bottom} = -\int_s \nabla_\perp \cdot \mathbf{J}_\perp \mathrm{d}s = -\nabla_\perp \cdot (\mathbf{\Sigma}_\perp \cdot \mathbf{E}_I)$ (where s is the field-aligned distance, and $\mathbf{\Sigma}_\perp$ the height-integrated conductivity). The current closes via horizontal ionospheric Pedersen currents, "Region 2" field-aligned currents, and the ring current. The ring current lies in the inner part of the plasma sheet, where ions and electrons drift in opposite directions around the earth due to the magnetic field gradient and curvature.

"Region 2" currents flow along closed magnetic field lines. They are related to the separation of charges in the inner magnetosphere. The charges come from the magnetotail plasma driven sunward by the cross-tail convective electric field $\mathbf{E}$. As they drift, relatively energetic electrons are moving dawnward around the Earth due to the presence of the gradient-curvature of the magnetic field. By contrast, relatively energetic ions are moving duskward. In auroral regions, the charges flow along magnetic field lines.

1.3 Electric field structuring

The large-scale convection electric field in the high-latitude regions provides a fair context for the average flow. However, a multitude of measurements from low-altitude satellites, rockets, radars, and from optical means have shown that electric field measurements with insufficient temporal resolution can sometimes hide very large fluctuations and sharp transitions over a wide range of spatial and temporal scales.

As a first example, Fig.1.5 reproduces observations made by the S23L1 rocket around an auroral arc (*Marklund et al.* 1982). The fourth panel from the top discloses that over a short distance electric field went down from ∼110 mV/m to ∼20 mV/m. The drop occurred in about 10 s, that is, on a scale of 10 km.

Moore (1996) studied a more complicated case. At ∼500 km altitudes, the ARCS-4 rocket obtained ionic O^+ and the DC electric field data shown in Fig.1.6. Some 570 s after launch time, the electric field oscillated violently. Note that the authors argued that the oscillations were related to vortical structures (more on this below).

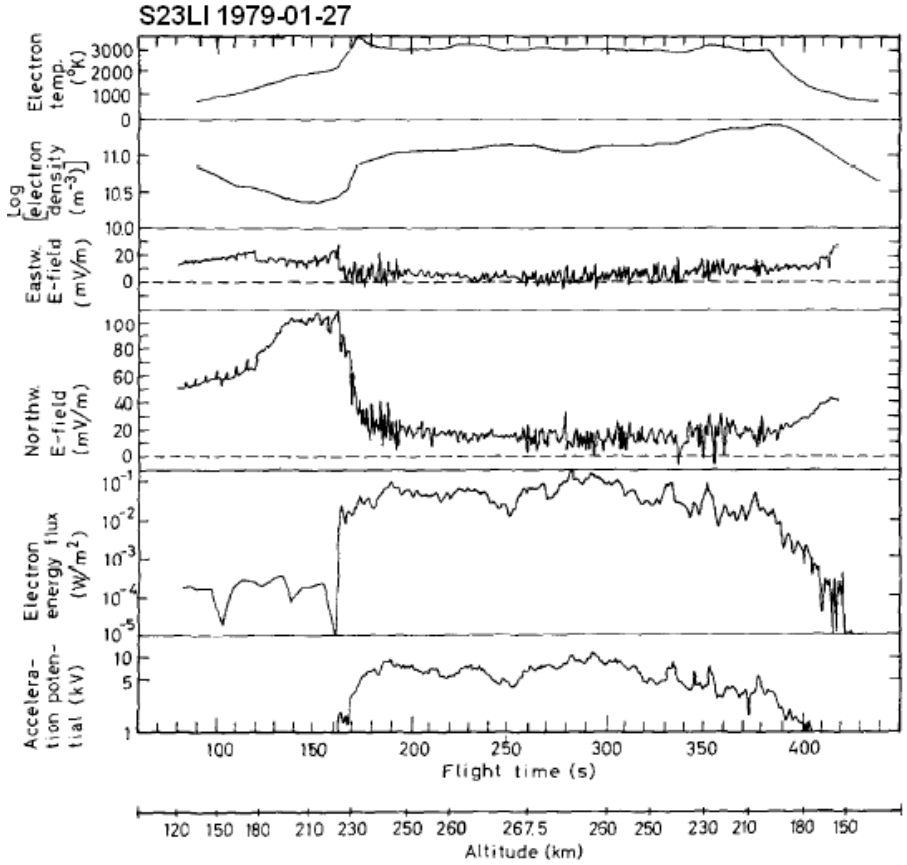

Figure 1.5: S23LI rocket measurements of the sharp transition region associated with a discrete auroral arc (*Marklund et al.* 1982). From top to bottom: electron temperature (°K), electron density (m^{-3}), eastward and northward components of electric field (mV/m), particle energy flux (W/m^2), and acceleration potential (kV) vs. flight time (s) and altitude (km).

The perpendicular drift could soar up to 3 km/s, with a velocity shear ∼0.75 m/s per meter or more. At similar altitudes, *Earle et al.* (1989) observed an even more structured event, namely, a change of 180 mV/m over 363 m, corresponding a shear of ∼11 m/s per meter. More strikingly, they even recorded a change larger than 200 mV/m over a short distance with a shear of ∼25 m/s per meter.

In addition to arcs, there are several examples of cylindrical structures or "vortices" at high latitudes. Some vortices have large scales (500-1000 km in diameter) and are seen easily by, e.g., radars like SuperDARN. Some of them have been la-

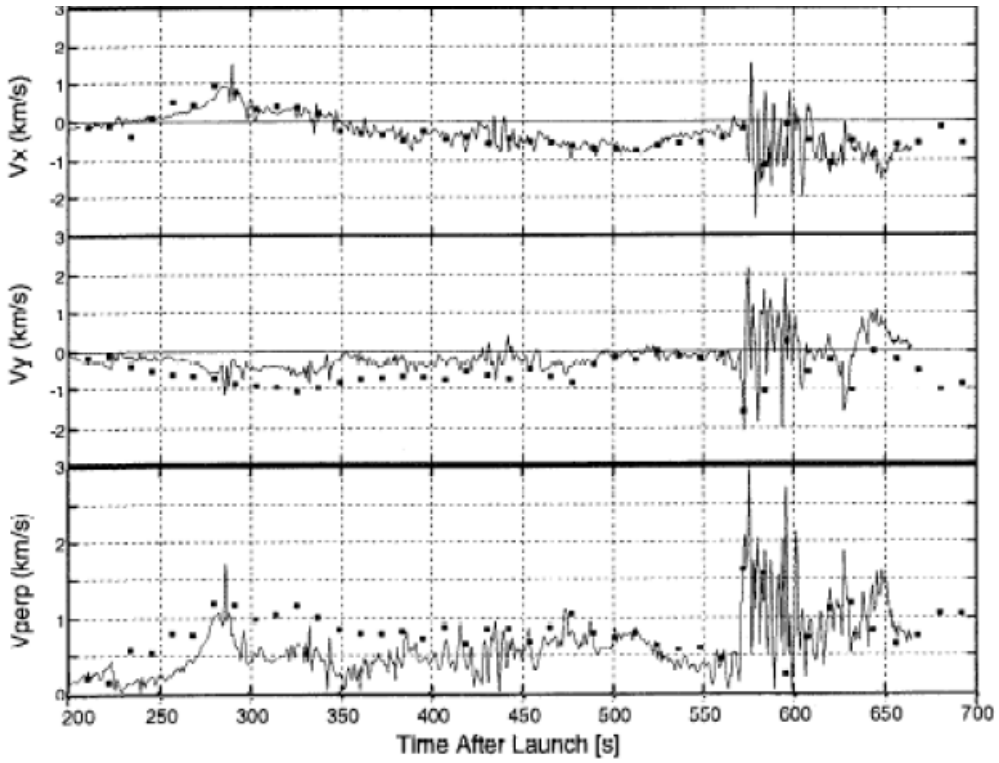

Figure 1.6: 3D plasma drift inferred from ARCS-4 rocket data of O^+ (squares) and DC electric field (lines). X-direction northward, and Y-direction perpendicular to X. Selected from Fig.11 in *Moore* (1996).

beled as "quasi-stationary convection vortices", and have been shown to be closely connected to the region-1 field-aligned currents, with a lifetime ∼10-20 min (up to 50 min). Fig.1.7 gives an example of such a giant vortex (∼30 min in lifetime, northward IMF, geographic latitude and longitude, solid curves represent the magnetic latitudes 70° and 80°) [*Huang et al.* (1998)]. The related potential drop is 5-10 kV. The center of the vortex was considered to link with a stable, upward, filament-like, field-aligned current (*Alexeev et al.* 1997).

At 400-500 km altitude, smaller vortices have also been observed by rockets. A multi-instrumental measurement campaign involving magnetometer, rocket, and all-sky camera data detected spirals of about 100 km in diameter. These usually rotate clockwise, but sometimes counterclockwise (*Pietrowski et al.* 1999; *Danielides & Kozlovsky* 2001). They appear at the poleward boundary of the nightside auroral

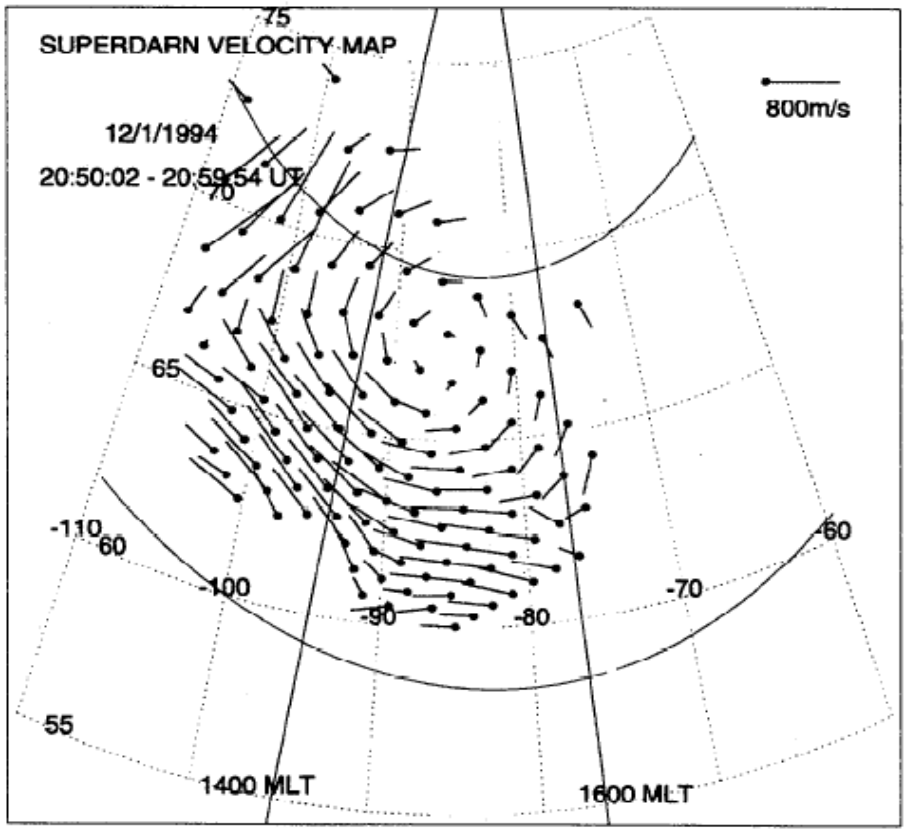

Figure 1.7: SuperDarn map of velocity vectors of a giant vortex (∼30 min in lifetime, northward IMF): Fig.2(c) in *Huang et al.* (1998).

oval. Afterwards, they form a poleward displaced bulge at the pre-or-post midnight sector. Auroral Turbulence II Rocket data (*Pietrowski et al.* 1999), shown in Fig.1.8, demonstrated that the electric field could reach up to 1.1 V/m with a shear 4 m/s per meter or more. The peak shear region (about 1 km) was devoid of precipitation.

Much smaller scales of cylindrical structures have also been confirmed in the topside ionosphere at 500∼1000 km altitudes. They are called lower-hybrid (LH) cavities. They have scales of tens of meters in width (or chord lengths). Fig.1.9 gives an example measured by the GEODESIC & OEDIPUS-C sounding rockets. The panels show the VLF electric field (upper left) & the magnetic field (lower left) (*Bock* 2005), the spatially density-depletion (upper right) (*Knudsen et al.* 2004),

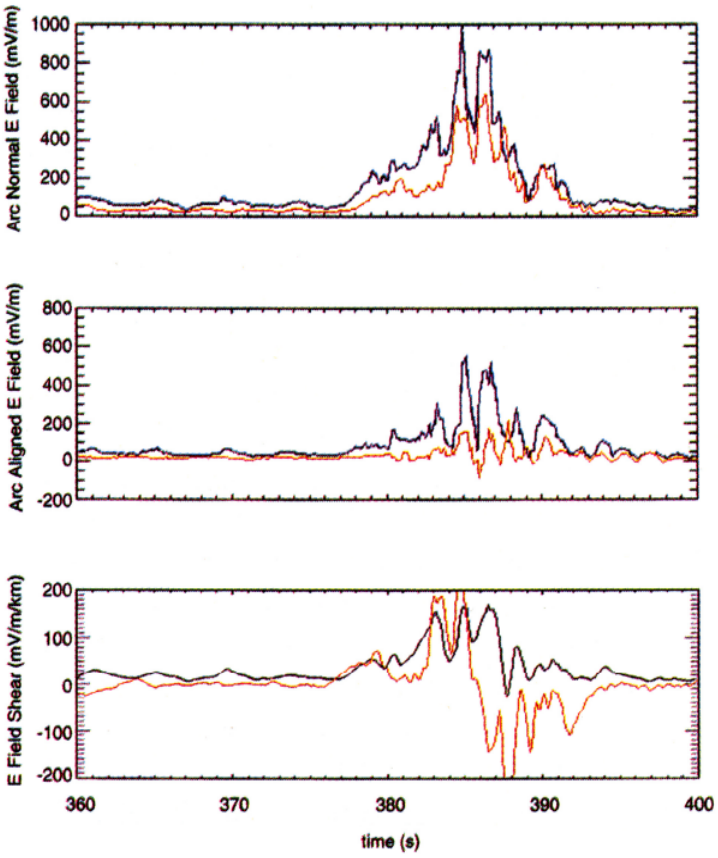

Figure 1.8: Rocket data for vortex electric fields (top and middle panels; blue and red curves correspond to two different payloads, respectively) and field shear (bottom panel; double and single payload measurements in black and red, respectively) (*Pietrowski et al.* 1999).

and count images in velocity space (lower right) (*Bock* 2005). Both the electric and magnetic signals are spikelike, either single-peaked or double-peaked. The electric field gradient can be up to 30 mV/m over a few Debye lengths (several tens of meters).

1.4 Ion velocity distributions

Clearly, in the auroral ionosphere, the transverse electric fields can become very strong locally (up to ∼1 V/m, as shown in the previous section). The regions are ei-

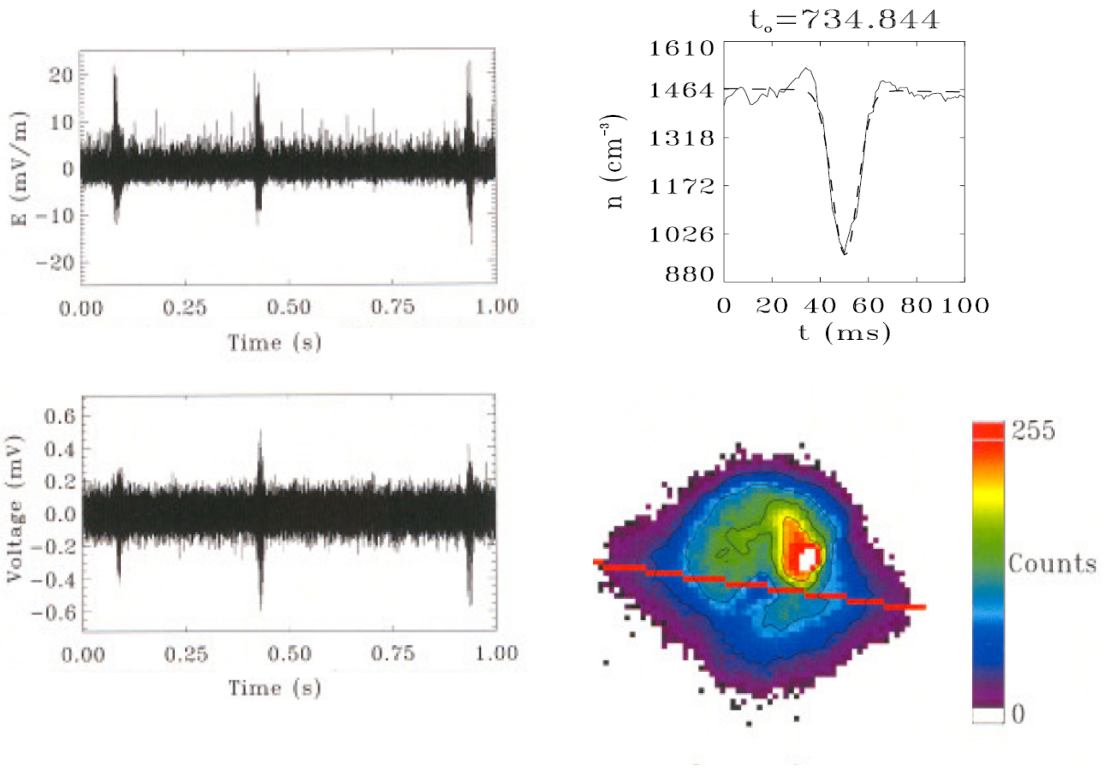

Figure 1.9: Rocket measurements of LH cavities (*Knudsen et al.* 2004; *Bock* 2005).

ther associated with elongated arcs (Cartesian geometry) or cylindrically symmetric. Shears existing in these regions have been observed to reach up to 25 m/s per meter. There are probably higher shears than that. As the spatial and temporal resolution of the observations is improving, more and more such events should be measured.

Once a localized DC electric field **E** is established in a crossed magnetic field **B**, an $\mathbf{E} \times \mathbf{B}$ drift is the result. For strong electric fields, the drift speed can reach several km/s. This drift is considerable compared to the normal ion thermal speed and compared to the thermal speed of the neutral gas with which the ions collide. As a result, there can be strong deviations for ions from a thermal (Maxwellian) velocity distributions (*St.-Maurice & Schunk* 1979). This is true of both the collisional and

collision-free problems. The later applies to time scales shorter than a collision time.

Until now, the study of ion velocity distributions in the ionosphere has been done for a uniform electric field in both collisional and collision-free cases. An initial study involving an inhomogeneous electric field in collisional cases has also been completed. The goal of the present research is to expand our knowledge beyond the early work and to see how ions respond to large electric fields in the ionosphere with arbitrary shears in the cylindrical geometry with and without collisions. To introduce the subject, I now offer a brief review on the subject.

1.4.1 Distributions perpendicular to magnetic field lines: Homogeneous electric fields

Understanding velocity distributions is very important if we are to understand the small-scale physics and the fundamental measurements made by incoherent scatter radars, rockets, and satellites. In physics, knowing what creates the distribution will tell us about the forces that act at any given instant; in experiments, we should rely on a known velocity distribution with the knowledge that we have a good command of what we measure, e.g., the temperature, compositions, etc.

In a pioneering study, *Cole* (1971) determined how far the ion distribution can deviate from the equilibrium Maxwellian in a uniform electric field in the collisionless case. He found that the distribution function is determined completely by the characteristics of ion motion, or, precisely, by the energy conservation of ion motion in the electromagnetic field. By considering an initial Maxwellian ion distribution in the absence of the electric field, he obtained an ion velocity distribution which pulsated about the $\mathbf{E} \times \mathbf{B}$ drift. For $E \geq 10$ mV/m, the average ion distribution started to deviate significantly from a Maxwellian.

Schunk & *Walker* (1972) generalized *Cole*'s work by including the collisional term. Formally, the collision term is described by the Boltzmann collision integral. By expanding the distribution function using a complete orthonomal polynomial series of the products of Sonine polynomials and spherical tensors, the authors obtained a Maxwellian-weighting, infinite-component solution of the Boltzmann equa-

tion. The results were applicable to small distortions from the initial Maxwellian, such as can be found with small electric fields, and/or high ion-neutral collision frequencies. They found that the departure from a Maxwellian was small below 120 km (where the collision frequency is comparable to the ion cyclotron frequency). Above that altitude, the departure was basically the same at all altitudes below 300 km. As with Cole's results, a 10 mV/m electric field was deemed to be strong enough to cause appreciable non-Maxwellian effects.

St-Maurice & *Schunk* (1973,1974) expanded *Schunk* & *Walker*'s work to strong electric fields. They used a simple relaxation model in place of the Boltzmann collision integral. Physically, this model assumes that the target neutral has a velocity $\mathbf{v}_{\mathrm{n}}$, satisfying a Maxwellian distribution. When an ion with velocity $\mathbf{v}_{\mathrm{i}}$ collides with the neutral, the particles exchange velocities ($\mathbf{v}_{\mathrm{n}}$ is replaced by $\mathbf{v}_{\mathrm{i}}$ and vice versa). The ion takes the neutral's Maxwellian velocity distribution in phase space before regaining momentum and energy from the electromagnetic fields. The neutral subsequently moves with the traded velocity until colliding with other neutrals. The time scales over which the entire ion velocity distribution will change is, not surprisingly, ν_{in}^{-1}, a time long enough for all ions to experience roughly one collision.

St-Maurice & *Schunk* (1973,1974) obtained analytical solutions to the Boltzmann equation for all electric field strengths and collision frequencies. In the small collision regime ($\nu_{in} \ll \Omega_i$), namely, above 150 km, the ion distribution formed a torus for electric fields higher than 40 mV/m. By contrast, in a region close to 120 km ($\nu_{in} \sim \Omega_i$), the distribution was bean-shaped for electric fields of 100 mV/m or more. The departure of the ion distribution from a Maxwellian was confirmed by radar measurements [possibly by *Swift* (1975), and later by *Lockwood et al.* (1987)], and, by satellite observations (*St-Maurice et al.*, 1976).

By scaling the analytical results for data analysis purposes, *St-Maurice et al.* (1976) developed a method to retrieve plasma data from the non-Maxwellian distribution in the small collision frequency regime. To explain how the observed velocity distributions were compared to the theory we introduce Fig.1.10 and 1.11. Fig.1.10 displays the shapes of the ion velocity distribution that were calculated form the

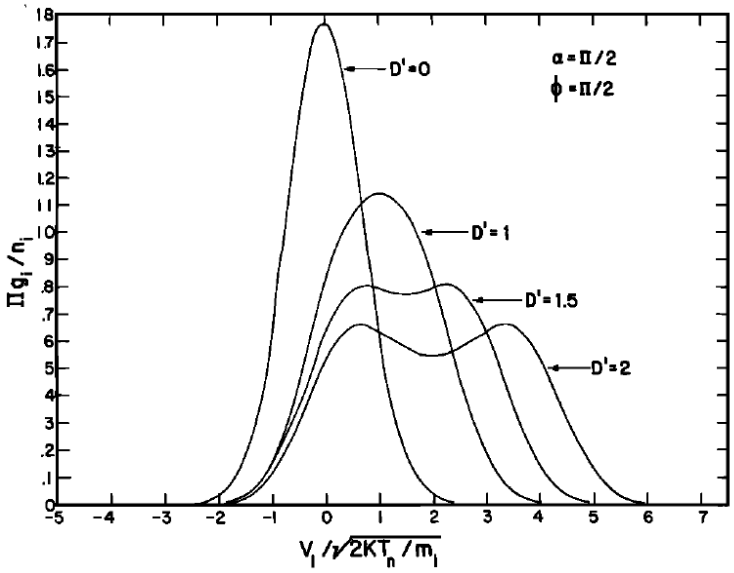

Figure 1.10: Behavior of the one-dimensional velocity distribution $\Pi g_i/n_i$ versus the normalized ion velocity $v_i/\sqrt{2kT_n/m_i}$ for various values of the ion Mach number D' (see text for details). From *St-Maurice et al.* (1976).

Boltzmann equation, using a relaxation model to describe ion-neutral collisions. The parameter D' in this case is the ion Mach number, $(Ec/B)/V_{Tn}$, where V_{Tn} is the neutral thermal speed. In Fig.1.10, $\Pi g_i/n_i$ is the one-dimensional ion distribution function (where "Π" is just "π", g_i is the distribution function perpendicular to the line of sight of the instrument, and n_i is the ion density).

Fig.1.10 shows that, according to the solutions obtained from the simple relaxation model, the shape of the one-dimensional ion velocity distribution function evolves from a singly-peaked Maxwellian form at $D' = 0$ to a double-humped distribution once D' exceeds 1.3. This has to be contrasted with Maxwellian distributions which would be broadened but remain singly peaked no matter what the Mach number would be. This brings us to Fig.1.11 which was obtained by fitting the shape of observed one-dimensional ion velocity distributions under various electric field (and, therefore, ion temperature) conditions. The fitting parameter was called $(Ec/B)/V_{ac}$ instead of D' in this case. In other words, D' in Fig.1.10 becomes a shape parameter called $(Ec/B)/V_{ac}$ in Fig.1.11. Thus, if the observed distributions were found to

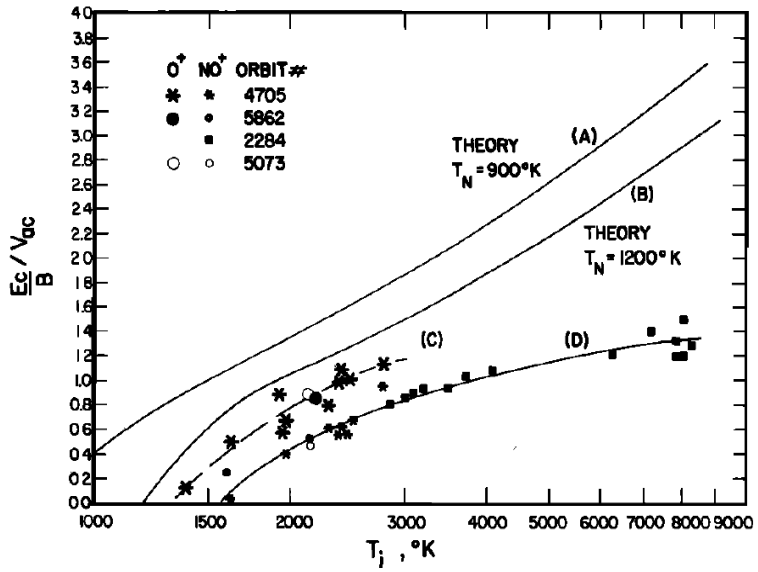

Figure 1.11: Shape of the drift speed Ec/B normalized by the neutral speed V_{ac} as a function of ion temperature T_j ("j" denotes O^+ or NO^+) without scaling (see text for details). From *St-Maurice et al.* (1976).

be Maxwellian, the parameter $(Ec/B)/V_{ac}$ in Fig.1.11 would be entered as zero. If the observed distributions were double-humped, say, like the shape obtained with $D' = 1.5$ in Fig.1.10, then we would enter a value $(Ec/B)/V_{ac} = 1.5$ in Fig.1.11.

Curves A and B in Fig.1.11 are the results of theoretical calculations for the relaxation collision model using neutral temperatures of 800 K and 1200 K, respectively. In these cases, the evolution of the shape parameter $(Ec/B)/V_{ac}$ against ion temperature matches the values of D' in Fig.1.10. Curves C and D in Fig.1.11 show that there is a similar but less pronounced evolution in the shape of the observed distributions. Fig.1.11 shows that (1) the departures of the observed ion velocity distribution from a Maxwellian, as quantified by the shape parameter $(Ec/B)/V_{ac}$ (later called $D*$ in the literature), are smaller than predicted from the simple theory; (2) the O^+ distribution function has larger departures from a Maxwellian than the NO^+ distribution; and (3) double-humped distributions were not observed even though the distributions were much flatter than Maxwellians near their peaks. Fig.1.11 also was used to infer that departures from a Maxwellian were detectable for electric field

strengths as small as 10 mV/m.

From the above, we can conclude that collisions play an important role in determining the shape of ion velocity distributions. Unfortunately, the relaxation collision model is crude. This is why the analytical results had to be scaled to account for observations. Furthermore, for very strong electric fields, the scaling does not always work at least not for O^+ ions. This was demonstrated when *Winkler et al.* (1992) applied a Monte-Carlo computation scheme to the Boltzmann collision intergral. The authors considered both the speed and angular dependence in several types of collisions between ions and a mixture of neutral constituents, all at once. They also included the effect of chemistry, which is important for short lived N_2^+ ions. The results showed that (1) if the electric field reaches ∼125 mV/m, the NO^+ velocity distribution will not change anymore, and will be scalable; (2) for O^+ and N_2^+, if the electric field exceeds 100 mV/m, the distribution becomes very complicated and no simple analytical expression could describe it; (3) any change in electric fields brings about variation in the ion temperature anisotropy, especially for O^+.

1.4.2 Distributions perpendicular to magnetic field lines: Inhomogeneous electric fields

If the electric field is not homogeneous, that is, if there are spatial divergences in $\mathbf{E}$ (and thus shears in the $\mathbf{E} \times \mathbf{B}$ drift), the physical mechanism and mathematical formulations become much more complex than what was presented in the last section in solving the Boltzmann equation. Even the simplest parameter, the ion gyrofrequency Ω_i, changes from $\Omega_i = qB/m_i$ in the homogeneous field to a new definition in the inhomogeneous field.

For example, if the first derivative of the field ($\nabla \cdot \mathbf{E} = \mathrm{d}E_x/\mathrm{d}x$) is nonzero, while the second derivative ($\mathrm{d}^2E_x/\mathrm{d}x^2$) is zero, *Cole* (1976) showed that the effective gyrofrequency ω satisfies $\omega^2 = \Omega_i^2 + \Omega_i \mathrm{d}(E_x/B)/\mathrm{d}x$. In addition, he found that it is possible to accelerate ions when the gyro-radius is larger than the scale length of the potential well. *Rothwell et al.* (1995) stated that for $\mathrm{d}^2E_x/\mathrm{d}x^2 \neq 0$, there are two criteria about the gradients: $\mathrm{d}\left(E_x/B\right)/\mathrm{d}x \geq \Omega_i$, and, $\mathrm{d}^2\left(E_x/B\right)/\mathrm{d}x^2 \geq 3\omega\Omega_i/(8v_0)$

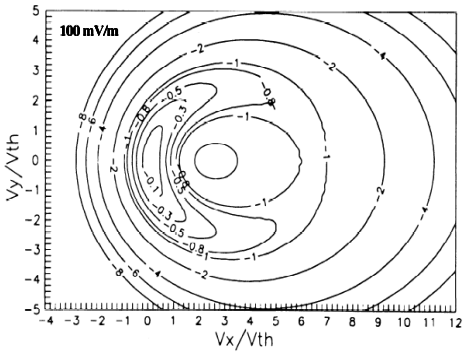

Figure 1.12: Logarithmic contours of ion velocity distributions in the presence of drift velocity shears for a local electric field strength 100 mV/m (*St-Maurice et al.* 1994).

(where v_0 is the initial velocity). For the first condition, the kinetic theory has to be used instead of either ideal or non-ideal MHD theory; if the second one is satisfied, untrapped ions occur. For a more complicated field, $E_x \sim x\mathrm{e}^{-x^2}$, *Rothwell et al.* (1992) and *Anastasiadis et al.* (2004) showed that particles are either trapped or untrapped in the potential well; and, if the characteristic length of the well is comparable to the gyroradius, stochastic heating can occur depending upon initial conditions of the phase angle $\theta = \arctan(v_{y0}/v_{x0})$ (where v_{x0}, v_{y0} are initial velocity components) and kinetic energy.

In the collision-free regime, *Ganguli et al.* (1988) obtained collision-free ion velocity distributions again following the onset of a perpendicular electric field with a linear divergence. The authors had in mind instability calculations in the presence of shears at high enough altitudes, so that collisions would not affect the velocity distributions for a sufficiently long time. After finding the invariants for the problem, the authors used an arbitrary distribution of this invariant without attempting to relate this distribution to a particular initial or boundary condition. This choice of solution may have been valid for a slowly changing electric field in time. However, the thesis shows that the task of actually linking the collision-free distribution even just to simple initial conditions for a fast change in the electric field can actually be surprisingly non-trivial even when all the invariants of the motion are known.

To our knowledge, there has only been one study of more complicated problems to obtain velocity distributions in the presence of perpendicular inhomogeneous electric fields in the collisional regime. The work was done by *St.-Maurice et al.* (1994). To solve the very complicated Boltzmann equation in the nonhomogeneous electric field, the authors selected a model with a relatively simple electric field varying linearly in space along a particular direction, perpendicular to the magnetic field: $\mathbf{E} = E_0(1 + y/L)\hat{\mathbf{y}}$ in Cartesian geometry (where E_0 is the field at $y = 0$, L the characteristic length, y the ion position). Focusing on the collision-dominated case, the authors found that a phase-average model involving ion characteristics could be used to solve for the ion velocity distribution, and associated transport properties.

The calculations were carried out for a simple relaxation collision model; a similar model had been used in earlier work to get the basic physical description of the velocity distribution for the uniform perpendicular electric field case. By comparison to the uniform case, the new velocity distributions in the F region were crescent-(or horseshoe-) shaped, while retaining their symmetries along the electric field direction (in agreement with the fact that Pedersen currents are weak in the F region). The distortions from the toroidal shape were found to be due to the fact that ions coming from more distant points in space had suffered more acceleration and were therefore more energetic than ions coming from closer locations. The study also established that the inhomogeneity in the field had to be on scales of the order of a few gyroradii in order for the departures from the more familiar toroidal shape to be substantial.

To set up the phase-averaging, the model used the phase angle ωt instead of time t in the integration over time. As a result, either the collisionless or collisional velocity distribution could be analytically expressed by a series of Bessel functions. The results showed "horseshoe-shaped" ion distributions as given in Fig.1.12. The stronger the electric field is, the more evident the horse-shoe shape becomes. Note that the mean ion drift velocity is different from the $\mathbf{E} \times \mathbf{B}$ drift velocity in the plots. This was shown to be the result of the shears in the mean flow. In spite of the different geometry, the theoretical results offer some similarities with recent rocket data of LH cavities (*Burchill et al.* 2004; *Knudsen et al.* 2004; *Bock* 2005).

1.4.3 Distributions parallel to magnetic field lines: With or without parallel electric fields

In the magnetosphere-ionosphere coupling, there are three main categories of non-Maxwellian ion outflow fluxes. They are thought to be connected with evaporation, or, wave-particle interaction (WPI), or, a "pressure cooker" effect from the lower ionosphere.

"Evaporation" is triggered when frictional heating increases the ion temperature in the region where collisions with neutrals are frequent enough (below 400 km). The heating is the result of temporary strong electric fields that accelerate the ions to large speeds. The region across which the ions stop colliding with neutrals is called the exobase and is near 400 km altitude (*Loranc & St.-Maurice* 1994; *Lundin & Guglielmi* 2006). Above the exobase, the newly created hot ions gradually replace the colder background ions.Rapidly, a net upward flux of ions is created with relative speeds that can exceed 1 km/s in the high-latitude F-region. By 1000 km altitude, the bi-modal nature of the velocity distribution can be very impressive. The parallel ion velocity distribution becomes a non-Maxwellian between 500 km and 2500 km with two groups of ions with different temperatures, as shown in Fig.1.13.

WPI is commonly accepted as a mechanism responsible for the energy gain of ions that produce conics in velocity space [see, e.g., *Gorney et al.* (1985); *Chang et al.* (1989); *Andre & Chang* (1994)]. Specific mechanisms include perpendicular acceleration through turbulent perpendicular electric fields near the lower-hybrid frequencies at lower altitudes (particularly in the region of discrete auroras), and, the perpendicular heating by broad-band waves overlapping the local ion cyclotron frequency over a large range of altitudes. Especially, the broad-band low-frequency (BBLF) waves extend over very long distances while interacting with ions. Alternatively, the ions could be bouncing between the mirror points of the two hemispheres as they slowly gain perpendicular energy.

Within the WPI mechanism, the presence of a parallel electric field ($E_{\parallel}$) could produce the ion conics through a so-called "pressure-cooker effect". For this, the presence of $E_{\parallel}$ is important. As early as in 1950s, *Alfvén* (1958) first predicted the

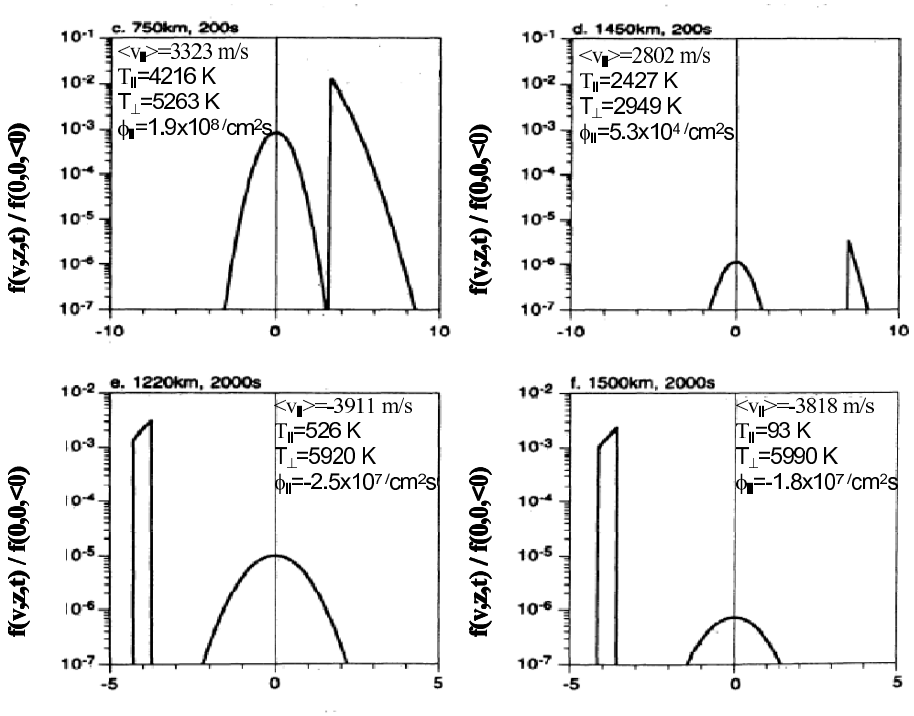

Figure 1.13: Ion parallel velocity distributions at different heights above the exobase and different elapsed time. Parameter $\phi_{\|}$ is the parallel ion flux (*Loranc & St.-Maurice* 1994).

existence of parallel electric fields, and then numerous rockets and satellites verified their existence in auroral regions [see, e.g., *McIlwain* (1960), *Albert* (1967), *Hoffman & Evans* (1968), *Evans* (1974), *Haerendel et al.* (1976), *Mozer* (1980), *Mizera et al.* (1982), *Carlson et al.* (1998), *Ergun et al.* (2000), *Mozer & Hull* (2001), *Janhunen et al.* (2004)]. Above $1R_E$, the measured parallel electric field strengths can be very strong, up to even higher than 1000 mV/m in general [see, e.g., *Mozer & Hull* (2001) and references therein]. They are connected with Birkeland currents, auroral electron precipitation, double layers, anormalous resistivity, etc.

With the presence of the cooking mechanism, if a downward $E_{\|}$ is present, the energized ions may be pushed back. In that case, they keep gaining perpendicular energy but they are retarded by $E_{\|}$ and then reflected at the mirror point and go up again while gaining yet more perpendicular energy. This process could happen repeatedly and the result of the confining parallel field is to keep all ions within the

heating region [see *Paschmann et al.* (2003), and references therein]. After some time when $E_{\parallel}$ is taken away, all ions can escape with a conic distribution in velocity space. The first ion conic was measured by satellite 1976-65B (*Sharp et al.* 1977). Fig.1.14 shows an example detected by the S3-3 satellite (*Kintner* 1980).

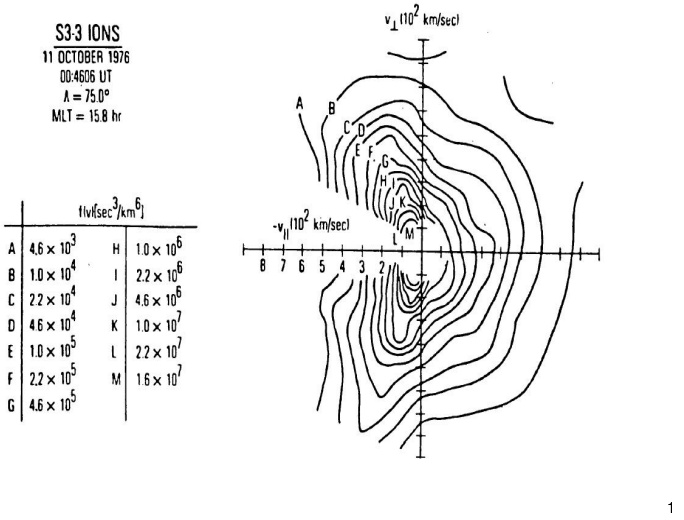

Figure 1.14: An ion conic measured by S3-3 (*Kintner* 1980).

1.5 Thesis description

This thesis will focus on the non-Maxwellian ion velocity distributions produced by inhomogeneous and time-dependent electric fields with and without collision effects in the auroral ionosphere. As discussed above, ionospheric plasmas have two types of geometries of interest: auroral arcs and vortices of various scales. These geometries can be described by a Cartesian frame (x, y, z) and a cylindrical frame (r, ϕ, z). Considering most previous work was done in the x, y, z-frame, but observations have shown many instances of cylindrical charge/electric field arrangements in the auroral ionosphere, I turn my attention to the ion velocity distributions that one should expect in the auroral plasma in a cylindrical geometry.

On larger scales, convection vortices, 1000 to 3000 km in size, have been reported

and studied by a number of authors [e.g., *Vogelsang et al.* (1993); *Huang et al.* (1998)]. Smaller cylindrical regions are also known to exist, for example in auroral rays (*Baranoski et al.* 2003). The smallest ionospheric cylindrical structures that we are aware of can be as small as 10 to 20 m, and have been described as lower hybrid cavities (*Schuck et al.* 2003). Based on the results obtained by *St.-Maurice et al.* (1994), the smaller the radii of the cylinders become, the more the inhomogeneity of the electric field is likely to affect the ion velocity distribution.

From a review of similar problems to a certain extent studied in other types of plasmas (fusion plasma, for example) by, e.g., *Vandenplas & Gould* (1964), *Whealton & Woo* (1971), *Roig & Schoutens* (1986), *Date & Shimozuma* (2001), and *Takahashi et al.* (2004), we realize that the complexity of the calculation in a cylindrical geometry requires that we approach the cylindrical geometry through a series of incremental steps, so as to be able to understand the physics and develop suitable approaches, and, based on which to solve more realistic problems.

As a first step, we deal with the most basic problem we can solve in Chapter 2 towards the goal to gain important insights into the more complicated situations, while still being able to obtain complete analytical solutions: we tackle a situation for which the strength of the ambient electric field increases linearly with the radius of the cylinder, but is constant in time. We focus on ions that are well inside the cylinder, thereby neglecting radial edge effects and features associated with the decaying field outside the cylinder. We also make the cylinder have negative space charge, and we solve the collision-free problem. The underlying physical model is that of a uniformly charged cylinder of excess electrons (i.e., space charge) that forms on a time scale much shorter than the ion gyroperiod. These electrons need not exceed the ambient density by more than one charge in 10^5. The ambient electrons, with their small gyroradii and large thermal speeds can be assumed to simply remain Maxwellian while experiencing $\mathbf{E} \times \mathbf{B}$ drift in response to the radially linear $\mathbf{E}$ produced by the uniform space charges. In this initial work, $\mathbf{E}$-field is assumed to be maintained, irrespective of the ion response. The solutions thus obtained have proved useful for more realistic applications such as in a collisional case, in $\mathbf{E}$-configurations

where E is not proportional to the radius, or, in temporally changing **E**-fields.

Chapter 3 applies the approach developed in Chapter 2 to solve ion velocity distributions and velocity moments for collisional F region problems in the electric field model used in Chapter 2. By simplifying the ion-neutral collision term with the relaxation model as done by *St.-Maurice et al.*(1994), we derive analytically the ion velocity distribution function, and related transport properties, e.g., the ion density, temperature, pressure, etc. I also show the connection between the collision-free solutions and collisional ones.

By generalizing the above analytical work, we introduce a semi-numerical method in Chapter 4 to produce various shapes of ion velocity distribution functions, as well as transport properties at the same time. The approach is under collision-free conditions for different electric field models which vary nonlinearly with radius, but are still constant in time. A backward ray-tracing method is applied to trace back ions from any position and velocity to the initial ones at the initial position and velocity.

Chapter 5 studies the effects of density inhomogeneities at initial time on the ion velocity distribution function at any time under temporally constant, but radially nonlinear electric field structures. In the collision-free case, a couple of space-charge models are adopted to give analytical solutions. In the collisional case, one space-charge model is used to produce analytical solutions.

Chapter 6 discusses the excitation of several fundamental plasma oscillations (such as cyclotron wave, hybrid waves, etc.). A fluid formalism is used in which the radially linear electric field is modulated by incoming particles and thus is a function of time.

The final part of the thesis, Chapter 7, summarizes the thesis work, and discusses some important extensions based on what we obtained.

Throughout the thesis, SI units are used. Physical constants and input parameters used in the analytical and numerical studies are summarized in Table 1.1.

Table 1.1: Physical constants and input parameters.

Notation	**Definition**	**Value**	**Unit**
B	Auroral F-region geomagnetic field	5×10^{-5}	Tesla
e	Elementary charge	1.6022×10^{-19}	C
E_c	Radially linear electric field -E_r at R_c	0.1	V/m
m_e	Electron mass	9.110×10^{-31}	kg
m_i	Ionic O^+ mass	2.6768×10^{-26}	kg
m_n	Atomic O mass	2.6768×10^{-26}	kg
n_0	Nonuniform ion density at maximum	$10^{10\sim12}$	m^{-3}
n_{i0}	Uniform ion density at equilibrium	$10^{10\sim12}$	m^{-3}
δn_e	Electron space-charge density	1.11×10^{6}	m^{-3}
r_T	Ionic O^+ thermal gyroradius (v_{th}/Ω)	3.3	m
R_c	Cylindrical radius at which $E_r = -E_c$	10	m
t_0	Initial time at which E_r is turned on	0	s
T_0	Ionic O^+ temperature at equilibrium	1000	K
v_{th}	Ionic O^+ thermal speed at equilibrium	1000	m/s
v_{Te}	Electron thermal speed at equilibrium	242 v_{th}	m/s
ϵ_0	permittivity of space	8.8542×10^{-12}	F/m
ν_{in}	Ion-neutral collision frequency	0.3	s^{-1}
ω	Ionic O^+ cyclotron frequency in linear E_r	1.915Ω	rad/s
ω_{pe}	Electron plasma frequency	6×10^{4}	rad/s
Ω_i	Ionic O^+ gyrofrequency	300	rad/s
Ω_e	Electron gyrofrequency, eB/m_e	8.813×10^{6}	rad/s

Chapter 2

Linear, Constant Electric Field: Collision-Free Case

The goal of this Chapter is to describe a fundamental approach to obtaining an ion velocity distribution and transport properties by solving a Boltzmann equation analytically in a simple radially linear, temporally constant electric field under collision-free conditions. The structure of the Chapter is as follows: At first, the ion motion in a cylindrical geometry will be discussed for an inward electric field that increases in proportion to radial distance and constant in time. These trajectories will then be used to obtain the collision-free ion distribution functions that are appropriate to our cylindrical geometry. The behavior of the ion transport properties will then be described in association with these distributions. Some mathematical details regarding the ion orbits are provided in Appendices at the end of this thesis.

2.1 Properties of electrons and ions

The simplest useful model we can consider for cylindrically symmetric electric fields is the one for which the net charge density is uniform within the cylindrical region. This model requires excess electrons but does not mean that the plasma violates quasi-neutrality: we assume here that the cylindrically charged region is made of a small number of electrons and that these electrons can be very dynamic so that the net charge produced by their accumulation over a cylindrical region can appear over a time scale that's faster than the ion gyroperiod. The time scale must not be so short as to produce magnetic perturbations that could compete with the ambient

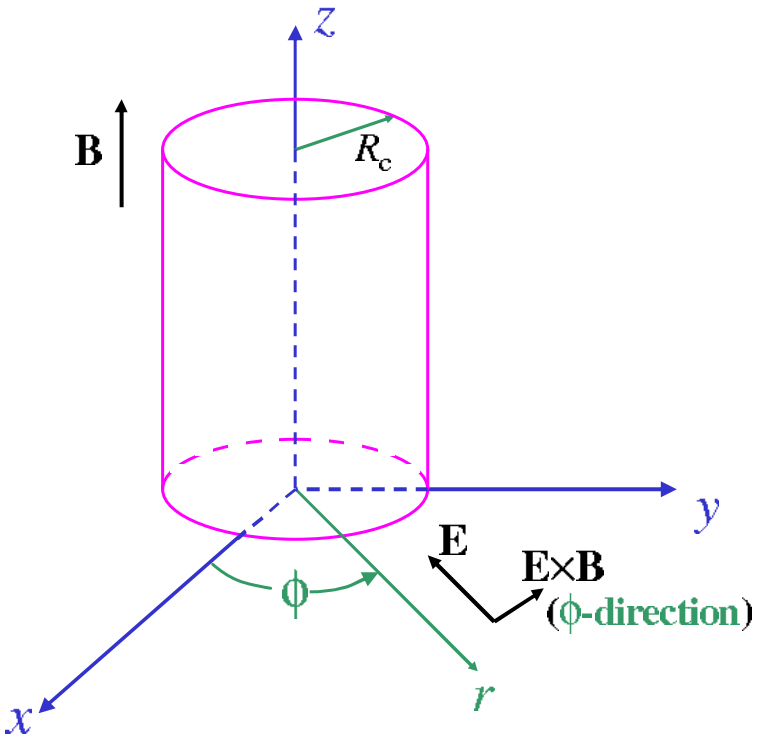

Figure 2.1: Cylindrical coordinates with reference to the Cartesian frame.

magnetic field. However, even with electric fields of 1 V/m at a distance of 100 m from the center it can be shown that a magnetic perturbation having 1% of the value of the ambient field would require a time scale as short as 1 nanosecond, which is much shorter than the time scales we have in mind here.

The framework for the problem considered in the present paper is described in Fig.2.1. As shown in that figure, we use coordinates (r, ϕ, z) in real space. We assume that at time $t = 0$ a negatively charged region is created along an infinitely long column, in which the plasma density in the column (n_c) is assumed to be uniform everywhere. The electric field, $\mathbf{E}$, points radially inward in the $-\mathbf{r}$ direction.

As stated already, inside our cylinder, the background electron density n_{e0} and the ion density n_0 satisfy $n_c \approx n_{e0} \approx n_0$ and the plasma is taken to be quasi-neutral. Let δn_e be the perturbed uniform electron density associated with the creation of the electric field. The spatial distribution of the resulting electrostatic field $\mathbf{E}$=$\mathbf{E_r}$=$E_r\hat{\mathbf{e}}_r$ (where $\hat{\mathbf{e}}_r$ is the unit radial vector) can be obtained from Gauss' law

$$\nabla \cdot \mathbf{E} = -\frac{e\delta n_e}{\epsilon_0} \tag{2.1}$$

in which ϵ_0 is the permittivity of space. As a result the electric field is given by the expression

$$E_r = -E_c \frac{r}{R_c} \tag{2.2}$$

where $E_c = \delta n_e[eR_c/(2\epsilon_0)]$ is positive and R_c is a characteristic radius at which $E_r = -E_c$. Clearly, the electric field within the cylinder is linear, and points radially inward. We can check that the plasma is quasi-neutral with the following numbers: if we were to let E_c=100 mV/m at R_c=10 m, the corresponding space-charge number density would need to be $\delta n_e \approx 1.11 \times 10^6$ m^{-3}. This is 10^4 to 10^6 times smaller than the ambient plasma density in the ionosphere.

In our model, the axis of the charged cylinder is along a geomagnetic field line. For the problem at hand, the magnetic field $\mathbf{B}$ can furthermore be assumed for now to be homogeneous in space: $\mathbf{B} = B\hat{\mathbf{e}}_z$ (where $\hat{\mathbf{e}}_z$ is the unit axial vector). It follows that the electric field is perpendicular to the ambient magnetic field. When $\mathbf{B}$ is upward, $\mathbf{E} \times \mathbf{B}$ points in the ϕ-direction. Using a typical value of 5×10^{-5} Tesla (0.5

Gauss) for the magnetic field, the $\mathbf{E} \times \mathbf{B}$ drift speed E/B becomes 2 km/s for a 100 mV/m electric field.

For O^+ ions in the auroral ionosphere at an equilibrium temperature $T_0 = 1000$ K, the speed E/B is typically larger than the ion thermal speed ($v_{th} = \sqrt{2k_b T_0/m_i}$ where k_b is the Boltzmann constant, and m_i is the ion mass) which is of the order of 1 km/s. The drift speed from a 100 mV/m field is likewise also large compared to the thermal speed of the neutral gas (< 1 km/s) with which the ions collide (although collisions are not considered in the present Chapter). We note, however, that for electrons, the $\mathbf{E} \times \mathbf{B}$ drift speed is very small relative to the thermal speed, which exceeds 100 km/s. Any departures from a Maxwellian velocity distribution due to the Lorentz force under such small ratios of the drift speed to the thermal speed have to be negligible [e.g., *St.-Maurice and Schunk* (1979)]. This also means that the thermal electrons can simply be assumed to be $\mathbf{E} \times \mathbf{B}$ drifting and Maxwellian for the situation at hand.

2.2 Solutions of ion equations of motion

In addition to the above considerations, we can of course safely neglect the influence of gravity in directions perpendicular to the geomagnetic field since it can easily be shown that the gravitational force is several orders smaller than the electromagnetic forces. In the crossed electric field $\mathbf{E}$ and magnetic field $\mathbf{B}$, individual ion trajectories in the plane perpendicular to the geomagnetic field are therefore determined by the following equations of motion:

$$\frac{\mathrm{d}\mathbf{r}}{\mathrm{d}t} = \mathbf{v} \quad , \quad m_i \frac{\mathrm{d}\mathbf{v}}{\mathrm{d}t} = e(\mathbf{E} + \mathbf{v} \times \mathbf{B}) \tag{2.3}$$

where $\mathbf{r}$ and $\mathbf{v}$ are the position and velocity vectors of the ion, respectively, in phase space.

The kinetic solutions that we seek require that we integrate the ion equations of motion for the situation at hand. This can be done using several methods, all of which have their advantages. It is appropriate to first express the equations in cylindrical coordinates in space. For our particular electric field model, Eq.(2.3) is

then written as

$$\ddot{r} = r(\dot{\phi}^2 + \Omega_i\dot{\phi}) - \frac{E_c}{B}R_c\Omega_i\frac{r}{R_c^2} \ , \quad r\ddot{\phi} = -2\dot{r}\dot{\phi} - \Omega_i\dot{r} \tag{2.4}$$

in which $\Omega_i = eB/m_i$ is the ion gyrofrequency. Eq.(2.4) provides expressions for Newton's second law of motion in both the radial and azimuthal directions.

It also proves useful to express the equations in terms of non-dimensional variables. Normalizing with respect to the thermal speed (v_{th}), the ion gyro-period ($T_\Omega = 2\pi/\Omega_i$), and the mean ion thermal gyro-radius ($r_\mathrm{T} = v_{th}T_\Omega$) for the speeds ($v_r = \dot{r}$ and $v_\phi = r\dot{\phi}$), time (t), and radial position (r), respectively, Eq.(2.4) gives a dimensionless set of first-order linear differential equations, along with initial conditions $\{r_0, \phi_0, v_{r0}, v_{\phi 0}\}$ at $t = 0$, as follows:

$$\dot{r} = v_r \ , \quad \dot{v}_r = -\pi^2 r - (2\pi)^2\left[c_d r - \frac{c_k^2}{r^3}\right] \ , \quad \dot{\phi} = \frac{c_k}{r^2} - \frac{1}{2} \tag{2.5}$$

in which $c_d = (E_c/B)/(R_c\Omega_i)$, and $c_k = r_0[v_{\phi 0}/(2\pi) + r_0/2]$ with the normalized variables.

In general the equations would have to be integrated numerically. However, for the linearly varying electric field used here, the equations are analytically integrable. In section 3, we use a direct integration of Eq.(2.4) to obtain the orbits. However, while this method works fine mathematically, it hides a lot of the important physics. In Appendix A and B, we therefore introduce two other methods of integration inspired from a presentation by *Davidson* (2001). These methods prove useful in that they deliver a much clearer physical understanding of the orbits. The first alternative approach expresses the equations in what is at first an arbitrary rotating coordinate system. In that system a centrifugal and a Coriolis acceleration term are both present.

As shown in Appendix A, there is one particular choice of a rotating frame, with a frequency ω_r, in which the acceleration is actually simply perpendicular to the velocity. Therefore, from the point of view of that rotating frame, the ions follow a circle in velocity space. The angular frequency observed in the rotating frame is a generalization of the usual cyclotron frequency. The frequency of the

rotating frame itself is much smaller than that. At small enough values of E_c/B (or large values of R_c), the period of rotation is in fact simply the time it takes for an $\mathbf{E} \times \mathbf{B}$ drifting particle to go around the cylinder. The emerging picture, at least in the presence of weaker electric fields, is that of ions suffering cyclotron-like velocity oscillations as they $\mathbf{E} \times \mathbf{B}$ drift around the cylinder. For larger electric fields the basic picture remains, but the frequencies are no longer equal to the simple expressions just discussed.

Another analytical approach that we studied is discussed in Appendix B. This method uses the complex variable $Z = x + iy$ to solve the coupled differential equations in x and y. The starting point is to express the original variables in the form $Z = Z' \exp(i\omega_r t)$. In effect, this is the same thing as expressing the equations in a suitable rotating frame. Not surprisingly, the frequency of choice is identical to what was found using rotating coordinates as our starting point. Beyond that, however, the integrals to perform are all first order differential equations. This has the virtue to produce analytical solutions in terms of clearly stated initial conditions and clear rotation frequencies.

In Figure 2.2a we have used our analytical solution from Appendix B to show how the ions travel in the $x-y$ plane (we double-checked that the solutions were the same as those obtained with a numerical integration). Initially, the ions are accelerated towards the center of the cylinder. As they move in, however, the electric force decreases (weakening electric field) while the velocity increases. This means that at some point the magnetic force becomes large enough to turn the ion around and send it back to a point where the initial conditions in r and $\mathbf{v}$ will be repeated so that the cycle will start anew. The velocity in the $x - y$ plane also oscillates, except that it goes through sign reversals and therefore passes through zero at the largest distances reached in the orbits: this can be seen in Figure 2.2b. In that figure we also note that the velocity oscillations undergo a systematic rotation in the $v_x - v_y$ plane. This suggests that a better way to look at the results is to examine the velocity components along the radial and tangential direction instead of in a fixed direction

specified by x or y. Namely, we should be looking at

$$v_r = \dot{r} = \frac{\mathbf{v}\cdot\mathbf{r}}{r}\ , \quad \text{and} \quad v_\phi = r\dot{\phi} = \frac{\mathbf{v}\times\mathbf{r}}{r} \tag{2.6}$$

When this is done, the velocity field becomes much simpler, taking the form of a somewhat distorted circle (see Figure 2.2c). This confirms that the better way to visualize the solution is to picture the ions in the rotating frame undergoing a circular motion, while the ions oscillate around the center of the circle. This way to look at the ion velocity is described by the first expression given in Eq.(B.25) (Appendix B) and is indeed the motivation for the approach used in the appendix.

2.3 Retrieval of the ion velocity distribution

To obtain the ion distribution function f_i in the absence of collisions, we have to solve the following Boltzmann equation, subject to proper initial and boundary conditions:

$$\frac{\mathrm{D}f_i}{\mathrm{D}t} = \frac{\partial f_i}{\partial t} + \mathbf{v}\cdot\nabla f_i + \frac{e}{m_i}(\mathbf{E}+\mathbf{v}\times\mathbf{B})\cdot\nabla_{\mathbf{v}} f_i = 0 \tag{2.7}$$

Notice here that the electric field is assumed to be 'external', i.e., maintained by dynamical processes that are supposed for now to be unaffected by the local behavior of the ions. In that sense, we are solving a Boltzmann equation, rather than a Boltzmann-Vlasov equation in which the electric field contains both 'external' and 'internal' components.

The function f_i describes the probability of finding an ion in a particular volume element in six-dimensional phase space. The system, in this case the ion component of the gas, is composed of identical particles occupying the volume element $\mathrm{d}\mathbf{r}\mathrm{d}\mathbf{v}$ around the phase-space point $\{\mathbf{r},\mathbf{v}\}$ [*Gartnhaus* (1964); *Schmidt* (1979); *Humphries* (2002)]. Eq.(2.7) states that, owing to the neglect, in the present work, of the short-range collision term $(\partial f_i/\partial t)_c$, f_i remains constant along 6-dimensional trajectories followed by the ions in phase space, once a particular initial condition is stated. This latter statement is important: the task at hand is not only simply to obtain the invariants of motion, but also to identify the one function of these invariants that satisfies the initial condition that we wish to impose on the ions (in this case, a cold stationary Maxwellian at the time the electric field is suddenly turned on).

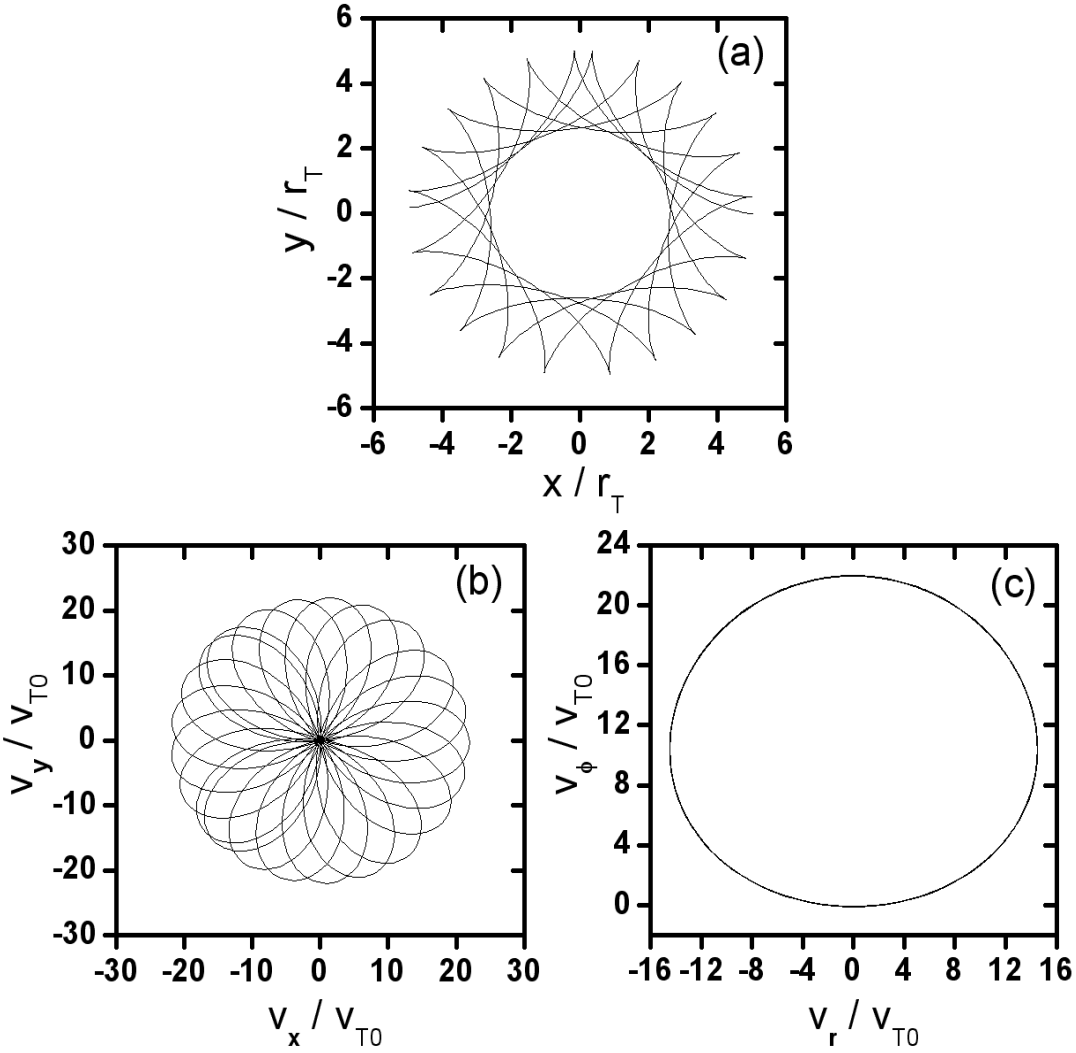

Figure 2.2: Ion orbits in real space (Panel a), in velocity space in terms of v_x and v_y (Panel b), and in velocity space in terms of the velocity components projected along the radial direction and perpendicular to it (Panel c). Input parameters are: $E_c = 0.1$ V/m, $B = 0.5 \times 10^{-4}$ T, $R_c = 10$ m, $\Omega_i = 300$ rad/s, and initial parameters $\{r_0, \phi_0, v_{r0}, v_{\phi 0}\} = \{5, 0, 2, 0\}$ in a temporal interval from $t = 0$ to 12 (or, 80π ms). The ion thermal gyro-radius $r_{\rm T}$ and the thermal speed v_{th} at the equilibrium are $\sim$21 m and $\sim$1 km/s, respectively (O^+ ions at 1000 K). Note that $R_T > R_c$ is allowable since R_c is not the radius of the space-charge cylinder but, rather, the radius at which the linearly increasing electric field reaches the value E_c.

To be more specific: after the initial time $t = 0$ (hereafter we will use the subscript '0' to indicate the initial state), we must first be able to describe the ions' phase-space trajectory that starts at an initial phase-space vector point $\{\mathbf{r}(t_0), \mathbf{v}(t_0)\} = \{\mathbf{r}_0, \mathbf{v}_0\}$. If we can do this, the distribution function $f_i(\mathbf{r}, \mathbf{v}, t)$ at any time $t > 0$ will remain constant. That is to say, the solution to the problem $Df_i/Dt = 0$ is simply formally given by

$$f_i[\mathbf{r}(t), \mathbf{v}(t), t] = f_i(\mathbf{r}_0, \mathbf{v}_0, 0) = f_0 \tag{2.8}$$

Of course, writing the solution in the above formal way still leaves us with the task of finding an explicit expression for f_i since

$$\{\mathbf{r}, \mathbf{v}, t\} \neq \{\mathbf{r}_0, \mathbf{v}_0, 0\} \tag{2.9}$$

The connection between the two phase-space positions can be obtained if we solve the set of differential equations of motion given by Eq.(2.4). We take advantage of the fact that these equations are symmetric in time, namely, that for two states $\{\mathbf{r}_0, \mathbf{v}_0, t_0\}$ and $\{\mathbf{r}, \mathbf{v}, t\}$, there are two identical solutions for the same set of equations of motion [*Gartnhaus* (1964)]: one provides $\{\mathbf{r}, \mathbf{v}, t\}$ expressed by using $\{\mathbf{r}_0, \mathbf{v}_0, t_0\}$ (*forward tracking*), while the other provides $\{\mathbf{r}_0, \mathbf{v}_0, t_0\}$ expressed by using $\{\mathbf{r}, \mathbf{v}, t\}$ (*backward tracking*), whereby the description of the characteristics of motion is traced backwards but is otherwise unaltered. Here, we use backward tracking to solve $f_i(\mathbf{r}, \mathbf{v}, t)$. The backward tracking method allows us to relate the 6-dimensional phase point $\{\mathbf{r}, \mathbf{v}\}$ at any time t to $\{\mathbf{r}_0, \mathbf{v}_0, 0\}$ and to therefore find the distribution at time t, since the initial distribution is assumed to be fully known. Finding the distribution function is then just a matter of expressing $\mathbf{r}_0$ and $\mathbf{v}_0$ in terms of $\mathbf{r}, \mathbf{v}$, and t in the expression for the initial condition f_0.

The most straightforward way to obtain the orbits is to use the conservation of energy and angular momentum and integrate. See Appendix C for details. Specifically, after a first integration, Eq.(2.4) produces the following set [Eq.(C.28)]:

$$\left.\begin{aligned} & r v_\phi + \frac{r^2 \Omega_i}{2} = r_0 v_{\phi 0} + \frac{r_0^2 \Omega_i}{2} = \frac{K}{m_i} \\ & v_r^2 + v_\phi^2 + \frac{E_c}{B} R_c \Omega_i \left[\left(\frac{r}{R_c} \right)^2 - \left(\frac{r_0}{R_c} \right)^2 \right] = v_{r0}^2 + v_{\phi 0}^2 \end{aligned} \right\} \tag{2.10}$$

in which K is the angular momentum. The first expression describes the conservation of angular momentum, and the second one describes the conservation of energy.

We can combine the two equations in Eq.(2.10) to obtain a canonical equation of motion that is sometimes associated with the 'pseudo-potential' method, where the angular momentum represents a form of potential energy. The final equation is then given by [Eq.(C.29)]:

$$v_r^2+\left(\frac{\Omega_i r}{2}\right)^2+\left(\frac{K}{m_i r}\right)^2+\frac{E_c}{B}R_c\Omega_i\left[\left(\frac{r}{R_c}\right)^2-\left(\frac{r_0}{R_c}\right)^2\right]=v_{r_0}^2+\left(\frac{\Omega_i r_0}{2}\right)^2+\left(\frac{K}{m_i r_0}\right)^2 \tag{2.11}$$

A detailed derivation of the solution to this equation of motion is given in Eq.(D.25) in Appendix D.

2.3.1 First form of the expression for the distribution function

Applying the backward tracking method to our system is a simple matter of noting that $v_{r_0}=\mathrm{d}r_0/\mathrm{d}t$, and integrating Eq.(2.11) for r_0 instead of r (first part of Appendix D). This amounts to formally integrating the expression

$$\frac{\mathrm{d}x_0}{\sqrt{-b_1x_0^2+b_2x_0-b_3}}=\pm\frac{2}{R_c}\mathrm{d}t_0 \tag{2.12}$$

in which

$$\left.\begin{aligned} x_0&=(r_0/R_c)^2\\ b_1&=(\Omega_i R_c/2)^2+(E_c/B)R_c\Omega_i\\ b_2&=b_1(r/R_c)^2+v_r^2+(v_\phi+\Omega_i r/2)^2\\ b_3&=[K/(m_iR_c)]^2=(r/R_c)^2\,(v_\phi+\Omega_i r/2)^2 \end{aligned}\right\} \tag{2.13}$$

The integration of Eq.(2.12) produces the solution:

$$\left(\frac{r_0}{R_c}\right)^2=A_0[1\mp\varepsilon_0\,\sin(\omega t+\phi_0)] \tag{2.14}$$

in which the sign "$\mp$" before ω takes "$-$" for $v_r>0$ and "$+$" for $v_r<0$, and

$$A_0=\frac{b_2}{2b_1}\ ,\quad \varepsilon_0=\sqrt{1-4\frac{b_1b_3}{b_2^2}}\ ,\quad \omega=\Omega_i\sqrt{1+4\frac{E_c/B}{R_c\Omega_i}}\ ,\quad \phi_0=\sin^{-1}\frac{\dfrac{(r/R_c)^2}{A_0}-1}{\varepsilon_0} \tag{2.15}$$

Note that $\omega = 2\omega_r + \Omega_i$ is nothing but the effective gyro-frequency given in Appendix A. Using, for example, the parameters given in Section 2, we obtain $\omega = 1.915\Omega_i$.

Eq.(2.14) indicates that the mapping from r^2 to r_0^2 oscillates with a frequency ω as a function of time. Physically, this is because even though r_0 actually describes a fixed initial position, the parameter r itself oscillates with time so that the backward tracking sends us to different values of r_0 (recall that we are supposed to know f_0 for any value of r_0). The oscillations in r can be seen in Fig.2.2(a).

Using Eqs.(2.10,2.14), we can now write an explicit expression for the ion velocity distribution function f_i via Eq.(2.8), assuming the initial distribution f_0 is known. Here we choose a stationary Maxwellian that is initially independent of position, with a uniform temperature T_0. A first expression for the ion velocity distribution function in terms of our non-dimensional variables therefore becomes

$$f_i(\mathbf{r}, \mathbf{v}, t) = f_0 = \frac{n_0}{\pi} e^{-(v_{r0}^2 + v_{\phi 0}^2)} = \frac{n_0}{\pi} e^{-(v_r^2 + v_\phi^2)} \cdot e^{B_2 \mp B_1 \sin(\omega t + \phi_0)} \tag{2.16}$$

In this expression,

$$\left.\begin{aligned} B_1 &= c_0 \varepsilon_0 A_0 \\ B_2 &= c_0 \left[A_0 - \left(\frac{r}{R_c} \right)^2 \right] \\ c_0 &= \frac{E_c}{B} R_c \Omega_i \end{aligned}\right\} \tag{2.17}$$

Also, recall that the velocities are normalized with respect to the thermal speed $v_{th} = \sqrt{2k_b T_0 / m_i}$.

Eq.(2.16) is useful in that it offers a formal solution to the problem at hand. This turns out to be of interest both in semi-numerical solutions to the more general problem of arbitrary electric fields or for the collisional problem (as will be seen in subsequent Chapters). However, the solution, as described here, does not describe the behavior of the distribution function in a way that is particularly enlightening. It allows the solution to be plotted for any time at any place, but the velocity moments of the velocity distribution are, for instance, difficult to obtain analytically. This stated, the expressions can be manipulated further to reveal a rather simple behavior which is speaking volumes about the nature of the distribution function (f_i), while making it easy to obtain velocity moments of f_i.

2.3.2 Second form of the expression for the distribution function

Using Eq.(2.14) back in the second equation of Eq.(2.10), we obtain, after a substantial amount of algebra (second part of Appendix D),

$$v_{r0}^2 + v_{\phi 0}^2 = a_0 \left[(v_r - v_{\mathrm{d}r})^2 + (v_\phi - v_{\mathrm{d}\phi})^2 \right] \tag{2.18}$$

in which

$$\left.\begin{aligned} a_0 &= 1 - \frac{1}{2}\left[1 - \left(\frac{\Omega_i}{\omega}\right)^2\right](1 - \cos\omega t) \\ v_{\mathrm{d}r} &= -\frac{E_c}{B}\frac{r}{R_c}\frac{1}{a_0}\frac{\Omega_i}{\omega}\sin\omega t \\ v_{\mathrm{d}\phi} &= \frac{E_c}{B}\frac{r}{R_c}\frac{1}{a_0}(\frac{\Omega_i}{\omega})^2 (1 - \cos\omega t) \end{aligned}\right\} \tag{2.19}$$

Rewritten in the form:

$$(v_r - v_{\mathrm{d}r})^2 + (v_\phi - v_{\mathrm{d}\phi})^2 = \frac{1}{a_0}\left(v_{r0}^2 + v_{\phi 0}^2\right) \tag{2.20}$$

Eq.(2.18) states that, at any given time t, the velocities (v_r, v_ϕ) are organized as loci of concentric circles in velocity space. The radii of the circles depend both on time t through a_0 and on the initial velocity conditions.

Furthermore, it can easily be seen from Eq.(2.19) that $\mathbf{v}_{\mathrm{d}} = (v_{\mathrm{d}r}, v_{\mathrm{d}\phi})$ itself describes a circle, namely,

$$v_{\mathrm{d}r}^2 + \left(v_{\mathrm{d}\phi} - \frac{E_c}{B}\frac{r}{R_c}\right)^2 = R_{\mathbf{v}}^2 \tag{2.21}$$

in which the radius $R_{\mathbf{v}}$ is simply given by $|\mathbf{E}\times\mathbf{B}/B^2| = \dfrac{E_c}{B}\dfrac{r}{R_c}$.

In concise vector form, Eqs.(2.20,2.21) can be rewritten as:

$$(\mathbf{v} - \mathbf{v}_{\mathrm{d}})^2 = \frac{v_0^2}{a_0}\ , \quad \left(\mathbf{v}_{\mathrm{d}} - \frac{\mathbf{E}\times\mathbf{B}}{B^2}\right)^2 = \left(\frac{E}{B}\right)^2 \tag{2.22}$$

The vector $\mathbf{v}_{\mathrm{d}}$ behaves as a velocity space guiding center which rotates around the $\mathbf{E}\times\mathbf{B}$ drift. Note that the radius of that velocity space circle, E/B, is not constant in space since it varies with the linearly varying electric field. Furthermore,

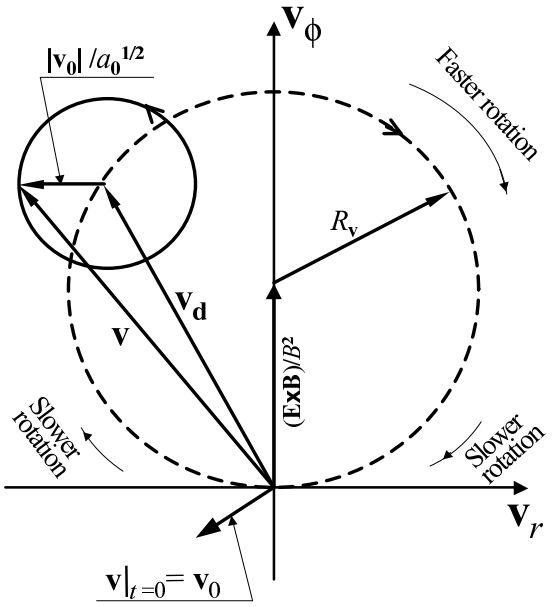

Figure 2.3: Characteristics of ion motions at an arbitrary radius r and time t described by the two velocity-vector circles shown in Eq.(2.22): $\mathbf{v}$ circulating around $\mathbf{v}_\mathrm{d}$, and, $\mathbf{v}_\mathrm{d}$ around the $\mathbf{E}\times\mathbf{B}$ drift point. The curved arrows outside the $R_\mathbf{v}$-circle denote the directions of rotations while $R_\mathbf{v} = |\mathbf{E}\times\mathbf{B}|/B^2$.

one curious thing about $\mathbf{v}_\mathrm{d}$ is that it does not go around its circle at a steady rate: when ωt is around 0 or a multiple of 2π, $\mathbf{v}_\mathrm{d}$ changes more slowly than if ωt is near an odd multiple of π.

Fig.2.3 illustrates how the loci of velocities at some time t and radial position r are related to a particular initial condition given by a particular choice of $\mathbf{v}_0$. It also illustrates the circular trajectory of $\mathbf{v}_\mathrm{d}$ for a full rotation of values for a particular value of E/B (or choice of r), with the $\mathbf{E}\times\mathbf{B}$ drift as its center.

The radius of the circle that is centered on $\mathbf{v}_\mathrm{d}(t)$ is determined by $a_0(t)$. While, for clarity, the change in this radius with time is not shown, notice that it is always a minimum at the beginning of a cycle ($\omega t = 0$ or multiple of 2π) and reaches its maximum value in the middle of a cycle, when ωt is an odd multiple of π. At any time other than 0 or a multiple of $2\pi/\omega$, the radius is greater than v_0 and oscillates between the two extreme values.

Using the first expression from Eq.(2.22), we can now write our ion distribution function in its second, physically more insightful form, namely,

$$f_i(\mathbf{r}, \mathbf{v}, t) = \frac{n_0}{\pi} e^{-a_0[(v_r - v_{\mathrm{d}r})^2 + (v_\phi - v_{\mathrm{d}\phi})^2]} \tag{2.23}$$

We have verified numerically that Eq.(2.16) and Eq.(2.23) are indeed identical solutions for the ion velocity distribution in the collision-free case. It is easy to see from the second form in particular that they clearly satisfy our initial conditions. However, we should also check that our solution(s) satisfies the Boltzmann equation.

2.3.3 Verifying the correctness of the solution

Checking that the solution not only satisfies the initial conditions but also the Boltzmann equation turns out not to be as trivial as it looks. Since we use cylindrical coordinates in real space and cartesian coordinates in velocity space with one component of the velocity pointing in the radial direction and the other in the tangential direction, a first task consists of describing the Boltzmann equation in these specific coordinates.

For our coordinates the Boltzmann equation takes the form

$$\frac{\partial f_i}{\partial t} + \dot{\mathbf{r}} \cdot \nabla f_i + \ddot{\mathbf{r}} \cdot \nabla_{\mathbf{v}} f_i|_{CR} = 0 \tag{2.24}$$

where the symbol $|_{CR}$ reminds us that the velocities are expressed as Cartesian velocities in a rotating cylindrical system. Specifically, at a particular radial distance r and angle ϕ, one component of the velocity is chosen to be along the radial direction and the second component along the tangential direction. The procedure is valid as long as the acceleration is expressed properly in the non-inertial rotating frame of reference associated with a rotation rate $\dot{\phi} = v_\phi / r$. This means that the Coriolis and centripetal acceleration terms have to be added to the acceleration terms, but that in return the acceleration is given by the components $\dot{v_r}$ and $r\ddot{\phi}$. These acceleration terms have already been described in Eq.(2.4): in addition to the Lorentz force contribution, the tangential component of the acceleration contains a Coriolis acceleration given by $-2\dot{r}\dot{\phi} = -2v_r v_\phi / r$. The radial contribution has an additional

non-inertial (centrifugal) contribution equal to $+r\dot{\phi}^2 = v_\phi^2/r$ which can be viewed as a superposition of an outward Coriolis contribution $+2r\dot{\phi}^2$ and a centripetal acceleration term equal to $-r\dot{\phi}^2$.

Therefore, for polar coordinates in real space and for Cartesian coordinates in velocity space that are attached to the polar coordinates, the equation $\mathrm{D}f_i/\mathrm{D}t = 0$ takes the form

$$\frac{\mathrm{D}f_i}{\mathrm{D}t} = \frac{\partial f_i}{\partial t} + v_r\frac{\partial f_i}{\partial r} + \left(\frac{v_\phi^2}{r} + v_\phi\Omega_i - \frac{E_c}{B}\Omega_i R_c\frac{r}{R_c^2}\right)\frac{\partial f_i}{\partial v_r} - \left(2\frac{v_r v_\phi}{r} + v_r\Omega_i\right)\frac{\partial f_i}{\partial v_\phi} = 0 \tag{2.25}$$

For an alternate derivation that is more direct but less physical we can state that we choose to express f_i in terms of $f_i = f_i(r, \phi, \dot{r}, \dot{\phi}; t)$. For this choice of variables the total rate of change in f with time is given by

$$\frac{Df_i}{Dt} = \frac{\partial f_i}{\partial t} + \frac{\partial r}{\partial t}\frac{\partial f_i}{\partial r} + \frac{\partial \phi}{\partial t}\frac{\partial f_i}{\partial \phi} + \frac{\partial \dot{r}}{\partial t}\frac{\partial f_i}{\partial \dot{r}} + \frac{\partial \dot{\phi}}{\partial t}\frac{\partial f_i}{\partial \dot{\phi}} = \frac{\partial f_i}{\partial t} + \dot{r}\frac{\partial f_i}{\partial r} + \dot{\phi}\frac{\partial f_i}{\partial \phi} + \ddot{r}\frac{\partial f_i}{\partial \dot{r}} + \ddot{\phi}\frac{\partial f_i}{\partial \dot{\phi}} \tag{2.26}$$

After this, we introduce the new notation $v_r = \dot{r}$ and $v_\phi = r\dot{\phi}$ to end up with the expression

$$\frac{Df_i}{Dt} = \frac{\partial f_i}{\partial t} + v_r\frac{\partial f_i}{\partial r} + \frac{v_\phi}{r}\frac{\partial f_i}{\partial \phi} + \ddot{r}\frac{\partial f_i}{\partial v_r} + r\ddot{\phi}\frac{\partial f_i}{\partial v_\phi} \tag{2.27}$$

and we use equation (2.4) to describe $\ddot{r}$ and $r\ddot{\phi}$ and end up with Eq.(2.25).

The next step in checking over the solution amounts to inserting Eq.(2.23) into our explicit Boltzmann equation Eq.(2.25). Note that $\mathrm{D}f_i/\mathrm{D}t = 0$ is equivalent to $f_i^{-1}\mathrm{D}f_i/\mathrm{D}t = 0$, or, $\mathrm{D}(\ln f_i)/\mathrm{D}t = 0$. Eq.(2.23) gives

$$\ln f_i = \ln\left(\frac{n_0}{\pi}\right) - a_0[(v_r - v_{\mathrm{d}r})^2 + (v_\phi - v_{\mathrm{d}\phi})^2] = \ln\left(\frac{n_0}{\pi}\right) - F \tag{2.28}$$

in which $F = a_0[(v_r - v_{\mathrm{d}r})^2 + (v_\phi - v_{\mathrm{d}\phi})^2]$. Using Eqs.(2.11,2.14) [or, directly from Eq.(2.16)], the function F is given by

$$\left.\begin{aligned} F &= a_0[(v_r - v_{\mathrm{d}r})^2 + (v_\phi - v_{\mathrm{d}\phi})^2] = v_r^2 + v_\phi^2 + \\ &+\frac{E_c}{B}R_c\Omega_i\left[\frac{rv_r}{R_c\sqrt{b_1}}\sin\omega t + \frac{\left(\frac{r}{R_c}\right)^2 b_1 - v_r^2 - \left(v_\phi + \frac{r\Omega_i}{2}\right)^2}{2b_1}(1 - \cos\omega t)\right] \end{aligned}\right\} \tag{2.29}$$

By using Eq.(2.29) in Eq.(2.25), and after a fair amount of algebra (see Appendix E for details), we obtain $\mathrm{d}F/\mathrm{d}t = 0$ as we should. Therefore, $\mathrm{D}f_i/\mathrm{D}t = 0$, that is, Eq.(2.23) satisfies the Boltzmann equation and is the solution for the ion distribution function for our particular choice of initial condition.

2.3.4 Physical description of the ion distribution function

Fig.2.4 describes in cartoon form how the collision-free ion velocity distribution evolves as a function of time after the initial jump in the ambient electric field. For the purpose of comparison we also present a cartoon of the velocity distribution for a uniform electric field in the top panel and a similar cartoon for the case studied here, namely, that of an electric field that grows linearly with radius in a cylindrical geometry (bottom panel).

In the top panel, which is the solution initially studied by *Cole* (1971), the ions oscillate in phase at the gyrofrequency, with sinusoidal motions in both their Pedersen and Hall drift components. The temperature (i.e., the width of the distribution) does not change and the rotation rate is constant, with the period equal to the ion gyroperiod.

In the bottom panel, the velocity distribution is rotating about the local $\mathbf{E} \times \mathbf{B}$ drift point at r, just as in the uniform electric field case. However, there are two important differences from the top panel. First, the width of the distribution is changing. The mathematical reason for this is easy to see from Eq.(2.23), which at any given time describes a drifting Maxwellian, albeit one with a variable width [as determined by $1/\sqrt{a_0}$ in our non-dimensional description where a_0 is described by Eq.(2.19)]. As discussed above, this means that when the drift is the largest in the Hall ($\mathbf{E} \times \mathbf{B}$) direction, the width is also the largest. The second feature of interest is that while, like the uniform electric field case, the distribution oscillates about the local ($\mathbf{E} \times \mathbf{B}$) drift point, we find that the rotation rate is not uniform, being faster when the Hall drift is larger. Specifically, while the phase angle θ relative to the $\mathbf{E} \times \mathbf{B}$ drift is a linear function of time in the uniform electric field case ($\theta = \Omega_i t$), in the case of the electric field strength that increases linearly with radial distance,

it evolves into a nonlinear function of time satisfying

$$\tan\theta = \frac{\dfrac{1}{a_0}\dfrac{\Omega_i}{\omega}\sin\omega t}{1 - \dfrac{1}{a_0}\left(\dfrac{\Omega_i}{\omega}\right)^2(1-\cos\omega t)} \tag{2.30}$$

In summary, our collision-free distribution is a pulsating Maxwellian distribution, just like in the uniform electric field case. However, the width (temperature) of that pulsating distribution clearly oscillates with time, while the Hall and Pedersen drifts do not follow the simple sinusoidal behavior of the uniform case, even though the center of the drift pattern is still given by the $\mathbf{E}\times\mathbf{B}$ drift.

The above discussion, quite naturally, brings us to a discussion of the various velocity moments (transport properties) of our velocity distribution. This subject is, of course, particularly easy to study using our second formula for the distribution function since it describes the velocity part of the distribution function in terms of a pulsating Maxwellian.

2.4 Velocity moments and related transport coefficients

The velocity moments of the ion velocity distribution are defined by the kth-order velocity moment $\langle v_j^k\rangle = \int v_j^k f_i d\mathbf{v}/n_i$ where n_i is the integral of the distribution function over all velocities (zeroth-order velocity moment). Using these definitions, plus Eq.(2.23), and switching back to dimensional units, it is very easy to show that

$$\left.\begin{aligned}
&n_i = n_0/a_0\ ,\quad \langle v_r\rangle = v_{\mathrm{d}r}\ ,\quad \langle v_\phi\rangle = v_{\mathrm{d}\phi}\\
&\langle v_r^2\rangle = v_{\mathrm{d}r}^2 + v_{T0}^2/(2a_0) = v_{\mathrm{d}r}^2 + k_bT_0/(m_ia_0)\\
&\langle v_\phi^2\rangle = v_{\mathrm{d}\phi}^2 + v_{T0}^2/(2a_0) = v_{\mathrm{d}\phi}^2 + k_bT_0/(m_ia_0)\\
&\langle v_r^3\rangle = v_{\mathrm{d}r}^3 + 3[v_{T0}^2/(2a_0)]v_{\mathrm{d}r} = v_{\mathrm{d}r}^3 + 3[k_bT_0/(m_ia_0)]v_{\mathrm{d}r}\\
&\langle v_\phi^3\rangle = v_{\mathrm{d}\phi}^3 + 3[v_{T0}^2/(2a_0)]v_{\mathrm{d}\phi} = v_{\mathrm{d}\phi}^3 + 3[k_bT_0/(m_ia_0)]v_{\mathrm{d}\phi}
\end{aligned}\right\} \tag{2.31}$$

Note that the density expression depends on time but not in position. It depends on time through a_0 which has been posted in Eq.(2.19).

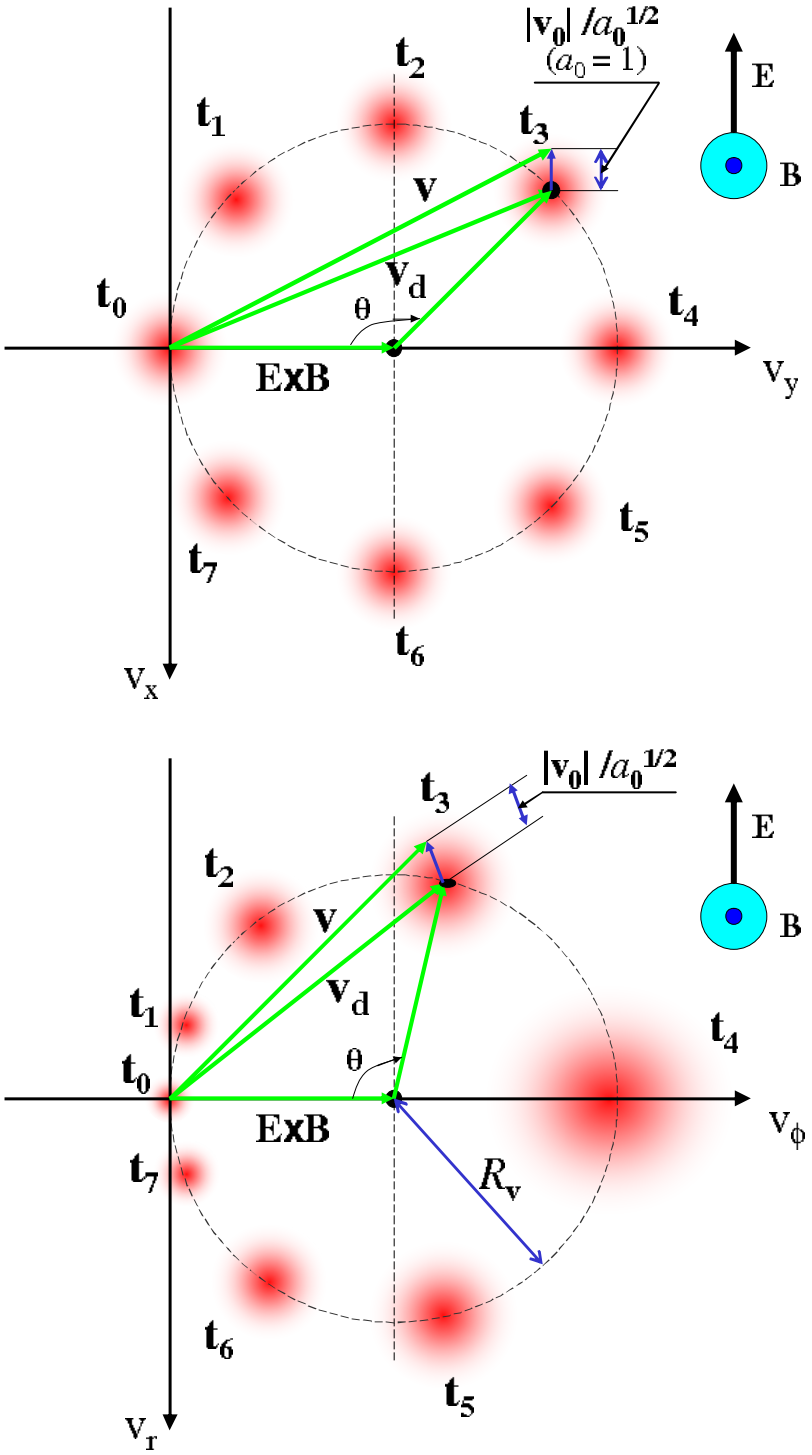

Figure 2.4: Temporal evolutions of a pulsating distribution function in a crossed uniform magnetic field. Upper: a uniform electric field $E = E_c$; Lower: a radially linear electric field $E = -E_c r/R_c$.

The above integrals are easily related to the various average transport properties [e.g., *Schunk & Nagy* (2000)]. Noticing that T_0 is not only the equilibrium temperature, but in the present context, also the temperature $T_\parallel$ which is parallel to the magnetic field direction, we end up with the following transport properties:

$$\left.\begin{aligned}
&v_{\rm aver} = \langle v_r \rangle \ , \quad v_{{\rm ave}\phi} = \langle v_\phi \rangle \\
&T_r = \frac{m_i}{k_b}(\langle v_r^2 \rangle - \langle v_r \rangle^2) = \frac{T_0}{a_0} \ , \quad T_\phi = \frac{m_i}{k_b}(\langle v_\phi^2 \rangle - \langle v_\phi \rangle^2) = \frac{T_0}{a_0} \ , \quad T_\parallel = T_0 \\
&p_{rr} = n_i k_b T_r \ , \quad p_{\phi\phi} = n_i k_b T_\phi \ , \quad p_{\parallel\parallel} = n_i k_b T_0 \\
&q_r = m_i(\langle v_r^3 \rangle - \langle v_r \rangle^3) - 3\langle v_r \rangle (k_b T_r) = 0 \ , \\
&q_\phi = m_i(\langle v_\phi^3 \rangle - \langle v_\phi \rangle^3) - 3\langle v_\phi \rangle (k_b T_\phi) = 0 \ , \quad q_\parallel = 0
\end{aligned}\right\} \tag{2.32}$$

where T_r and T_ϕ are the ion temperature along the r and ϕ directions, respectively; p_{rr}, $p_{\phi\phi}$ and $p_{\parallel\parallel}$ are the rr- $\phi\phi$- and $\parallel\parallel$- elements of the ion pressure tensor $\vec{\vec{P}}_i$; and q_r and q_ϕ are components of ion heat flow $\mathbf{q}_i$ in the radial and ϕ directions, respectively. As a result we can write

$$\left.\begin{aligned}
&T_i = \frac{T_r + T_\phi + T_\parallel}{3} = \frac{1}{3} T_0 \left(1 + \frac{2}{a_0}\right) \ , \\
&\{p_{rr}, p_{\phi\phi}, p_{\parallel\parallel}\} = p_0 \left\{ \frac{1}{a_0^2}, \frac{1}{a_0^2}, 1 \right\} \\
&\mathbf{q}_i = 0
\end{aligned}\right\} \tag{2.33}$$

Note that (1) all non-diagonal elements of the pressure tensor are zero, (2) the scalar pressure p_i, defined as one-third of the trace of the pressure tensor, is $p_i = p_0(2/a_0^2 + 1)$.

Fig.2.5 displays the bulk parameters for one cycle of oscillation. It shows the average velocity $\mathbf{v}_{\rm ave}$ through the drift velocity $\mathbf{v}_{\rm d} = \{\langle v_r \rangle, \langle v_\phi \rangle\}$. It also shows just how the density, temperature and pressure undergo their temporal oscillations. We note that both the ion density and perpendicular temperatures share the same temporal variation, namely, $n_{\rm i}(r,t)/n_{\rm i0} = T_r(r,t)/T_0 = 1/a_0$. Furthermore there is no heat flow at any given time in either the r, ϕ, or z directions, consistent with the fact that the distribution is symmetric about its drift point at all times.

One feature that requires comment is the in-phase oscillation in the density and the perpendicular temperatures, which resembles adiabatic heating in the sense that

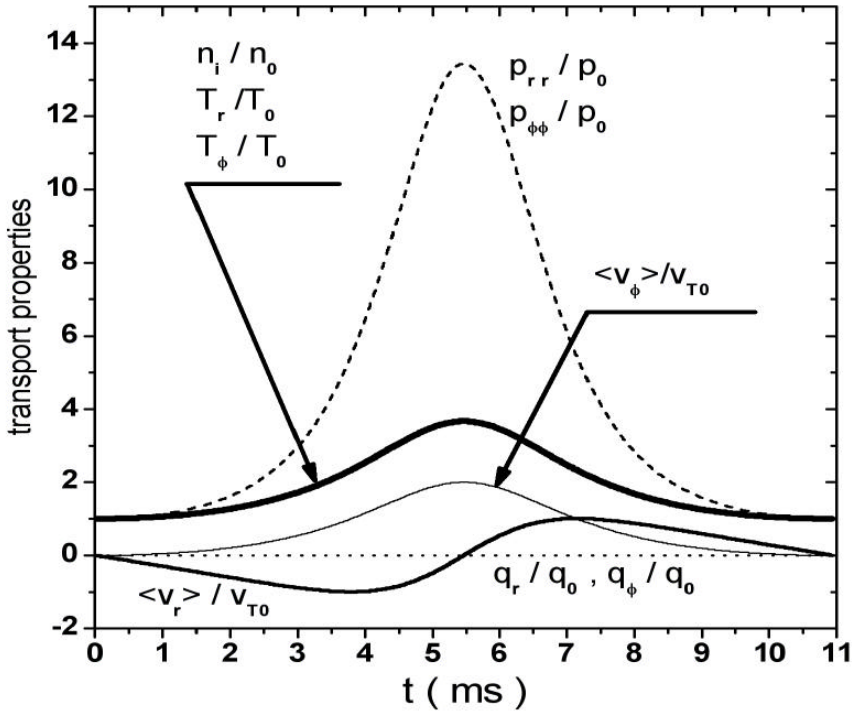

Figure 2.5: Bulk properties associated with the ion velocity distribution function in our cylindrical geometry in the collision-free case.

the higher densities are accompanied by internal ion heating. The physical origin of this behavior is that when the electric field, E_r, is turned on at $t = 0$, the ions are all attracted to the negative center of charge and, on average, move towards the center of the cylinder. However, because the electric field is stronger at larger radial distances, distant ions starting at larger electric fields are accelerated more than inner ions. This means that the distant ions travel more and gain more energy than inner ions. During the first half of an acceleration cycle the ions, which oscillate in phase in our particular case, therefore converge (higher densities) and are on average more energetic (higher perpendicular temperatures). The peak density and temperature values are reached when the magnetic force becomes large enough to deflect the ions back to their initial radial positions.

2.5 Summary and discussion

In this Chapter, the collision-free Boltzmann equation has been solved in a cylindrical geometry for a uniform magnetic field crossed with a negative electric field that increases linearly in strength with radial distance and keeps constant in time. The electric field was assumed to be produced by a cloud of electrons brought about by external processes, e.g., precipitating beams of electrons. In order to provide a useful reference and offer physical insights into solving more complicated situations, I used as simple a model as possible. This meant that there are no attempts to compute the ion feedback on the ambient electric field, and that collisions were neglected. The solutions were meant to apply well inside the uniformly charged cylinder. Also neglected were the gravitational field, possible electric field components parallel to the magnetic field, and changes in the magnetic field with position.

For the problem at hand, the resulting ion distribution function took a surprisingly simple shape, becoming a pulsating Maxwellian (if initially assumed to be a uniform Maxwellian in space). During the pulsation, the density, the two components of the perpendicular drift and temperature, were all found to change with time. The drift velocity oscillated about the local $\mathbf{E} \times \mathbf{B}$ drift, but the oscillation was not represented by a simple sinusoidal oscillation, with the mean drift spending more time at the smaller values than at the larger ones. The temperature and density were found to oscillate in phase and to take their largest values when the drift reached it maximum value.

One interesting feature of the solutions is with the ion density oscillation. If this oscillation were not to be accompanied by a similar oscillation in the electron density, the charge neutrality assumption would break down. This means that, were the electrons not able to follow the ions, the ions would be able to modify the ambient electric field. However, if the initial electric field were to be maintained by some voltage generator, extra electrons would have to be brought up along the magnetic field to compensate for the reduction. This would contrast with an initial value problem, where the ions would change the electric field so that the system

that we have studied here might start to behave more like a large-amplitude upper-hybrid (UH) oscillator (I will pursue this study in Chapter 5). One important point to notice is that the density oscillation is caused by the fact that all ions oscillate in phase, which is a peculiarity of the linearly increasing electric field in a collision-free environment. Therefore, the density oscillation will disappear once collisions are added, since one of the features collisions add is a randomization of the phases (this is clearly seen in the homogeneous problem when we compare collisional and collision-free solutions). Also, for fields that do not depend linearly on radius, the ions do not oscillate in phase, so that the density response would at least be less pronounced, if present at all. A few possibilities along these lines are considered in Chapter 4.

Chapter 3

Linear And Constant Electric Field: The Collisional Case

The approach used in the previous Chapter provides a reference and offers physical insights in the process of obtaining ion distribution functions and transport properties for more realistic, but also more complicated, electric field configurations. In this Chapter, I will show that the solutions given in Chapter 2 turn out to prove very useful for the solution of the collisional F region problem.

Above 80 km in the atmosphere, the gas is dilute enough that we need only consider binary collisions between neutrals, or, between charged particles and neutral atoms or molecules. The general collision operator in the case is the Boltzmann collision operator, e.g., *Bernstein* (1964).

3.1 Selection of a collision operator

Ideally, an appropriate full collision operator (i.e., the *Boltzmann collision integral*) should be used to describe ion-neutral collisions [e.g., *Schunk* & *Nagy* (2000)]:

$$\left.\begin{aligned}\left(\frac{\partial f_i}{\partial t}\right)_c &= \\ &= \int \mathrm{d}\mathbf{v}_n \int g\sigma_{in}(g,\theta)[f_i(\mathbf{x},\mathbf{v}_i',t)f_n(\mathbf{x},\mathbf{v}_n',t) - f_i(\mathbf{x},\mathbf{v}_i,t)f_n(\mathbf{x},\mathbf{v}_n,t)]\mathrm{d}\Omega\end{aligned}\right\} \tag{3.1}$$

where the subscripts "i, n" denote "ion, neutral", respectively; $\mathrm{d}\mathbf{v}_n$ is the velocity-space volume element for neutrals; $\mathbf{v}_i$ and $\mathbf{v}_n$ are the ion and the neutral velocities, respectively, before the collision, while $\mathbf{v}_i'$ and $\mathbf{v}_n'$ are their velocities, respectively, after the collision; $g = |\mathbf{v}_i - \mathbf{v}_n|$ is the relative speed of the colliding ions and neutrals; σ_{in} is the differential scattering cross section, defined as the number of particles

scattered into an element of solid angle, $d\Omega$, per unit time in the colliding particles' center-of-mass reference frame; and, θ is the center-of-mass scattering angle.

In Eq.(3.1), the first term in the brackets corresponds to the particles scattered into a given region of velocity space (production term) and the second term corresponds to the particles scattered out of the same region of velocity space (loss term). This operator is so complicated that it is impossible to obtain simple analytical solutions for the ion velocity distribution with it.

Series expansion based on arbitrary zeroth order functions are normally used to obtain limited solutions that are associated with the convergence of the series being used [*Minther* (1965)]. Note that the series converges faster if an appropriate guess is used for the zeroth order distribution function.

When collisions play a dominant role, Maxwellian velocity distributions are often used as appropriate weighing functions. However, in cases collisions are infrequent enough, the zeroth order distribution may itself depart significantly from a Maxwellian (see Chapter 1). It therefore proves useful to use other methods than series expansions after the zero order weighing function.

One approach that has been used in reference to the ionosphere is the Monto Carlo method [*Winkler et al.* (1992)]. However, this method does not converge rapidly away from the peak of the distribution function.

A second approach that has been used in the ionosphere with some success has been to use a relaxation model (RM) [e.g., *St-Maurice* & *Schunk* (1973)]. This model has a simple form that allows the collisional Boltzmann equation to be integrated relatively easily. The model is similar to the BGK model originally proposed by *Bhatnagar et al.* (1954), except for the fact that the latter was created to describe self-collisions whereas the former is describing collisions between different species. One important difference is with what the collisions drive the distribution to. In the BGK model, collisions drive the species to a Maxwellian that has the actual drift and temperature of the species under consideration. In the RM used by ionospheric physicists, the collisions drive the distribution function of a minor constituent to the distribution function of the major constituent. The latter is usually assumed to be

a Maxwellian at rest. The collision operator is then described by

$$\left(\frac{\partial f_i}{\partial t}\right)_c = -\nu_{in}\left(f_i - \frac{n_i}{n_n} f_n\right) \tag{3.2}$$

where f_n is a Maxwellian distribution at rest and having the temperature of the neutral gas. In this equation, ν_{in} is the ion-neutral momentum transfer collision frequency, n_i the ion density, and n_n the neutral density.

A first point to realize is that the RM does not conserve energy and momentum unless the ion and neutral masses are equal. Fortunately, this is often the case in the ionosphere. A second point to realize is that the RM can greatly exaggerate the effect of collisions. The reason for this has been highlighted by *St.-Maurice* & *Schunk* (1979), who showed that the RM can be derived from the Boltzmann collision operator under the assumption that the collision cross-section is given by

$$\sigma_{in}(g, \theta) = \frac{C}{g}\delta(\theta - \pi) \tag{3.3}$$

and $m_i = m_n$, where C is a constant. The angular dependence means that, in a RM, all collisions are "head-on" collisions in the center of mass system. In the laboratory system, this is akin to a pure charge-exchange between an ion and a neutral of the same mass (as often happens to ions in their parent gas).

The $(1/g)$-dependence in σ_{in} is also needed to insure that the RM is recovered. When the cross section has this speed dependence, the interaction is described as a "Maxwell-molecule" interaction. This interaction turns out to be a good description of the induced dipole interaction between an ion and a neutral particle ($1/r^4$-potential). It often applies to the kinds of energies that ionospheric particles have. Note that the collision frequency is a constant in this case.

We will in this Chapter use the RM in order to obtain a first order description of the non-Maxwellian characteristics of the ion velocity distribution under a strongly driven cylindrical electric field configuration. From the above discussion, we will expect that (1) the distortions driven by collisions will be exaggerated; (2) all velocity moments will have a same relaxation time; and, (3) particle diffusion driven by temperature gradients will not be present because of the constant collision frequency

implied by the RM. In spite of these limitations, the solutions should offer valuable insights into the effect of ion-neutral collisions on the ion velocity distribution. This has been demonstrated by *St.-Maurice et al.* (1976) and *Winkler et al.* (1992) when comparing RM solutions to observations or to Monte-Carlo calculations. The comparisons showed that while the RM solutions did indeed exaggerate the trends away from Maxwellian distributions, the essential characteristics of the distribution function could be recovered, to the point that a simple scaling of the solution to weaker actual conditions could often be enough to produce a very realistic description of the actual distribution function.

3.2 Collisional ion velocity distribution solutions

With the RM collision term the Boltzmann equation becomes

$$\left.\begin{aligned}\frac{\mathrm{D}f_i}{\mathrm{D}t} = \frac{\partial f_i}{\partial t} + v_r\frac{\partial f_i}{\partial r} + v_z\frac{\partial f_i}{\partial z} + \left(\frac{v_\phi^2}{r} + v_\phi\Omega_i - \frac{E_c}{B}\Omega_i R_c\frac{r}{R_c^2}\right)\frac{\partial f_i}{\partial v_r} - \\ -\left(2\frac{v_r v_\phi}{r} + v_r\Omega_i\right)\frac{\partial f_i}{\partial v_\phi} = -\nu_{in}\left(f_i - \frac{n_i}{n_n}f_n\right)\end{aligned}\right\} \tag{3.4}$$

where $\partial f_i/\partial\phi = 0$ is used owing to cylindrical symmetry. This equation has

$$\frac{\mathrm{D}f_i}{\mathrm{D}t} = -\nu_{in}\left(f_i - \frac{n_i}{n_n}f_n\right), \text{ or, } \frac{\mathrm{D}f_i}{\mathrm{D}t} + \nu_{in}f_i = \nu_{in}\frac{n_i}{n_n}f_n \tag{3.5}$$

from which the ion distribution function can be formally solved as

$$f_i = f_{i1}e^{-\nu_{in}t} + \frac{\nu_{in}}{n_n}e^{-\nu_{in}t}\int_0^t n_i(t')f_n(t')e^{\nu_{in}t'}\mathrm{d}t' \tag{3.6}$$

where the time integral must be performed by following the characteristics of ion motion, and, where f_{i1} is the collision-free ion velocity distribution function solved in Chapter 2, namely,

$$f_{i1}(\mathbf{r},\mathbf{v},t) = \frac{n_{i0}}{\pi}e^{-(v_r^2+v_\phi^2)}\cdot e^{B_2\mp B_1\sin(\omega t+\phi_0)} \tag{3.7}$$

or

$$f_{i1}(\mathbf{r},\mathbf{v},t) = \frac{n_{i0}}{\pi}e^{-a_0[(v_r-v_{\mathrm{d}r})^2+(v_\phi-v_{\mathrm{d}\phi})^2]} \tag{3.8}$$

where all parameters have been given in Chapter 2. Eq.(3.6) requires that we use another equation for the density, which can be obtained by integrating this equation itself, namely,

$$n_i = \int f_i(\mathbf{v})\mathrm{d}\mathbf{v} = \int f_{\mathrm{i1}}(\mathbf{v})\mathrm{d}\mathbf{v} \cdot e^{-\nu_{in}t} + \frac{\nu_{in}}{n_n} e^{-\nu_{in}t} \int \mathrm{d}\mathbf{v} \int_0^t n_i(t') f_n(t') e^{\nu_{in}t'} \mathrm{d}t' \quad (3.9)$$

Defining $N_i = n_i e^{\nu_{in}t}$, the above equation becomes

$$N_i = \frac{n_{i0}}{a_0(t)} + \frac{\nu_{in}}{n_n} \int_0^t N_i(t') \left[\int f_n(t')\mathrm{d}\mathbf{v} \right] \mathrm{d}t' \quad (3.10)$$

where Eq.(2.23) has been used to get the first term on the RHS.

Note that $0 \leq t' < t$ in Eqs.(3.9,3.10), and, at t' ion and neutral collide with each other.

Clearly, there are three problems to solve before obtaining a final solution for f_i in Eq.(3.6). The first is the expression of the distribution function $f_n(t')$, the second is to obtain the density $n_i(t')$ or $N_i(t')$ for ions colliding with neutrals, and the last is to perform the integration from 0 to t. Fortunately, *St.-Maurice et al.* (1994) provided an effective approach in solving these problems, though the authors focused on ion velocity distributions in electric fields that varied linearly along the x-direction. In particular, they developed a "phase-angle integration" method. I apply the same method here to obtain f_i in the cylindrical geometry.

3.2.1 Expression for $f_n(t')$

The RM states that when the ions collide, their velocity distribution immediately after a collision is that of the neutrals, namely, a Maxwellian at the neutral drift and temperature, i.e., a stationary Maxwellian at a temperature T_n. While this is not necessary, we will assume here that this temperature is also T_{i0}, the temperature of the ions prior to the electric field onset. This means that we will use the same normalization for f_n as we used for f_{i1}. In reality we should expect to have $T_{i0} > T_n$ in ionospheric situations above 200 km. However, this would only change the parameter normalization in solving Eq.(3.6).

The task to find $f_n(t')$ given that $f_n(0)$ is a stationary Maxwellian is identical to the task of finding $f_{i1}(t')$ when $f_{i1}(0)$ is a Maxwellian. This means that we have

already solved the problem of finding $f_n(t')$: if the distribution is a Maxwellian at $t' = 0$, then for $t' \neq 0$, we only need to follow the characteristics of motion to determine how f_n evolves. This is to say,

$$f_n(t') = \frac{n_n}{\pi} e^{-(v_r^2+v_\phi^2)} \cdot e^{B_2 \pm B_1 \sin[\omega(t'-t)+\phi_0]} \tag{3.11}$$

or

$$f_n(t') = \frac{n_n}{\pi} e^{-a_0'\left[(v_r - v_{\mathrm{d}r}')^2 + (v_\phi - v_{\mathrm{d}\phi}')^2\right]} \tag{3.12}$$

in which

$$\left.\begin{aligned} a_0' &= a_0(t') = \frac{a_1 + a_2 \cos\omega(t'-t)}{a_1 + a_2} \\ v_{\mathrm{d}r}' &= v_{\mathrm{d}r}(t') = \frac{E_c}{B}\frac{r}{R_c}\frac{1}{a_0}\frac{\Omega_i}{\omega}\sin\omega(t'-t) \\ v_{\mathrm{d}\phi}' &= v_{\mathrm{d}\phi}(t') = \frac{E_c}{B}\frac{r}{R_c}\frac{1}{a_0}\left(\frac{\Omega_i}{\omega}\right)^2 [1 - \cos\omega(t'-t)] \end{aligned}\right\} \tag{3.13}$$

where $a_1 = 1 + 2\dfrac{E_c/B}{R_c\Omega_i}$, $a_2 = 2\dfrac{E_c/B}{R_c\Omega_i}$. It follows from these considerations that

$$\int f_n(t')\mathrm{d}\mathbf{v} = \frac{n_n}{a_0'} \tag{3.14}$$

3.2.2 Obtaining n_i from the collisional solution

Using Eq.(3.14) in Eq.(3.10) we obtain

$$N_i = \frac{n_{i0}}{a_0(t)} + \nu_{in} \int_0^t \frac{N_i(t')}{a_0(t')}\mathrm{d}t' \tag{3.15}$$

the differential form of which is

$$\frac{\mathrm{d}N_i}{\mathrm{d}t} = \frac{\mathrm{d}}{\mathrm{d}t}\left(\frac{n_{i0}}{a_0}\right) + \frac{\nu_{in}}{a_0} N_i \tag{3.16}$$

or

$$\frac{\mathrm{d}N_i}{\mathrm{d}t} - \frac{\nu_{in}}{a_0} N_i = \frac{\mathrm{d}}{\mathrm{d}t}\left(\frac{n_{i0}}{a_0}\right) \tag{3.17}$$

Applying the initial condition $N_i|_{t=0} = n_i|_{t=0} = n_{i0}$, the solution of Eq.(3.17) is

$$N_i = \frac{n_{i0}}{a_0(t)} + n_{i0}\nu_{in} e^{\int_0^t [\nu_{in}/a_0(t')]\mathrm{d}t'} \cdot \int_0^t \frac{e^{-\int_0^{t'} [\nu_{in}/a_0(t'')]\mathrm{d}t''}}{a_0^2(t')}\mathrm{d}t' \tag{3.18}$$

Introduce as a new variable, the phase angle is $\alpha = \omega t$. Eq.(3.18) then becomes

$$N_i = \frac{n_{i0}}{a_0(t)} + n_{i0}\frac{\nu_{in}}{\omega} e^{\frac{\nu_{in}}{\omega}\int_0^{\omega t} \mathrm{d}\alpha'/a_0(\alpha')} \int_0^{\omega t} \frac{e^{-\frac{\nu_{in}}{\omega}\int_0^{\omega t'} \mathrm{d}\alpha''/a_0(\alpha'')}}{a_0^2(\alpha')}\mathrm{d}\alpha' \tag{3.19}$$

Appendix F introduces the mathematical steps to obtain the final expression of N_i. For a sufficient number of gyro-cycles, the integer of $[\omega t/(2\pi)]$ is $\sim \omega t/(2\pi)$, Eq.(F.16) gives

$$N_i = n_{i0}\left[\frac{1}{a_0} + a_1\left(e^{\frac{\nu_{in}}{\Omega_i}\omega t} - 1\right)\right] \tag{3.20}$$

Then, by definition of N_i, we obtain

$$\frac{n_i}{n_{i0}} = \left(\frac{1}{a_0} - a_1\right)e^{-\nu_{in}t} + a_1 e^{(\omega/\Omega_i - 1)\nu_{in}t} = \begin{cases} \dfrac{1}{a_0} & \text{for} \quad t \to 0 \\ a_1 e^{(\omega/\Omega_i - 1)\nu_{in}t} & \text{for} \quad t \to \infty \end{cases} \tag{3.21}$$

which reveals that the ion density contains two components. One is determined by a_0, oscillating with time. But this term decreases exponentially in time. By contrast, due to the fact that $\omega > \Omega_i$, the other one increases exponentially in time. There are two extreme cases. At $t = 0$, Eq.(3.21) states that $n_i = n_{i0}/a_0$, which is the same as that in the collision-free case covered in Chapter 2. The other extreme situation is $t \to \infty$. Now the first component disappears and the second one controls the evolution of the density.

The relative importance of the two components can be estimated as follows. Using $a_1 = 1 + 2(E_c/B)/(R_c\Omega_i) = 7/3$, $a_2 = 2(E_c/B)/(R_c\Omega_i) = 4/3$, $\omega/\Omega_i = 1.915$, we know that after a half relaxation time $0.5\nu_{in}^{-1}$, the second RHS term in Eq.(3.21) is 6.1, more than four times greater than the first term which is between -4/3 and 4/3. For longer times, the first term is negligible. For shorter times, it should not be dropped off. This allows the relation of $n_i \to n_{i0}/a_0$ for $t \to 0$ to be kept. Fig.3.1 shows the density evolution under different electric fields. In this figure and from this point on, the unit of time is $T = 2\pi/\omega$.

At this point the time-dependence of n_i needs to be discussed briefly. For small times during which the effects of collisions are not being felt yet, the density oscillates, as discussed in Chapter 2. The oscillation is rooted in the fact that after the negative charges are suddenly introduced in the system, the ions are drawn to the negative charges. As a result, the density increases. However, after some time, the ions are reflected by the magnetic field and the density decreases again. This is basically the physics behind electrostatic ion cyclotron waves in general (here though the

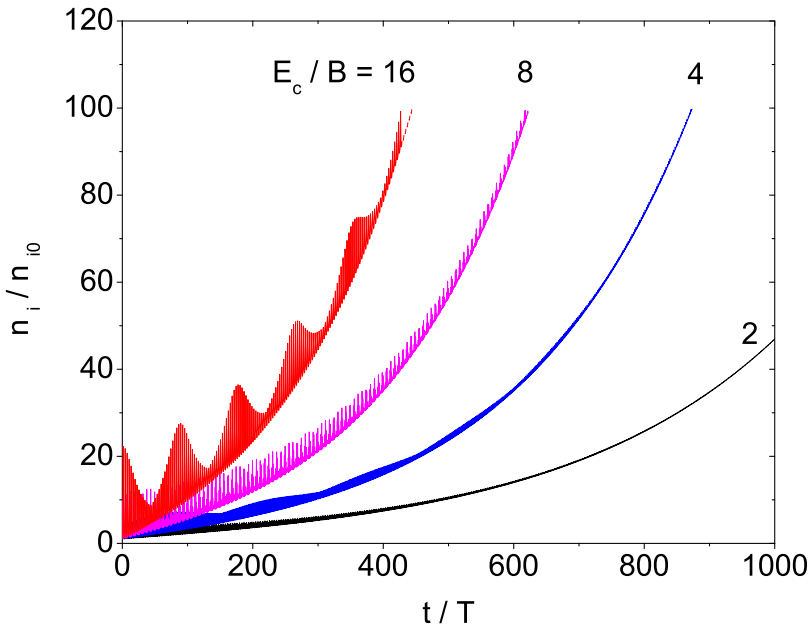

Figure 3.1: Evolution of ion density under different electric fields E_c.

oscillation is at $\omega > \Omega_i$, it is still the basic cyclotron physics).

When collisions with the neutrals are introduced we find that the ion density increases. At first, this is because with collisions, weak currents are set up along the electric field direction (these are called "Pedersen currents" in the ionospheric literature). The currents are set up because the ions are gaining kinetic energy as they approach the negative center of charges. This also means that the ion density increases as well. As long as the electric field is maintained, more electrons will have to be brought up from outside to maintain the electric field. Thus, as the ions are accumulating, the total density (ion plus electron) will increase first so as to maintain the electric field strength. This situation does not necessarily happen in ionospheric situations, but it is consistent with our model.

3.2.3 Putting the two components of f_i together

By substituting Eq.(3.21) directly in Eq.(3.6), Appendix F also gives the expression of f_i as shown in Eq.(F.21). From it, we have

$$\left.\begin{aligned} & f_i = f_{i1}e^{-\nu_{in}t} + \frac{n_{i0}}{n_{\rm n}}e^{-\nu_{in}t}. \\ & \cdot\left\{\frac{\nu_{in}t}{2\pi}\int_0^{2\pi}\left(\frac{1}{a_0}-a_1\right)f_{\rm n}(\alpha')\mathrm{d}\alpha' + a_1\frac{\Omega_i}{\omega}\frac{e^{\frac{\omega}{\Omega_i}\nu_{in}t}-1}{2\pi}\int_0^{2\pi}f_{\rm n}(\alpha')\mathrm{d}\alpha'\right\} = \\ & = \left[f_{i1} - \frac{n_{i0}}{n_{\rm n}}a_1\frac{\Omega_i}{\omega}\frac{1}{2\pi}\int_0^{2\pi}f_{\rm n}(\alpha')\mathrm{d}\alpha'\right]e^{-\nu_{in}t} + \\ & + \frac{n_{i0}}{n_{\rm n}}\left\{\frac{\nu_{in}t\cdot e^{-\nu_{in}t}}{2\pi}\int_0^{2\pi}\left(\frac{1}{a_0}-a_1\right)f_{\rm n}(\alpha')\mathrm{d}\alpha' + a_1\frac{\Omega_i}{\omega}\frac{e^{(\frac{\omega}{\Omega_i}-1)\nu_{in}t}}{2\pi}\int_0^{2\pi}f_{\rm n}(\alpha')\mathrm{d}\alpha'\right\} \end{aligned}\right\} \tag{3.22}$$

Clearly, the first term in the "$\{\cdot\}$"-expression of the result is smaller than the second. Similar to the previous discussion, this term can be neglected after several gyrations of ions due to its insignificance in the contribution to f_i, e.g., only a half collision time, the second term contributes five-fold more. Consequently, we have

$$\left.\begin{aligned} & f_i = \left[f_{i1} - \frac{n_{i0}}{n_{\rm n}}a_1\frac{\Omega_i}{\omega}\frac{1}{2\pi}\int_0^{2\pi}f_{\rm n}(\alpha')\mathrm{d}\alpha'\right]e^{-\nu_{in}t} + \\ & + \left[\frac{n_{i0}}{n_{\rm n}}a_1\frac{\Omega_i}{\omega}\frac{1}{2\pi}\int_0^{2\pi}f_{\rm n}(\alpha')\mathrm{d}\alpha'\right]e^{\left(\frac{\omega}{\Omega_i}-1\right)\nu_{in}t} \end{aligned}\right\} \tag{3.23}$$

As a test for the f_i-solution given above, let's integrate it over velocity space to see if it gives the same density n_i as shown in Eq.(3.21):

$$\left.\begin{aligned} & n_i = \int f_i\mathrm{d}\mathbf{v} = \left[\frac{n_{i0}}{a_0} - \frac{n_{i0}}{n_{\rm n}}a_1\frac{\Omega_i}{\omega}\frac{1}{2\pi}\int_0^{2\pi}\frac{n_{\rm n}}{a_0(\alpha')}\mathrm{d}\alpha'\right]e^{-\nu_{in}t} + \\ & + \left[\frac{n_{i0}}{n_{\rm n}}a_1\frac{\Omega_i}{\omega}\frac{1}{2\pi}\int_0^{2\pi}\frac{n_{\rm n}}{a_0(\alpha')}\mathrm{d}\alpha'\right]e^{\left(\frac{\omega}{\Omega_i}-1\right)\nu_{in}t} = \\ & = \left(\frac{n_{i0}}{a_0} - n_{i0}a_1\right)e^{-\nu_{in}t} + \left(n_{i0}a_1e^{\frac{\omega}{\Omega_i}\nu_{in}t}\right)e^{-\nu_{in}t} \end{aligned}\right\} \tag{3.24}$$

or,

$$\frac{n_i}{n_{i0}} = \left(\frac{1}{a_0}-a_1\right)e^{-\nu_{in}t} + a_1e^{(\frac{\omega}{\Omega_i}-1)\nu_{in}t} = \left\{\begin{array}{ll} \dfrac{1}{a_0} & \text{for} \quad t\to 0 \\ a_1e^{(\frac{\omega}{\Omega_i}-1)\nu_{in}t} & \text{for} \quad t\to\infty \end{array}\right. \tag{3.25}$$

the same expression as Eq.(3.21).

Using Eqs.(3.8,3.11), Eq.(3.23) provides

$$\left.\begin{aligned} & \frac{f_i}{n_{i0}} = \frac{1}{\pi}e^{-a_0[(v_r-v_{\rm dr})^2+(v_\phi-v_{\rm d\phi})^2]}\cdot e^{-\nu_{in}t} + \\ & + \frac{\Omega_i}{\omega}\frac{a_1}{2\pi^2}\cdot\int_0^{2\pi}e^{-(v_r^2+v_\phi^2)+(B_2\pm B_1\sin\alpha')}\mathrm{d}\alpha'\left(e^{\frac{\omega}{\Omega_i}\nu_{in}t}-1\right)e^{-\nu_{in}t} \end{aligned}\right\} \tag{3.26}$$

Noting the following points: (1) parameters B_1 and B_2 are neither explicit functions of α (or t), nor of α' (or t'), (2) the integration $\frac{1}{2\pi}\int_0^{2\pi} e^{\pm B_1 \sin\alpha'} \mathrm{d}\alpha'$ is the zeroth-order modified Bessel function $I_0(\pm B_1) = I_0(+B_1) = I_0(-B_1)$, we rewrite Eq.(3.26) as

$$\left.\begin{array}{l} \dfrac{f_i}{n_{i0}} = \dfrac{1}{\pi} e^{-a_0[(v_r - v_{\mathrm{d}r})^2 + (v_\phi - v_{\mathrm{d}\phi})^2]} \cdot e^{-\nu_{in} t} + \\ + \dfrac{1}{\pi} e^{B_2 - (v_r^2 + v_\phi^2)} \cdot \dfrac{\Omega_i}{\omega} a_1 \cdot I_0(B_1) \cdot \left(e^{\frac{\omega}{\Omega_i}\nu_{in} t} - 1 \right) e^{-\nu_{in} t} \end{array}\right\} \tag{3.27}$$

Obviously, f_i contains two components. One is the collision-free term $f_{i\mathrm{Cfree}}$, and the other is the collisional term $f_{i\mathrm{Cnal}}$, satisfying

$$f_i = f_{i\mathrm{Cfree}} + f_{i\mathrm{Cnal}} = f_{i1} \cdot e^{-\nu_{in} t} + f_{i2} \cdot \left(e^{\frac{\omega}{\Omega_i}\nu_{in} t} - 1 \right) e^{-\nu_{in} t} \tag{3.28}$$

in which

$$\left.\begin{array}{l} f_{i\mathrm{Cfree}} = f_{i1} \cdot e^{-\nu_{in} t} \\ f_{i\mathrm{Cnal}} = f_{i2} \cdot \left(e^{\frac{\omega}{\Omega_i}\nu_{in} t} - 1 \right) e^{-\nu_{in} t} \\ f_{i1}/n_{i0} = \dfrac{1}{\pi} e^{-a_0[(v_r - v_{\mathrm{d}r})^2 + (v_\phi - v_{\mathrm{d}\phi})^2]} \\ f_{i2}/n_{i0} = \dfrac{1}{\pi} e^{B_1 + B_2 - (v_r^2 + v_\phi^2)} \dfrac{\Omega_i}{\omega} a_1 \left[e^{-B_1} I(B_1) \right] \end{array}\right\} \tag{3.29}$$

Fig.3.2 shows the ratios, $f_{i\mathrm{Cfree}}/f_{i1}$ and $f_{i\mathrm{Cnal}}/f_{i2}$, versus time. Obviously, the first ratio decreases exponentially to zero from the initial value of 1, while the second one increases exponentially from zero to 20 at the end of time selected in calculations.

3.2.4 Evolution of f_i

The evolution of f_i depends on the temporal behaviors of $f_{i\mathrm{Cfree}}(t)$ [which contains $f_{i1}(t)$] and $f_{i\mathrm{Cnal}}(t)$ [which contains $f_{i2}(t)$]. Chapter 2 has shown that $f_{i1}(t)$ is a shifted, pulsating Maxwellian in time. The shifting center rotates around the $\mathbf{E} \times \mathbf{B}$ drift, while the distribution relative to the center pulsates periodically. As one component of f_i, however, this shifted, pulsating Maxwellian decays with time exponentially, as shown by $f_{i\mathrm{Cfree}}$ in Eq.(3.29).

By contrast with $f_{i1}(t)$, f_{i2} is not a function of time, but it contains a Bessel function. Figs.3.3 & 3.4 describe the evolution of f_{i2} as a function of radial position and electric field strength, respectively. The panels in the two figures show that the collisional component in the ion velocity distribution exhibits a horse-shoe shape

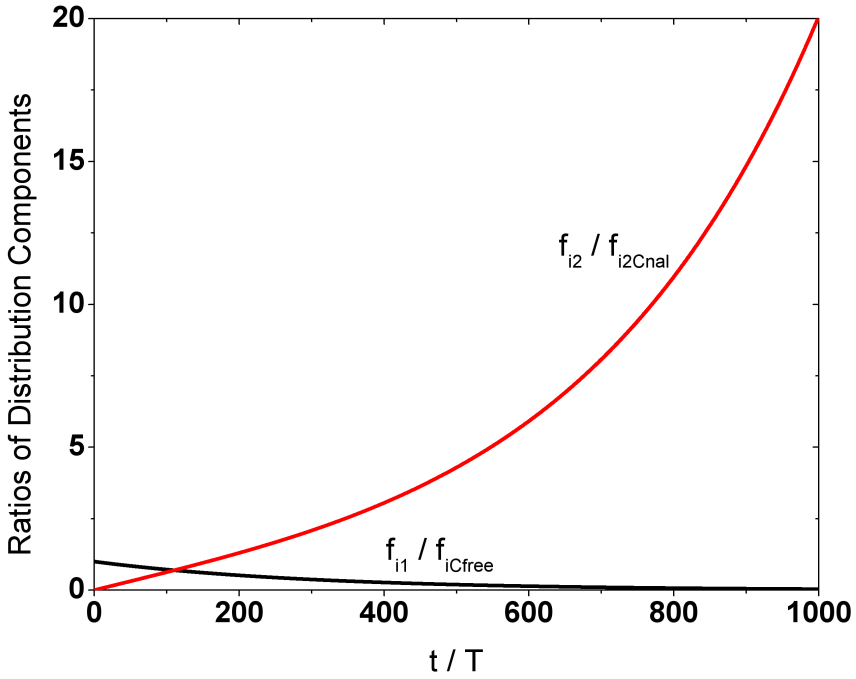

Figure 3.2: Evolution of the two ratios: $f_{i1}/f_{i\mathrm{Cfree}}$ and $f_{i2}/f_{i\mathrm{Cnal}}$.

which can be with a hollow or a solid core. In the extreme cases (large distance from the center, or strong electric field), energetic tails form. This means that ions are heated transversely.

As discussed earlier, though f_{i2} is independent of time, $f_{i\mathrm{Cnal}}(t)$ grows exponentially with time due to $\omega > \Omega_i$. This term increasingly dominates f_i. Fig.3.5 presents the temporal evolution of f_i at $t = 5T$, $t = 10T$, $t = 50T$, and $t = 500T$ in four panels, respectively. Let's consider two extremes. In the first panel, $t = 5T = 10\pi/\omega = 55$ ms. Then, $\nu_{in}t = 1.6 \times 10^{-2}$, producing $e^{-\nu_{in}t} \approx 1$, and $e^{(\omega/\Omega_i)\nu_{in}t} - 1 \approx 0$. Consequently, f_i is chiefly determined by $f_{i\mathrm{Cfree}}(t)$, showing a Maxwellian shape. By contrast, in the last panel, $t = 500T = 5500$ ms. Then, $\nu_{in}t = 1.6$, producing $e^{-\nu_{in}t} \approx 0.2$, and $e^{\frac{\omega}{\Omega_i}\nu_{in}t} - 1 \approx 23.5$. Consequently, f_i is completely controlled by $f_{i\mathrm{Cnal}}(t)$, exhibiting a horse-shoe shape.

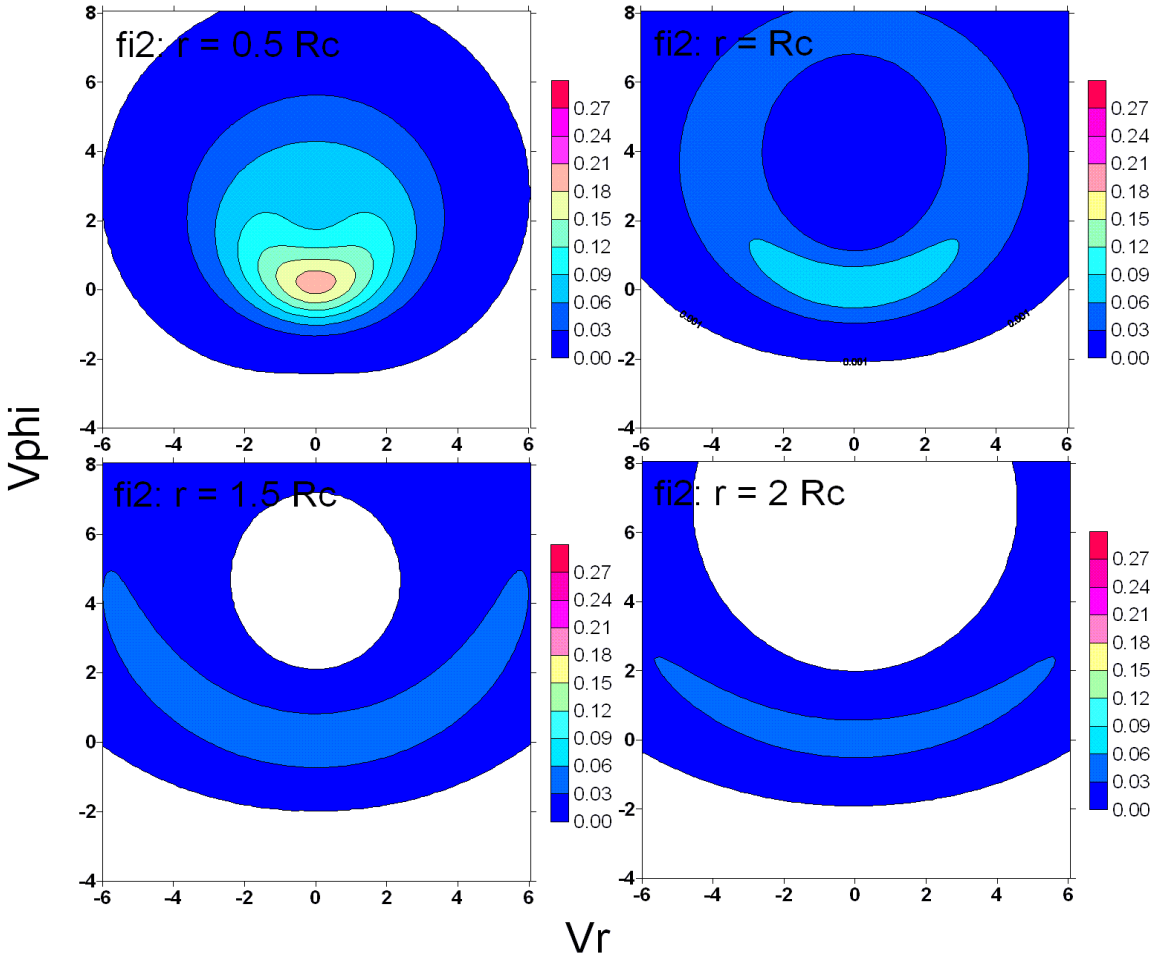

Figure 3.3: Development of f_{i2} horse-shoe distribution versus radial position r.

3.3 Velocity moments and transport properties

In Appendix G, a series of mathematical expressions is provided in order to calculate velocity moments. The six formulae in Eq.(G.19) are used in following expressions.

Using Eqs.(3.8,3.12) with the velocity in vector form, the velocity moments can

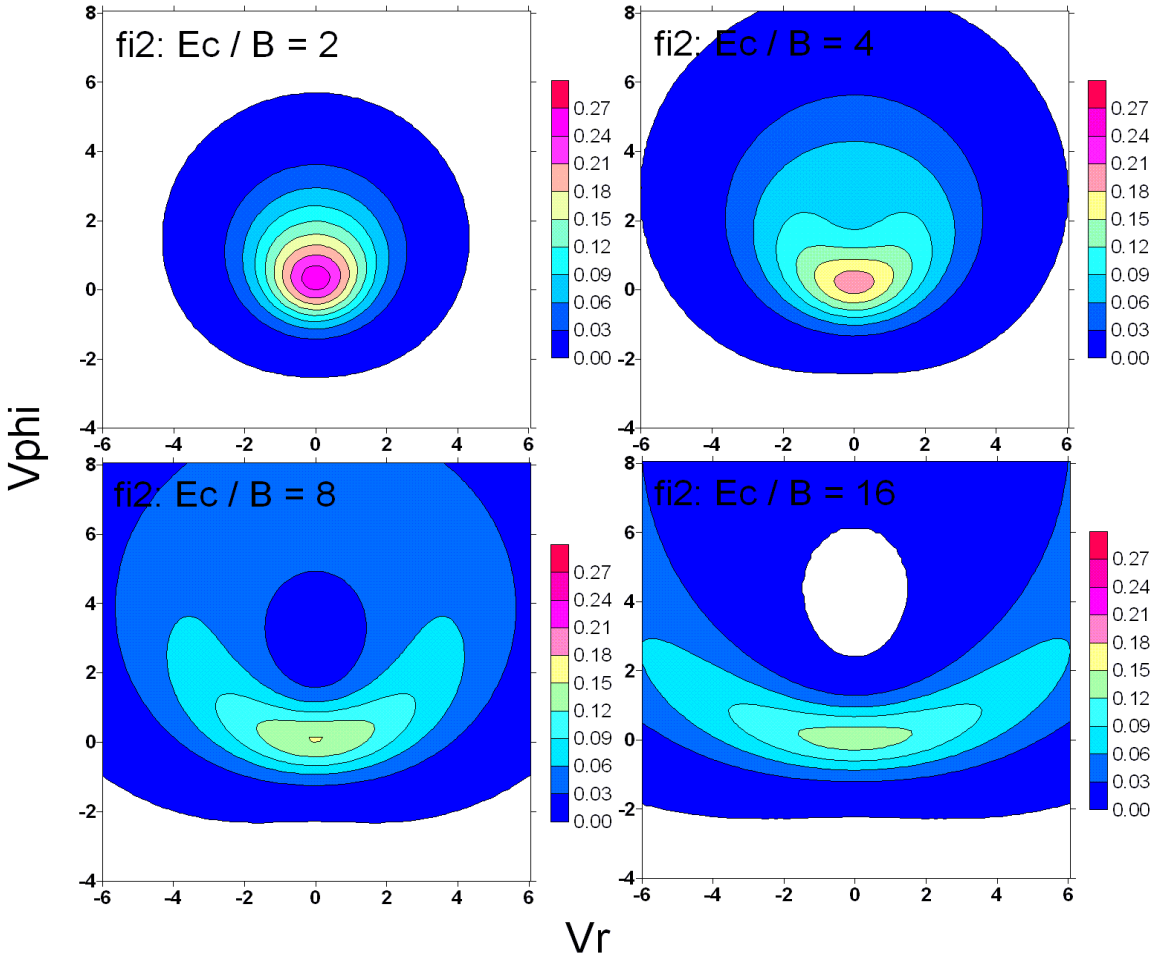

Figure 3.4: Development of f_{i2} horse-shoe distribution versus electric field E_c.

be obtained as follows:

$$\left.\begin{aligned}
&\langle v_j^k \rangle = \frac{1}{n_i} \int v_j^k f_i \mathrm{d}\mathbf{v} = \\
&= \frac{\int v_j^k \left[\frac{f_{\mathrm{i1}}}{n_{\mathrm{i0}}} + \frac{a_1}{n_{\mathrm{n}}} \frac{\Omega_i}{\omega} \frac{1}{2\pi} \int_0^{2\pi} f_{\mathrm{n}}(\alpha') \mathrm{d}\alpha' \cdot \left(e^{\frac{\omega}{\Omega_i} \nu_{in} t} - 1 \right) \right] \mathrm{d}\mathbf{v}}{\left(\frac{1}{a_0} - a_1 \right) + a_1 e^{\frac{\omega}{\Omega_i} \nu_{in} t}} = \\
&= \frac{\frac{1}{\pi} \int v_j^k e^{-a_0 (\mathbf{v} - \mathbf{v}_d)^2} \mathrm{d}\mathbf{v} + \frac{a_1 \Omega_i}{2\pi^2 \omega} \int_0^{2\pi} \left[\int v_j^k e^{-a_0'(\alpha)[\mathbf{v} - \mathbf{v}_d'(\alpha)]^2} \mathrm{d}\mathbf{v} \right] \mathrm{d}\alpha \left(e^{\frac{\omega}{\Omega_i} \nu_{in} t} - 1 \right)}{\frac{1}{a_0} + a_1 \left(e^{\frac{\omega}{\Omega_i} \nu_{in} t} - 1 \right)}
\end{aligned}\right\} \quad (3.30)$$

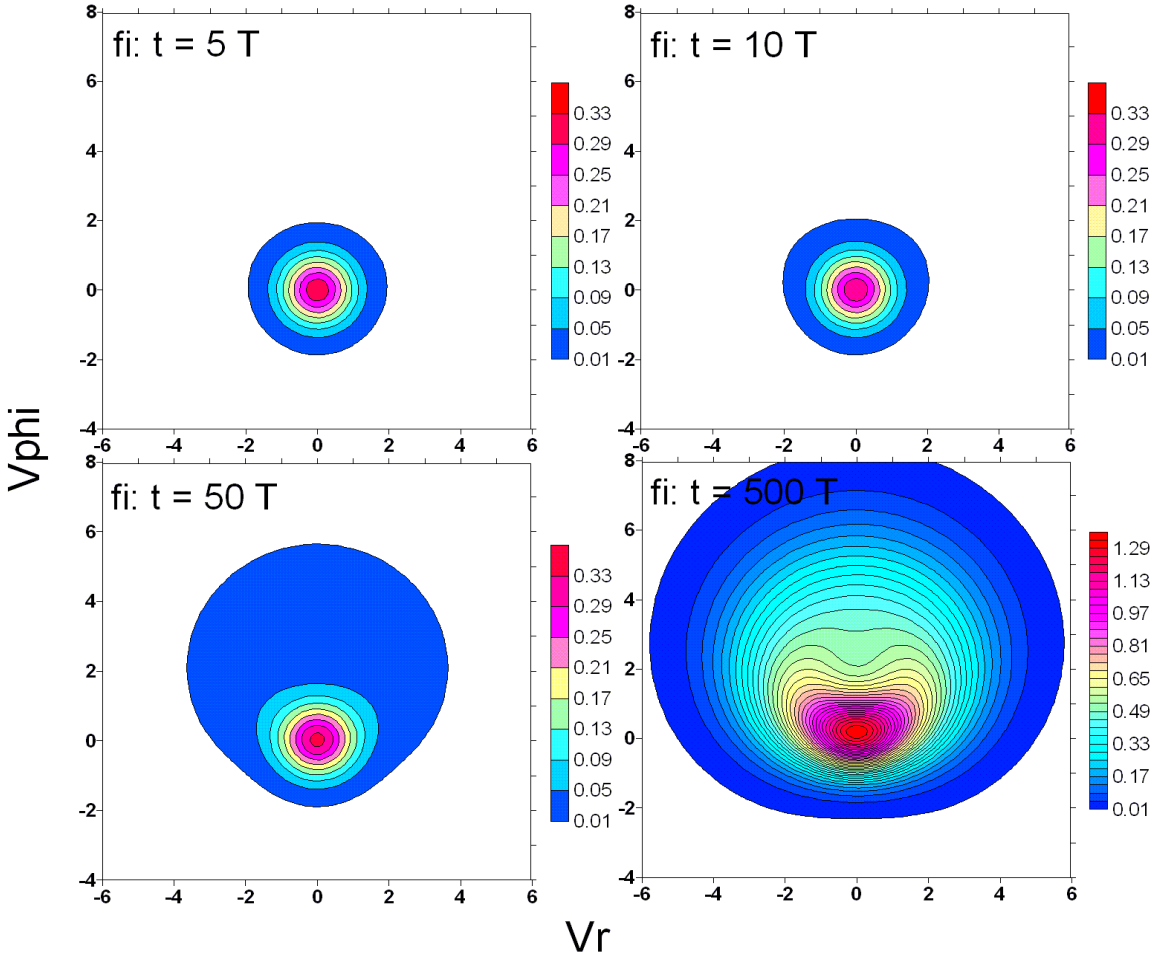

Figure 3.5: Evolution of f_i horse-shoe distribution versus time t.

which provides following dimensionless components of velocity moments:

$$\langle v_r \rangle = \frac{v_{\mathrm{d}r}}{1 + a_0 a_1 \left(e^{\frac{\omega}{\Omega_i} \nu_{in} t} - 1 \right)} = \begin{cases} v_{\mathrm{d}r} & \text{for } t \to 0 \\ 0 & \text{for } t \to \infty \end{cases} \tag{3.31}$$

$$\langle v_\phi \rangle = \frac{v_{\mathrm{d}\phi} + \dfrac{E_c}{B} \dfrac{r}{R_c} a_0 a_1 \left(e^{\frac{\omega}{\Omega_i} \nu_{in} t} - 1 \right)}{1 + a_0 a_1 \left(e^{\frac{\omega}{\Omega_i} \nu_{in} t} - 1 \right)} = \left\{ \begin{array}{ll} v_{\mathrm{d}\phi} & \text{for } t \to 0 \\ \dfrac{E_c}{B} \dfrac{r}{R_c} & \text{for } t \to \infty \end{array} \right\} \tag{3.32}$$

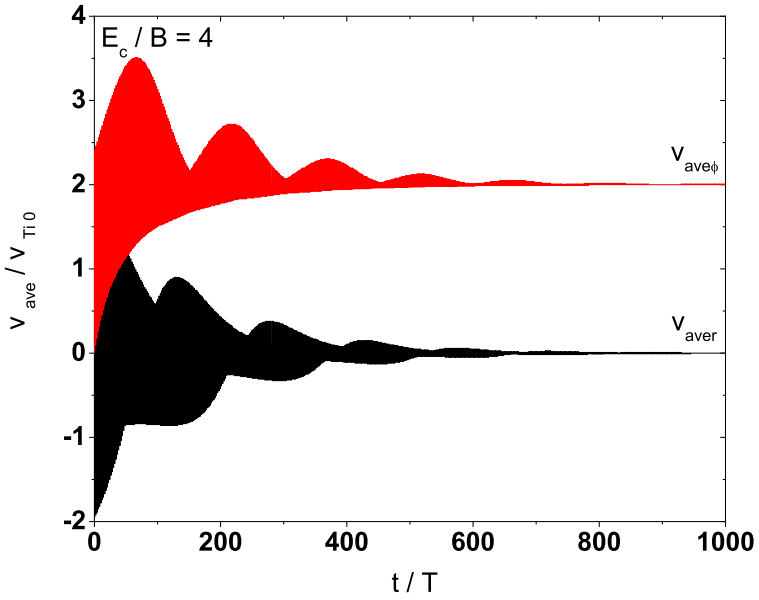

Figure 3.6: Evolution of the average ion velocity for $E_c/B = 4$ at $r = 0.5R_c$.

$$\langle v_r^2 \rangle = \frac{v_{\mathrm{d}r}^2 + \dfrac{1}{2a_0} + \left[\dfrac{1}{2}\left(\dfrac{E_c}{B}\dfrac{r}{R_c}\right)^2 + \dfrac{a_1}{2}\right] a_0 a_1 \left(e^{\frac{\omega}{\Omega_i}\nu_{in}t} - 1\right)}{1 + a_0 a_1 \left(e^{\frac{\omega}{\Omega_i}\nu_{in}t} - 1\right)} = \left.\begin{cases} v_{\mathrm{d}r}^2 + \dfrac{1}{2a_0} & \text{for } t \to 0 \\ \dfrac{1}{2}\left(\dfrac{E_c}{B}\dfrac{r}{R_c}\right)^2 + \dfrac{a_1}{2} & \text{for } t \to \infty \end{cases}\right\} \tag{3.33}$$

$$\langle v_\phi^2 \rangle = \frac{v_{\mathrm{d}\phi}^2 + \dfrac{1}{2a_0} + \left[\dfrac{3}{2}\left(\dfrac{E_c}{B}\dfrac{r}{R_c}\right)^2 + \dfrac{a_1}{2}\right] a_0 a_1 \left(e^{\frac{\omega}{\Omega_i}\nu_{in}t} - 1\right)}{1 + a_0 a_1 \left(e^{\frac{\omega}{\Omega_i}\nu_{in}t} - 1\right)} = \left.\begin{cases} v_{\mathrm{d}\phi}^2 + \dfrac{1}{2a_0} & \text{for } t \to 0 \\ \dfrac{3}{2}\left(\dfrac{E_c}{B}\dfrac{r}{R_c}\right)^2 + \dfrac{a_1}{2} & \text{for } t \to \infty \end{cases}\right\} \tag{3.34}$$

$$\langle v_r^3 \rangle = \frac{v_{\mathrm{d}r}^3 + \dfrac{3v_{\mathrm{d}r}}{2a_0}}{1 + a_0 a_1 \left(e^{\frac{\omega}{\Omega_i}\nu_{in}t} - 1\right)} = \begin{cases} v_{\mathrm{d}r}^3 + \dfrac{3v_{\mathrm{d}r}}{2a_0} & \text{for } t \to 0 \\ 0 & \text{for } t \to \infty \end{cases} \tag{3.35}$$

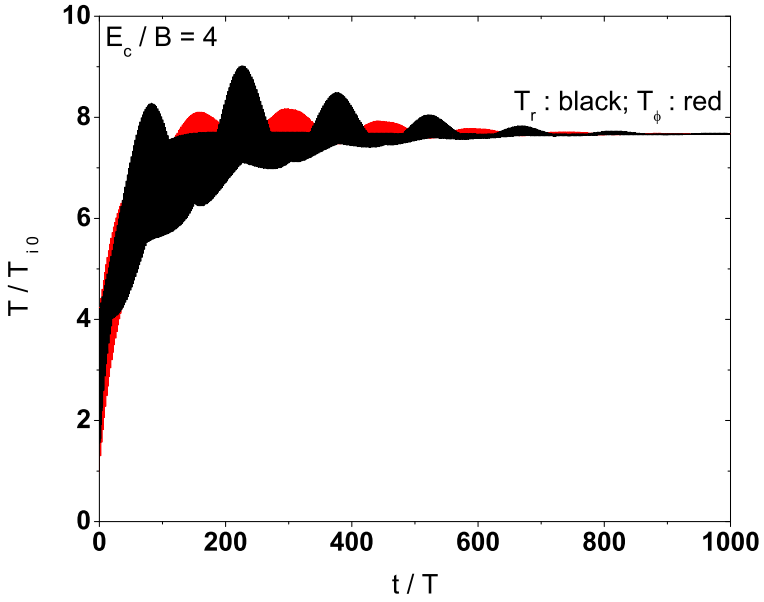

Figure 3.7: Evolution of the ion temperature for $E_c/B = 4$ at $r = 0.5R_c$.

$$\left.\begin{aligned}\langle v_\phi^3\rangle = \frac{v_{\mathrm{d}\phi}^3 + \dfrac{3v_{\mathrm{d}\phi}}{2a_0}}{1 + a_0a_1\left(e^{\frac{\omega}{\Omega_i}\nu_{in}t} - 1\right)} + \\ + \frac{\dfrac{E_c}{B}\dfrac{r}{R_c}\left\{\dfrac{5}{2}\left(\dfrac{E_c}{B}\dfrac{r}{R_c}\right)^2 + \dfrac{3}{2}\left[\left(\dfrac{\omega}{\Omega_i}\right)^2 - \dfrac{E_c/B}{R_c\Omega_i}\right]\right\} a_0a_1\left(e^{\frac{\omega}{\Omega_i}\nu_{in}t} - 1\right)}{1 + a_0a_1\left(e^{\frac{\omega}{\Omega_i}\nu_{in}t} - 1\right)} = \\ = \begin{cases} v_{\mathrm{d}\phi}^3 + \dfrac{3v_{\mathrm{d}\phi}}{2a_0} & \text{for } t \to 0 \\ \dfrac{E_c}{B}\dfrac{r}{R_c}\left\{\dfrac{5}{2}\left(\dfrac{E_c}{B}\dfrac{r}{R_c}\right)^2 + \dfrac{3}{2}\left[\left(\dfrac{\omega}{\Omega_i}\right)^2 - \dfrac{E_c/B}{R_c\Omega_i}\right]\right\} & \text{for } t \to \infty \end{cases}\end{aligned}\right\} \quad (3.36)$$

The normalization for the ion density n_i is n_{i0}, for the average velocity components v_{aver} and $v_{\mathrm{ave}\phi}$ is v_{Ti0}, for the temperature components T_r and T_ϕ is T_{i0}, for the pressure tensor compponents p_{rr} and $p_{\phi\phi}$ is $n_{i0}k_bT_{i0}$, and for the heat-flow components q_r and q_ϕ is mv_{Ti0}^3. The velocity moments are therefore provide transport

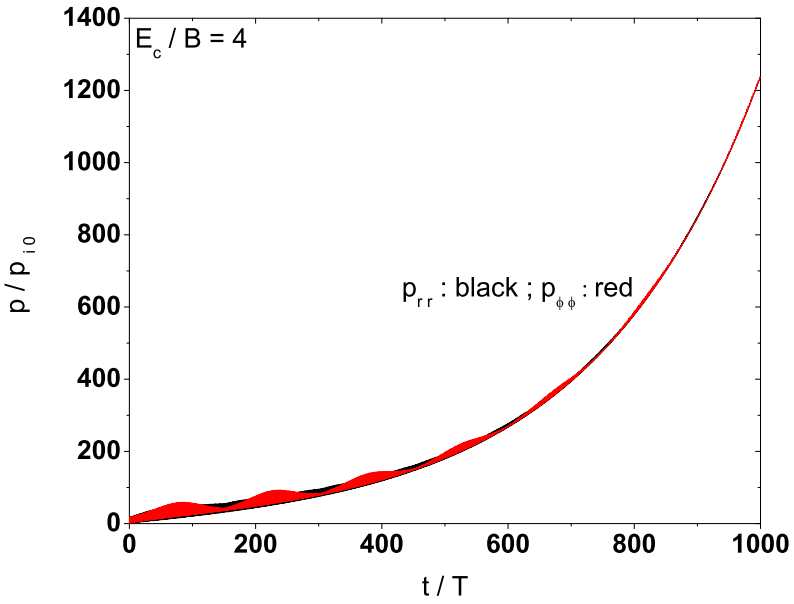

Figure 3.8: Evolution of the ion pressure for $E_c/B = 4$ at $r = 0.5R_c$.

parameters as follows in dimensional units:

$$\left.\begin{aligned} v_{\text{aver}} = \langle v_r \rangle &= \begin{cases} v_{\text{dr}} \text{ for } t \to 0 \\ 0 \quad \text{for } t \to \infty \end{cases} \\ v_{\text{ave}\phi} = \langle v_\phi \rangle &= \begin{cases} v_{\text{d}\phi} & \text{for } t \to 0 \\ \dfrac{E_c}{B}\dfrac{r}{R_c} & \text{for } t \to \infty \end{cases} \end{aligned}\right\} \tag{3.37}$$

$$\left.\begin{aligned} T_r = 2(\langle v_r^2 \rangle - \langle v_r \rangle^2) &= \begin{cases} \dfrac{1}{a_0} & \text{for} \quad t \to 0 \\ a_1 + \left(\dfrac{E_c}{B}\dfrac{r}{R_c}\right)^2 & \text{for} \quad t \to \infty \end{cases} \\ T_\phi = 2(\langle v_\phi^2 \rangle - \langle v_\phi \rangle^2) &= \begin{cases} \dfrac{1}{a_0} & \text{for} \quad t \to 0 \\ a_1 + \left(\dfrac{E_c}{B}\dfrac{r}{R_c}\right)^2 & \text{for} \quad t \to \infty \end{cases} \end{aligned}\right\} \tag{3.38}$$

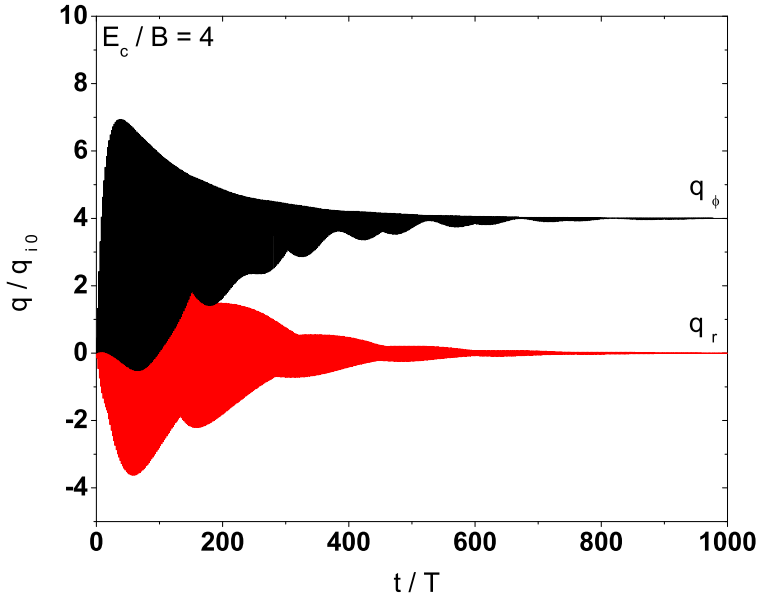

Figure 3.9: Evolution of the ion heat flow for $E_c/B = 4$ at $r = 0.5R_c$.

$$p_{rr} = n_i T_r = \left\{ \begin{array}{lll} \dfrac{1}{a_0^2} & & \text{for} \quad t \to 0 \\ a_1 \left[a_1 + \left(\dfrac{E_c}{B} \dfrac{r}{R_c} \right)^2 \right] e^{(\frac{\omega}{\Omega_i} - 1)\nu_{in} t} & & \text{for} \quad t \to \infty \end{array} \right\}$$

$$p_{\phi\phi} = n_i T_\phi = \left\{ \begin{array}{lll} \dfrac{1}{a_0^2} & & \text{for} \quad t \to 0 \\ a_1 \left[a_1 + \left(\dfrac{E_c}{B} \dfrac{r}{R_c} \right)^2 \right] e^{(\frac{\omega}{\Omega_i} - 1)\nu_{in} t} & & \text{for} \quad t \to \infty \end{array} \right\} \tag{3.39}$$

$$q_r = (\langle v_r^3 \rangle - \langle v_r \rangle^3) - \frac{3}{2} \langle v_r \rangle T_r = \left\{ \begin{array}{lll} 0 & \text{for} & t \to 0 \\ 0 & \text{for} & t \to \infty \end{array} \right\}$$

$$q_\phi = \left(\langle v_\phi^3 \rangle - \langle v_\phi \rangle^3 \right) - \frac{3}{2} \langle v_\phi \rangle T_\phi = \left\{ \begin{array}{lll} 0 & & \text{for} \quad t \to 0 \\ \dfrac{3}{2} \left(\dfrac{E_c}{B} \dfrac{r}{R_c} \right) \dfrac{E_c/B}{R_c \Omega_i} & & \text{for} \quad t \to \infty \end{array} \right\} \tag{3.40}$$

For $E_c/B = 4$ and at $r = 0.5R_c$ (that is, the $\mathbf{E} \times \mathbf{B}$ drift is $4 \times 0.5 = 2$), Eqs.(3.37-3.40) state that at $t = 0$, the bulk parameters have their initial values as follows: $v_{\text{aver}} = v_{\text{ave}\phi} = 0$, $T_r = T_\phi = 1$, $p_{rr} = p_{\phi\phi} = 1$, and, $q_r = q_\phi = 0$; for $t = 1000$, they have the final values as follows: $v_{\text{aver}} = 0$, $v_{\text{ave}\phi} = 2$, $T_r = T_\phi = 7.67$, $p_{rr} = p_{\phi\phi} =$

1237, and, $q_r = 0$, $q_\phi = 4$.

Figs.3.6-3.9 illustrate the time evolution of the above transport properties. Similar to the evolution of ion density, the temporal variation of these parameters also show two parts, namely, an oscillating one and a monotonic one. Initially, the oscillating part takes the leading role. With time, it gives its way to the second part.

3.4 Summary and discussion

By contrast with Chapter 2 where the case $(\partial f/\partial t)_{\rm c} = 0$ has been discussed for time scales much shorter than a collision time (or, $t \ll \nu_{in}^{-1}$; $\nu_{in} \ll \Omega_i$ in the ionosphere), this Chapter has focused on the response of the ion velocity distribution function to intense electric fields under collisional conditions, namely, $(\partial f/\partial t)_{\rm c} \neq 0$. In this Chapter, we have dealt mainly with long time scales ($t \gg \nu_{in}^{-1}$).

In this collisional case, the Boltzmann collision integral is replaced by a relaxation model. The solution to the full collision operator would have required a numerical Monte Carlo approach [*Winkler et al.* (1992)]. Several results have been obtained: distribution functions with horseshoe shapes in velocity space; ion density increasing exponentially; mean drift speed equal to the local value of the $\mathbf{E} \times \mathbf{B}$ drift; the two temperatures in the r and ϕ directions, respectively, leveling off with a same value; no ion heat flow in the r-direction, and a strong ion heat flow in the ϕ-direction.

One interesting aspect of the results is the ion density increasing with time, which is illustrated in Fig.3.1. In other words,

$$\frac{\partial n_i}{\partial t} \neq 0 \quad \text{for} \quad t \to \infty \tag{3.41}$$

However, the continuity equation,

$$\frac{{\rm d}n_i}{{\rm d}t} = \frac{\partial n_i}{\partial t} + \nabla \cdot (n_i \langle \mathbf{v} \rangle) = 0 \tag{3.42}$$

shows

$$\frac{\partial n_i}{\partial t} = -\frac{n_i}{r}\frac{\partial}{\partial r}(r\langle v_r \rangle) = -2\frac{n_i}{r}\langle v_r \rangle \to 0 \quad \text{for} \quad t \to \infty \tag{3.43}$$

when using Eqs.(3.25,3.31). These are contradictory results.

We have shown in Chapter 2 that in the collision-free case the density oscillates. We will also show in Chapter 6 that this is consistent with Eq.(3.43) and the result of the fluid equations. However, when we introduce collisions, the oscillations not only decay, but are replaced with a steady density increase. We now argue that this is due to small Pedersen currents that were neglected when we obtained $\langle v_r \rangle$. This can be seen relatively easily if we consider situations over which the nonlinear effects are not large. In that case we expect to have the Pedersen drift given by

$$\langle v_r \rangle = \frac{\nu_{in}}{\Omega_i} \langle v_\phi \rangle = -\frac{\nu_{in}}{\Omega_i} \frac{E_c}{B} \frac{r}{R_c} \tag{3.44}$$

for small ν_{in} (i.e., $\nu_{in}/\Omega_i \ll 1$). In the above equation, the sign "-" is because the ions are drawn in by the negative charges. Then, Eq.(3.43) gives

$$\frac{\partial n_i}{\partial t} = 2 n_i \frac{\nu_{in}}{\Omega_i} \frac{E_c}{B} \frac{1}{R_c} \tag{3.45}$$

the solution of which is

$$n_i = n'_{i0} \exp\left(2 \frac{E_c}{B} \frac{1}{R_c \Omega_i} \nu_{in} t \right) \tag{3.46}$$

Note that n'_{i0} is an ion density at $t > 0$ which is not known after a transition from collision-free to collisional conditions. But it can be considered as an initial condition here.

Now let's see what we have for n_i as $t \to \infty$ under the same weakly nonlinear condition using Eq.(3.25). After a long time, this equation tells us that

$$n_i \to n_{i0} a_1 e^{(\omega/\Omega_i - 1)\nu_{in} t} = n_{i0} a_1 \exp\left[\left(\sqrt{1 + 4 \frac{E_c/B}{R_c \Omega_i}} - 1 \right) \nu_{in} t \right] \tag{3.47}$$

For small nonlinear effects, the argument under the square root is close to 1 (see Chapter 6 for more), and we then obtain

$$n_i \approx n_{i0} a_1 \exp\left(2 \frac{E_c/B}{R_c \Omega_i} \nu_{in} t \right) \tag{3.48}$$

So, indeed if nonlinear effects are weak we recover what is expected from the continuity equation. Roughly, we also have $n'_{i0} \sim n_{i0} a_1$ by balancing Eq.(3.46) and Eq.(3.48).

In fact, this ionic Pedersen drift can be derived from Eq.(F.19) in Appendix F by using a leading order correction through a Taylor expansions of $e^{(\nu_{in}/\Omega_i)\alpha'} \approx 1 + (\nu_{in}/\Omega_i)\alpha'$. This produces an extra term in Eq.(F.21), namely,

$$\Delta f_i = \frac{n_{i0}}{n_{\rm n}}\frac{\nu_{in}}{\omega}\cdot\frac{a_1}{2\pi}\int_0^{2\pi}\alpha' f_{\rm n}(\alpha'){\rm d}\alpha'\cdot\left[e^{(\omega/\Omega_i)\nu_{in}t}-1\right]e^{-\nu_{in}t} \tag{3.49}$$

Using Eq.(3.25), we obtain the additional term for the average radial speed $\Delta\langle v_r\rangle$ for $t\to\infty$, namely,

$$\left.\begin{aligned}\Delta\langle v_r\rangle &= \frac{\int v_r(\Delta f_i/n_{i0}){\rm d}\mathbf{v}}{n_i/n_{i0}} = \frac{\nu_{in}}{\omega}\frac{a_1}{2\pi}\int_0^{2\pi}\alpha'\frac{v_{\rm dr}(\alpha')}{a_0(\alpha')}{\rm d}\alpha' = -C^*\frac{\nu_{in}}{\Omega_i}\frac{E_c}{B}\frac{r}{R_c}\\ C^* &= -\frac{a_1+a_2}{2\pi}\int_0^{2\pi}\frac{\alpha'\sin\alpha'}{(a_1+a_2\cos\alpha')^2}{\rm d}\alpha' > 0\end{aligned}\right\} \tag{3.50}$$

in which C^* is a coefficient less than 1 and anti-correlated with E_c/B. For example, at $E_c/B = v_{th}, 2v_{th}, 3v_{th}, 4v_{th}$, $C^* = 0.7461, 0.6348, 0.5635, 0.5124$, respectively. For $R_c = 10$ m at $E_c/B = 0.001v_{th}$ (or, $E_c = 50$ μV/m), $C^* = 0.969$; at $E_c = 0$, $C^* = 1$. The same result holds if R_c is large (weak nonlinearities).

Thus, for long times, Eq.(3.31) now gives a general ionic Pedersen drift under any electric field strengths which is equal to

$$\langle v_r\rangle = \Delta\langle v_r\rangle = -C^*\frac{\nu}{\Omega_i}\frac{E_c}{B}\frac{r}{R_c} \tag{3.51}$$

and

$$n_i = n'_{i0}\exp\left(2C^*\frac{E_c/B}{R_c\Omega_i}\nu t\right) \to n'_{i0}\exp\left(2\frac{E_c/B}{R_c\Omega_i}\nu t\right) \tag{3.52}$$

if the electric field is so weak or R_c so large that Eq.(3.48) is valid, and Eq.(3.51) simplifies to Eq.(3.45).

The final question is: what is the physics behind the increase in density? To answer this, recall that the electric field is kept constant in our calculations. This means that in order to maintain the electric field, every time an ion gets trapped in the negative charge region, an additional electron has to be brought in to neutralize it. For this reason, the plasma density has to go up. This increase is feasible because the electrons that provide the electric field come from "outside generator(s)", like precipitating electrons, or those that get trapped by high frequency turbulence. One

alternative would be to let the ions neutralize the electric field with Pedersen currents instead of triggering an increase in the plasma density.

Some caution should also be exercised before applying our horseshoe results to actual observations in that our results have been obtained under the assumption of cylinders with infinite radii. In practice, we should expect our results to be valid well inside cylinders with finite radii, but certainly not near their edges, or, outside of them. We discuss those situations for collision-free conditions in the next Chapter.

Chapter 4

Electric Fields That Are Constant In Time But Vary Arbitrarily With Radial Distance: Collision-Free Situations

The analytical model and calculations of ion velocity distributions and transport properties in a linear and constant electric field presented in Chapter 2 and 3 are a first step in the evaluation of more complicated situations. In this Chapter we now study the response of ions to spatially more realistic electric field structures.

The situation is now more complicated because the space-charge cylinder no longer has an infinite radius. This forces the electric field strength to change nonlinearly. Even the collision-free problem becomes complicated because the ion orbits are no longer locked in phase, except, maybe, in the extreme inner part of the cylinder. Elsewhere, ions that start at different radial distances will feel different oscillation frequencies.

To study this problem, I have generalized the analytical work to produce a semi-numerical method. By establishing a backmapping model to get ion trajectories of motion, the approach describes numerically various shapes of ion velocity distribution functions, as well as the associated transport properties, for arbitrary electric field structures. These fields are radially nonlinear but still constant in time. Only collision-free cases are considered. A flow chart describing the computer procedure used to solve the problem is given in Fig.4.1.

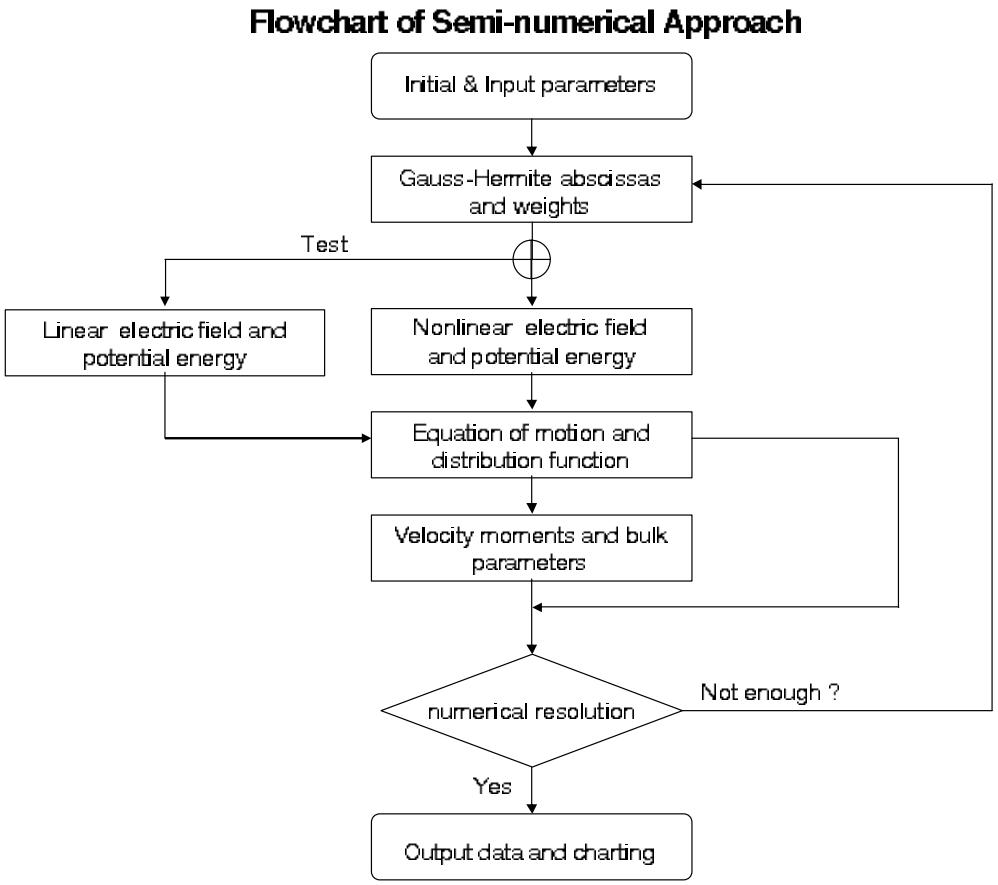

Figure 4.1: Flowchart of the semi-numerical approach used for generalized nonlinear electric fields which are constant in time.

4.1 Electric field profile and potential energy

For an arbitrary electric field structure, the cylindrically symmetric space charges are no longer extending to infinity but localized to form a cylinder in real space. Various situations are possible for the electric field strength as a function of radial distance. These can, for instance, be a negative charge density peaking near the edge of the cylinder, or, fast or slow changing profile crossing the edge, etc. Different charge density distributions produce different space-charge electric fields. The general problem is simply described by

$$\mathbf{E} = E_r \hat{\mathbf{r}} = E_c \cdot f\left(r\right) \hat{\mathbf{r}} \tag{4.1}$$

in which $f(r)$ is constant in time, but an arbitrary radial function versus r/R_c, defined as $f(r) = E_r/E_c$, and E_c is a constant. Fig.4.2 gives several examples of $f(r)$ that will be considered in this Chapter. For comparison, the linear electric field used in Chapter 2 and 3 is also given.

As discussed in Chapter 2, the ion velocity distribution is evidentally affected by the electrostatic potential energy P. The change in P as an ion moves from r_0 to r is given by

$$P_{rr_0} = P_r - P_{r_0} = e[\varphi(r) - \varphi(r_0)] = e\int_{r_0}^{r} \mathbf{E}\cdot \mathrm{d}\mathbf{r} = e\int_{r_0}^{r} E_r \mathrm{d}r = eE_c \int_{r_0}^{r} f(r)\mathrm{d}r \tag{4.2}$$

For a linear electric field as supposed in Chapter 2, $f(r) = r/R_c$, we have obtained

$$P = \frac{1}{2} eE_c R_c \left[\left(\frac{r}{R_c}\right)^2 - \left(\frac{r_0}{R_c}\right)^2\right] = \frac{1}{2} m_i \frac{E_c}{B} R_c \Omega_i \left[\left(\frac{r}{R_c}\right)^2 - \left(\frac{r_0}{R_c}\right)^2\right] \tag{4.3}$$

For nonlinear electric fields, however, the potential energy may not take such a simple analytical shape. Furthermore, even even for simple cases [e.g., $E_r = E_c(R_c/r)$], we still do not know how to connect r to r_0 and then to determine the potential energy. The problem gets worse for the "exponential" or the "cube" electric field structures introduced in Fig.4.2. However, this relation can be provided by solving the equation of motion analytically or numerically.

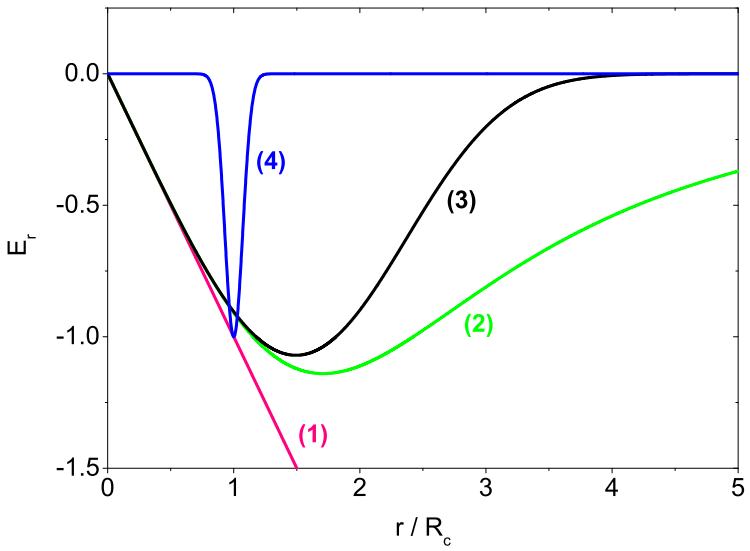

Figure 4.2: Arbitrary radial electric field examples which are constant in time: (1) $E_r = -E_c(r/R_c)$; (2) $E_r = -E_c(r/R_c)/[1 + 0.1\,(r/R_c)^3]$; (3) $E_r = -E_c(r/R_c)e^{-0.1(r/R_c)^3}$; and (4) $E_r = -E_c e^{-(r/R_c-1)^2/0.1^2}$.

4.2 Numerically solving the equation of motion

The equation of motion in an arbitrary radial electric field has the form [e.g., Eq.(2.5)]

$$\frac{\mathrm{d}r}{\mathrm{d}t} = v_r \ , \quad \frac{\mathrm{d}v_r}{\mathrm{d}t} = -\left(\frac{\Omega_i}{2}\right)^2 r - \frac{E_c}{B}\Omega_i \cdot f(r) + \frac{K^2}{m_i^2 r^3} \ , \quad \frac{\mathrm{d}\phi}{\mathrm{d}t} = \omega = \frac{K}{m_i r^2} - \frac{1}{2}\Omega_i \quad (4.4)$$

For convenience, I use a dimensionless formulation hereafter. However, in this set of differential equations of motion, the exact relation between the effective gyro-frequency ω and the magnetic gyro-frequency Ω_i is unknown. I therefore choose Ω_i as the timescale parameter in the numerical calculations. Using the backmapping

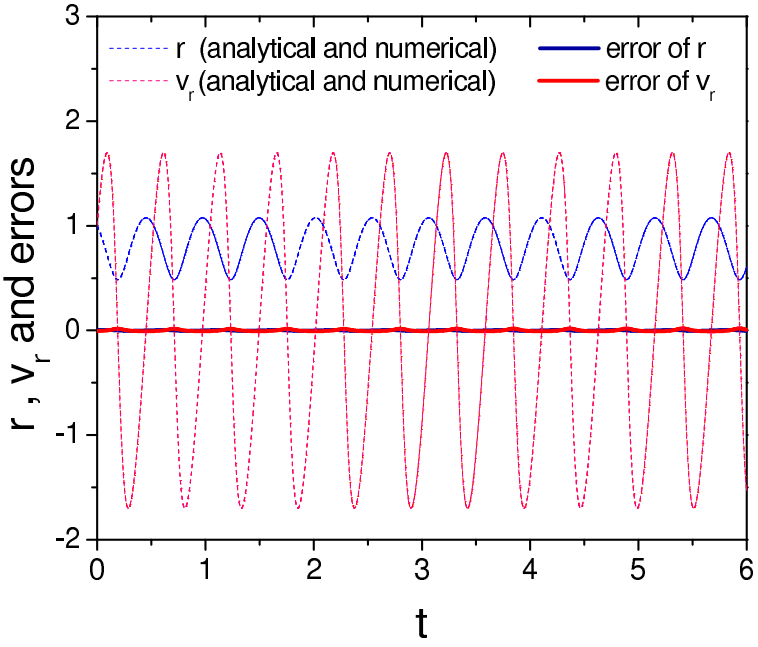

Figure 4.3: Analytical and numerical results for the evolution of r (in R_c units) and v_r (in v_{th} units) with time and their respective numerical errors under the radially linear electric field structure used in Chapter 2.

ray-tracing technique, Eq.(4.4) becomes

$$\left.\begin{aligned}
\frac{\mathrm{d}r_0}{\mathrm{d}t} &= -\frac{2\pi}{R_c\Omega_i}v_{r0} \\
\frac{\mathrm{d}v_{r0}}{\mathrm{d}t} &= \frac{2\pi}{R_c\Omega_i}\left[\left(\frac{R_c\Omega_i}{2}\right)^2 r_0 + \frac{E_c}{B}R_c\Omega_i\cdot f(r) - \frac{c_k^2}{r_0^3}\right] \\
v_{\phi 0} &= \frac{r}{r_0}v_\phi + \frac{1}{2}R_c\Omega_i\left(\frac{r^2}{r_0} - r_0\right) \\
c_k &= r^2\left(\frac{v_\phi}{r} + \frac{1}{2}R_c\Omega_i\right)
\end{aligned}\right\} \tag{4.5}$$

where all parameters of position, speed, or time are dimensionless in units of R_c, v_T, or, $2\pi/\Omega_i$, respectively. Note that $\{r, v_r, v_\phi\}$ are input parameters, $\{r_0, v_{r0}, v_{\phi 0}\}$ are outputs, and $r_0 = r_0(r, v_r, v_\phi)$, $v_{r0} = v_{r0}(r, v_r, v_\phi)$, $v_{\phi 0} = v_{\phi 0}(r, v_r, v_\phi)$. To verify the agreement between analytical and numerical calculations, Fig.4.3 offers the errors of ion radial position and radial speed produced in two ways in the case of the radially linear electric field structure used in Chapter 2. The analytical expressions of r and v_r are obtained simply from Eqs.(2.6,2.14).

4.3 Numerical calculations for distribution function and bulk properties

In the absence of collisions, Chapter 2 tells us that the ion distribution function $f_i[\mathbf{r}(t), \mathbf{v}(t)]$ in phase space at any time t is determined by the initial distribution function $f_i(\mathbf{r}_0, \mathbf{v}_0)$ at $t = 0$, as given in Eq.(2.8):

$$f_i[\mathbf{r}(t), \mathbf{v}(t), t] = f_i(\mathbf{r}_0, \mathbf{v}_0, 0) = f_0 = \frac{n_0}{\pi} e^{-(v_{r0}^2 + v_{\phi 0}^2)} \tag{4.6}$$

Here, I still assume the initial ion distribution function to be Maxwellian.

Using Eq.(4.2), we immediately find

$$f_i[\mathbf{r}(t), \mathbf{v}(t), t] = \frac{n_0}{\pi} e^{-[v_r^2 + v_\phi^2 + (P_r - P_{r_0})]} = \frac{n_0}{\pi} e^{-\left[v_r^2 + v_\phi^2 - 2\frac{E_c}{B} R_c \Omega_i \int_r^{r_0} f(r) \mathrm{d}r\right]} \tag{4.7}$$

in which P is dimensionless with $mv_T^2/2$, and $r_0 = r_0(r, v_r, v_\phi)$ is numerically calculated from Eq.(4.5). Using f_i, the following velocity moments can be expressed from the definitions:

$$\left.\begin{aligned} & n_i = \int f_i \mathrm{d}\mathbf{v} \\ & \langle v_r \rangle = \frac{1}{n_i} \int v_r f_i \mathrm{d}\mathbf{v} \ , \quad \langle v_\phi \rangle = \frac{1}{n_i} \int v_\phi f_i \mathrm{d}\mathbf{v} \\ & \langle v_r^2 \rangle = \frac{1}{n_i} \int v_r^2 f_i \mathrm{d}\mathbf{v} \ , \quad \langle v_\phi^2 \rangle = \frac{1}{n_i} \int v_\phi^2 f_i \mathrm{d}\mathbf{v} \\ & \langle v_r^3 \rangle = \frac{1}{n_i} \int v_r^3 f_i \mathrm{d}\mathbf{v} \ , \quad \langle v_\phi^3 \rangle = \frac{1}{n_i} \int v_\phi^3 f_i \mathrm{d}\mathbf{v} \end{aligned}\right\} \tag{4.8}$$

The moments are obtained numerically by applying the Gauss-Hermite weight integrations. From there, the bulk parameters can be calculated as follows:

$$\left.\begin{aligned} & v_{\mathrm{d}r} = \langle v_r \rangle \ , \quad v_{\mathrm{d}\phi} = \langle v_\phi \rangle \\ & T_r = 2\left(\langle v_r^2 \rangle - \langle v_r \rangle^2\right) \ , \quad T_\phi = 2\left(\langle v_\phi^2 \rangle - \langle v_\phi \rangle^2\right) \\ & p_{rr} = n_i T_r \ , \quad p_{\phi\phi} = n_i T_\phi \\ & q_r = \langle v_r^3 \rangle - \langle v_r \rangle^3 - \frac{3}{2} \langle v_r \rangle \cdot T_r \ , \quad q_\phi = \langle v_\phi^3 \rangle - \langle v_\phi \rangle^3 - \frac{3}{2} \langle v_\phi \rangle \cdot T_\phi \end{aligned}\right\} \tag{4.9}$$

The validity of the semi-numerical code was checked against analytical solutions from Chapter 2. Specifically, the analytical solutions came from Eq.(2.14). The radial position is at $r = R_c$ and the time is at $t/T = 3/4$ where $T = 2\pi/\omega$. The check is shown in Fig.4.4. The error is within 9×10^{-6}.

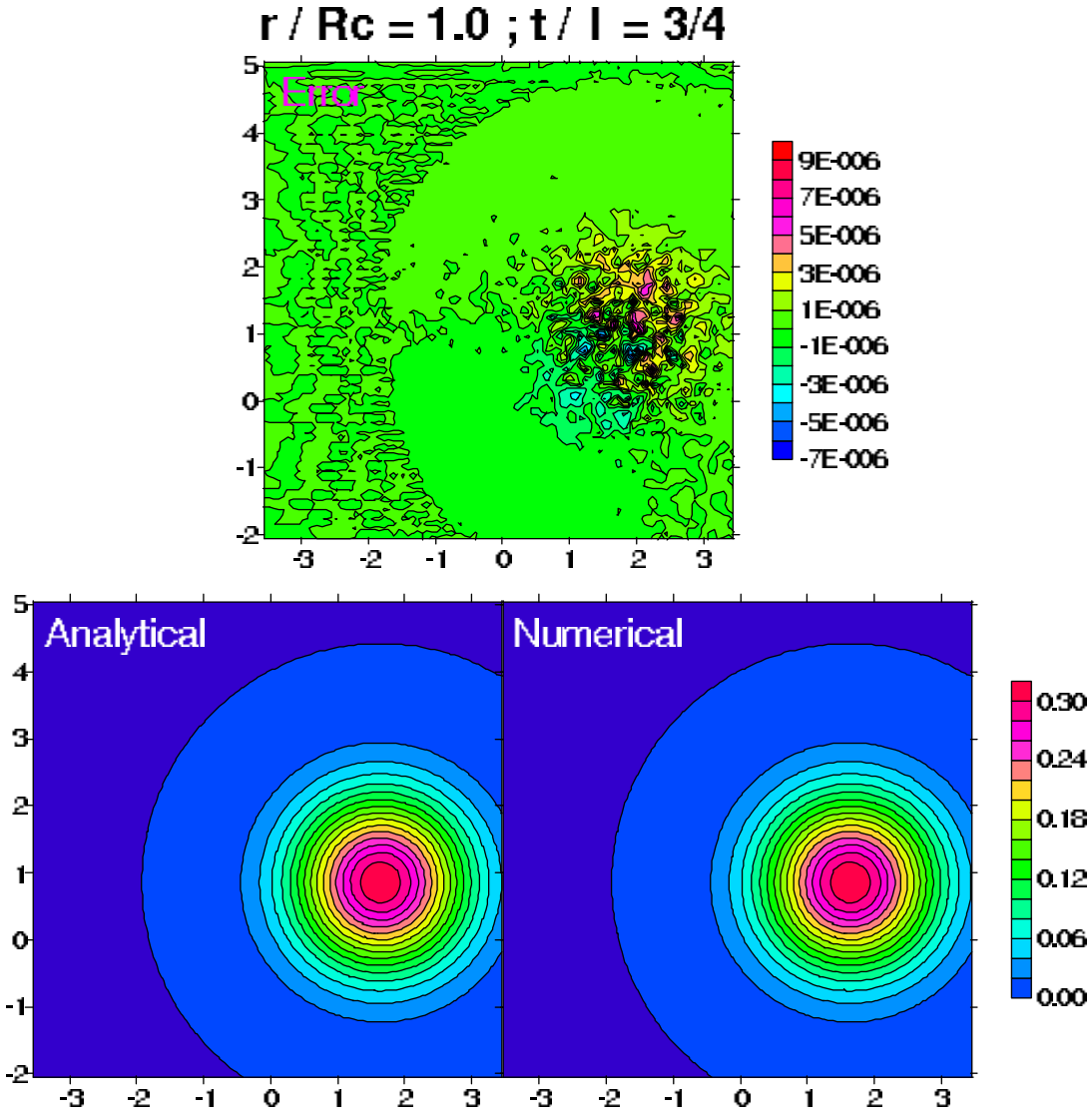

Figure 4.4: Numerical verifications for the ion velocity distribution function in the case of the radially linear electric field used in Chapter 2.

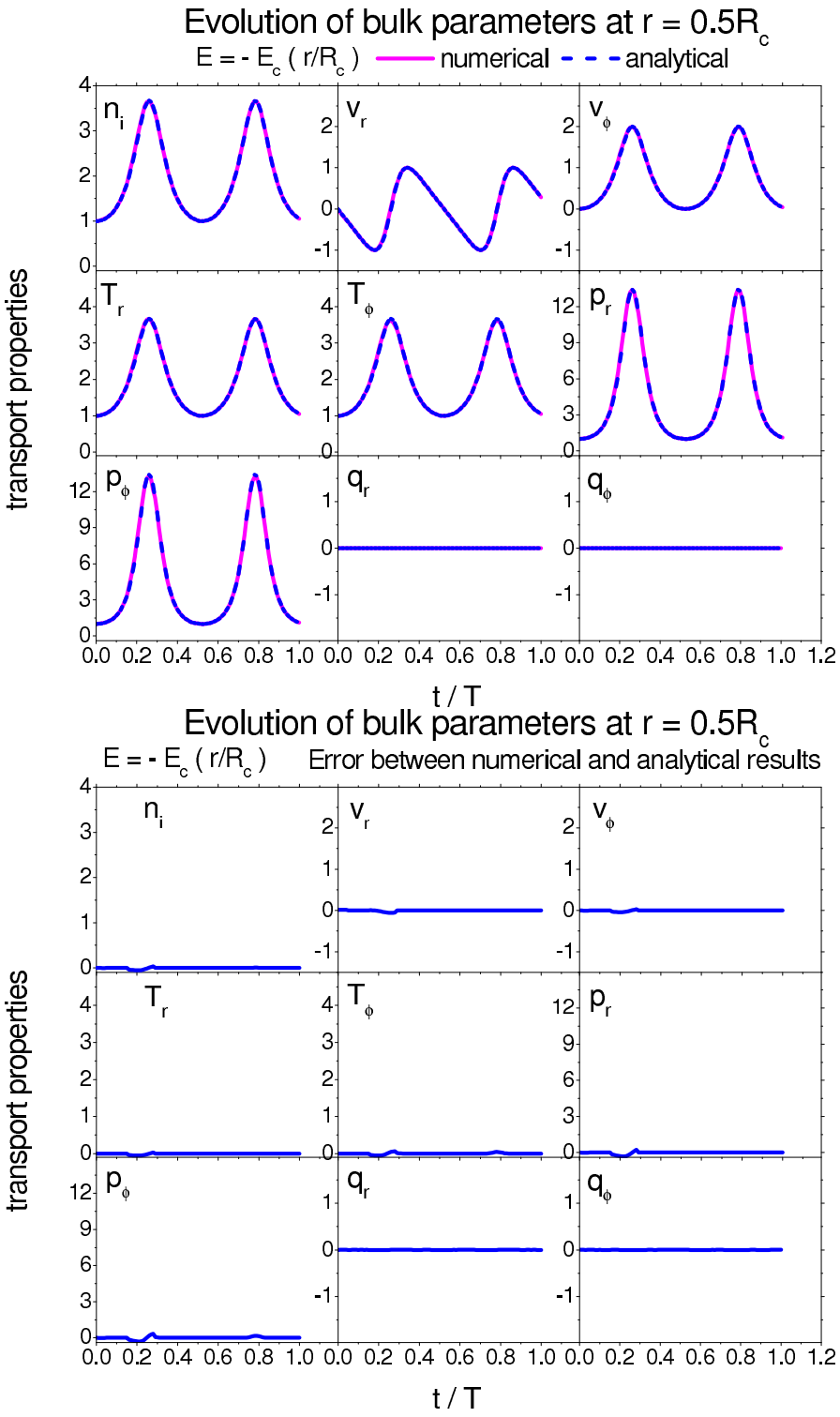

Figure 4.5: Upper: Verification of numerical calculations for the ion bulk properties in the case of the radially linear electric field used in Chapter 2. Lower: Error between the numerical and analytical calculations.

In addition, I have also checked the fit of the bulk parameters between the analytical and numerical calculations. The analytical expressions I used are Eq.(2.32). Fig.4.5 shows that they are in good agreement, except that in $t \in (0.2 \sim 0.3)$ and $t \in (0.7 \sim 0.8)$ the heat flow deviates from zero up to 0.0839.

The next section presents the results of calculations of the velocity distributions and associated transport properties for the electric field variations introduced in Fig.4.2, which should cover a reasonable range of ionospheric possibilities at least qualitatively.

4.3.1 Ion distribution function

Fig.4.2 shows three types of radial electric field structures which are not proportional to the radial position:

(1) Curve 2: $E_r = -E_c(r/R_c)/[1+0.1\,(r/R_c)^3]$. Within $r = R_c$, E_r is proportional to r; outside $r = R_c$, E_r decreases to zero slowly relative to Curve 3.

(2) Curve 3: $E_r = -E_c(r/R_c)e^{-0.1(r/R_c)^3}$. Within $r = R_c$, E_r is proportional to r; outside $r = R_c$, E_r decreases to zero quickly relative to Curve 2.

(3) Curve 4: $E_r = -E_c e^{-(r/R_c-1)^2/0.1^2}$. At an arbitrary position in space ($r = R_c$ is taken as an example), there is an electric field jump.

Case 1

Fig.4.6 uses nine panels to show the evolution of the ion O^+ distribution function in velocity space from $t = 0$ to the same length of time in a magnetic gyro-period $[T = 2\pi/\Omega_i = 2\pi m/(eB)]$. Notice that this gyro-period is that of ions under zero electric field. So, it is not the actual "gyro-period" of ions gyrating under the electric field 2 in Fig.4.2.

However, there may or may not be such a "gyro-period" shared by all particles in motion. In a field which does not change linearly along the radial direction, ions are not in phase. This is the difference from what Chapter 2 describes: the motion of all ions are in phase under linear electric fields. This means in the present case that ions with different initial conditions move in different characteristics in space with their

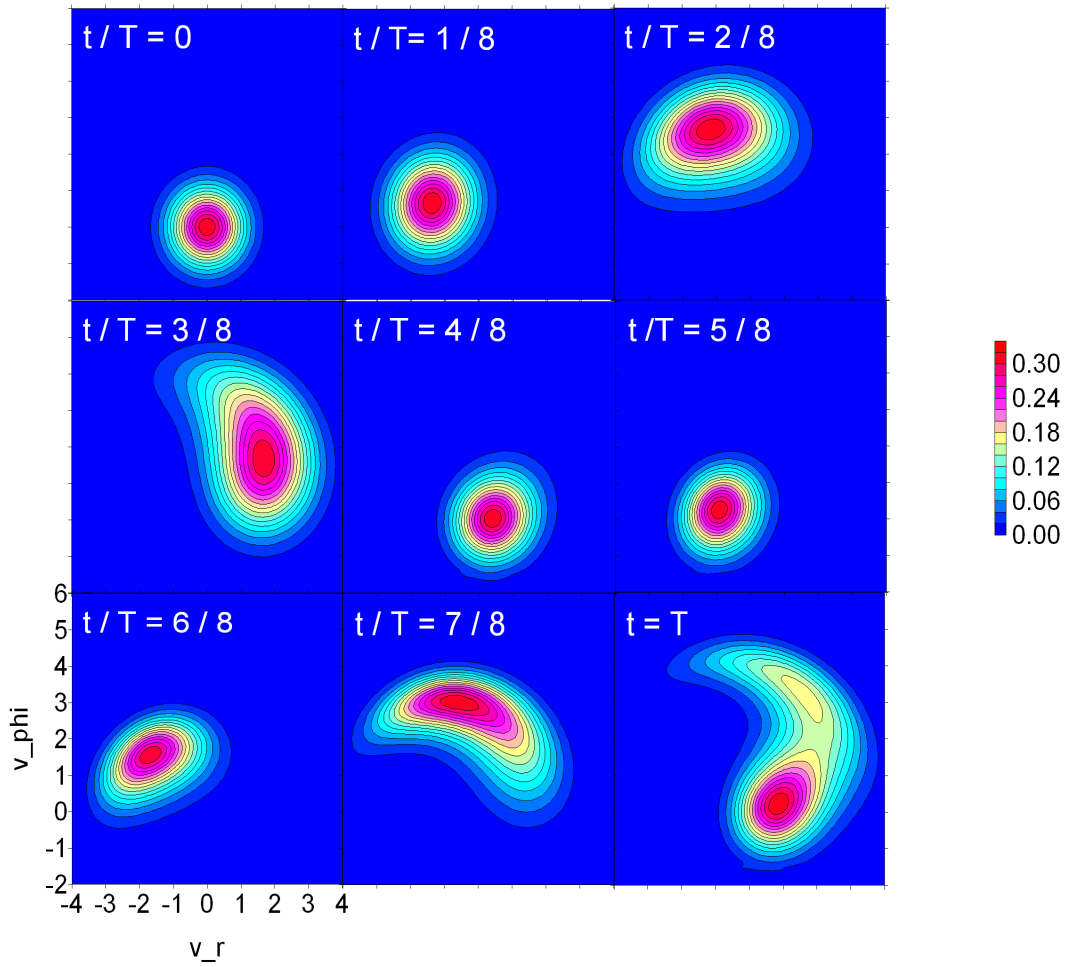

Figure 4.6: Ion velocity distribution function versus time at $r = R_c$ and at $E_c/B = 2$ for $E_r = -E_c(r/R_c)/\left[1 + 0.1\,(r/R_c)^3\right]$. In all panels, $T = 2\pi/\Omega_i$.

respective gyro-frequencies. Thus, when we use the phrase "guiding center (GC)" in the following text, we do not refer to the center of the distribution function for all ions as a whole, but only to the so called "center" of the dominant part of the distribution functions (maybe several parts) in velocity space.

Fig.4.6 is plotted with two input parameters: the radial position is at $r = R_c$ and $E_c/B = 2$. Though the electric field is nonlinear in the radial direction, we notice that it contains a linear component: if r is small, the field turns out to be a linear electric field, meaning the charge density is still uniform close to the center of the space charge cylinder as discussed in Chapter 2. Thus, we guess that the ion velocity distribution at $r = R_c$, a radial position not very far from and not very close to the center, should bring, more or less, the features of the distributions introduced in Chapter 2. Let's have a close look at the figure.

Firstly, the figure shows a similar rotation feature as that in Chapter 2: the ion distribution function rotates continuously around some center related to the $\mathbf{E} \times \mathbf{B}$ drift on the v_ϕ-axis. The panels at $t/T = 3/8$ and $t = T$ illustrate that the center seems to be located at $v_\phi = 2$. We know from Chapter 2 that the $\mathbf{E} \times \mathbf{B}$ drift is $E_r/B = (E_c/B) \times (r/R_c) = 2$ at $r = R_c$. Secondly, all panels together show roughly a periodic change in sizes of the evolving ion distribution function. At first as in the panel at $t/T = 0$, the area of the distribution is small; then it increases, decreases, and increases, oscillating in time. This is exactly the feature shown in Chapter 2 for the evolution of the ion distribution in time. Lastly, the gyration of ions appears to have the same effective gyro-frequency as that given in Chapter 2: In a linear electric field, the effective gyro-frequency ω is given by Eq.(2.15) which turns out to be $\sim 1.9\Omega_i$ for $E_c/B = 2$. This means during one magnetic gyro-period $(1/\Omega_i)$, ions have experienced approximately 2 rotations with the effective gyro-frequency ω. See the nine panels in Fig.4.6: they roughly have rotated twice from $t = 0$ to $t = T = 2\pi/\Omega_i$.

Though with so many similar features to the case in Chapter 2, Fig.4.6 does tell us obvious differences of ion velocity distributions from that under the linear radial electric field structures. For example, because ions are no longer in phase, the ap-

pearance of the distribution function does not keep the original "cake" shape at panel $t/T = 0$ they are evolving from, unlike that in Chapter 2. At panel $t/T = 3/8$, the distribution function becomes teardrop-shaped; while at panel $t = T$, it is scattered to such a weird shape that a tail emerges out from the core body. Another related feature different from that in Chapter 2 is: both the density and temperature are no longer keeping the same variations; more than that, each of them does not oscillate in the same way from one gyration to the other. For instance, it is impossible to find two panels in Fig.4.6 which have areas (indicating ion density) or the diameters (indicating ion temperature), respectively, of the same size. Moreover, the so called "GC" speed never reaches twice the $\mathbf{E} \times \mathbf{B}$ drift as obtained in Chapter 2. See panel $t/T = 2/8$. The "GC" speed is obviously lower than 4. Unlike the linear field case where ions at larger radius feel stronger electric force to accelerate them inward to higher speeds when deflected into the region of interest by the magnetic field, the nonlinear field we are using is localized and no ions outside several R_c are driven inward. Thus, ions with higher speeds are lacking in the region of interest. Naturally, the bulk speed of all ions is unable to touch the top of the circle delineated by the GC motion in velocity space around the $\mathbf{E} \times \mathbf{B}$ drift shown in Fig.2.3 in Chapter 2.

Case 2

If the space charge diffusion outside the region of interest is not as high as in Case 1, the ion velocity distribution function is still determined by the localized electric field structure in the region. Curve 3, on the one hand, is not much different from Curve 2 for small r and is still linear along the radial direction. This means the evolution of the distribution function should still have, more or less, the features given in Chapter 2. On the other hand, at larger radius, the electric field falls to zero, just like in Curve 2. Thus, we can predict reasonably that the evolution of the distribution function should have, more or less, the features given in Case 1. See Fig.4.7 for these similarities.

The nine panels show nearly the same evolving features as Case 1 in the gyration period, the top GC speed, the distribution shapes, etc. The only conspicuous differ-

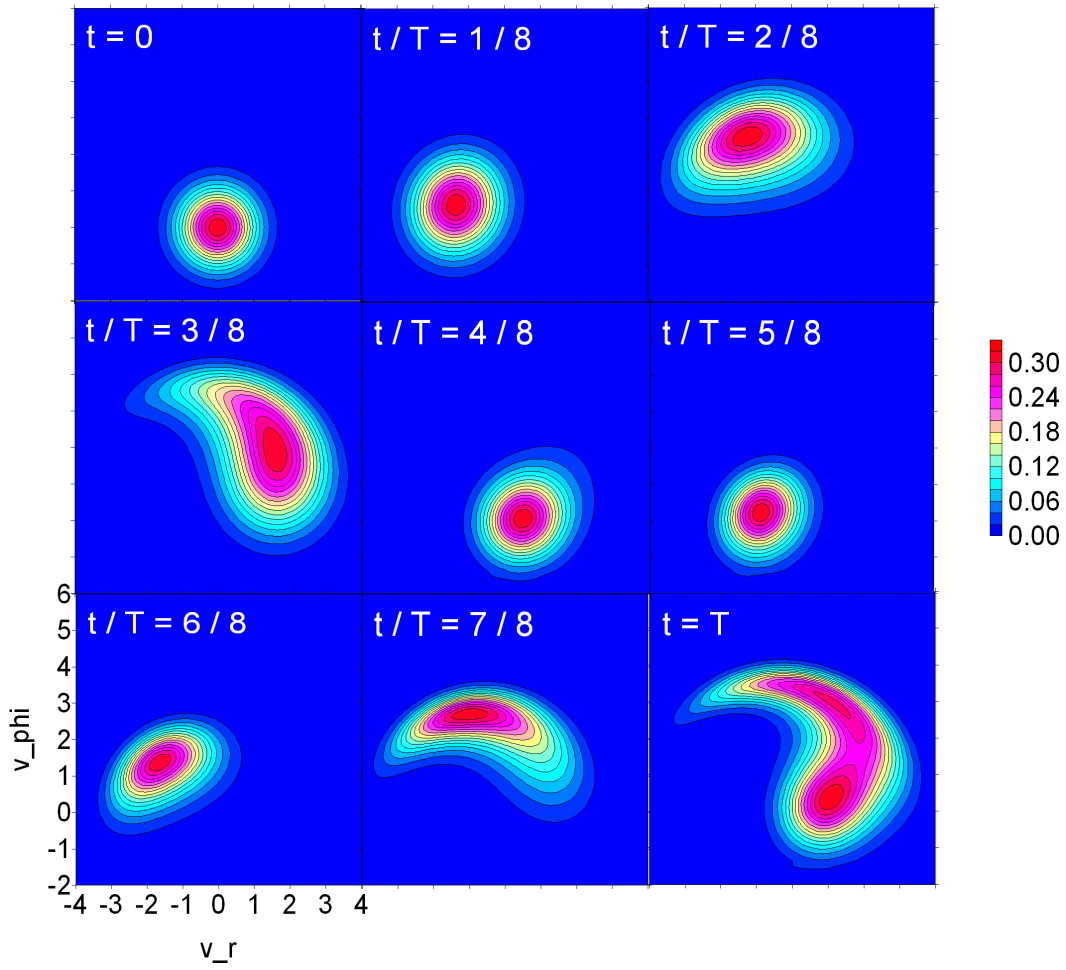

Figure 4.7: Ion velocity distribution function versus time at $r = R_c$ and at $E_c/B = 2$ for $E_r = -E_c(r/R_c)e^{-0.1(r/R_c)^3}$. In all panels, $T = 2\pi/\Omega_i$.

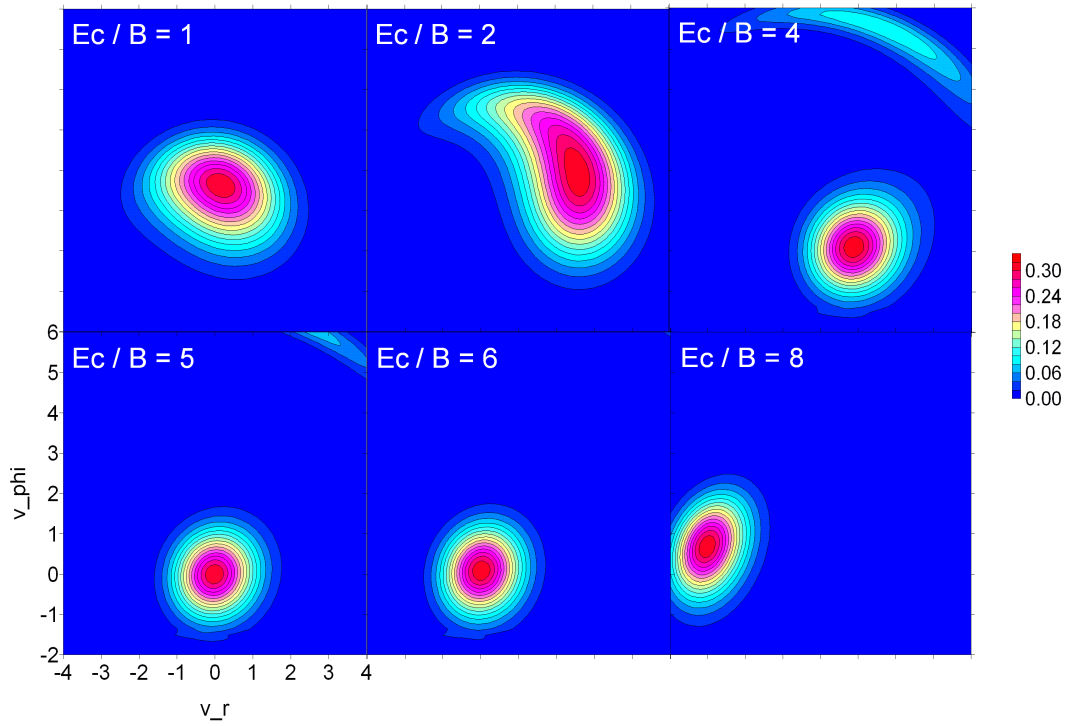

Figure 4.8: Ion velocity distribution function versus E_c at $r = R_c$ and at $t = 3T/8$ (where $T = 2\pi/\Omega_i$) for $E_r = -E_c(r/R_c)e^{-0.1(r/R_c)^3}$. The halo is flying away from the core distribution. In an enlarged figure given by Fig.4.12 below, the center of the halo is at $v_r = 1$ and $v_\phi = 7.3$ for $E_c/B = 6$.

ence lies in the tail shown in the last panel at $t = T$: the ion distribution appears to be larger even in the core and tail parts than that shown in Fig.4.6. This may be explained by the fact that a narrower space charge boundary brings about a sharper drop in the electric field strength, which leads to fewer energetic ions in the tail to be deflected away by the $\mathbf{E} \times \mathbf{B}$ drift from the region of interest.

At this point, I would like to show another interesting feature the ion velocity distribution function reveals: a core-halo shaped appearance. This unexpected shape originates from the application of stronger electric field strengths, as shown in Fig.4.8. With an increasing electric field, the ion distribution function first moves in velocity space as a whole. But at $E_c/B = 4$, the teardrop-shaped distribution is separated into two parts: a core continuing to move downward, and a halo peeling off but moving upward. Different from the core-tail case, this core-halo distribution is directly related to the formation of an energetic ion beam. If the electric field continues to increase, the halo flies away from its parental core as shown in panel $E_c/B = 5$. Noticeably, the core shrinks to a smaller size than before giving off the halo. In an enlarged figure given by Fig.4.12 below, numerical calculations show that the center of the halo is at $v_r = 1$ and $v_\phi = 7.3$.

Case 3

We intentionally choose $r = R_c$ as the layer (or surface) where space charges produce a δ-function-like radial electric field. Both inside and outside the layer, the electric field drops to zero abruptly (Curve 4 in Fig.4.2).

This kind of electric field structure brings about a few bizarre features to the ion velocity distribution function. First of all, at any time, the distributions are completely deformed in shape from the initial Maxwellian. However, generally speaking, the incomplete "bee"-shaped body is staying still at the initial position in velocity space, though some parts of the body move in time. An associated feature is that though there exists the strong electric field at $r = R_c$, no GC motion related to the $\mathbf{E} \times \mathbf{B}$ drift is seen to be triggered as happened in Cases 1 and 2. Both Figs.4.9 and 4.10 confirms this static evolution of the distribution function in time, respectively.

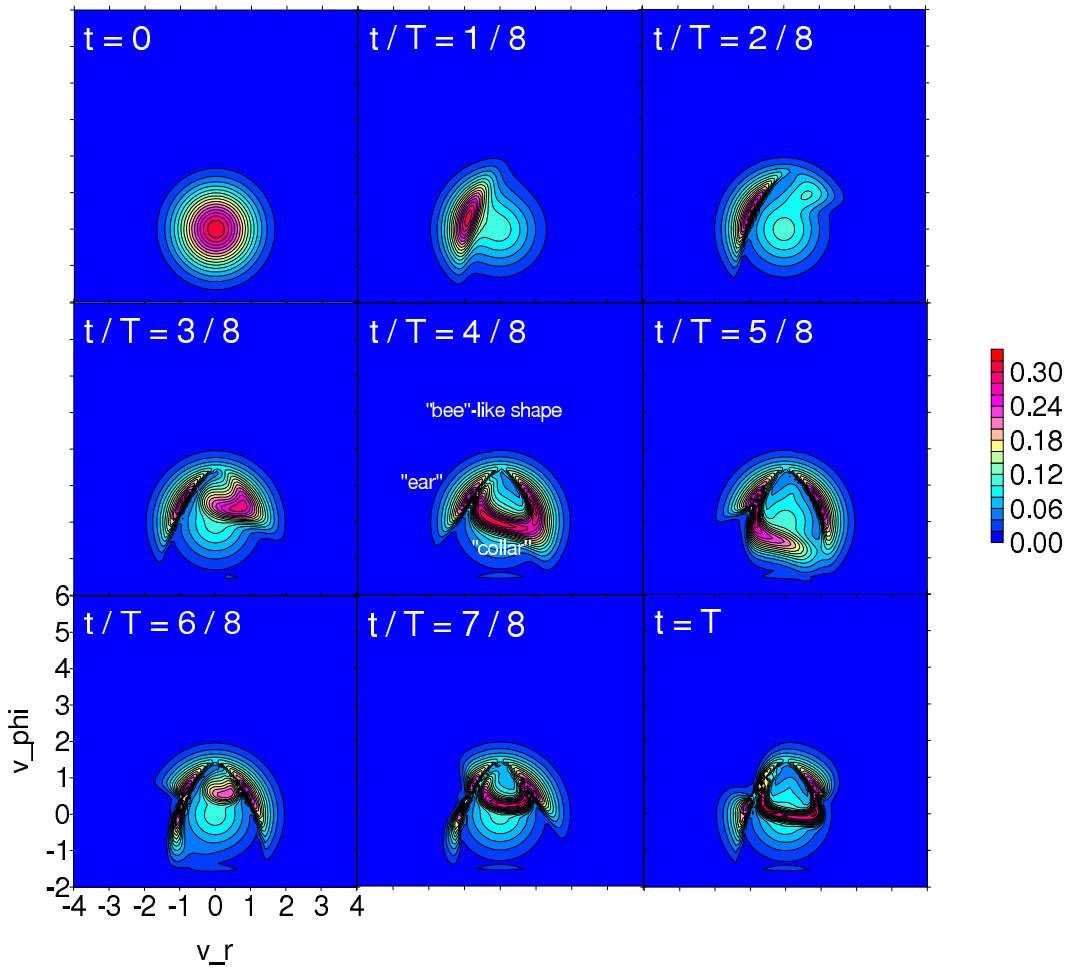

Figure 4.9: Ion velocity distribution function versus time at $r = R_c$ and at $E_c/B = 2$ for $E_r = -E_c e^{-(r/R_c-1)^2/0.1^2}$: panels for time $t = 0-T$. In all panels, $T = 2\pi/\Omega_i$. In the central panel, " 'bee-like' shape", "ear", "collar" are labeled.

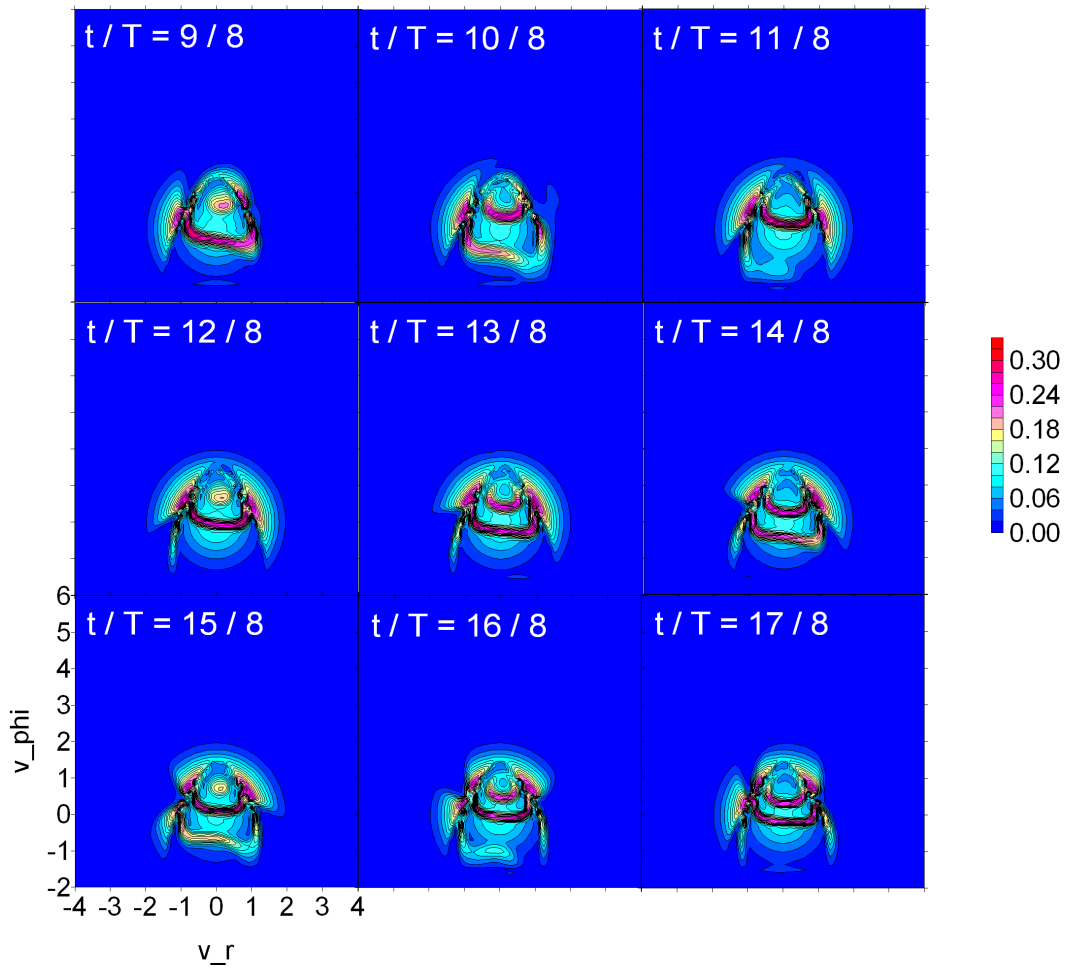

Figure 4.10: Ion velocity distribution function versus time at $r = R_c$ and at $E_c/B = 2$ for $E_r = -E_c e^{-(r/R_c-1)^2/0.1^2}$: panels for time $t = T - 2T$. In all panels, $T = 2\pi/\Omega_i$.

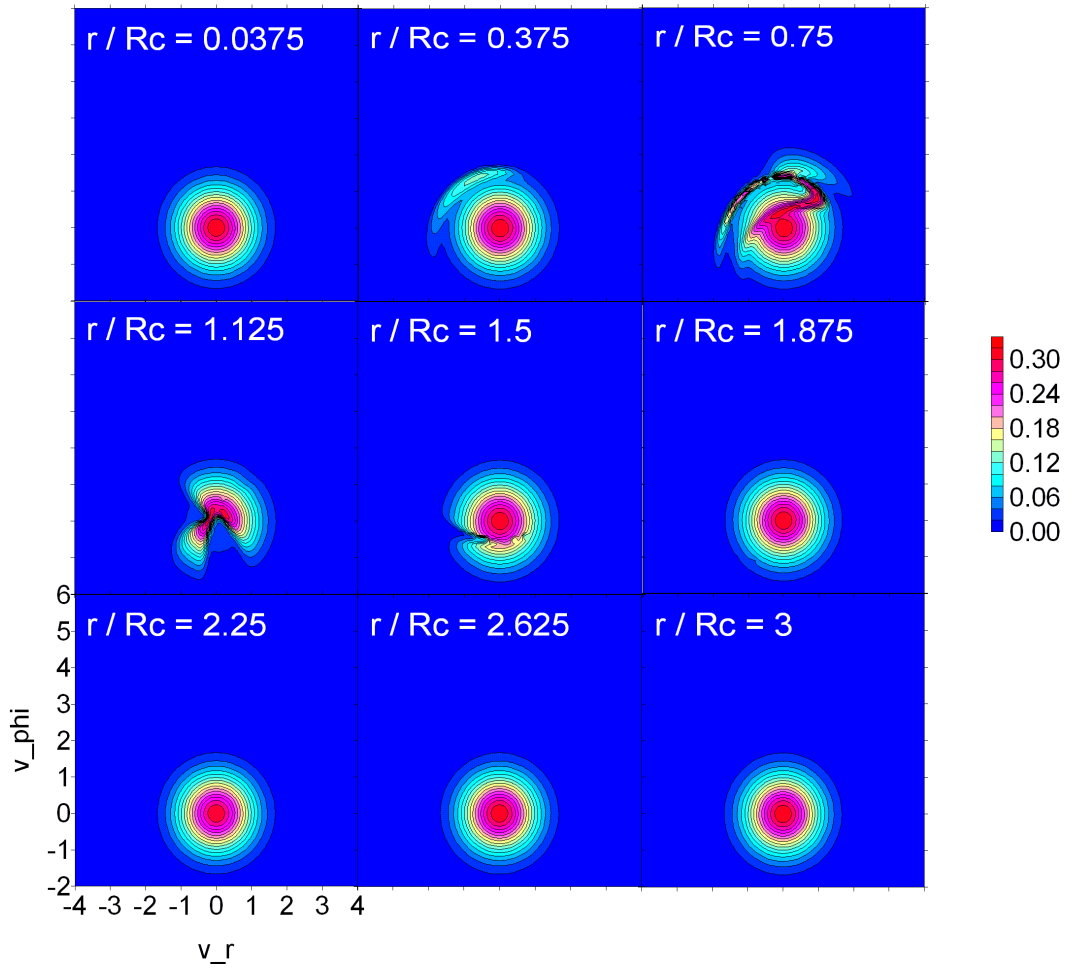

Figure 4.11: Ion velocity distribution function versus radial position at $t = 7T/8$ (where $T = 2\pi/\Omega_i$) and at $E_c/B = 2$ for $E_r = -E_c e^{-(r/R_c-1)^2/0.1^2}$.

Finally, an ear-collar shaped distribution is evolving on the bee-shaped body. At panel $t/T = 1/8$ in Fig.4.9, a bigger LHS ear first develops. This ear extends wider in velocity space and then moves up to the top to meet with another smaller RHS ear which is also moving up from another side. At the same time, a collar is formed and moves downward while the ears move up. Fig.4.10 depicts this process more clearly.

At this stage, it is intriguing to know the dependence of the ion velocity distribution function on the radial position. From the profile of the electric field structure, $E_r = -E_c \exp[-(r/R_c - 1)^2/0.1^2]$, we know that the field strength decreases to zero

if r deviates far away from R_c. So, at both small or large r/R_c, there is no electric field locally to drive ions. Thus, either inside or outside the cylinder the ion distribution function should keep its initial Maxwellian form. Luckily, Fig.4.11 reveals this feature: from panel $r/R_c = 0.0375$ to $r/R_c = 0.375$, we can see that the distribution functions are mainly Maxwellian at smaller radius. However, closer to $r/R_c = 1$, the ear-collar bee-shaped distribution is emerging from the Maxwellian till panel $r/R_c = 1.5$. After that, at larger radius the distribution returns to Maxwellian again.

4.3.2 Back-tracking phase-space parameters

In case 2, a core-halo distribution function has been found under $E_c/B \geq 4$. The ions in the halo are more energetic with a much larger drift speeds. For example, at $E_c/B = 6$, $t/T = 3/8$, numerical calculations show that the center of the halo is at $v_r = 1$ and $v_\phi = 7.3$ in velocity space at the radial position $r = R_c$. This gives a perpendicular speed $v_\perp = \sqrt{v_r^2 + v_\phi^2} \sim \sqrt{54}$ which is 5.2 times the initial perpendicular speed. Accordingly, the perpendicular ion energy has increased to 27 times of the initial energy.

The origin of these energetic ions has been found by using a back-tracing approach. By picking up a halo point in velocity space and then using the $\{v_r, v_\phi\}$ values as the initial conditions in the back-mapping equation of motion, we can immediately obtain $\{r_0, v_{r0}, v_{\phi 0}, \phi_0\}$ in phase space. Let's use the above velocity point $\{v_r = 1, v_\phi = 7.3\}$ in the halo as an example, at which the halo distribution function is maximal, $f_{i10} = 0.07758$ as shown in Fig.4.12. The numerical results are shown in Fig.4.13: this maximum halo distribution has contributions from all the ions with initial phase-space values designated by the curves from $t = 0$ to $t = 3T/8$, respectively.

4.3.3 Transport properties

Various transport properties (density, average speeds, temperatures, heat flows, etc.) are numerically calculated from velocity moments of the ion velocity distributions.

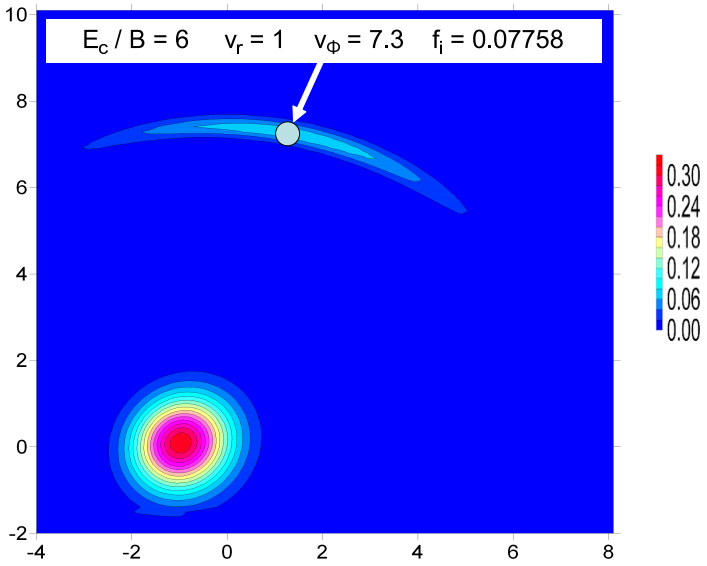

Figure 4.12: Core-halo distribution function and its peak at $E_c/B = 6$ (in units of v_{th}) at $r = R_c$ and at $t = 3T/8$ (where $T = 2\pi/\Omega_i$) under the electric field structure $E_r = -E_c(r/R_c) \cdot e^{-0.1(r/R_c)^3}$.

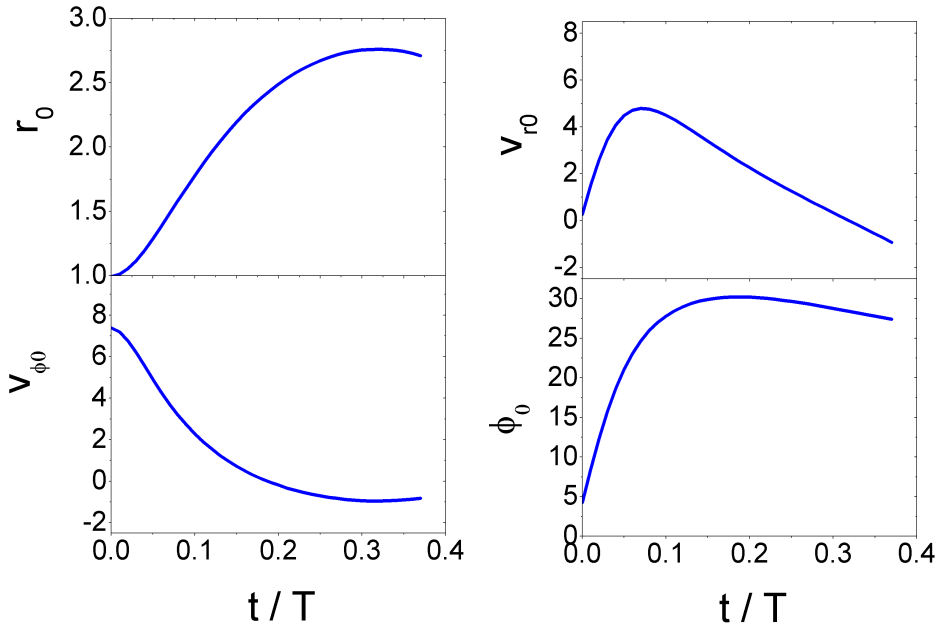

Figure 4.13: Ion parameter spectra in phase space resulting in a halo distribution peak of $f_{i10} = 0.07758$ at $r = R_c$ and at $t = 3T/8$ (where $T = 2\pi/\Omega_i$) under the electric field structure used in Fig.4.12 for $v_r = 1$ and $v_\phi = 7.3$.

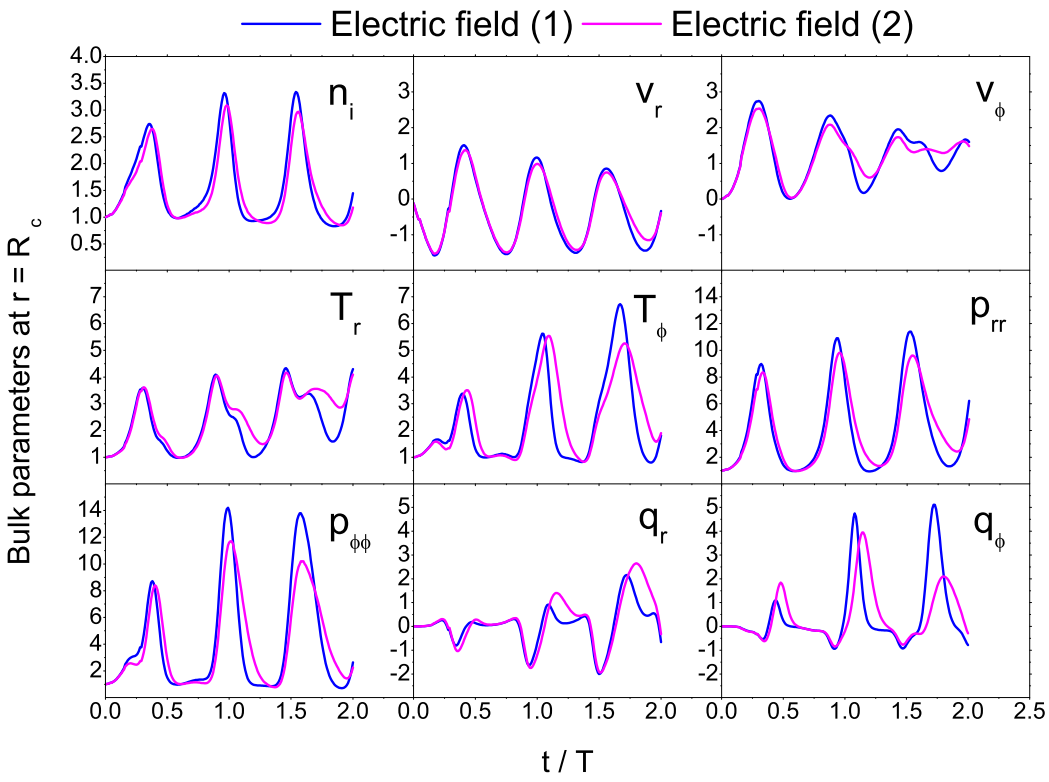

Figure 4.14: Ion bulk properties as a function of time for two nonlinear electric field structures: (1) $E_r = -E_c(r/R_c)/[1 + 0.1(r/R_c)^3]$; (2) $E_r = -E_c(r/R_c)e^{-0.1(r/R_c)^3}$.

For a direct comparison, Fig.4.14 shows these bulk parameters under the first two nonlinear electric field structures.

The evolution of these parameters in time reveals a quasi-periodic feature under either electric field structure. There is not much difference in the quasi-oscillations for the two different electric fields. However, the quasi-oscillations are not totally the same. For example, the electric field which drops more slowly outside the cylinder [electric field (1) in the figure] appears to give oscillations with higher amplitudes in density (n_i) and azimuthal components of the bulk properties (e.g., v_ϕ, T_ϕ, and q_ϕ). By contrast, the electric field which drops more quickly outside the cylinder [electric field (2) in the figure] triggers oscillations with higher amplitudes in the radial components of the bulk parameters (e.g., T_r and q_r). It deserves to be mentioned here that the existence of the heat flows indicates local temperature gradients in real space.

Under the situation of the sharp electric field case, Fig.4.15 shows two nine-panel plots. The upper nine panels tell us the evolution of the bulk parameters with time, while the lower nine ones show their changes as a function of radial position. A striking feature of the upper panels is that all bulk parameters oscillate relatively steadily with time in comparison to those under previous two electric fields. For example, they all have a time-average value plus a fluctuating component; and, the time-average values of both q_r and q_ϕ are around zero.

The lower nine panels describe that these bulk properties are localized ones. For example, outside $r = 2R_c$, they all turn out to be zero. However, in the region from $r = 0$ to $r = 2R_c$, the parameters changes violently. No doubt there are radial gradients for all of them.

4.4 Summary

This Chapter has discussed the ion velocity distribution functions and transport properties under different radial electric field structures which change arbitrarily in space. Three typical examples of the fields have been chosen: an electric field which is proportional to the radius inside a space charge cylinder but drops off slowly out

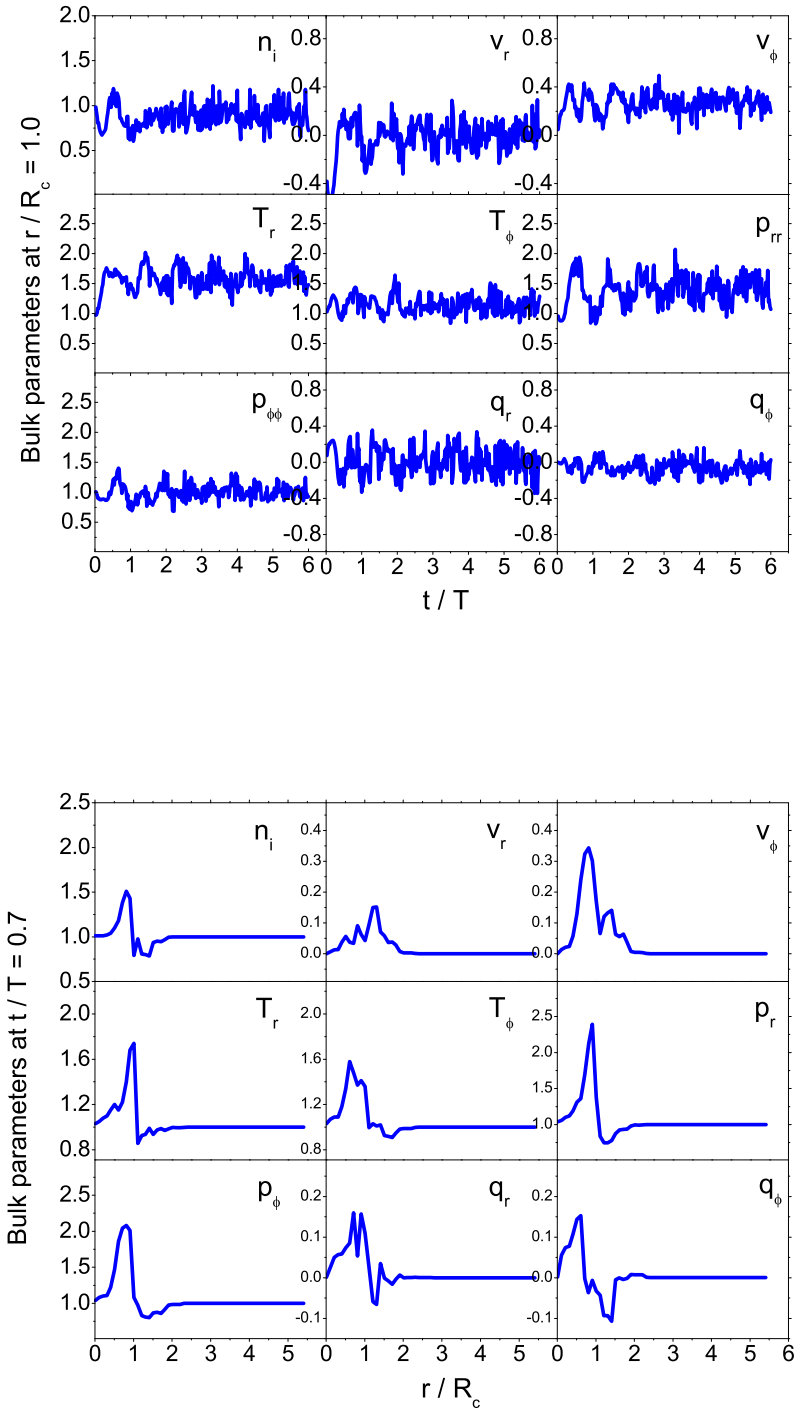

Figure 4.15: Ion bulk properties under a nonlinear electric field structure $E_r = -E_c e^{-(r/R_c-1)^2/0.1^2}$. Upper 9 panels: as a function of time. Lower 9 panels: as a function of radial position.

side the cylinder, an electric field which is still proportional to the radius inside a space charge cylinder but drops off more quickly out side the cylinder, and, an electric field which is localized at the edge of the cylinder.

A back-mapping semi-numerical technique has been applied in the study. Numerical calculations have shown that these electric fields produce various shapes of ion distributions in velocity space: "pancake"-like, "teardrop"-like, "core-halo", "ear-collar", etc. In addition, by employing the back-tracing calculation, the original phase-space parameters of ions can be found to contribute to the ion velocity distribution at any specific points in velocity space. Moreover, the features of ion transport parameters under three electric field structures have been revealed.

Chapter 5

Linear, Constant Electric Field But With Initial Ion Density Inhomogeneities

Chapters 2 and 3 discussed the ion velocity distributions and related transport properties in the collision-free and collisional cases, respectively, when the electric field produced by an electron space charges is radially linear and temporally constant. The initial ion density n_{i0} was assumed to be homogeneous in space.

This Chapter will relax the density constraints and take into account the inhomogeneities of an initial ion density to study how they affect the ion velocity distribution function and its velocity moments. I will only consider the collision-free case. A motivation for this study is that small cylindrical regions with density cavities (known as "lower hybrid cavities") are often seen in the ionosphere, in conjunction with electric fields that also happen to be radial in space (but not necessarily to be DC in time) [see, e.g., *Pécseli et al.* (1997); *Knudsen et al.* (2004)].

5.1 General considerations

In Chapter 2, Eqs.(2.16,2.23) give two different interpretations for the solution of the Boltzmann equation, Eq.(2.7), in a linear and constant electric field under the following conditions: (1) no ion-neutral collisions; (2) an initial Maxwellain distribution function in velocity space; and (3) an initial ion density, n_{i0}, which is constant in time and homogeneous in real space. For convenience, they are rewritten here.

The first description is given by Eq.(2.16), namely,

$$f_i(\mathbf{r},\mathbf{v},t) = f_0 = \frac{n_{i0}}{\pi} e^{-(v_{r0}^2+v_{\phi 0}^2)} = \frac{n_{i0}}{\pi} e^{-(v_r^2+v_\phi^2)} \cdot e^{B_2+B_1\sin(\mp\omega t+\phi_0)} \tag{5.1}$$

in which the sign "$\mp$" before ω takes "$-$" for $v_r > 0$ and "$+$" for $v_r < 0$, and

$$\left.\begin{aligned} B_1 &= c_0\varepsilon_0 A_0 \ , \quad B_2 = c_0\left[A_0 - \left(\frac{r}{R_c}\right)^2\right] \ , \\ \omega &= \Omega_i\sqrt{1+4\frac{E_c/B}{R_c\Omega_i}} \ , \quad \phi_0 = \sin^{-1}\frac{\dfrac{(r/R_c)^2}{A_0}-1}{\varepsilon_0} \end{aligned}\right\} \tag{5.2}$$

where

$$c_0 = \frac{E_c}{B}R_c\Omega_i \ , \quad \varepsilon_0 = \sqrt{1-4\frac{b_1 b_3}{b_2^2}} \ , \quad A_0 = \frac{b_2}{2b_1} \tag{5.3}$$

with

$$\left.\begin{aligned} b_1 &= \left(\frac{\Omega_i R_c}{2}\right)^2 + R_c\Omega_i\frac{E_c}{B} \\ b_2 &= b_1\left(\frac{r}{R_c}\right)^2 + v_r^2 + \left(v_\phi + \frac{\Omega_i r}{2}\right)^2 \\ b_3 &= \left(\frac{r}{R_c}\right)^2\left(v_\phi + \frac{\Omega_i r}{2}\right)^2 \end{aligned}\right\} \tag{5.4}$$

The other description, which is totally equivalent, is in terms of a pulsating Maxwellian mode:

$$f_i(\mathbf{r},\mathbf{v},t) = \frac{n_{i0}}{\pi}e^{-a_0[(v_r-v_{\mathrm{d}r})^2+(v_\phi-v_{\mathrm{d}\phi})^2]} \tag{5.5}$$

in which

$$\left.\begin{aligned} a_0 &= 1-\frac{1}{2}\left[1-\left(\frac{\Omega_i}{\omega}\right)^2\right](1-\cos\omega t) = \frac{a_1+a_2\cos\omega t}{a_1+a_2} \\ v_{\mathrm{d}r} &= -\frac{E_c}{B}\frac{r}{R_c}\frac{1}{a_0}\frac{\Omega_i}{\omega}\sin\omega t \ \text{ and } \ v_{\mathrm{d}\phi} = \frac{E_c}{B}\frac{r}{R_c}\frac{1}{a_0}\left(\frac{\Omega_i}{\omega}\right)^2(1-\cos\omega t) \end{aligned}\right\} \tag{5.6}$$

where

$$a_1 = 1+a_2 \ , \quad \text{and} \quad a_2 = 2\frac{E_c/B}{R_c\Omega_i} \tag{5.7}$$

Now, consider the initial ion density to be a function of position, that is, $n_{i0} = n_{i0}(r_0, t=0)$. Fig.5.1 shows a few arbitrary examples. Note that a background ion density, n_0, is included, which is constant in time and homogeneous in space. Because r_0 can be traced back from a phase-space position $\{r, v_r, v_\phi\}$ at time t, or, written as $r_0 = r_0(r, v_r, v_\phi, t)$, we can easily see that $n_{i0}(r_0, t=0)$ can be obtained by the backmapping method and expressed as $n_{i0}(r_0) = n_{i0}[r_0(r, v_r, v_\phi, t)]$, or directly,

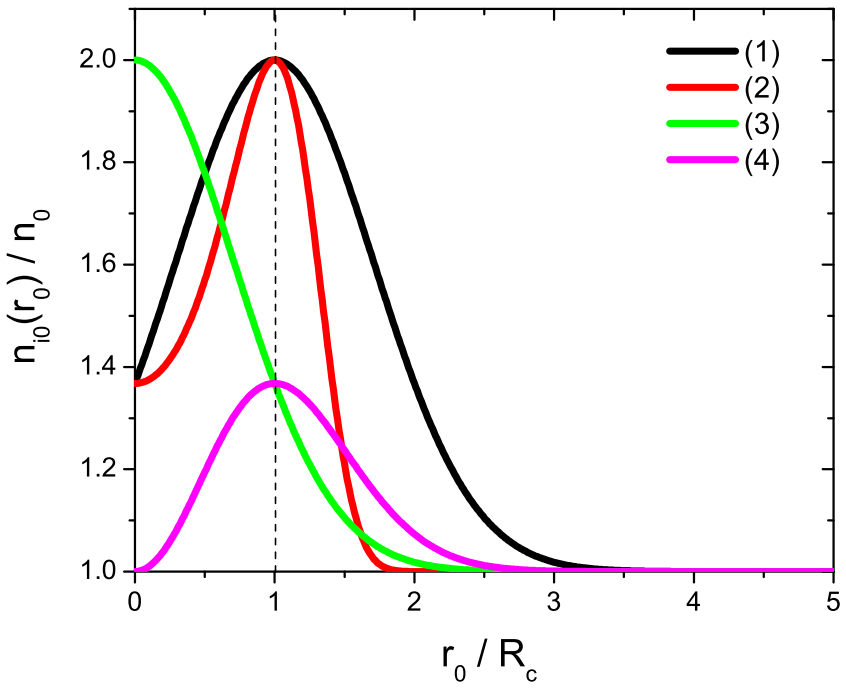

Figure 5.1: A few initially inhomogeneous ion density profiles ($\kappa = 1$ is assumed): (1) $n_{i0}(r_0)/n_0 = 1 + e^{-(r_0/R_c-1)^2}$; (2) $n_{i0}(r_0)/n_0 = 1 + e^{-\left[(r_0/R_c)^2-1\right]^2}$; (3) $n_{i0}(r_0)/n_0 = 1 + e^{-(r_0/R_c)^2}$; (4) $n_{i0}(r_0)/n_0 = 1 + (r_0/R_c)^2\, e^{-(r_0/R_c)^2}$.

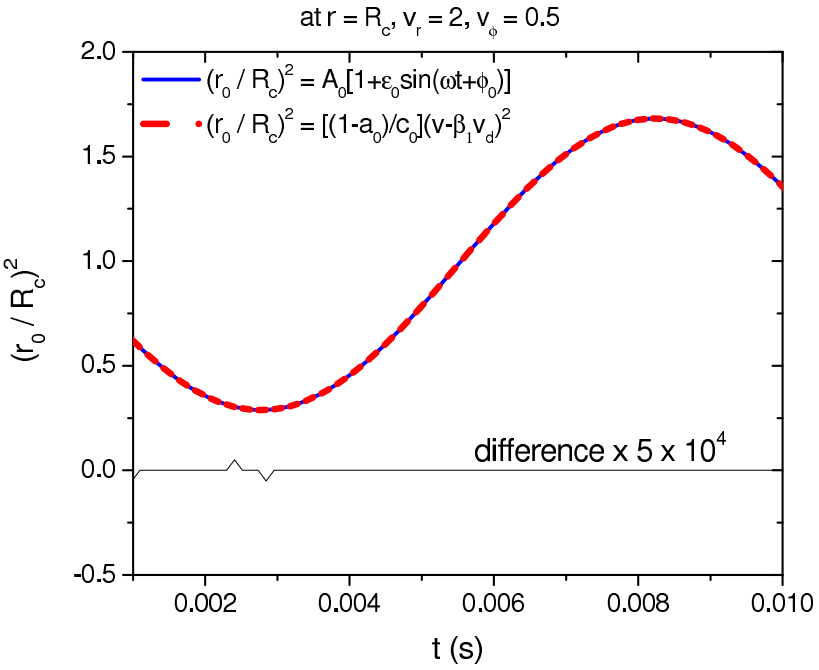

Figure 5.2: A check for the $(r_0/R_c)^2$ expressions.

$n_{i0}(r_0) = n_{i0}(r, v_r, v_\phi, t)$. This means that n_{i0} is a function of position r and velocity $\mathbf{v} = \{v_r, v_\phi\}$ when looking back from an arbitrary time t to the initial time $t = 0$.

Let's derive the collision-free ion distribution function in this complicated case. First of all, we must know the relation between r_0 and $\{r, v_r, v_\phi, t\}$. Luckily, Eq.(D.25) in Appendix D has given this relation:

$$\left(\frac{r_0}{R_c}\right)^2 = A_0[1 + \varepsilon_0 \sin(\mp\omega t + \phi_0)] = \frac{1 - a_0}{c_0}\left[(v_r - \beta_1 v_{\mathrm{d}r})^2 + (v_\phi - \beta_1 v_{\mathrm{d}\phi})^2\right] \quad (5.8)$$

where $c_0 = (E_c/B)R_c\Omega_i$ and $\beta_1 = -a_0/(1 - a_0)$ are used. In a more compact form using vector notation, Eq.(5.8) can be expressed as

$$\left(\frac{r_0}{R_c}\right)^2 = A_0[1 + \varepsilon_0 \sin(\mp\omega t + \phi_0)] = \frac{1 - a_0}{c_0}(\mathbf{v} - \beta_1 \mathbf{v}_{\mathrm{d}})^2 \quad (5.9)$$

Fig.5.2 shows that these two expressions for $(r_0/R_c)^2$ are indeed equivalent for an arbitrary phase space position: $\{r = R_c, v_r = 2, v_\phi = 0.5\}$.

Using Eq.(5.8), we immediately obtain

$$r_0 = R_c\sqrt{\frac{1 - a_0}{c_0}\left[(v_r - \beta_1 v_{\mathrm{d}r})^2 + (v_\phi - \beta_1 v_{\mathrm{d}\phi})^2\right]} = r_0(r, v_r, v_\phi, t) \quad (5.10)$$

Therefore, when the electric field strength increases linearly with radial distance, and when the initial ion density is inhomogeneous, we can calculate the ion distribution function at any time for $t > 0$ by using Eq.(5.10), namely,

$$f_i(\mathbf{r}, \mathbf{v}, t) = \frac{n_{i0}[r_0(r, v_r, v_\phi, t)]}{\pi} e^{-(v_r^2+v_\phi^2)} \cdot e^{B_2+B_1 \sin(\mp\omega t+\phi_0)} \tag{5.11}$$

or

$$f_i(\mathbf{r}, \mathbf{v}, t) = \frac{n_{i0}(r, v_r, v_\phi, t)}{\pi} e^{-a_0[(v_r-v_{\mathrm{d}r})^2+(v_\phi-v_{\mathrm{d}\phi})^2]} \tag{5.12}$$

where the new parameter occurring in Eq.(5.12) is $n_{i0}(r, v_r, v_\phi, t, c_0)$.

Our next purpose is to find simple enough n_{i0} expressions for which an analytical expression for f_i, as well as all velocity moments, could be derived. This will provide a reference for future numerical studies with arbitrary initial ion densities. We have tried a few cases for $n_{i0}(r_0)$.

5.2 Distributions with various inhomogeneous initial ion densities under collision-free conditions

5.2.1 Case 1: $n_{i0}(r_0) \sim e^{-(r_0-R_c)^2/R_c^2}$

Define

$$n_{i0}(r_0) = n_0 \left[1 + \kappa e^{-(r_0-R_c)^2/R_c^2}\right] \tag{5.13}$$

where n_0 is the background ion density, constant in time and homogeneous in space. Parameter κ is an arbitrary coefficient. By applying Eq.(5.10), Eq.(5.13) becomes

$$n_{i0}(r_0) = n_0 \left[1 + \kappa e^{-(\sqrt{\Gamma}-1)^2}\right] \tag{5.14}$$

in which

$$\Gamma = \frac{1-a_0}{\dfrac{E_c}{B} R_c \Omega_i} \left[\left(v_r + \frac{a_0}{1-a_0} v_{\mathrm{d}r}\right)^2 + \left(v_\phi + \frac{a_0}{1-a_0} v_{\mathrm{d}\phi}\right)^2\right] \tag{5.15}$$

Thus, the ion distribution function can be expressed as

$$f_i(\mathbf{r}, \mathbf{v}, t) = \frac{n_0}{\pi} e^{-a_0\left[(v_r-v_{\mathrm{d}r})^2+(v_\phi-v_{\mathrm{d}\phi})^2\right]} \left[1 + \kappa e^{-(\sqrt{\Gamma}-1)^2}\right] \tag{5.16}$$

However,

$$n_i(\mathbf{r},t) = \int f_i(\mathbf{r},\mathbf{v},t)\mathrm{d}\mathbf{v} \tag{5.17}$$

does not seem to reduce to a simple analytical expression. This means in both the collision-free case and the collisional case we cannot obtain analytical bulk properties for the initial ion density given by Eq.(5.13). Thus, we have to look for other simple cases.

5.2.2 Case 2: $n_{i0}(r_0) \sim e^{-(r_0^2-R_c^2)^2}$

We now try

$$n_{i0}(r_0) = n_0\kappa e^{-(r_0^2-R_c^2)^2} \tag{5.18}$$

By applying Eq.(5.10), Eq.(5.18) becomes

$$n_{i0}(r_0) = n_0\kappa e^{-R_c^4\left(r_0^2/R_c^2-1\right)^2} = n_0\kappa e^{-R_c^4\{\Gamma-1\}^2} \tag{5.19}$$

Thus, the ion distribution function can be expressed as

$$f_i(\mathbf{r},\mathbf{v},t) = \frac{n_0}{\pi}\kappa e^{-a_0\left[(v_r-v_{\mathrm{d}r})^2+(v_\phi-v_{\mathrm{d}\phi})^2\right]}e^{-R_c^4(\Gamma-1)^2} \tag{5.20}$$

Clearly,

$$n_i(\mathbf{r},t) = \int f_i(\mathbf{r},\mathbf{v},t)\mathrm{d}\mathbf{v} \tag{5.21}$$

still does not reduce to a simple analytical expression. Thus, we continue to look for simple initial ion density models.

5.2.3 Case 3: $n_{i0}(r_0) \sim (r_0^2/R_c^2)e^{-r_0^2/R_c^2}$

Considering that (1) the ionospheric plasma would have a background density n_0 on which a cylindrical distribution of inhomogeneous initial ion density is superposed, and (2) the density should peak away from the origin, let's consider a profile of the form

$$n_{i0}(r_0) = n_0 + n_0\kappa\frac{r_0^2}{R_c^2}e^{-r_0^2/R_c^2} \tag{5.22}$$

Using Eqs.(5.10), Eq.(5.22) becomes

$$n_{i0}(r_0) = n_0 + n_0\kappa\Gamma\cdot e^{-\Gamma} \tag{5.23}$$

Thus, the ion distribution function can be expressed as

$$f_i(\mathbf{r},\mathbf{v},t)=\frac{n_0}{\pi}e^{-a_0\left[(v_r-v_{\mathrm{d}r})^2+(v_\phi-v_{\mathrm{d}\phi})^2\right]}+\frac{n_0}{\pi}\kappa\Gamma e^{-\Gamma}\cdot e^{-a_0\left[(v_r-v_{\mathrm{d}r})^2+(v_\phi-v_{\mathrm{d}\phi})^2\right]} \tag{5.24}$$

With the following definitions:

$$\left.\begin{aligned}
&n_{0r}=n_0\kappa e^{-\beta_3(v_{\mathrm{d}r}^2+v_{\mathrm{d}\phi}^2)}\ ,\quad \alpha_{0c}=\frac{1-a_0}{\frac{E_c}{B}R_c\Omega_i}\\
&\beta_1=-\frac{a_0}{1-a_0}\ ,\quad \beta_2=\frac{\alpha_{0c}\beta_1+a_0}{\alpha_{0c}+a_0}\ ,\quad \beta_1-\beta_2=\frac{\beta_1}{\alpha_{0c}+a_0}\\
&\beta_3=\alpha_{0c}\beta_1^2+a_0-\frac{(\alpha_{0c}\beta_1+a_0)^2}{\alpha_{0c}+a_0}=\frac{a_0/(1-a_0)}{1+a_0\left(\frac{E_c}{B}R_c\Omega_i-1\right)}
\end{aligned}\right\} \tag{5.25}$$

Eq.(5.24) becomes

$$\left.\begin{aligned}
&f_i(\mathbf{r},\mathbf{v},t)=\frac{n_0}{\pi}e^{-a_0\left[(v_r-v_{\mathrm{d}r})^2+(v_\phi-v_{\mathrm{d}\phi})^2\right]}+\\
&+\frac{n_{0r}}{\pi}\alpha_{0c}\left[(v_r-\beta_1v_{\mathrm{d}r})^2+(v_\phi-\beta_1v_{\mathrm{d}\phi})^2\right]e^{-(\alpha_{0c}+a_0)\left[(v_r-\beta_2v_{\mathrm{d}r})^2+\left(v_\phi-\beta_2v_{\mathrm{d}\phi}\right)^2\right]}
\end{aligned}\right\} \tag{5.26}$$

The density n_{0r} depends on time through both a_0 and $\mathbf{v}_d$, and on position through $\mathbf{v}_d$ only. For convenience in the following derivations of velocity moments, we write Eq.(5.26) in one of the two forms. One is

$$\left.\begin{aligned}
&\frac{f_i(\mathbf{r},\mathbf{v},t)}{n_0\kappa}=\frac{1}{\pi}\frac{1}{\kappa}e^{-a_0\left[(v_r-v_{\mathrm{d}r})^2+(v_\phi-v_{\mathrm{d}\phi})^2\right]}+\\
&+\frac{e^{-\beta_3(v_{\mathrm{d}r}^2+v_{\mathrm{d}\phi}^2)}}{\pi}\alpha_{0c}\left[(v_r-\beta_1v_{\mathrm{d}r})^2+(v_\phi-\beta_1v_{\mathrm{d}\phi})^2\right]\cdot\\
&\cdot e^{-(\alpha_{0c}+a_0)\left[(v_r-\beta_2v_{\mathrm{d}r})^2+\left(v_\phi-\beta_2v_{\mathrm{d}\phi}\right)^2\right]}
\end{aligned}\right\} \tag{5.27}$$

and the other is

$$\left.\begin{aligned}
&f_i(\mathbf{r},\mathbf{v},t)=\frac{n_0}{\pi}e^{-a_0\left[(v_r-v_{\mathrm{d}r})^2+(v_\phi-v_{\mathrm{d}\phi})^2\right]}+\\
&+\frac{n_{0r}}{\pi}\alpha_{0c}\left[v_r^2+v_\phi^2+\beta_1^2\left(v_{\mathrm{d}r}^2+v_{\mathrm{d}\phi}^2\right)-2\beta_1\left(v_{\mathrm{d}r}v_r+v_{\mathrm{d}\phi}v_\phi\right)\right]\cdot\\
&\cdot e^{-(\alpha_{0c}+a_0)\left[(v_r-\beta_2v_{\mathrm{d}r})^2+\left(v_\phi-\beta_2v_{\mathrm{d}\phi}\right)^2\right]}
\end{aligned}\right\} \tag{5.28}$$

As an integral of the distribution function over velocity space, the ion density is

$$n_i=\int f_i\mathrm{d}\mathbf{v}=\frac{n_0}{a_0}+\frac{n_{0r}\alpha_{0c}}{\alpha_{0c}+a_0}\left[\frac{1}{\alpha_{0c}+a_0}+(\beta_1-\beta_2)^2\left(v_{\mathrm{d}r}^2+v_{\mathrm{d}\phi}^2\right)\right] \tag{5.29}$$

or

$$\frac{n_i}{n_0}=\frac{1}{a_0}+\frac{\kappa\alpha_{0c}}{(\alpha_{0c}+a_0)^2}\left(1+\beta_1^2\frac{v_{\mathrm{d}r}^2+v_{\mathrm{d}\phi}^2}{\alpha_{0c}+a_0}\right)e^{-\beta_3(v_{\mathrm{d}r}^2+v_{\mathrm{d}\phi}^2)} \tag{5.30}$$

Due to the fact that the background terms in the distribution and density expressions have been studied in Chapter 2 and 3, I have excluded them from the calculations. The remaining calculations has been performed in two ways: analytical and semi-numerical. The former uses the analytical solutions just shown, and the other employs the backtracking approach of Chapter 4.

The first task is to verify that the analytical and numerical calculations agree with one another. Fig.5.3 offers such a comparison for the ion velocity distribution at $r/R_c = 0.03$ and $t/T = 3/16$ where $T = 2\pi/\omega$. The error is within one part in 10^{-6}. For the ion density, Fig.5.4 presents a similar comparison at $r/R_c = 0.5$. The two curves are superimposed upon each other with an error of 0.00112 on average. These comparisons not only provide a verification for the analytical work but also illustrate that we have a proper numerical algorithm for doing arbitrarily complicated initial density problems if necessary.

Both the radial and temporal evolution of the ion velocity distribution are described in Figs.5.5-5.7, based on Eq.(5.27). In the three figures, the LHS bottom panel shows the v_r and v_ϕ scales used in all the panels where the data have been normalized with respect to the maximum value of the velocity distribution function.

As the radial position increases, the ion distribution function in Fig.5.5 at $t/T = 3/16$ evolves from being a torus at the center, to a horse-shoe, to a crescent, and finally to a more Maxwellian like "pancake" at $r/R_c = 3$. Another obvious feature is the shift in the center of the distribution, which rotates clockwise about the initial position in velocity space. At $r/R_c = 0.1$ and 1.0, the distribution function rotates about a pseudo-$\mathbf{E} \times \mathbf{B}$ drift periodically, as shown in Figs.5.6 and 5.7. This drift no longer has a value of E/B. Meanwhile, the shape deviates from a conventional shifted Maxwellian. Especially at $r/R_c = 0.1$, the shape throughout a period is changing continually in a pancake-crescent-horseshoe-crescent-pancake form. However, the gyrofrequency is still ω, i.e., the same as that for the uniform initial ion density case presented in Chapter 2.

Finally, we have a look at the ion density as a function of position and time.

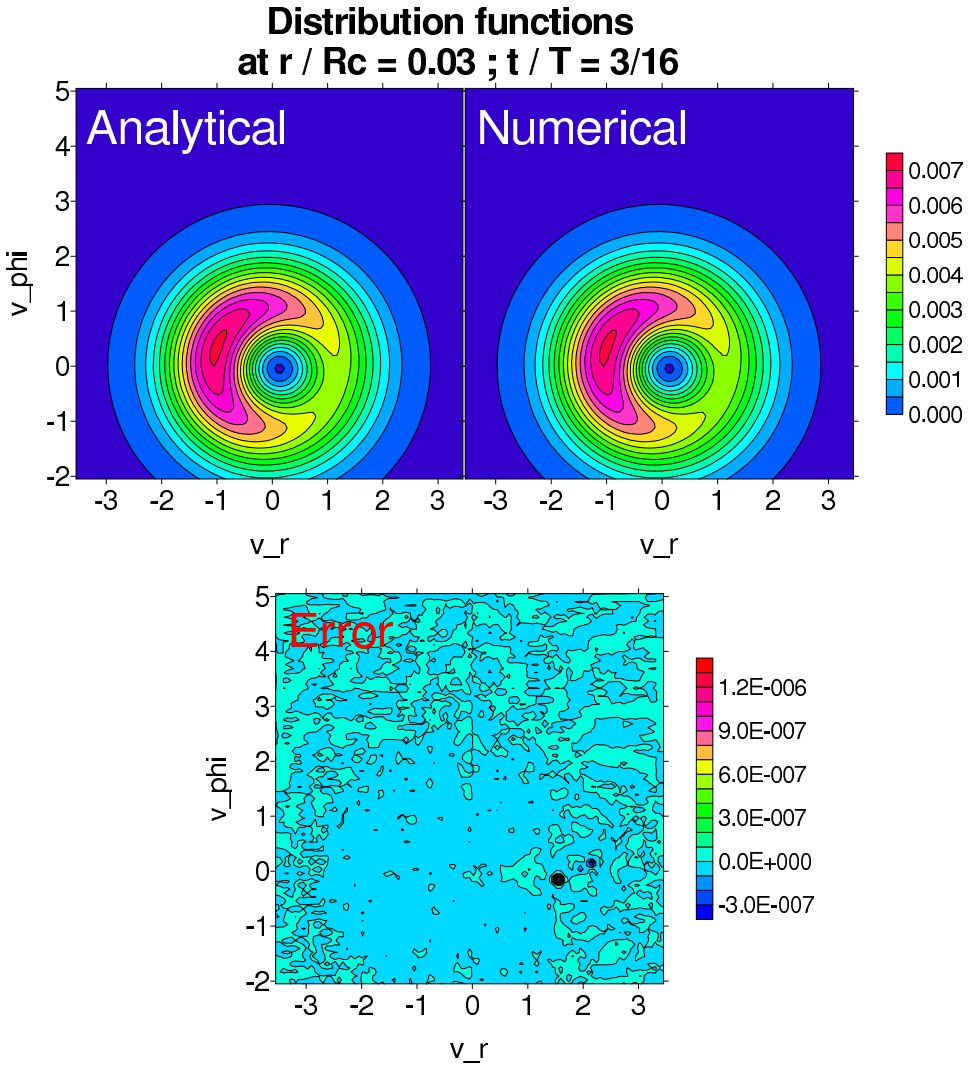

Figure 5.3: Difference between the analytical and numerical calculations of the ion distribution function resulting from the non-uniform initial ion density in Eq.(5.23).

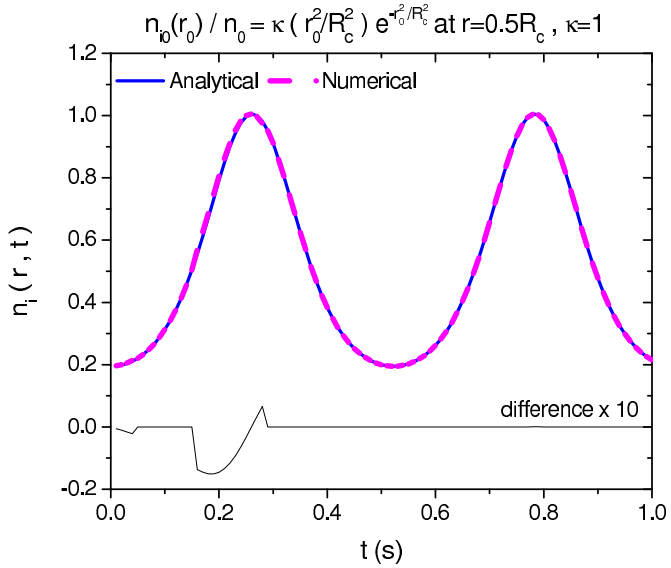

Figure 5.4: Difference between analytical and numerical calculations of the ion density resulting from the non-uniform initial condition in Eq.(5.23).

We turn to Panel n_i in a later Fig.5.13, where all bulk parameters are calculated, shows the evolution of the density over two gyroperiods and radial positions to $5R_c$. Obviously, the density stays periodic in time, similar to Fig.5.1 under the initially homogeneous ion density profile. However, along the radial direction, the position of the density maximum is at a radius smaller than R_c. By comparing with the initial ion density profile as given by curve (4) in Fig.5.1, we find that the maxmum ion density moves closer to the center and the region periodically comes into being after the negative electric field is switched on.

5.2.4 Case 4: $n_{i0}(r_0) \sim e^{-r_0^2/R_c^2}$

For a simpler case that can still be solved analytically, we turn to

$$n_{i0}(r_0) = n_0 \kappa e^{-r_0^2/R_c^2} \tag{5.31}$$

By applying Eq.(5.10), Eq.(5.31) after $t = 0$ turns into

$$n_{i0}(r_0) = n_0 \kappa e^{-\Gamma} \tag{5.32}$$

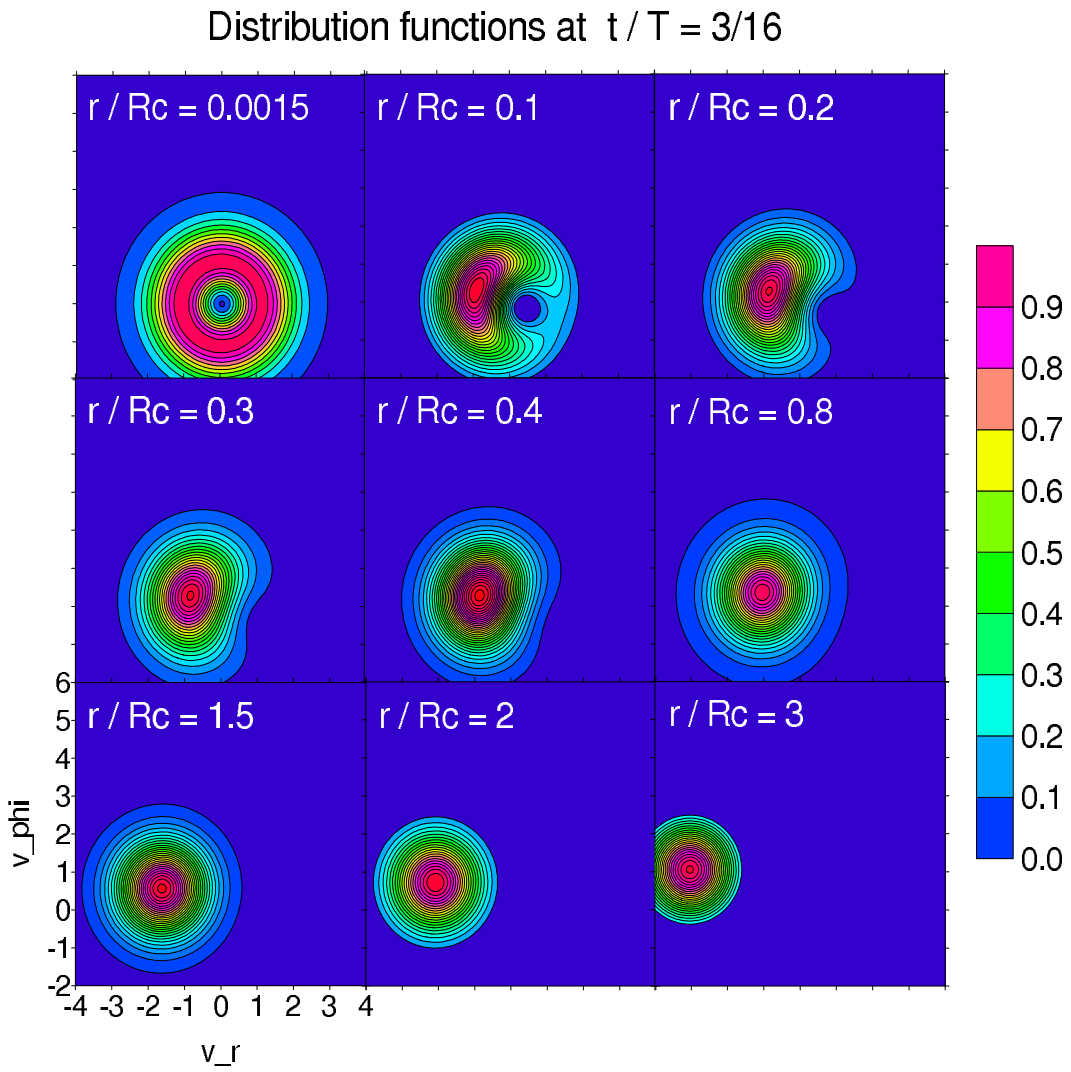

Figure 5.5: Evolution of the ion velocity distribution function versus radial positions at $t/T = 3/16$ resulting from the non-uniform initial ion density in Eq.(5.23).

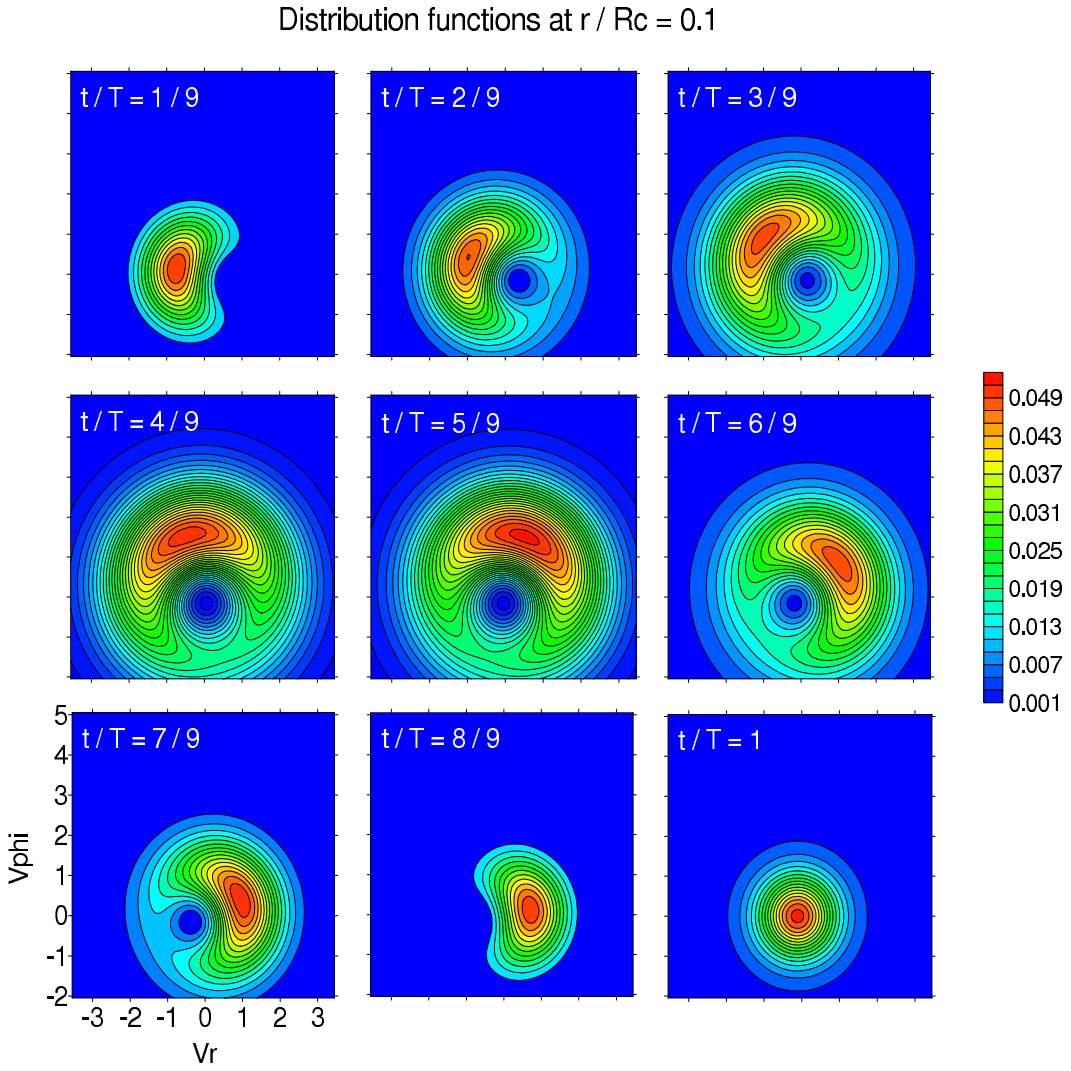

Figure 5.6: Evolution of ion velocity distribution function versus time during one gyroperiod at $r/R_c = 0.1$ for the same conditions as in Fig.5.5.

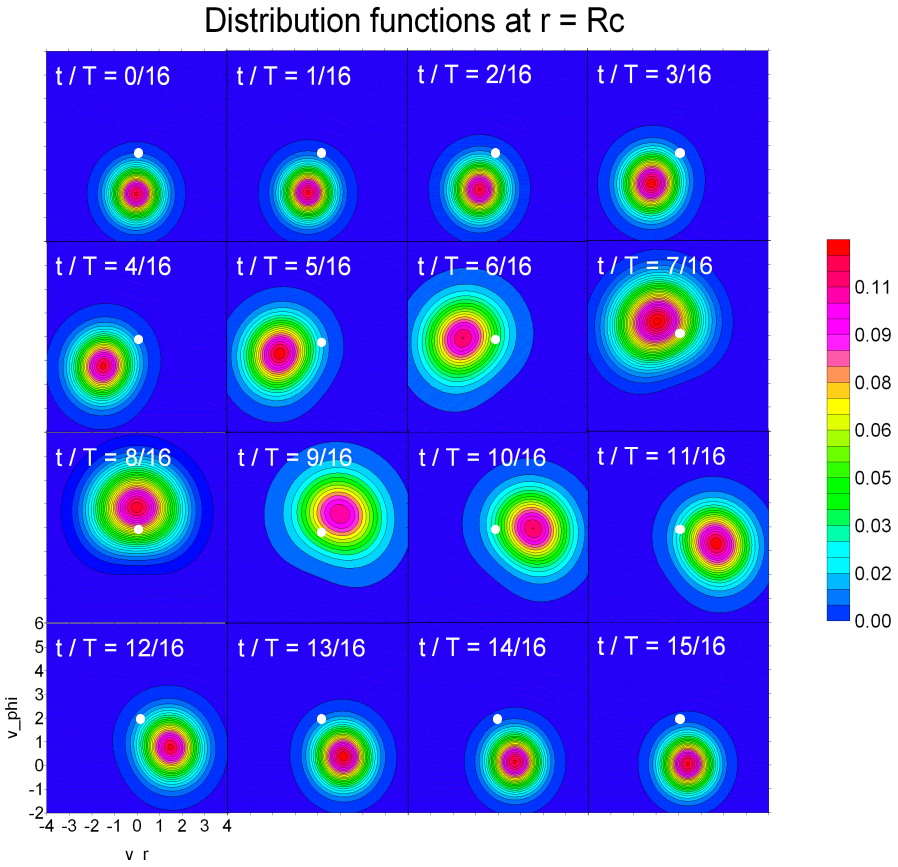

Figure 5.7: Same as Fig.5.6, but for $r/R_c = 1$. The white spot is the center of the panels.

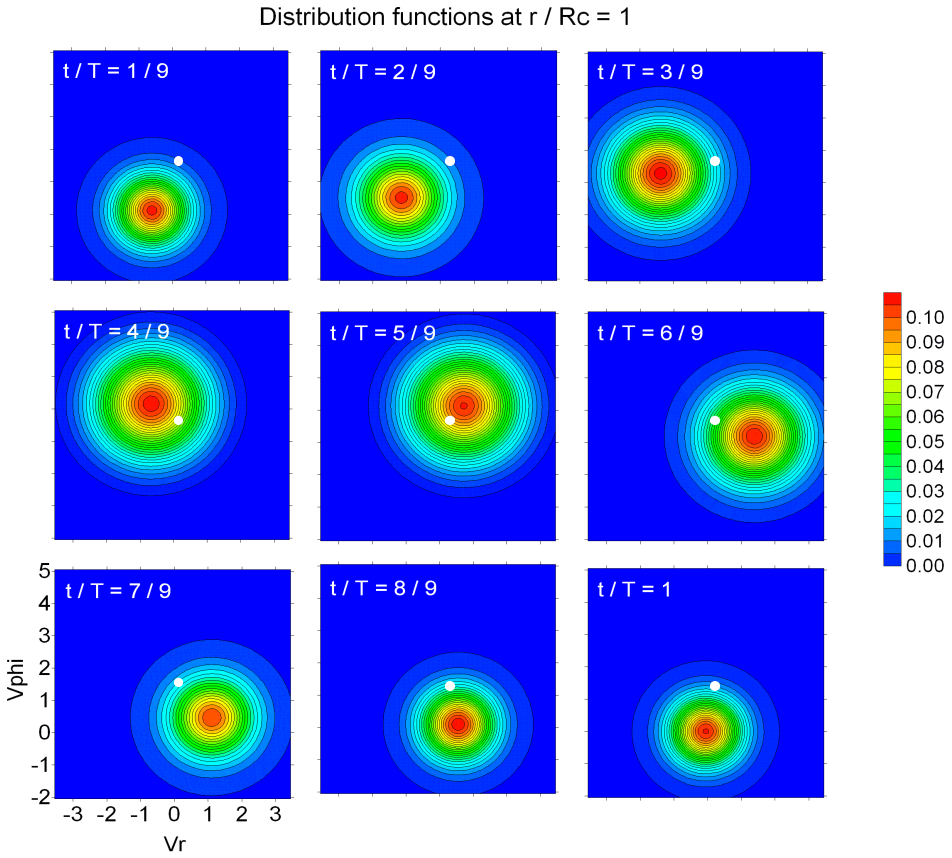

Figure 5.8: Evolution of ion velocity distribution function versus time during one gyroperiod at $r/R_c = 1$ resulting from the non-uniform initial ion density in Eq.(5.31). The white spot is the center of the panels.

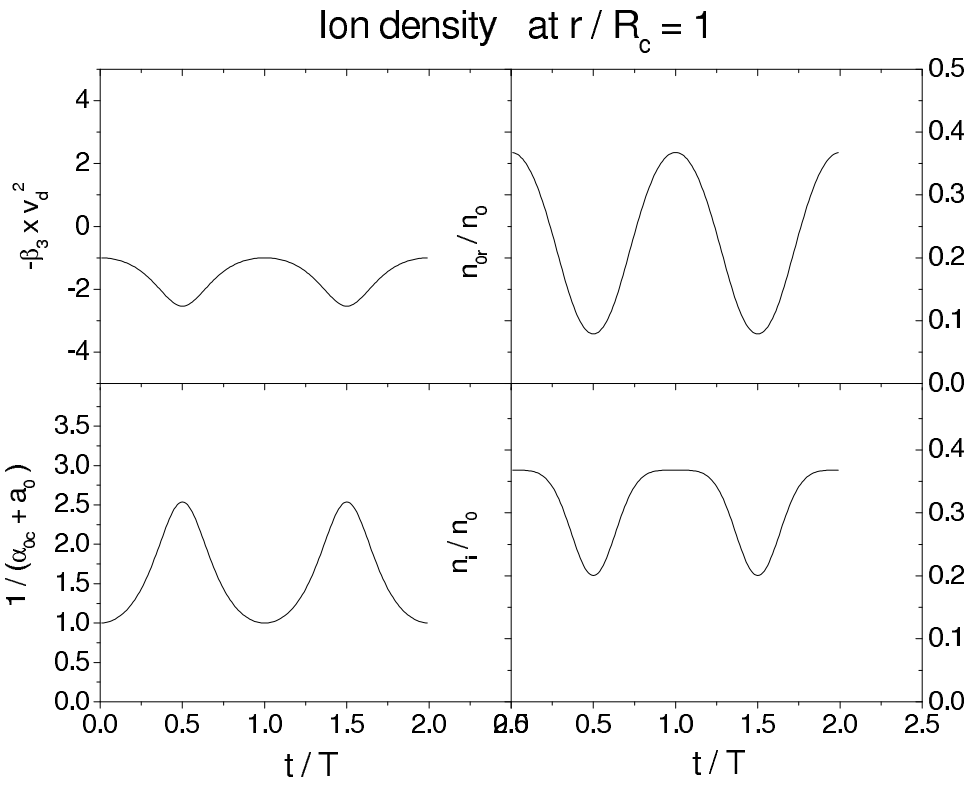

Figure 5.9: Evolutions of β_3, n_{0r}, α_{0c}, and n_i versus time during two gyroperiods at $r/R_c = 1$ resulting from the non-uniform initial ion density in Eq.(5.31).

Thus, the ion distribution function can be expressed as

$$f_i(\mathbf{r},\mathbf{v},t)=\frac{n_0}{\pi}\kappa e^{-\Gamma}\cdot e^{-a_0\left[(v_r-v_{\mathrm{d}r})^2+(v_\phi-v_{\mathrm{d}\phi})^2\right]} \tag{5.33}$$

Define as before

$$\alpha_{0c}=\frac{1-a_0}{\frac{E_c}{B}R_c\Omega_i},\quad \text{and}\quad \beta_1=-\frac{a_0}{1-a_0} \tag{5.34}$$

Eq.(5.33) becomes

$$f_i(\mathbf{r},\mathbf{v},t)=\frac{n_{0r}}{\pi}e^{-(\alpha_{0c}+a_0)\left[(v_r-\beta_2 v_{\mathrm{d}r})^2+\left(v_\phi-\beta_2 v_{\mathrm{d}\phi}\right)^2\right]} \tag{5.35}$$

in which

$$\left.\begin{aligned} n_{0r}&=n_0\kappa e^{-\beta_3(v_{\mathrm{d}r}^2+v_{\mathrm{d}\phi}^2)}\ ,\quad \beta_2=\frac{\alpha_{0c}\beta_1+a_0}{\alpha_{0c}+a_0}\\ \beta_3&=\alpha_{0c}\beta_1^2+a_0-\frac{(\alpha_{0c}\beta_1+a_0)^2}{\alpha_{0c}+a_0}=\frac{\dfrac{a_0}{1-a_0}}{1+a_0\left(\frac{E_c}{B}R_c\Omega_i-1\right)} \end{aligned}\right\} \tag{5.36}$$

As with Case 3, the density depends on time through both a_0 and $\mathbf{v}_d$, and on position through $\mathbf{v}_d$ only. This can easily be seen if we rewrite the ion velocity distribution as

$$\frac{f_i(\mathbf{r},\mathbf{v},t)}{n_0\kappa}=\frac{1}{\pi}e^{-\beta_3(v_{\mathrm{d}r}^2+v_{\mathrm{d}\phi}^2)}\cdot e^{-(\alpha_{0c}+a_0)\left[(v_r-\beta_2 v_{\mathrm{d}r})^2+\left(v_\phi-\beta_2 v_{\mathrm{d}\phi}\right)^2\right]} \tag{5.37}$$

This distribution is plotted in Fig.5.8. It has the same temporal features as formed in Fig.2.4 in the linear electric field case. For the ion density, we obtain

$$n_i=\int v_j^0 f_i\mathrm{d}\mathbf{v}=\int f_i\mathrm{d}\mathbf{v}=\frac{n_{0r}}{\alpha_{0c}+a_0} \tag{5.38}$$

which is a function of both position and time. Both Fig.5.9 and Panel n_i in Fig.5.11 give the density evolution in two gyroperiods. The former is at $r=R_c$ and the latter is for radial positions up to $5R_c$. Similar to Fig.5.1 under the initially homogeneous ion density profile, the density stays periodic in time. However, along the radial direction, the density is no longer independent of the radial position but decreases with it. Initially at $t=0$, the maximum density occurs at $r_0=0$ as shown by curve (3) in Fig.5.1. For $t>0$, the maximum density is in a region within $r<0.5R_c$, and this region oscillates in time.

The advantage of having an analytical expression for the ion density function at any time is that it makes the velocity moments and transport properties relatively easy to obtain from analytical work. This is demonstrated in the next section.

5.3 Transport properties with two inhomogeneous initial ion densities under collision-free conditions

5.3.1 A brief review

For the last two cases presented in the last section, we now derive various velocity moments of the ions under collision-free conditions of the form

$$\langle v_j^k \rangle = \frac{1}{n_i} \int v_j^k f_i \mathrm{d}\mathbf{v} \tag{5.39}$$

The transport properties are then obtained from these moments.

When $k = 0$, we obtain the ion density from $\int f_i \mathrm{d}\mathbf{v}$. This first moment of the velocity distribution for the inhomogeneous situation was already discussed in the last Section. Here we deal with $k = 1, 2, 3$. We recall that the drift, temperature, and heat flow are recovered from the velocity moments through the same relations that were posted in Chapter 2, namely,

$$\left.\begin{aligned}
&v_{\mathrm{aver}} = \langle v_r \rangle \ , \quad v_{\mathrm{ave}\phi} = \langle v_\phi \rangle \ , \quad v_\parallel = v_{\parallel 0} \\
&T_r = \frac{m_i}{k_b}(\langle v_r^2 \rangle - \langle v_r \rangle^2) \ , \quad T_\phi = \frac{m_i}{k_b}(\langle v_\phi^2 \rangle - \langle v_\phi \rangle^2) \ , \quad T_\parallel = T_0 \\
&p_{rr} = n_i k_b T_r \ , \quad p_{\phi\phi} = n_i k_b T_\phi \ , \quad p_{\parallel\parallel} = p_{0r} \\
&q_r = m_i(\langle v_r^3 \rangle - \langle v_r \rangle^3) - 3\langle v_r \rangle (k_b T_r) \ , \\
&q_\phi = m_i(\langle v_\phi^3 \rangle - \langle v_\phi \rangle^3) - 3\langle v_\phi \rangle (k_b T_\phi) \ , \quad q_\parallel = 0
\end{aligned}\right\} \tag{5.40}$$

from which the average temperature and pressure are also given by

$$T_i = \frac{T_r + T_\phi + T_\parallel}{3} \ , \quad p_i = \frac{p_{rr} + p_{\phi\phi} + p_{\parallel\parallel}}{3} \tag{5.41}$$

The velocity moments in the inhomogeneous case differ from the uniform initial density case because $n_{i0}(r_0)$ maps into a function of $\mathbf{r}$, $\mathbf{v}$, and t. That was simply equal to n_{i0} itself in the uniform case. These are therefore new contributions to the original velocity moments that are superimposed on the moments formed in Chapter 2. Appendices G and H have listed a series of useful Gaussian integrations for the calculation of velocity moments.

5.3.2 Transport properties for Case 4

As seen in Section 5.1.5, the velocity distribution has the form of a pulsating Maxwellian, albeit with a more complicated character than in Chapter 2 [see Eq.(5.37)]. The velocity moments are therefore similar in form to those obtained in Chapter 2, once the proper coefficients are adjusted properly. Aside from the density, which is given in Eq.(5.38), we obtain

$$\left.\begin{aligned}
&\langle v_r\rangle = \beta_2 v_{\mathrm{d}r}\ , \quad \langle v_\phi\rangle = \beta_2 v_{\mathrm{d}\phi} \\
&\langle v_r^2\rangle = \beta_2^2 v_{\mathrm{d}r}^2 + \frac{v_{T0}^2}{2(\alpha_{0c}+a_0)} = \beta_2^2 v_{\mathrm{d}r}^2 + \frac{k_b T_0}{m_i(\alpha_{0c}+a_0)} \\
&\langle v_\phi^2\rangle = \beta_2^2 v_{\mathrm{d}\phi}^2 + \frac{v_{T0}^2}{2(\alpha_{0c}+a_0)} = \beta_2^2 v_{\mathrm{d}\phi}^2 + \frac{k_b T_0}{m_i(\alpha_{0c}+a_0)} \\
&\langle v_r^3\rangle = \beta_2^3 v_{\mathrm{d}r}^3 + 3\beta_2 v_{\mathrm{d}r}\frac{v_{T0}^2}{2(\alpha_{0c}+a_0)} = \beta_2^3 v_{\mathrm{d}r}^3 + 3\beta_2 v_{\mathrm{d}r}\frac{k_b T_0}{m_i(\alpha_{0c}+a_0)} \\
&\langle v_\phi^3\rangle = \beta_2^3 v_{\mathrm{d}\phi}^3 + 3\beta_2 v_{\mathrm{d}\phi}\frac{v_{T0}^2}{2(\alpha_{0c}+a_0)} = \beta_2^3 v_{\mathrm{d}\phi}^3 + 3\beta_2 v_{\mathrm{d}\phi}\frac{k_b T_0}{m_i(\alpha_{0c}+a_0)}
\end{aligned}\right\} \tag{5.42}$$

This means that the bulk transport properties are given by

$$\left.\begin{aligned}
&v_{\mathrm{aver}} = \langle v_r\rangle = \beta_2 v_{\mathrm{d}r}\ , \quad v_{\mathrm{ave}\phi} = \langle v_\phi\rangle = \beta_2 v_{\mathrm{d}\phi}\ , \quad v_\parallel = v_{\parallel 0} \\
&T_r = \frac{m_i}{k_b}(\langle v_r^2\rangle - \langle v_r\rangle^2) = \frac{T_0}{\alpha_{0c}+a_0}\ , \\
&T_\phi = \frac{m_i}{k_b}(\langle v_\phi^2\rangle - \langle v_\phi\rangle^2) = \frac{T_0}{\alpha_{0c}+a_0}\ , \quad T_\parallel = T_0 \\
&p_{rr} = n_i k_b T_r = \frac{p_{0r}}{(\alpha_{0c}+a_0)^2}\ , \quad p_{\phi\phi} = n_i k_b T_\phi = \frac{p_{0r}}{(\alpha_{0c}+a_0)^2}\ , \quad p_{\parallel\parallel} = p_{0r} \\
&q_r = m_i(\langle v_r^3\rangle - \langle v_r\rangle^3) - 3\langle v_r\rangle(k_b T_r) = 0\ , \\
&q_\phi = m_i(\langle v_\phi^3\rangle - \langle v_\phi\rangle^3) - 3\langle v_\phi\rangle(k_b T_\phi) = 0\ , \quad q_\parallel = 0
\end{aligned}\right\} \tag{5.43}$$

in which $p_{0r} = n_{0r} k_b T_0$, and

$$\left.\begin{aligned}
T_i &= \frac{T_r + T_\phi + T_\parallel}{3} = \frac{T_0}{3}\left(\frac{2}{\alpha_{0c}+a_0} + 1\right) \\
p_i &= \frac{p_{rr} + p_{\phi\phi} + p_{\parallel\parallel}}{3} = p_{0r}\left[\frac{2}{(\alpha_{0c}+a_0)^2} + 1\right]
\end{aligned}\right\} \tag{5.44}$$

Note that all non-diagonal elements of the pressure tensor are zero, and the scalar pressure p_i is, as usual, defined as one-third of the trace of the pressure tensor.

In fact, these bulk parameters can be directly written out from Eq.(5.37) by following the same procedure as shown in Chapter 2. Fig.(5.10) shows the temporal change of the bulk properties at $r/R_c = 0.5$ in two gyroperiods. Interestingly, all

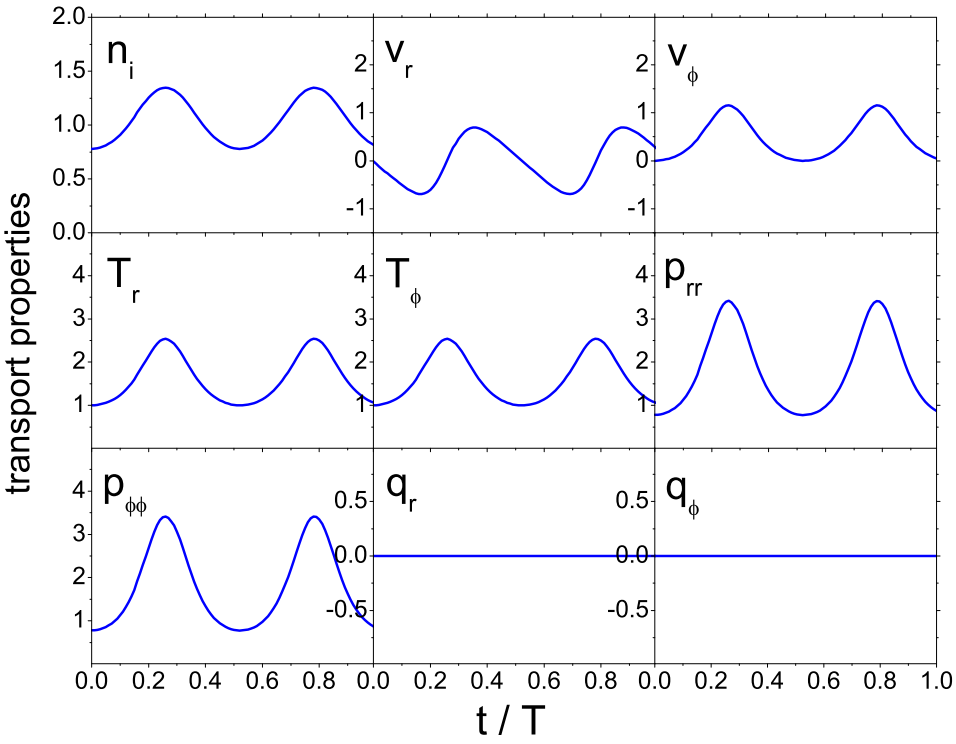

Figure 5.10: Bulk parameters in time at $r = 0.5R_c$ for Case 4 under $E_r = -E_c(r/R_c)$: $n_{i0}(r_0) = n_0\left(1 + \kappa e^{-r_0^2/R_c^2}\right)$ ($\kappa = 1$ is assumed).

the bulk parameters change in a very similar way to those in Chapter 2, especially with zero heat flows. This feature can be easily seen from the temporally pulsating Maxwellian distributions given in Eq.(5.35). In Fig.5.11, all bulk parameters are depicted versus time and radial position.

5.3.3 Transport properties for Case 3

The transport properties for Case 3 are more complicated than in Case 4 because the factor r_0^2/R_c^2 introduces extra polynomials in the velocity moments. The calculation of these moments remains straightforward but is a bit tedious. The details are

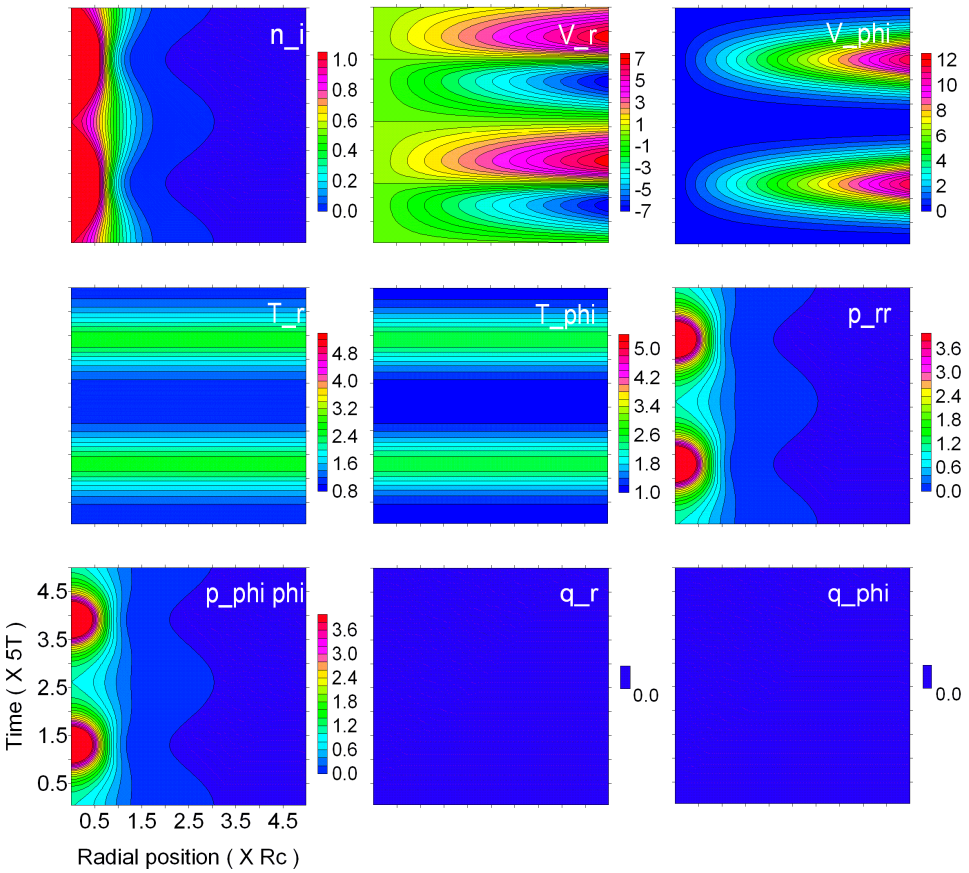

Figure 5.11: Bulk parameters in time and radial position for Case 4.

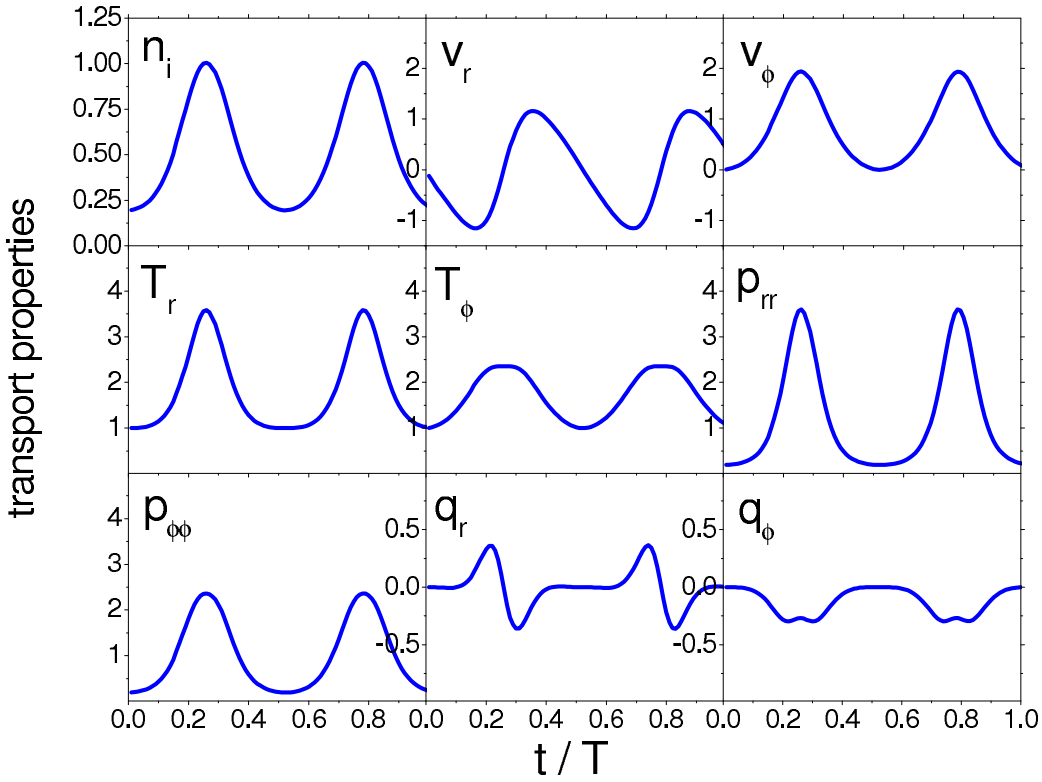

Figure 5.12: Bulk parameters in time at $r = 0.5R_c$ for Case 3 under $E_r = -E_c(r/R_c)$: $n_{i0}(r_0) = n_0\left[1+\kappa(r_0^2/R_c^2)e^{-r_0^2/R_c^2}\right]$ ($\kappa = 1$ is assumed).

therefore left to Appendix H, where $I_1 - I_6$ relates to the final products, namely,

$$\langle v_r\rangle = \frac{I_1}{n_i}\ , \quad \langle v_\phi\rangle = \frac{I_2}{n_i}\ , \quad \langle v_r^2\rangle = \frac{I_3}{n_i}\ , \quad \langle v_\phi^2\rangle = \frac{I_4}{n_i}\ , \quad \langle v_r^3\rangle = \frac{I_5}{n_i}\ , \quad \langle v_\phi^3\rangle = \frac{I_6}{n_i} \tag{5.45}$$

The bulk parameters associated with these moments do not have more simplified analytical expressions than Eq.(5.40) above. By making use of these expressions, we compute the transport properties and show them in Fig.5.12 and 5.13.

Fig.5.12 describes the temporal change of the bulk properties at $r/R_c = 0.5$ over two gyroperiods. Though other bulk parameters change in a very similar way to those in Chapter 2, the heat flows are at present nonzero. This means that the initially inhomogeneous ion density brings about thermal interchanges with the background plasma. In the figure, analytical and numerical results are shown together as a check for the equivalence of the calculations. In Fig.5.13, all bulk parameters are given as

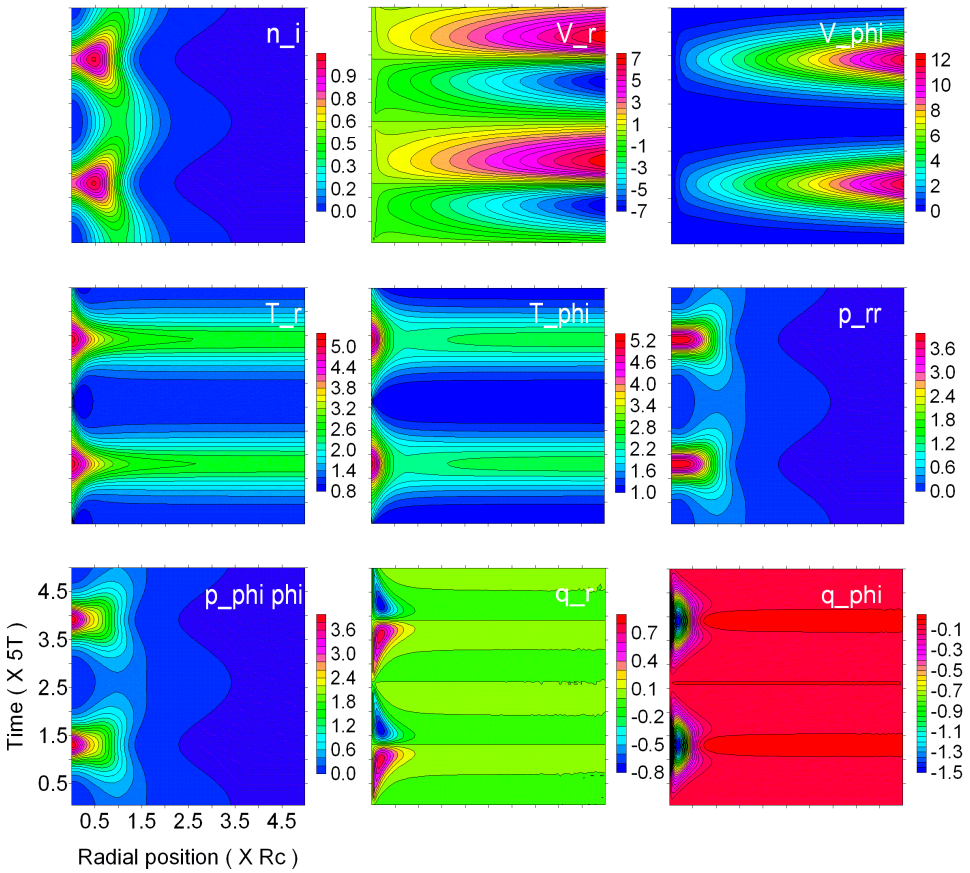

Figure 5.13: Bulk parameters in time and radial position for Case 3.

a function of time and radial position.

5.4 Distribution and transport parameters with an inhomogeneous initial ion density under collisional conditions: Case 4

The inhomogeneous initial ion density also has an impact on the ion distribution function and transport properties under collisional conditions. However, the algebra becomes much more complicated. Only under an initial ion density structure described by Case 4 can we derive the math to obtain analytical results. The steps are completely the same as done in Chapter 3, but with extra parameters (e.g., α_{0c}, β) in all expressions introduced by the inhomogeneous Initial Ion Density. A new parameter, η, is defined.

5.4.1 Expressing the ion density

Considering a process identical to that done in Chapter 3 but with $n_{i0}(r_0) \sim e^{-r_0^2/R_c^2}$, we obtain that

$$f_{i1}(\mathbf{r},\mathbf{v},t) = \frac{n_{0r}}{\pi} e^{-(\alpha_{0c}+a_0)\left[(v_r-\beta_2 v_{\mathrm{d}r})^2+\left(v_\phi-\beta_2 v_{\mathrm{d}\phi}\right)^2\right]} \tag{5.46}$$

and

$$N_i = \frac{n_{0r}}{\alpha_{0c}+a_0} + \frac{\nu_{in}}{n_n}\int_0^t N_i(t')\left[\int f_n(t')\mathrm{d}\mathbf{v}\right]\mathrm{d}t' \tag{5.47}$$

which eventually turns out to be

$$N_i = n_0\kappa\left[\frac{e^{-\beta_3(v_{\mathrm{d}r}^2+v_{\mathrm{d}\phi}^2)}}{\alpha_{0c}+a_0} + \eta\left(e^{\frac{\omega}{\Omega_i}\nu_{in}t}-1\right)\right] \tag{5.48}$$

in which η is an integration coefficient defined by

$$\left.\begin{aligned}\eta &= \frac{1}{2\pi}\frac{\Omega_i}{\omega}\int_0^{2\pi}\frac{e^{-\beta_3\mathbf{v}_{\mathrm{d}}^2-\frac{\nu_{in}}{\Omega_i}\alpha}}{a_0(\alpha)[\alpha_{0c}(\alpha)+a_0(\alpha)]}\mathrm{d}\alpha \\ &= \frac{1}{2\pi}\frac{\Omega_i}{\omega}C_1\int_0^{2\pi}\frac{e^{-\beta_3\mathbf{v}_{\mathrm{d}}^2-\frac{\nu_{in}}{\Omega_i}\alpha}}{\cos^2\alpha+C_2\cos\alpha+C_3}\mathrm{d}\alpha\end{aligned}\right\} \tag{5.49}$$

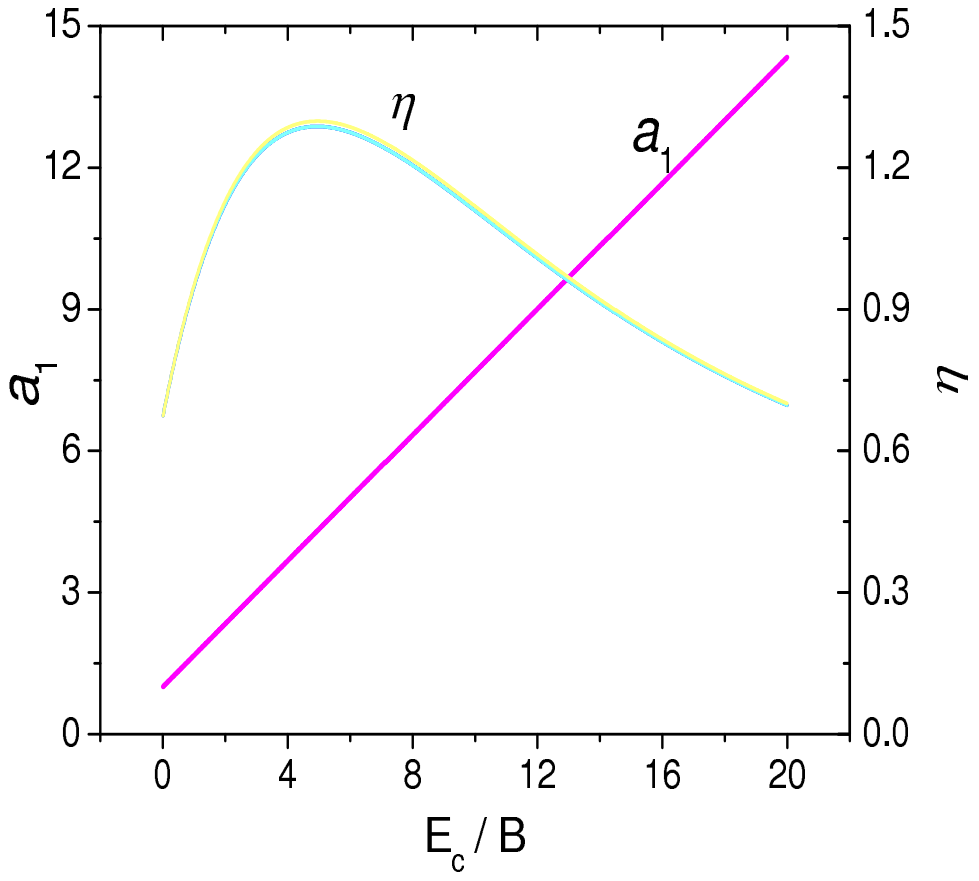

Figure 5.14: Change of η and a_1 versus E_c/B.

in which

$$\left.\begin{aligned} C_1 &= \left(1+\frac{a_1}{a_2}\right)^2 \frac{(E_c/B)R_c\Omega_i}{(E_c/B)R_c\Omega_i - 1} \\ C_2 &= \frac{1}{a_2}\frac{2a_1(E_c/B)R_c\Omega_i - 1}{(E_c/B)R_c\Omega_i - 1} \\ C_3 &= \left(\frac{a_1}{a_2}\right)^2 \frac{(E_c/B)R_c\Omega_i + \dfrac{a_2}{a_1}}{(E_c/B)R_c\Omega_i - 1} \end{aligned}\right\} \tag{5.50}$$

This is a new, nonzero parameter determined by the electric field. If the initial ion density is uniform in space, parameters β_3 and α_{0c} disappear in Eq.(5.49) and then η is simplified to a_1 [see Eq.(F.15) in Appendix F]. Fig.5.14 shows the change of η versus E_c/B, in which the linear a_1 variation is also given for comparison. η is always smaller than a_1, about one order lower. With the increase of the electric field, η changes nonlinearly. Around $E_c/B = 5$, η has a maximum value $\sim$1.3.

Because η is smaller than a_1, the ion density n_i with the nonuniform initial density becomes different from that with the uniform initial density given in Chapter 3. From Eq.(5.48), we obtain the ion density changes with time via

$$n_i = N_i e^{-\nu_{in}t} = n_0\kappa \left\{ \left[\frac{e^{-\beta_3(v_{\mathrm{d}r}^2 + v_{\mathrm{d}\phi}^2)}}{\alpha_{0c} + a_0} - \eta \right] e^{-\nu_{in}t} + \eta e^{(\omega/\Omega_i - 1)\nu_{in}t} \right\} \tag{5.51}$$

in which the first term in the bracket on the RHS oscillates with time but decreases exponentially, whileas the second one increases exponentially. Two panels in Fig5.15 show n_i as a function of time and of radial position, respectively. The upper panel contains two curves versus time at $r/R_c = 0.5$ under $E_c/B = 2$ and $E_c/B = 8$, respectively, and the small panel inside it gives the density variation in the range 350-360 cycles under $E_c/B = 8$. The lower panel gives two curves versus radius under $E_c/B = 2$ at 45 and 450 cycles, respectively.

A direct comparison between the upper panel and Fig.3.1 tells us that smaller η values give lower ion densities. However, the oscillation remains in the density evolution. More importantly, unlike the result found in Chapter 3, the density is at present a function of r. But the related parameters (β_3 and α_{0c}) occur only in the first term in the RHS brackets. See Fig.5.1. Initially, the density $n_{i0}(r_0)$ is 1 at $r_0 = 0$ and around 0 at $r_0 = 2R_c$ (curve 3; note that we are now discussing a case excluding the background density n_0 for simplicity). When more ions are attracted

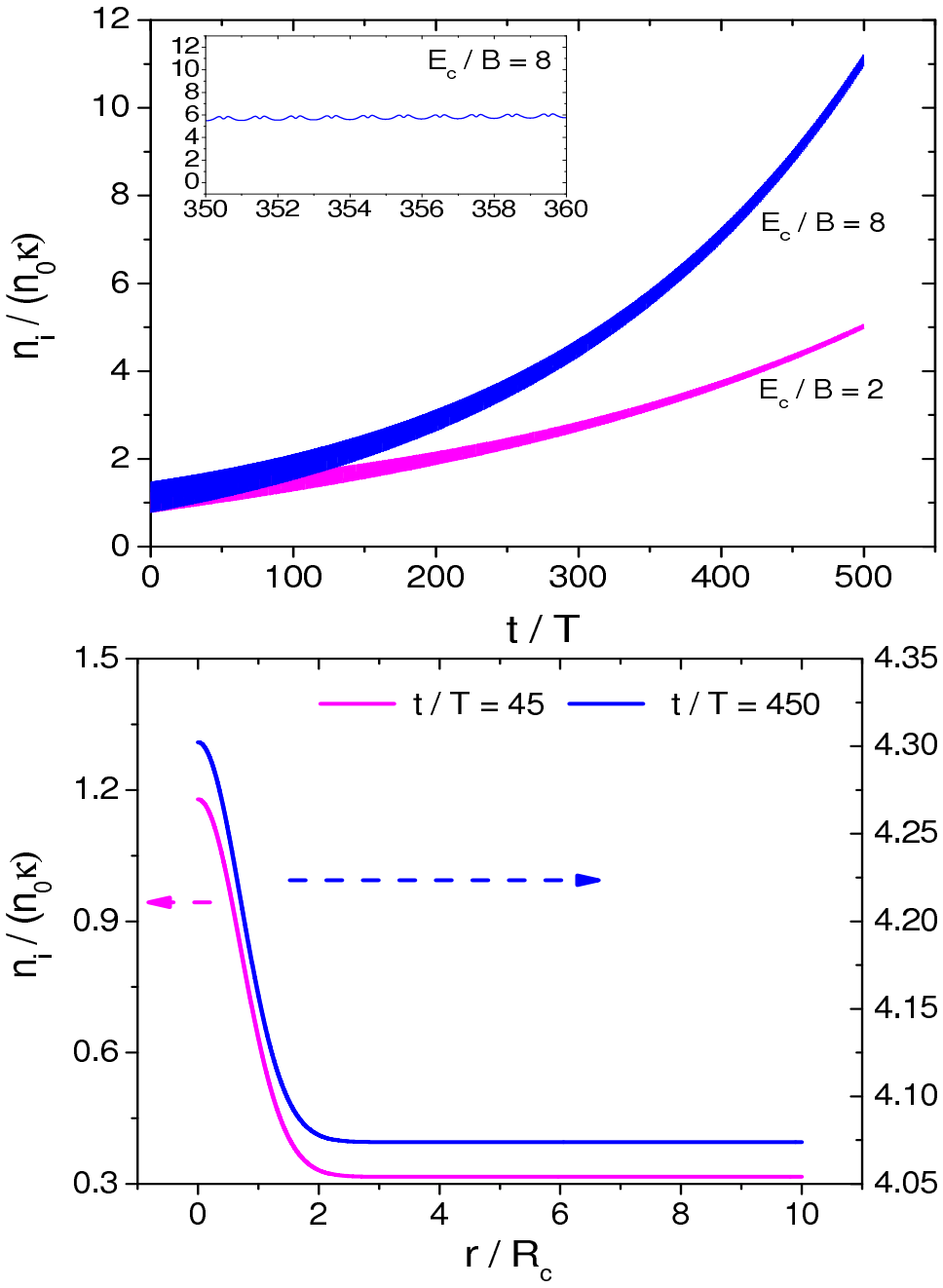

Figure 5.15: Upper: Profile of ion density versus time under $E_c/B = 2$ and $E_c/B = 8$ at $r/R_c = 0.5$. Lower: Profile of ion density versus radius under $E_c/B = 2$ at $t/T = 45$ and $t/T = 450$. The arrows indicate the curves are linked to corresponding vertical coordinates, respectively.

to the center, the ion density should increase, while the gradient of the density in the radial direction should decrease. This feature is shown in the lower panel. At 45 cycles, the ion density drops from 1.2 to 0.3; but at 450 cycles, it decreases from 4.3 to 4.08. That is to say, the density becomes higher while the gradient becomes more even. However, at any time, the region with higher density is within $r \leq 2R_c$, in agreement with the initial density profile.

5.4.2 Expressing the ion velocity distribution function

By using the n_i solution, a series of tedious derivations then gives

$$f_i = f_{i1} e^{-\nu_{in} t} + \frac{n_0 \kappa}{n_{\rm n}} \frac{\Omega_i}{\omega} \frac{\eta}{2\pi} \int_0^{2\pi} f_{\rm n}(\alpha') {\rm d}\alpha' \left[e^{(\omega/\Omega_i)\nu_{in} t} - 1 \right] e^{-\nu_{in} t} \tag{5.52}$$

in which $f_{\rm n}$ has been shown in Eq.(3.11) or Eq.(3.12). Using Eq.(5.36,5.46), we rewrite Eq.(5.53) as follows:

$$\left. \begin{array}{l} \dfrac{f_i}{n_0 \kappa} = \dfrac{e^{-\beta_3 (v_{\rm dr}^2 + v_{\rm d\phi}^2)}}{\pi} e^{-(\alpha_{0c} + a_0) \left[(v_r - \beta_2 v_{\rm dr})^2 + \left(v_\phi - \beta_2 v_{\rm d\phi} \right)^2 \right]} e^{-\nu_{in} t} + \\ + \dfrac{\Omega_i}{\omega} \dfrac{\eta}{2\pi^2} \int_0^{2\pi} e^{-(v_r^2 + v_\phi^2) + (B_2 \pm B_1 \sin\alpha')} {\rm d}\alpha' \left[e^{(\omega/\Omega_i)\nu_{in} t} - 1 \right] e^{-\nu_{in} t} \end{array} \right\} \tag{5.53}$$

This equation is similar to Eq.(3.26), except for a few minor differences: in the second term, a_1 is now substituted by η; in the first term, an extra factor, $e^{-\beta_3 \mathbf{v}_{\rm d}^2}$, occurs, a_0 is substituted by $\alpha_{0c} + a_0$, and β_2 is present. In a more convenient form to use as done in Chapter 3, Eq.(5.53) is rewritten as follows:

$$\left. \begin{array}{l} f_i = f_{i1} \cdot e^{-\nu_{in} t} + f_{i2} \cdot \left(e^{\frac{\omega}{\Omega_i} \nu_{in} t} - 1 \right) e^{-\nu_{in} t} \\ \dfrac{f_{i1}}{n_0 \kappa} = \dfrac{e^{-\beta_3 (v_{\rm dr}^2 + v_{\rm d\phi}^2)}}{\pi} e^{-(\alpha_{0c} + a_0) \left[(v_r - \beta_2 v_{\rm dr})^2 + \left(v_\phi - \beta_2 v_{\rm d\phi} \right)^2 \right]} \\ \dfrac{f_{i2}}{n_0 \kappa} = \dfrac{1}{\pi} e^{B_1 + B_2 - (v_r^2 + v_\phi^2)} \cdot \dfrac{\Omega_i}{\omega} \eta \cdot \left[e^{-B_1} I_0(B_1) \right] \end{array} \right\} \tag{5.54}$$

where I_0 is the zeroth-order modified Bessel function as introduced in Chapter 3.

Similar to Eq.(3.27), the distribution function f_i also contains two parts. The first part decreases exponentially in time, while the second one increases exponentially. At the beginning $t = 0$, the result gives the collision-free result. For $t \to \infty$, the first component disappears and the second one controls the evolution. In the two components of f_i in the present nonuniform initial density case, f_{i1} decreases more

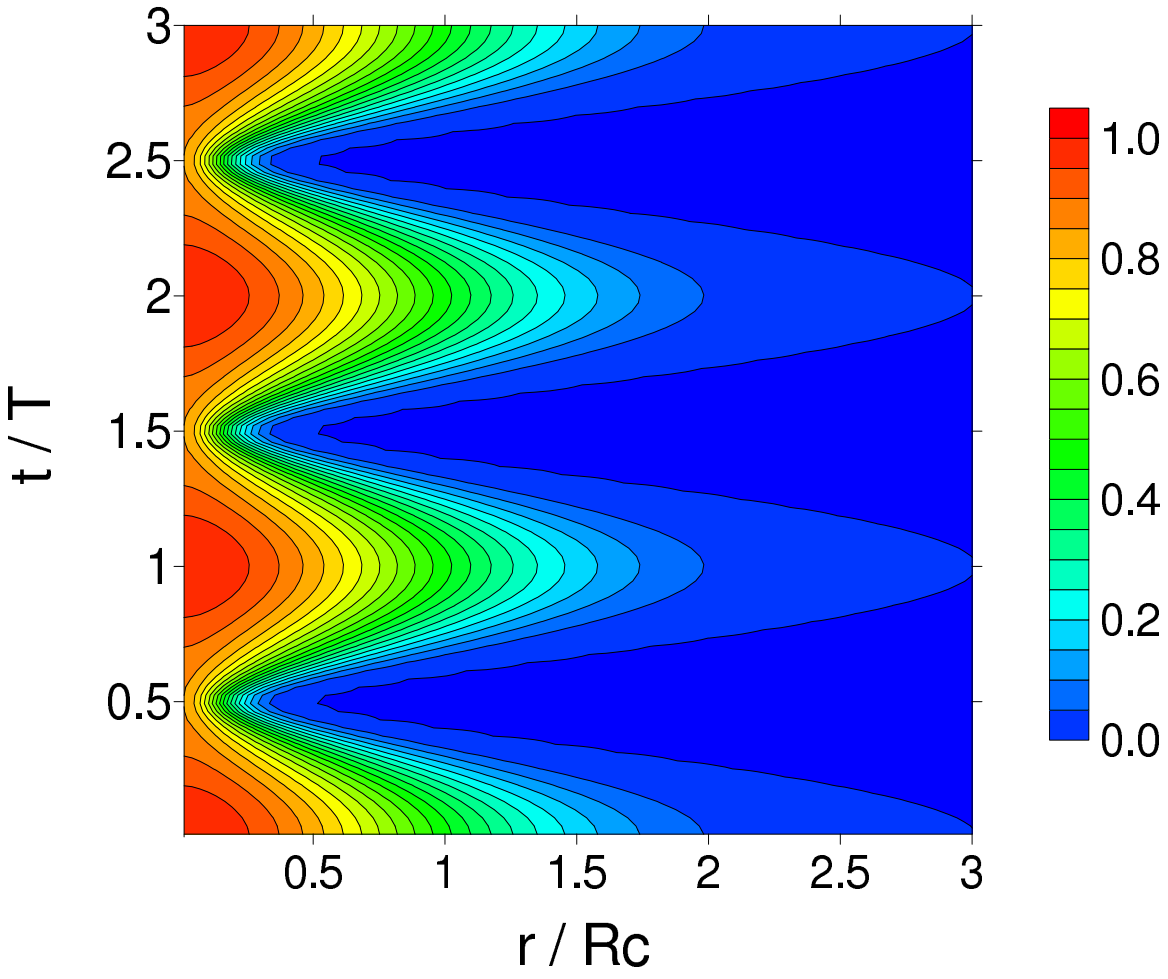

Figure 5.16: Factor, χ, in f_{i1} as a function of time and radius at $E_c/B = 2$.

quickly with time than that in Eq.(3.29) (the uniform initial density case discussed Chapter 3), due to an extra factor introduced as

$$\chi = e^{-\left[\alpha_{0c}+\beta_3(v_{\mathrm{d}r}^2+v_{\mathrm{d}\phi}^2)\right]} \tag{5.55}$$

As shown in Fig.5.16, χ is always smaller than 1. Only at around complete cycles can it reach the maximum, but only within $r < 0.3R_c$. Beyond that range to $r \sim 2R_c$, it turns to zero quickly.

It is thus reasonable to conclude that in regions $r > 2R_c$, the ion velocity distribution is only controlled by f_{i2}. Within $2R_c$, term $e^{-\nu_{in}t}$ tells us that after 320 cycles (in one collision time, $\nu_{in}^{-1} = 3.3$s), the contribution of f_{i1} becomes $1/e$ (even faster, as argued in the last paragraph), and can then be neglected. This is the same consideration as discussed in Chapter 3. Naturally, f_{i2} determines f_i everywhere and at any time after one or two relaxation times.

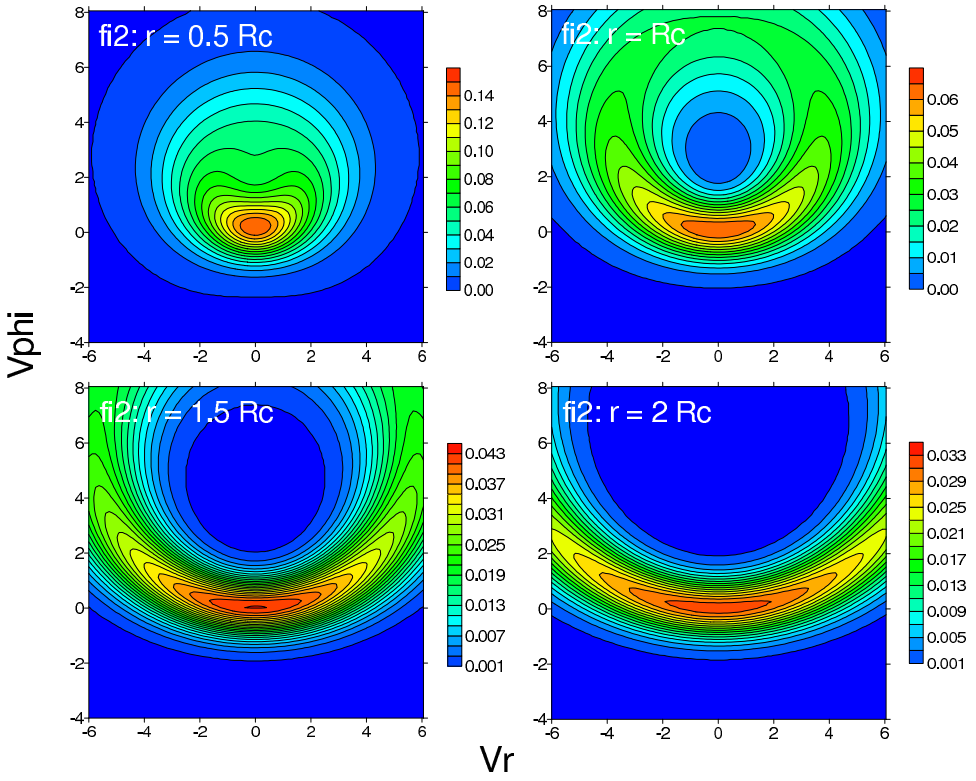

Figure 5.17: Horse-shoe distribution f_{i2} versus radial position r.

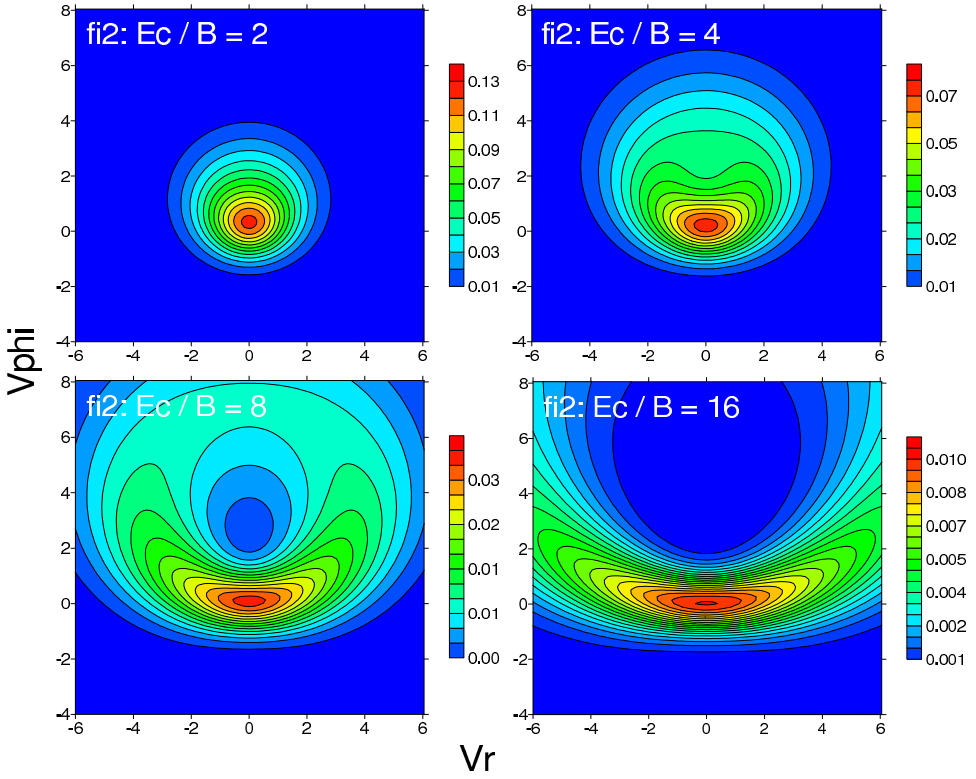

Figure 5.18: Horse-shoe distribution f_{i2} versus electric field E_c.

Let's turn to f_{i2} in Eq.(5.54). A comparison with Eq.(3.29) shows that this function is totally a reiteration of what is given in Chapter 3, except for substituting η for a_1. Consequently, f_{i2} should have toroidal shapes. Fig.5.17 shows the variation of f_{i2} versus the radial position r for $E_c/B = 4$. When the radius increases, the horse-shaped distribution deforms to a ring-shaped ones, similar to Fig.3.3. At $r = 0.5R_c$, Fig.5.18 exposes the evolution of f_{i2} versus the electric field strength E_c. The trend is still the same as Fig.3.4 by being a Maxwellian-like distribution under a smaller electric field to horseshoe and ring shapes when the field goes up. When looking at the development of the total ion velocity distribution function, f_i, with time, a similar change is also presented to that in Fig.3.5 of Chapter 3. It deserves to be mentioned that although these figures resemble those in Chapter 3, the distributions are all weaker in magnitude than those figures. No doubt this is caused by the difference between a_1 and η occurring in f_{i2}.

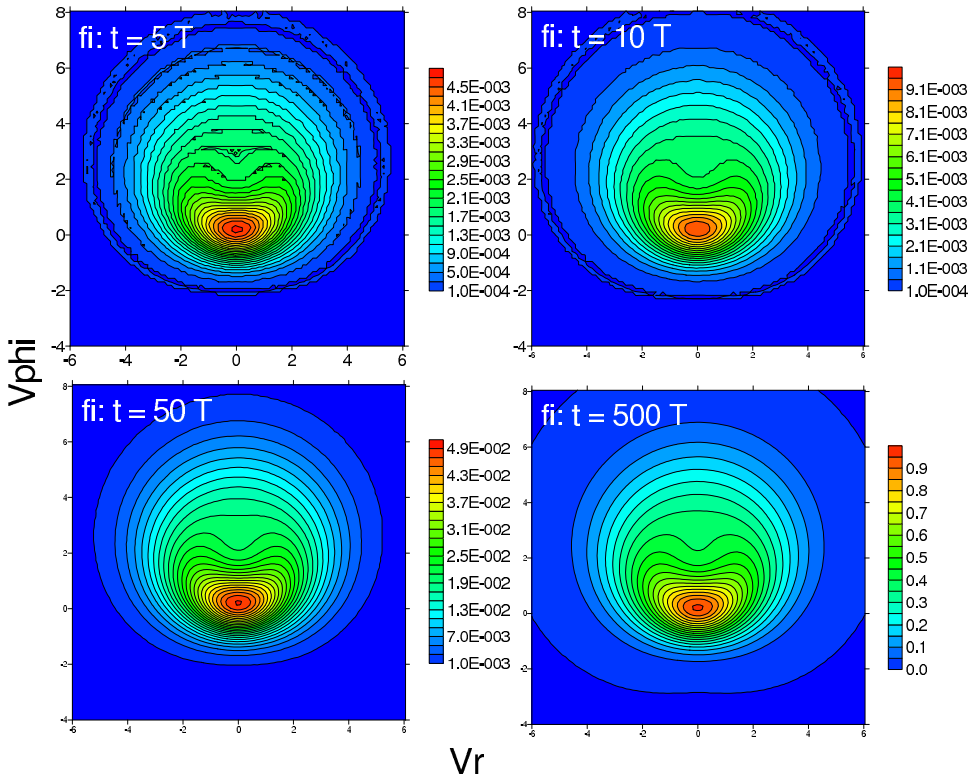

Figure 5.19: Horse-shoe distribution f_i versus time t.

5.4.3 Expressing the bulk parameters

With the ion distribution function at hand, it is feasible to obtain velocity moments and then bulk parameters as done in Chapter 3. To produce the ion velocity moments and then the transport properties, we must calculate the neutral velocity moments first of all. This means we have to deal with a 2-fold integration in velocity and time space by using Eq.(5.53). A generalized expression of the velocity moments is

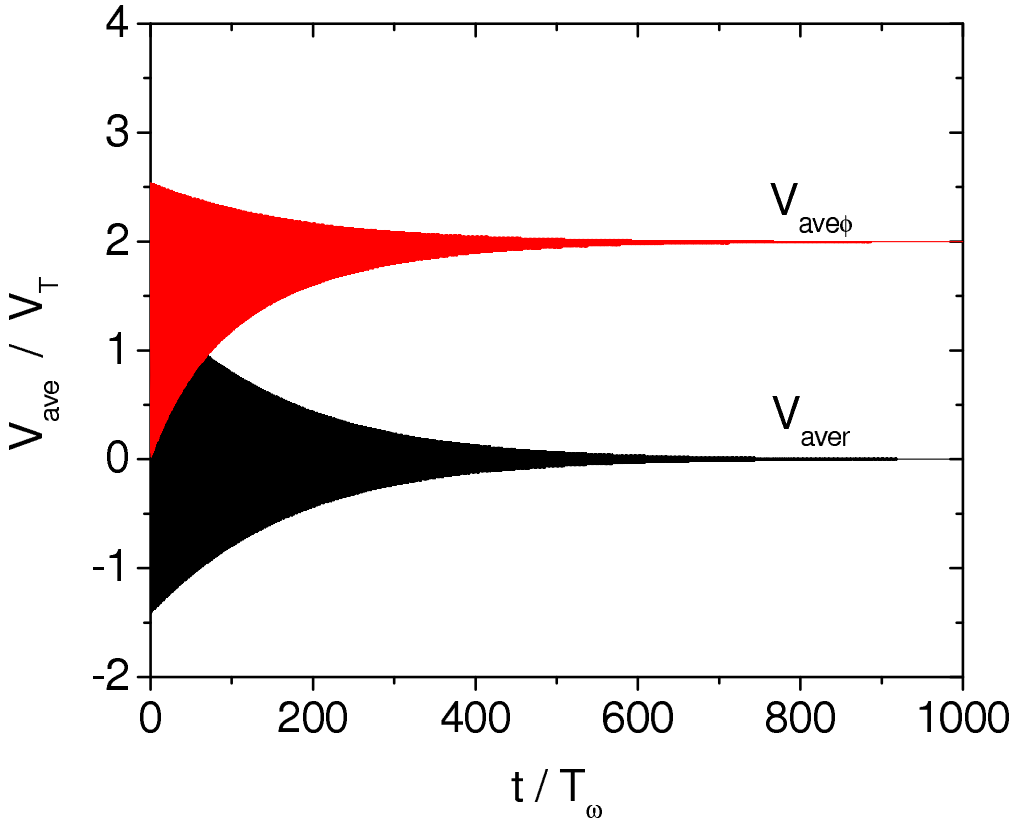

Figure 5.20: Evolution of the average ion speeds for $E_c/B = 4$ at $r = 0.5R_c$.

$$\left.\begin{aligned}
&\langle v_j^k \rangle = \frac{1}{n_i} \int v_j^k f_i \mathrm{d}\mathbf{v} = \\
&= \frac{\int v_j^k \frac{1}{\pi} e^{-(\alpha_{0c}+a_0)(\mathbf{v}-\beta_2\mathbf{v}_\mathrm{d})^2} \mathrm{d}\mathbf{v}}{\frac{e^{-\beta_3 \mathbf{v}_\mathrm{d}^2}}{\alpha_{0c}+a_0} + \eta\left(e^{\frac{\omega}{\Omega_i}\nu_{in}t} - 1\right)} e^{-\beta_3 \mathbf{v}_\mathrm{d}^2} + \\
&+ \frac{\eta}{2\pi}\frac{\Omega_i}{\omega} \frac{\int_0^{2\pi}\left[\int v_j^k \frac{1}{\pi} e^{-a_0'(\alpha)[\mathbf{v}-\mathbf{v}_d'(\alpha)]^2}\mathrm{d}\mathbf{v}\right]\mathrm{d}\alpha}{\frac{e^{-\beta_3 \mathbf{v}_\mathrm{d}^2}}{\alpha_{0c}+a_0} + \eta\left(e^{\frac{\omega}{\Omega_i}\nu_{in}t} - 1\right)} \left(e^{\frac{\omega}{\Omega_i}\nu_{in}t} - 1\right)
\end{aligned}\right\} \tag{5.56}$$

from which we obtain

$$\langle v_r \rangle = \frac{\beta_2 v_{\mathrm{d}r}}{1 + e^{\beta_3 \mathbf{v}_\mathrm{d}^2}(\alpha_{0c}+a_0)\eta\left(e^{\frac{\omega}{\Omega_i}\nu_{in}t} - 1\right)} = \left\{ \begin{array}{ll} \beta_2 v_{\mathrm{d}r} & \text{for } t \to 0 \\ 0 & \text{for } t \to \infty \end{array} \right\} \tag{5.57}$$

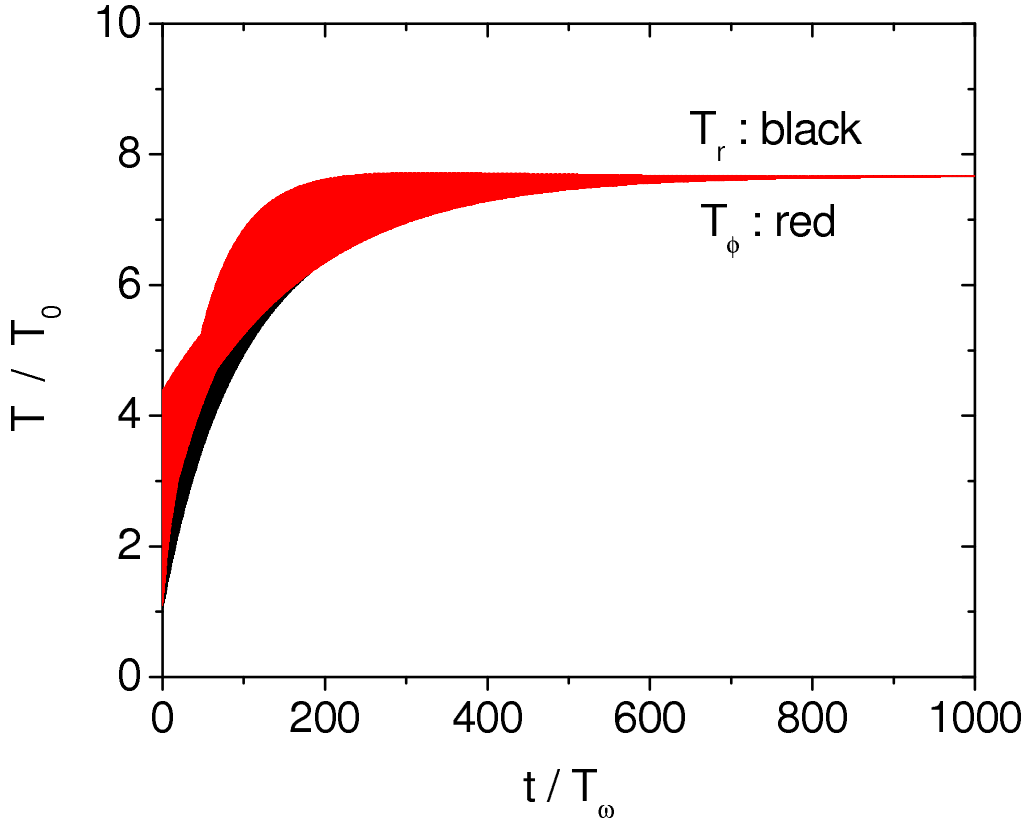

Figure 5.21: Evolution of the ion temperature for $E_c/B = 4$ at $r = 0.5R_c$.

in which the first integration in Eq.(G.19) in Appendix G is used. And,

$$\langle v_\phi \rangle = \frac{\beta_2 v_{\mathrm{d}\phi} + e^{\beta_3 \mathrm{v}_\mathrm{d}^2}(\alpha_{0c} + a_0)\eta \dfrac{E_c}{B}\dfrac{r}{R_c}\left(e^{\frac{\omega}{\Omega_i}\nu_{in}t} - 1\right)}{1 + e^{\beta_3 \mathrm{v}_\mathrm{d}^2}(\alpha_{0c} + a_0)\eta\left(e^{\frac{\omega}{\Omega_i}\nu_{in}t} - 1\right)} = \left\{ \begin{array}{l} \beta_2 v_{\mathrm{d}\phi} \text{ for } t \to 0 \\ \dfrac{E_c}{B}\dfrac{r}{R_c} \text{ for } t \to \infty \end{array} \right\} \tag{5.58}$$

in which the second integration in Eq.(G.19) is used. Clearly, $\langle v_\phi \rangle < (E_c/B)(r/R_c)$ is always valid for large t. And,

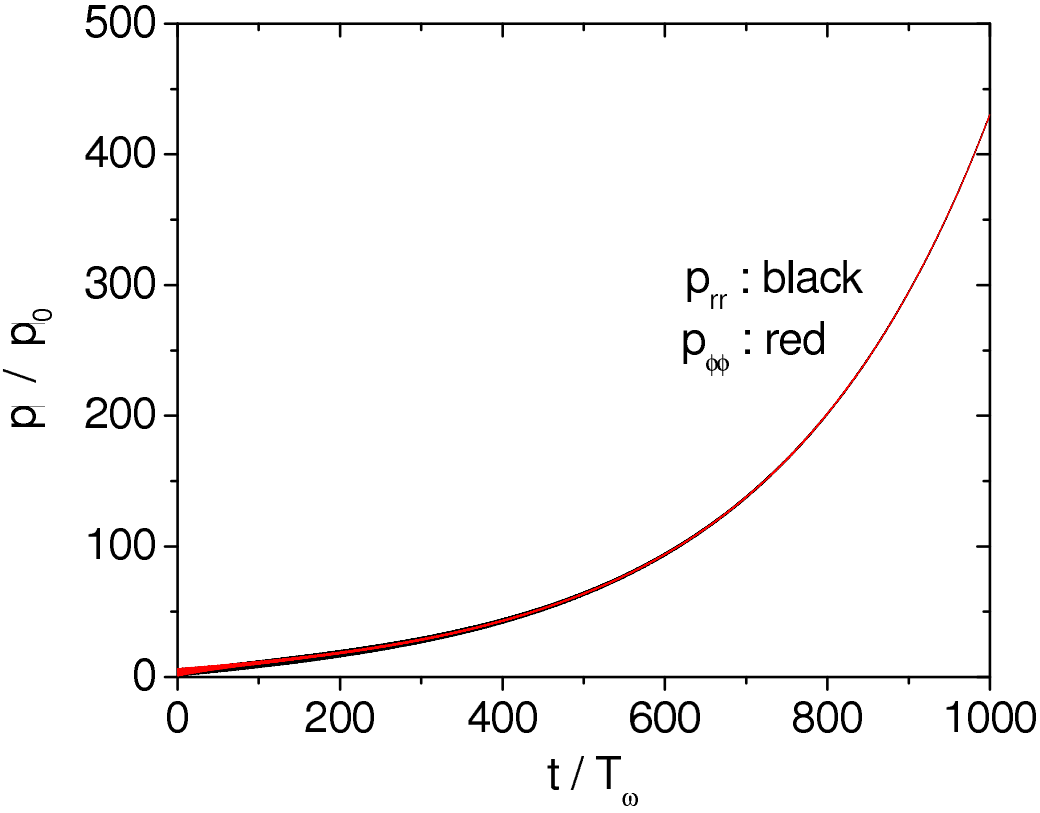

Figure 5.22: Evolution of the ion pressure for $E_c/B = 4$ at $r = 0.5R_c$.

$$\langle v_r^2 \rangle = \frac{(\beta_2 v_{\rm dr})^2 + \dfrac{1}{2(\alpha_{0c}+a_0)}}{1 + e^{\beta_3 \mathbf{v}_{\rm d}^2}(\alpha_{0c}+a_0)\eta\left(e^{\frac{\omega}{\Omega_i}\nu_{in}t} - 1\right)} + \\ + \frac{e^{\beta_3 \mathbf{v}_{\rm d}^2}(\alpha_{0c}+a_0)\eta\left[\dfrac{1}{2}\left(\dfrac{E_c}{B}\dfrac{r}{R_c}\right)^2 + \dfrac{a_1}{2}\right]\left(e^{\frac{\omega}{\Omega_i}\nu_{in}t} - 1\right)}{1 + e^{\beta_3 \mathbf{v}_{\rm d}^2}(\alpha_{0c}+a_0)\eta\left(e^{\frac{\omega}{\Omega_i}\nu_{in}t} - 1\right)} = \\ = \begin{cases} (\beta_2 v_{\rm dr})^2 + \dfrac{1}{2(\alpha_{0c}+a_0)} & \text{for } t \to 0 \\ \dfrac{1}{2}\left(\dfrac{E_c}{B}\dfrac{r}{R_c}\right)^2 + \dfrac{a_1}{2} & \text{for } t \to \infty \end{cases} \tag{5.59}$$

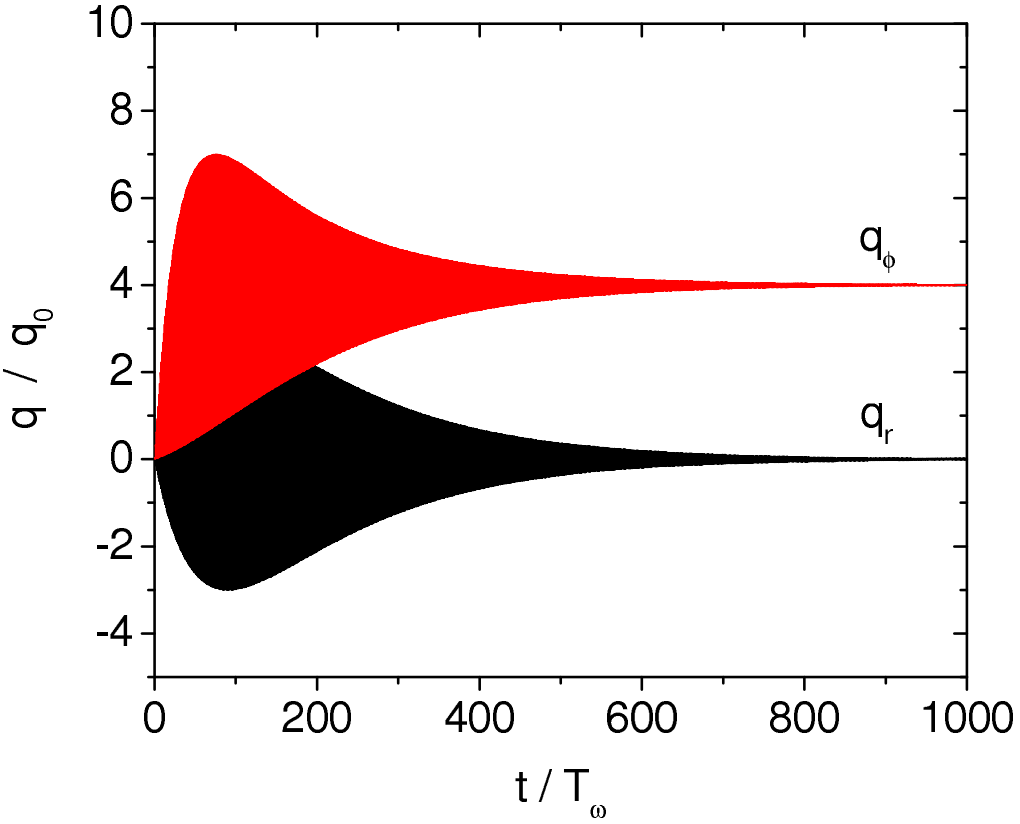

Figure 5.23: Evolution of the ion heat flow for $E_c/B = 4$ at $r = 0.5R_c$.

in which the third integration in Eq.(G.19) is used. And,

$$\langle v_\phi^2 \rangle = \frac{(\beta_2 v_{\mathrm{d}\phi})^2 + \dfrac{1}{2(\alpha_{0c}+a_0)}}{1 + e^{\beta_3 \mathbf{v}_\mathrm{d}^2}(\alpha_{0c}+a_0)\eta\left(e^{\frac{\omega}{\Omega_i}\nu_{in}t} - 1\right)} + \\ + \frac{e^{\beta_3 \mathbf{v}_\mathrm{d}^2}(\alpha_{0c}+a_0)\eta\left[\dfrac{3}{2}\left(\dfrac{E_c}{B}\dfrac{r}{R_c}\right)^2 + \dfrac{a_1}{2}\right]\left(e^{\frac{\omega}{\Omega_i}\nu_{in}t} - 1\right)}{1 + e^{\beta_3 \mathbf{v}_\mathrm{d}^2}(\alpha_{0c}+a_0)\eta\left(e^{\frac{\omega}{\Omega_i}\nu_{in}t} - 1\right)} = \\ = \begin{cases} (\beta_2 v_{\mathrm{d}\phi})^2 + \dfrac{1}{2(\alpha_{0c}+a_0)} & \text{for } t \to 0 \\ \dfrac{3}{2}\left(\dfrac{E_c}{B}\dfrac{r}{R_c}\right)^2 + \dfrac{a_1}{2} & \text{for } t \to \infty \end{cases} \tag{5.60}$$

in which the fourth integration in Eq.(G.19) is used. And,

$$\left.\begin{aligned}\langle v_r^3\rangle &= \frac{(\beta_2 v_{\mathrm{d}r})^3 + \dfrac{3\beta_2 v_{\mathrm{d}r}}{2(\alpha_{0c}+a_0)}}{1+e^{\beta_3 \mathbf{v}_{\mathrm{d}}^2}(\alpha_{0c}+a_0)\eta\left(e^{\frac{\omega}{\Omega_i}\nu_{in}t}-1\right)} = \\ &= \begin{cases} (\beta_2 v_{\mathrm{d}r})^3 + \dfrac{3\beta_2 v_{\mathrm{d}r}}{2(\alpha_{0c}+a_0)} & \text{for } t\to 0 \\ 0 & \text{for } t\to\infty \end{cases}\end{aligned}\right\} \tag{5.61}$$

in which the fifth integration in Eq.(G.19) is used. And,

$$\left.\begin{aligned}\langle v_\phi^3\rangle &= \frac{(\beta_2 v_{\mathrm{d}\phi})^3 + \dfrac{3\beta_2 v_{\mathrm{d}\phi}}{2(\alpha_{0c}+a_0)}}{1+e^{\beta_3 \mathbf{v}_{\mathrm{d}}^2}(\alpha_{0c}+a_0)\eta\left(e^{\frac{\omega}{\Omega_i}\nu_{in}t}-1\right)} + \\ &+e^{\beta_3 \mathbf{v}_{\mathrm{d}}^2}(\alpha_{0c}+a_0)\eta\frac{E_c}{B}\frac{r}{R_c}\left(e^{\frac{\omega}{\Omega_i}\nu_{in}t}-1\right)\cdot \\ &\cdot\frac{\left\{\dfrac{5}{2}\left(\dfrac{E_c}{B}\dfrac{r}{R_c}\right)^2+\dfrac{3}{2}\left[\left(\dfrac{\omega}{\Omega_i}\right)^2-\dfrac{E_c/B}{R_c\Omega_i}\right]\right\}}{1+e^{\beta_3 \mathbf{v}_{\mathrm{d}}^2}(\alpha_{0c}+a_0)\eta\left(e^{\frac{\omega}{\Omega_i}\nu_{in}t}-1\right)} = \\ &= \begin{cases} (\beta_2 v_{\mathrm{d}\phi})^3 + \dfrac{3\beta_2 v_{\mathrm{d}\phi}}{2(\alpha_{0c}+a_0)} & \text{for } t\to 0 \\ \dfrac{E_c}{B}\dfrac{r}{R_c}\left\{\dfrac{5}{2}\left(\dfrac{E_c}{B}\dfrac{r}{R_c}\right)^2+\dfrac{3}{2}\left[\left(\dfrac{\omega}{\Omega_i}\right)^2-\dfrac{E_c/B}{R_c\Omega_i}\right]\right\} & \text{for } t\to\infty \end{cases}\end{aligned}\right\} \tag{5.62}$$

in which the last integration in Eq.(G.19) is used.

Using these velocity moments and employing Eq.(5.40), we can compute transport properties, e.g., average speeds v_{aver} and $v_{\mathrm{ave}\phi}$ (with a unit v_{th}), temperatures T_r and T_ϕ (with a unit T_0), pressures p_r and p_ϕ (with a unit $n_i T_0$), and heat flows q_r and q_ϕ (with a unit mv_{th}^3), as done in Chapter 3. Figs.5.20-5.23 show their evolutions with time at $r/R_c = 0.5$ and $E_c/B = 4$ in 1000 cycles, for convenience to compare with Figs.3.6-3.9. All the bulk parameters run in agreement with the trends shown in Chapter 3, especially when t is long. This is because η plays no role at this time. For short times, several large fluctuations within 400 cycles exhibited in figures of Chapter 3 are compressed to be absent in the present nonuniform initial density case. This is also related to the factor χ given in Eq.(5.55).

5.5 Discussion

In this Chapter, we have solved for the first time a problem for which the initial ion density was not uniform in auroral ion velocity distribution calculations. Under both collision-free and collisional conditions, completely analytical solutions of the distribution and bulk properties have been obtained with two initial ion density profiles and one initial ion density profile, respectively.

In the collision-free case, the distribution function and bulk parameters still maintain the basic pulsating features identified in Chapter 2. However, there are three differences: (1) The distribution function is not restricted only to the shifted Maxwellian distribution. It can be either a pulsating Maxwellian, or, a pulsating horseshoe distribution. (2) Even when the distribution remains a pulsating Maxwellian, the magnitude of the distribution function in velocity space (or, equivalently, the ion density) is smaller than that given in Chapter 2. (3) Both the distribution and the transport parameters depend on the radial position.

In the collisional case, the ion distribution functions and bulk parameters are the same as those obtained in Chapter 3, namely, the dependence on electric field, radial position, and time. However, there are two new features: the magnitude of the distribution function is smaller than in Chapter 3; and the ion density is at present a function of radial position.

The inhomogeneity of the initial ion density certainly influences the ion distribution functions and transport properties. Without doubt, introducing the density inhomogeneity into the Chapter 3 case makes originally complicated solutions more complicated. We have therefore chosen simple profiles of the initial ion density to produce complete analytical results as the first study on practical situations where the inhomogeneous initial plasma density influences measurable distribution functions and bulk parameters. This approach will provide a reference to solve this kind of problems numerically, at least semi-numerically. It also opens the door for developing a data-fitting algorithm for the modeling of measurements obtained via rockets and satellites in real situations.

Chapter 6

Exploring The Connection Between Fluid Equations And The Kinetic Results From Chapter 2

For the purpose of gaining additional insights into the physics, we explore the fluid equations that describe the system explored in Chapter 2, namely, (1) an electric field that is proportional to radius and does not change with time, (2) initially stationary ions with temperature T_0.

In the second part of this Chapter, we explore additional possibilities, namely, situations for which the electric field is not maintained by a constant generator. In particular, we explore situations for which either ions or electrons are allowed to modify the initial electric field. We end by speculating on the kinds of conditions that could lead to the various situations.

6.1 Fluid results when the electric field is constant with time

The momentum equation for ions states that

$$\frac{\partial \mathbf{u}_i}{\partial t} + \mathbf{u}_i \cdot \nabla \mathbf{u}_i = -\frac{1}{\rho_i} \nabla \cdot \mathbb{P} + \Omega_i \frac{\mathbf{E}}{B} + \mathbf{u}_i \times \mathbf{\Omega}_i \tag{6.1}$$

in which $\mathbf{u}_i = \{u_r, u_\phi\}$ is the bulk velocity of ions. In the above equation, $\mathbb{P}$ denotes the pressure tensor. Cylindrical symmetry implies $\partial/\partial\phi = 0$. Also, the electric field is proportional to the radius, namely,

$$\mathbf{E} = E_c \frac{r}{R_c} \hat{\mathbf{e}}_r \tag{6.2}$$

Using

$$\mathbf{u}_i \cdot \nabla \mathbf{u}_i = \{u_r, u_\phi\} \cdot \left\{ \frac{\partial}{\partial r}, \frac{1}{r}\frac{\partial}{\partial \phi} \right\} \mathbf{u}_i = \left\{ u_r \frac{\partial \mathbf{u}_i}{\partial r}, \frac{u_\phi}{r}\frac{\partial \mathbf{u}_i}{\partial \phi} \right\} \tag{6.3}$$

where

$$\frac{\partial \mathbf{u}_i}{\partial r} = \frac{\partial}{\partial r}(u_r \hat{\mathbf{e}}_r + u_\phi \hat{\mathbf{e}}_\phi) = \frac{\partial u_r}{\partial r}\mathbf{e}_r + u_r \frac{\partial \hat{\mathbf{e}}_r}{\partial r} + \frac{\partial u_\phi}{\partial r}\hat{\mathbf{e}}_\phi + u_\phi \frac{\partial \hat{\mathbf{e}}_\phi}{\partial r} = \left\{ \frac{\partial u_r}{\partial r}, \frac{\partial u_\phi}{\partial r} \right\} \tag{6.4}$$

$$\frac{\partial \mathbf{u}_i}{\partial \phi} = \frac{\partial}{\partial \phi}(u_r \hat{\mathbf{e}}_r + u_\phi \hat{\mathbf{e}}_\phi) = u_r \frac{\partial \hat{\mathbf{e}}_r}{\partial \phi} + u_\phi \frac{\partial \hat{\mathbf{e}}_\phi}{\partial \phi} = u_r \hat{\mathbf{e}}_\phi - u_\phi \hat{\mathbf{e}}_r = \{-u_\phi, u_r\} \tag{6.5}$$

and then Eq.(6.3) changes to

$$\mathbf{u}_i \cdot \nabla \mathbf{u}_i = \left\{ u_r \frac{\partial u_r}{\partial r} - \frac{u_\phi^2}{r}, u_r \frac{\partial u_\phi}{\partial r} + \frac{u_r u_\phi}{r} \right\} \tag{6.6}$$

Thus, Eq.(6.1) becomes

$$\left.\begin{aligned} \frac{\partial u_r}{\partial t} + u_r \frac{\partial u_r}{\partial r} - \frac{u_\phi^2}{r} &= -\Omega_i \frac{E_c}{B}\frac{r}{R_c} + \Omega_i u_\phi + \hat{\mathbf{e}}_r \cdot (\nabla \cdot \mathbb{P}) \\ \frac{\partial u_\phi}{\partial t} + u_r \frac{\partial u_\phi}{\partial r} + \frac{u_r u_\phi}{r} &= -\Omega_i u_r + \hat{\mathbf{e}}_\phi \cdot (\nabla \cdot \mathbb{P}) \end{aligned}\right\} \tag{6.7}$$

At this stage, let's do power series expansions for u_r and u_ϕ in powers of r. Due to the fact that the electric field term on the RHS of the upper equation is proportional to r, the valid power is 1 for both u_r and u_ϕ. We then come to the conclusion that $u_r \propto r$ and $u_\phi \propto r$. As a result, we then express

$$u_r = V_r r, \quad \text{and} \quad u_\phi = V_\phi r \tag{6.8}$$

where V_r and V_ϕ are coefficients independent of r. Consequently, Eq.(6.7) becomes

$$\left.\begin{aligned} \frac{\partial V_r}{\partial t} + V_r^2 - V_\phi^2 &= -\frac{\Omega_i}{R_c}\frac{E_c}{B} + \Omega_i V_\phi + \frac{1}{r}\hat{\mathbf{e}}_r \cdot (\nabla \cdot \mathbb{P}) \\ \frac{\partial V_\phi}{\partial t} + 2V_r V_\phi &= -\Omega_i V_r + \frac{1}{r}\hat{\mathbf{e}}_\phi \cdot (\nabla \cdot \mathbb{P}) \end{aligned}\right\} \tag{6.9}$$

in which, by looking for a similar power decomposition in $\mathbb{P}$ as done to Eq.(6.7), we know that either $\nabla \cdot \mathbb{P} \propto r$ or $\nabla \cdot \mathbb{P} = 0$.

Interestingly, if we use Eq.(6.8) in the continuity equation of ions, it turns out to be as follows:

$$\left.\begin{aligned} \frac{\partial n_i}{\partial t} &= -\nabla \cdot (n_i \mathbf{u}_i) = -\frac{1}{r}\frac{\partial}{\partial r}(r n_i u_r) = \\ &= -\frac{1}{r}\frac{\partial}{\partial r}(r^2 n_i V_r) = -2n_i V_r - r V_r \frac{\partial n_i}{\partial r} \end{aligned}\right\} \tag{6.10}$$

The initial condition for n_i is that it is uniform in space at $t = 0$, i.e., n_{i0} is independent of r. Another expansion for n_i in Eq.(6.10) tells us that either $n_i(t)$ is independent of r at any time, including $t = 0$. This agrees with the initial condition. We conclude that

$$\frac{\partial n_i}{\partial t} = -2 n_i V_r \ , \quad \text{or,} \quad n_i(t) = n_{i0} e^{-2\int_0^t V_r(t)\mathrm{d}t} \tag{6.11}$$

As stated above, the components of the divergence of the pressure tensor, $\nabla \cdot \mathbb{P}$, should be zero or proportional to r. The pressure tensor $\mathbb{P}$ is a 3×3 matrix:

$$\mathbb{P} = \begin{pmatrix} p_{rr} & p_{r\phi} & p_{rz} \\ p_{\phi r} & p_{\phi\phi} & p_{\phi z} \\ p_{zr} & p_{z\phi} & p_{zz} \end{pmatrix} \tag{6.12}$$

and the components in three directions of $\nabla \cdot \mathbb{P}$ are as follows:

$$\left.\begin{aligned} (\nabla \cdot \mathbb{P})_r &= \frac{1}{r}\frac{\partial}{\partial r}(r p_{rr}) - \frac{p_{\phi\phi}}{r} \\ (\nabla \cdot \mathbb{P})_\phi &= \frac{1}{r}\frac{\partial}{\partial r}(r p_{r\phi}) + \frac{1}{r}\frac{\partial p_{\phi\phi}}{\partial \phi} + \frac{\partial p_{z\phi}}{\partial z} + \frac{p_{\phi r}}{r} \\ (\nabla \cdot \mathbb{P})_z &= \frac{1}{r}\frac{\partial}{\partial r}(r p_{rz}) + \frac{1}{r}\frac{\partial p_{\phi z}}{\partial \phi} + \frac{\partial p_{zz}}{\partial z} \end{aligned}\right\} \tag{6.13}$$

The ionospheric plasma is so magnetized and so rarified that only the normal viscous stress part (the diagonal elements in $\mathbb{P}$ with the same two indices) are dominant, whileas the shear viscous stress part (off-diagonal elements with two different indices) are often neglected [see, e.g., *Dartevelle* (2003), *Smirnov* (2007)]. Thus, only the thermodynamic pressure components (i.e., $p_{rr} = n_i k_b T_r$ and $p_{\phi\phi} = n_i k_b T_\phi$) are left in $\mathbb{P}$. Also, $\partial/\partial\phi = 0$ due to the cylindrical symmetry. Moreover, we do not consider the changes of components in the z-direction along magnetic field lines and thus $\partial/\partial z = 0$, as adopted in Chapter 2. Therefore, we obtain

$$(\nabla \cdot \mathbb{P})_r = \frac{n_i k_b (T_r - T_\phi)}{r} + \frac{\partial}{\partial r}(n_i k_b T_r), \quad (\nabla \cdot \mathbb{P})_\phi = 0, \quad (\nabla \cdot \mathbb{P})_z = 0 \tag{6.14}$$

In the momentum equation, Eq.(6.9), since the momentum terms are proportional to r, while n_i is independent of r, we require that either (T_r, T_ϕ) be proportional to r^2, or be independent of r. In the latter case, we must impose $T_r = T_\phi$ in order to avoid a $1/r$ term in Eq.(6.9).

Because the initial condition is that $T_{r0} = T_{\phi 0} = T_0$ independent of r, the solution is therefore $T_r = T_\phi$ independent of r.

The above tell us that $T_r = T_\phi$ and is independent of r. But it does not tell us how T_r or T_ϕ changes with time. However, the conservation of entropy in an adiabatic process gives us

$$p_{rr}\rho^{-\gamma} = Const. \ , \quad \text{and,} \quad p_{\phi\phi}\rho^{-\gamma} = Const. \tag{6.15}$$

where $\gamma = 1+2/\iota$ is the ratio of specific heat at constant pressure to that at constant volume and ι is the number of degrees of freedom. In our case, we have two degrees of freedom in the r and ϕ directions. Thus, $\gamma = 2$. Eq.(6.15) then gives

$$n_i T_r = Const. \times n_i^2 \ , \quad \text{and,} \quad n_i T_\phi = Const. \times n_i^2 \tag{6.16}$$

Employing the initial isothermal conditions, $T_{r0} = T_{\phi 0} = T_0$ at $t = 0$ while the ion density is n_{i0}, we obtain

$$\frac{T_r}{T_0} = \frac{T_\phi}{T_0} = \frac{n_i}{n_{i0}} \tag{6.17}$$

This is the same as what was obtained from the kinetic approach in Chapter 2. Note that the above equation is consistent with having T_r and T_ϕ independent of r, since n_i is also independent of r.

We are now left with solving the following momentum equations

$$\left.\begin{aligned} \frac{\partial V_r}{\partial t} + V_r^2 - V_\phi^2 &= -\frac{\Omega_i}{R_c}\frac{E_c}{B} + \Omega_i V_\phi \\ \frac{\partial V_\phi}{\partial t} + 2V_r V_\phi &= -\Omega_i V_r \end{aligned}\right\} \tag{6.18}$$

to reproduce the bulk parameters given in Chapter 2. Define a complex variable, $V = V_r + iV_\phi$ which gives $V^2 = V_r^2 - V_\phi^2 + i2V_rV_\phi$. The sum of the first equation and the product of $i\times$ the second one in Eq.(6.18) gives

$$\frac{\partial V}{\partial t} = -V^2 - i\Omega_i V - \frac{\Omega_i}{R_c}\mathcal{E} \tag{6.19}$$

in which $\mathcal{E} = E_c/B$ is a constant. Noticing that V is only a function of time, we can rewrite Eq.(6.19) as

$$\frac{\mathrm{d}V}{\mathrm{d}t} = -\left[\left(V + i\frac{\Omega_i}{2}\right)^2 + \frac{\Omega_i}{R_c}\mathcal{E} + \left(\frac{\Omega_i}{2}\right)^2\right] \tag{6.20}$$

or

$$\frac{\mathrm{d}\left(V+i\frac{\Omega_i}{2}\right)}{\left(V+i\frac{\Omega_i}{2}\right)^2+\frac{\Omega_i}{R_c}\mathcal{E}+\left(\frac{\Omega_i}{2}\right)^2}=-\mathrm{d}t \tag{6.21}$$

Before integrating this equation, we have to look at the singularities in the complex plane. They are at

$$V=i\frac{\Omega_i}{2}\left[\pm\sqrt{1+\frac{4\mathcal{E}}{R_c\Omega_i}}-1\right] \tag{6.22}$$

We can choose an integration path along a large circle when $V\to\infty$ to integrate above singularities. Thus, there is no residue and we can deal with the integral as if the argument were real. The result of the integration is

$$\frac{1}{\sqrt{\frac{\Omega_i}{R_c}\mathcal{E}+\left(\frac{\Omega_i}{2}\right)^2}}\tan^{-1}\frac{V+i\frac{\Omega_i}{2}}{\sqrt{\frac{\Omega_i}{R_c}\mathcal{E}+\left(\frac{\Omega_i}{2}\right)^2}}=-t+C \tag{6.23}$$

Using the initial condition: $V=0$ at $t=0$, we then find

$$C=\frac{1}{\sqrt{\frac{\Omega_i}{R_c}\mathcal{E}+\left(\frac{\Omega_i}{2}\right)^2}}\tan^{-1}\frac{i\frac{\Omega_i}{2}}{\sqrt{\frac{\Omega_i}{R_c}\mathcal{E}+\left(\frac{\Omega_i}{2}\right)^2}} \tag{6.24}$$

The final solution is therefore

$$V=\frac{\omega}{2}\frac{(\Omega_i^2-\omega^2)\tan\left(\frac{\omega t}{2}\right)+i\omega\Omega_i\left[1+\tan^2\left(\frac{\omega t}{2}\right)\right]}{\omega^2+\Omega_i^2\tan^2\left(\frac{\omega t}{2}\right)}-i\frac{\Omega_i}{2} \tag{6.25}$$

in which $\frac{\omega}{2}=\sqrt{\frac{\Omega_i}{R_c}\mathcal{E}+\left(\frac{\Omega_i}{2}\right)^2}$ is used. This means that we have

$$\left.\begin{aligned} V_r&=-\frac{\omega}{4}\frac{\left[1-\left(\frac{\Omega_i}{\omega}\right)^2\right]\sin\omega t}{\cos^2\left(\frac{\omega t}{2}\right)+\left(\frac{\Omega_i}{\omega}\right)^2\sin^2\left(\frac{\omega t}{2}\right)}\\ V_\phi&=\frac{\Omega_i}{2}\frac{1}{\cos^2\left(\frac{\omega t}{2}\right)+\left(\frac{\Omega_i}{\omega}\right)^2\sin^2\left(\frac{\omega t}{2}\right)}-\frac{\Omega_i}{2}\end{aligned}\right\} \tag{6.26}$$

These expressions can be easily converted to those already given in Chapter 2:

$$\left.\begin{aligned} &\cos^2\left(\frac{\omega t}{2}\right)+\left(\frac{\Omega_i}{\omega}\right)^2\sin^2\left(\frac{\omega t}{2}\right)=1-\frac{1}{2}\left[1-\left(\frac{\Omega_i}{\omega}\right)^2\right](1-\cos\omega t)=a_0 \\ &V_r=-\mathcal{E}\frac{1}{R_c}\frac{1}{a_0}\frac{\Omega_i}{\omega}\sin\omega t=\frac{v_{\mathrm{d}r}}{r}=\frac{u_r}{r} \\ &V_\phi=\mathcal{E}\frac{1}{R_c}\frac{1}{a_0}(\frac{\Omega_i}{\omega})^2\,(1-\cos\omega t)=\frac{v_{\mathrm{d}\phi}}{r}=\frac{u_\phi}{r} \end{aligned}\right\} \quad (6.27)$$

What is more, it is easy to obtain a relation between V_r and a_0 from the above set of equations:

$$V_r=\frac{1}{2a_0}\frac{\mathrm{d}a_0}{\mathrm{d}t}=\frac{1}{2}\frac{\mathrm{d}(\ln a_0)}{\mathrm{d}t} \quad (6.28)$$

From this expression we obtain the ion density by using Eqs.(6.11,6.28), namely,

$$\frac{n_i(t)}{n_{i0}}=e^{-2\int_0^t V_r(t)\mathrm{d}t}=e^{-\int_0^t(\mathrm{d}(\ln a_0)/\mathrm{d}t)\mathrm{d}t}=\frac{1}{a_0} \quad (6.29)$$

which with Eq.(6.17) leads to the result of

$$\frac{n_i}{n_{i0}}=\frac{T_r}{T_0}=\frac{T_\phi}{T_0}=\frac{1}{a_0} \quad (6.30)$$

This is exactly what was obtained in Chapter 2 for the density and the temperature.

In summary, we have shown here that the kinetic solutions of Chapter 2 are describing an adiabatic system that is initially isothermal and at rest. In addition, the changes in the density are due to the fact that $\nabla\cdot\langle\mathbf{v}\rangle$ is constant in space though oscillating in time. The velocity dependence is related to the fact that $E\propto r$ so that both components of the velocity increase linearly with radial distance. What is more, the temperature variation is similar to the density variation with time because the system is adiabatic (no outside heat source or heat flow) and because it has only two degrees of freedom. Finally, the frequency of oscillation is not Ω_i but ω because the Coriolis and centrifugal forces introduce the $V_r^2-V_\phi^2$ and $2V_rV_\phi$ terms in the r and ϕ components of the momentum equations, respectively. Notice that $\omega=\Omega_i$ if we can neglect the nonlinear terms in the momentum equation. These points are reminiscent of the arguments used in Appendix A & B except that we are now using them for the mean flow as opposed to the individual particles.

6.2 Fluid results when the electric field is modified by ions

We now consider a situation for which the fixed voltage generator is replaced by a system where the electrons are introducing a radial electric field, but ions are able by their motions to change the electric field by changing the charge density. The important difference with the previously described system is that in the old system the net electron density would have increased in sync with the ion density to maintain the net electric field. Notice that this mechanism is the way by which electrostatic ion cyclotron waves are generated (just generate a system for which the Coriolis and centrifugal terms are too small to compete with the magnetic force).

In the new system, we have to add the contribution from Gauss's law to relate it to the changing ion density. We have

$$\nabla \cdot \mathbf{E} = \frac{e}{\epsilon_0}(n_i - n_e) \tag{6.31}$$

Since the charge densities are uniform we have

$$\mathbf{E} = E_c \frac{r}{R_c}\hat{\mathbf{e}}_r \tag{6.32}$$

where $E_c = E_c(t)$ is introduced at $t = 0$.

If somehow the electron density is kept fixed, Gauss's law implies next that

$$2\frac{E_c}{R_c} = \frac{e}{\epsilon_0}(n_i - n_{e0}) = \frac{e}{\epsilon_0}\delta n_i \tag{6.33}$$

Even for large electric fields we still have $\delta n_i \ll n_{i0}$. The continuity equation therefore becomes

$$\frac{\partial \delta n_i}{\partial t} = -2n_i(t)V_r \approx -2n_{e0}V_r \tag{6.34}$$

In the previous section, we used n_i on the RHS, and not n_{e0} (or n_{i0}), but here we use the approximation because δn_i is linked to the electric field as given in Eq.(6.33), namely,

$$\frac{\partial \delta n_i}{\partial t} = 2\frac{\partial}{\partial t}\left[\frac{\epsilon_0}{eR_c}E_c(t)\right] \tag{6.35}$$

From Eqs.(6.34,6.35) we obtain

$$\frac{\partial E_c(t)}{\partial t} = -\frac{e n_{e0} R_c}{\epsilon_0} V_r \tag{6.36}$$

Defining $\mathcal{E}(t) = E_c(t)/B$, we have

$$\frac{\partial \mathcal{E}}{\partial t} = -\lambda V_r \;\; ; \;\; \lambda = \frac{e n_{e0} R_c}{\epsilon_0 B} \tag{6.37}$$

The radial component of the momentum equation is given in Eq.(6.18), namely,

$$\frac{\partial V_r}{\partial t} = -\frac{\Omega_i}{R_c}\mathcal{E} - V_r^2 + V_\phi^2 + \Omega_i V_\phi \tag{6.38}$$

Taking $\partial/\partial t$ and using the previous equation, we get

$$\frac{\partial^2 V_r}{\partial t^2} = \lambda \frac{\Omega_i}{R_c} V_r - \frac{\partial}{\partial t}\left(V_r^2 - V_\phi^2 - \Omega_i V_\phi\right) \tag{6.39}$$

However,

$$\lambda \frac{\Omega_i}{R_c} = \frac{e n_{e0} R_c}{\epsilon_0 B}\frac{\Omega_i}{R_c} = \frac{n_{e0} e^2}{\epsilon_0 m_i} = \omega_{pi}^2 \tag{6.40}$$

At this step, using the other momentum equation in Eq.(6.18), we obtain

$$\frac{\partial^2 V_r}{\partial t^2} = -\left(\omega_{pi}^2 + \Omega_i^2\right) V_r - \frac{\partial}{\partial t}\left(V_r^2 - V_\phi^2\right) - 2\Omega_i V_r V_\phi \tag{6.41}$$

A dimensional analysis in terms of a frequency ω gives

$$\omega^2 = \left(\omega_{pi}^2 + \Omega_i^2\right) - i(\omega V_r)\left(1 - \frac{V_\phi^2}{V_r^2}\right) + 2(\Omega_i V_r)\frac{V_\phi}{V_r} \tag{6.42}$$

From this we can see that the two nonlinear terms on the RHS can be neglected if

$$|\omega V_r| \sim |\Omega_i V_r| = \left|\Omega_i \frac{v_{\rm dr}}{r}\right| \sim \left|\Omega_i \frac{E_c/B}{R_c}\right| < |\Omega_i \cdot \Omega_i| = \Omega_i^2 \ll \omega_{pi}^2 + \Omega_i^2 \tag{6.43}$$

That is, if $\omega_{pi}^2 \gg \Omega_i^2$ and $\omega \sim \Omega_i$, the central inequality was already met in Chapter 2, namely, ω and Ω_i are of the same order, and

$$\left|\frac{E_c/B}{R_c \Omega_i}\right| < 1 \tag{6.44}$$

even for very strong cylindrical electric field structures with $E_c/B \sim 2$ km/s and $R_c\Omega_i \sim 3$ km/s. Therefore, the nonlinear terms can be dropped even for these strong fields. This being the case we then get

$$\omega^2 = \omega_{pi}^2 + \Omega_i^2 = \omega_{UH}^2 \quad \text{(ions)} \tag{6.45}$$

Therefore, the oscillation frequency is now at the ion upper-hybrid frequency unless the ion plasma frequency (i.e., the ion density) is very small. However in the latter case we are back to the case discussed in Section 6.1.

6.3 Fluid results when the electric field is modified by electrons

It is also possible that a small number of electrons may be sent down magnetic field lines through precipitation. If the onset of these charges were to be very fast, the ambient electrons would react to the lack of charge neutrality. But the ions have not enough time to respond because of their inertia. In the present case, Poisson's equation becomes

$$2\frac{E_c}{R_c} = \frac{e}{\epsilon_0}(n_{i0} - n_e) \tag{6.46}$$

while all the other equations would be identical to those of the previous section with Ω_e replacing Ω_i and ω_{pe} replacing ω_{pi}. That is to say, the frequency of oscillation would now be the electron upper hybrid frequency, ω_{UH} (electrons).

In both upper hybrid situations discussed in last two sections, the background charges are drawn to (or repelled from) the cylinder. At first, the motion is that of the cyclotron oscillation. However, the electric field is quickly affected by the new charge density and the ambient charges may overshoot but not by much. The situation is very similar to a plasma oscillation with a frequency $\omega_p^2 \gg \Omega^2$. At low densities, the magnetic field is responsible for the return of the charge and the oscillation is then that of electrostatic cyclotron waves. Indeed, the electric field modification is negligible if ω_p^2 is small.

6.4 Lower-hybrid oscillations

If the electric field increases more slowly than the electron upper hybrid period, lower hybrid waves may also be excited. In this case, the description proceeds the same as the previous two sections except that both ions and electrons are reacting to the electric field. Gauss's law now applies to $(\delta n_i - \delta n_e)$, both of which are changing with time.

Take electrons as an example for a discussion. As done in the last Section, we consider the perturbed electron density δn_e (i.e., the electron space-charge density) as a function of time and the background electron density n_{e0} to be uniform in space

and constant in time. Note that $n_e \approx n_{e0}$ due to the very small δn_e. The continuity equation for electrons gives

$$\delta n_e = -2\frac{n_{e0}}{i\omega} V_r^{(e)} \tag{6.47}$$

From the momentum equation, we have, using the same treatment as in the previous subsections:

$$V_r^{(e)} = -\frac{1}{i\omega}\frac{\Omega_e}{R_c}\mathcal{E}\frac{\omega^2}{\Omega^2 - \omega_e^2} \tag{6.48}$$

Thus, the last two equations give

$$\delta n_e = \frac{2n_{e0}}{\omega^2 - \Omega_e^2}\frac{\Omega_e}{R_c}\mathcal{E} \tag{6.49}$$

The ions have a similar density perturbation:

$$\delta n_i = 2\frac{n_{i0}}{\Omega_i^2 - \omega^2}\frac{\Omega_i}{R_c}\mathcal{E} \tag{6.50}$$

Using Eqs.(6.49,6.50) in Gauss's law: $\nabla \cdot \mathbf{E} = \dfrac{e}{\epsilon_0}(\delta n_i - \delta n_e)$, and noticing that $\nabla \cdot \mathbf{E} = -2E_c/R_c$, we obtain

$$\frac{\omega_{pi}^2}{\omega^2 - \Omega_i^2} - \frac{\omega_{pe}^2}{\Omega_e^2 - \omega^2} = 1 \tag{6.51}$$

Applying the condition $\Omega_i \ll \omega \ll \Omega_e$, we then have

$$\omega^2 = \frac{\omega_{pi}^2}{1 + \dfrac{\omega_{pe}^2}{\Omega_e^2}} = \omega_{LH}^2 \tag{6.52}$$

which is the LH frequency. If $\Omega_e \ll \omega_{pe}$, we find

$$\omega_{LH} = \sqrt{\Omega_i \Omega_e} \tag{6.53}$$

under weak magnetic field conditions. In addition, if $\Omega_e \gg \omega_{pe}$,

$$\omega_{LH} = \omega_{pi} \tag{6.54}$$

which appears under strong magnetic field conditions (e.g., pulsar/black-hole plasmas).

6.5 Summary and discussion

Using a fluid formalism, we have established the origin of the oscillations found under the particularly simple situation depicted in Chapter 2. We have found that as long as the electric field could be maintained by a generator so that ion feedbacks could not affect the field the system produced electrostatic ion cyclotron waves that were modified by the Coriolis and centrifugal forces.

We have showed that for similar systems based on uniform cylindrical distributions of charges, the oscillations would become (1) ion upper-hybrid waves if the electron density was not allowed to change; (2) electron upper-hybrid waves if the electrons were fully able to respond to the electric field perturbations; and, (3) lower-hybrid waves if the external field was introduced slowly enough for intermediate frequencies involving both ion and electron electrostatic responses.

Thus, in collision-free situations, much depends on the processes responsible for the introduction of the electric field in the system. For the problem of interest in this thesis, the electron response has to be taken out. This can be done if the electrons are the cause of the electric field. For instance, we could surmise that if high frequency turbulence was affecting the electrons in the process of, say, currents along the magnetic field lines, anomalous resistivity would slow down the electrons, and introduce cylindrical regions of space charge. At this point, all the electrons would be involved in the introduction of the electric field, leaving it to the ions to respond. Under small plasma density conditions (i.e., $\omega_{pi} \ll \Omega_i$), the results of Chapter 2 would automatically apply. The results would also apply if the space charge was introduced as a voltage generator, so that the neutralizing ion effect could not take place. One way or the other, the fact remains that cylindrical electric fields are maintained in the ionosphere, so that something allowing the processes described here has to take place.

Chapter 7

Summary, Conclusion, and Future Work

7.1 Summary of problems addressed in this thesis

This thesis has made progress toward a better understanding of the physics of ion velocity distributions, transport properties, and wave excitation mechanisms in the auroral ionosphere under various perpendicular electric fields (**E**) crossed to the local geomagnetic field (**B**) in a cylindrical geometry. This subject had been studied in detail in the past, but only for situations in which the ambient electric field was homogeneous in space and constant in time after an initial quick transition.

The emphasis of this thesis has been on more realistic general problems when the electric field is inhomogeneous and/or modulated by charged particles. There had only been one study of these problems so far [*St.-Maurice et al.* (1994)] in which the electric field changed linearly in space along a particular direction perpendicular to the local magnetic field. However, in last two decades, space observations via satellites, rockets, and radars, have shown that there are numerous instances of cylindrical space-charge/electric-field arrangements in the auroral ionosphere (such as traveling vortices, auroral rays, and lower-hybrid cavities) in different spatial and temporal scales. This motivated the present study of ions response to electric fields in cylindrically symmetric situations.

Starting from a simple electric field structure which is proportional to the radius, we have used the Boltzmann equation coupled with equations of motion to study the ion kinetics, velocity distribution function, and bulk parameters of the distribution function. Complete analytical solutions have been obtained (Chapter 2). Next, to investigate the effects of ion-neutral collisions on the ion velocity distribution, we

have introduced a relaxation model for collisions so as to obtain complete analytical solutions and gain physical insights into the problem (Chapter 3). Further, under more realistic inhomogeneous electric field structures that were constant in time, we have developed a semi-numerical back-mapping model to calculate the distribution function and transport properties in a number of collision-free cases (Chapter 4). The model developed in that Chapter can be applied to any electric field structures which are either homogeneous or inhomogeneous in space. In a further generalization, we have also relaxed the constraint of uniform initial ion density to the above problems (Chapter 5). As the first step for this study, we have chosen a couple of initial ion density profiles that produced completely analytical solutions under both collision-free (with two profiles) and collisional (with one profile) conditions. Finally, we have employed a fluid formulation to discuss the excitation of ion cyclotron waves, ion upper-hybrid waves, electron upper-hybrid waves, and lower-hybrid waves within the content of our cylindrical geometry and initial conditions (Chapter 6).

7.2 Basic results from the thesis

Non-Maxwellian velocity distribution function and related observable transport parameters (e.g., bulk velocity, temperature, etc.) produced by different auroral electric field structures have been studied since the early seventies. Earlier studies had established that the ion velocity distributions under homogeneous electric fields can differ in important ways from the conventionally assumed Maxwellian (Gaussian) velocity distribution by becoming ring-shaped in velocity space under very strong electric field conditions. By comparison to this homogeneous case, early studies had also shown that the velocity distributions under an inhomogeneous electric field which increases linearly in a specific direction in space were found to be crescent-shaped (as opposed to ring-shaped) in the velocity plane transverse to the magnetic field direction under similarly very strongly driven conditions.

However, the aurora often breaks down into elongated filaments that are aligned with the geomagnetic field. It is natural to infer from this that when important structures are found in the electrostatic fields they, too, will follow a cylindrical

geometry. Our work has been oriented towards these types of ionospheric electric field structures.

Our first study (Chapter 2) acts as the basis of the thesis. We have assumed a simple electric field structure which is "constant" in time, but proportional to the radial position, i.e., a "radially linear" electric field in space. In addition, the initial ion density was assumed "uniform" in space, and we considered only collision-free conditions. We solved the Boltzmann equation by tracking the ions back in time, using the temporal link between the initial position and velocity of an ion and the arbitrary position and velocity at any time. We obtained completely analytical solutions for the ion trajectories and the ion distribution function, in addition to the transport properties everywhere in space and at any time. We found that individual ions gyrate in phase at an effective gyrofrequency (ω) which is different from the conventional magnetic gyrofrequency (Ω_i), while the associated velocity distribution pulsated at a non-steady rate with time. Nevertheless, for an initially uniform Maxwellian velocity distribution, the distribution remained Maxwellian for all the times, although the drift, density and temperature of that distribution kept changing with time but stayed independent of position.

The purpose of Chapter 3 was to elucidate the effects of collisions on the evolution of velocity distributions and bulk parameters in cylindrical situations at lower altitudes. We have selected a relaxation model to replace the Boltzmann collision integral in the Boltzmann equation. This model provides a simple description of ion-neutral interactions that makes it possible to solve the Boltzmann equation entirely analytically. Our calculations showed that collisions drive the velocity distribution to a horseshoe-shaped velocity distribution over long enough times. This feature has been found to extend to any radial positions at which the radially linear electric fields exists. The transition period from pulsating Maxwellians to horseshoe shapes is of the order of one collision time and the transport properties evolve accordingly from oscillating to non-oscillating in the same short time intervals.

In a third part of this thesis, we removed the "radially linear" constraint from the electric field structures (Chapter 4). We solved the problem of an electric field

that could follow any radially nonlinear evolution in space. At this stage, there was no way to seek a generalized approach for complete analytical solutions. We instead developed a back-mapping semi-numerical method based on energy conservation and the equations of motion. We verified first of all the validity of the code by reproducing all the results given in the first study. After that, we calculated the ion velocity distributions and bulk properties under several realistic electric field models. In regimes where the electric field dropped outside a space-charge region, the evolving velocity distribution with time was found to have many possible types of shapes, such as, deformed pancake, horseshoe, teardrop, core-halo, etc. If the electric field dropped sharply on both sides of the boundary of a region, the distribution developped an ear-collar appearance with time. Under all electric field structures, the non-Maxwellian distributions and related transport parameters were localized to the region with an electric field. In this study, we also used a backward ray-tracing technique to find where those ions contributing to a specific distribution point in velocity space came from.

In the fourth part of the thesis, we have relaxed the "uniform" condition from the initial ion density (Chapter 5). The complexity brought about by the new factor is that the initial density, as a function of initial radius (r_0) at t_0, is now linked through r_0 to the phase-space parameters (r, v_r, v_ϕ) at t. We obtained analytical solutions for a couple of initial density profiles as a function of radius. The results were at first sight similar to those for which the ion density was initially uniform. However, the results became strongly radially dependent for the inhomogeneous initial density conditions. This was a common feature in both the collision-free and collisional cases we investigated.

In the collisional case, the ion distribution functions and bulk parameters have the same evolutions as those obtained in Chapter 3, namely, the dependence on the electric field, the radial position, and time. Especially for bulk parameters at $r = 0.5R_c$, their steady-state values are very much the same as those in Chapter 3. However, there are two differences: one is that the magnitude of the distribution function is smaller than in Chapter 3; and the other is that the ion density depends

on the radial position and increases exponentially with time, unlike in Chapter 3.

In the last part of the work, we established a fluid context for our kinetic results and investigated the origin of the velocity oscillations and other results obtained in Chapter 2. We then discussed how different sorts of initial conditions would lead to the excitation of other oscillations in the context of our cylindrical geometry. Not too surprisingly, we identified electrostatic ion cyclotron modes and various hybrid modes where excitation depended on the particular generator and ambient plasma density.

7.3 Future work

The present thesis offers both qualitative and quantitative insights into auroral ion distributions, as well as into their bulk properties as they are driven by different types of electric fields in auroral regions. The work has also been related to the excitations of fundamental plasma oscillations. Still, much work is needed for more complicated situations and to explain important ionospheric phenomena measured by rockets and/or satellites.

For one thing, the thesis work should be extended to tackle an important issue in auroral physics: transverse ion energization and ion outflows in the formation of ion conics in velocity space. The first ion conic was measured by Satellite 1976-65B [*Sharp et al.* (1977)]. In that work, conic H^+ and O^+ ions were detected at about $1R_E$ in the northern dayside polar cusp. Since then, many satellites have observed ion conics in geospace [e.g., *Klumpar* (1986); *Ergun et al.* (2001); *Ergun* (2003); *McFadden et al.* (2003)].

A widely accepted process for the evolution of ion conics was described by, e.g., *Mozer* (1980); *Mozer et al.* (1980); *Gorney et al.* (1985); *Lysak* (1986); *Wu et al.* (2002): at first, some kind of mechanism has to produce transverse ion heating; heated ions are then driven upward by the geomagnetic mirror force which is proportional to the transverse kinetic energy under the conservation of the first adiabatic invariant; the total velocity of the ions takes a conic appearance at higher altitudes; the presence of parallel electric fields may contribute to a more complicated picture

through "a pressure cooker" effect [*Gorney et al.* (1985); *Barakat & Barghouthi* (1994); *Wu* (2000)].

The mechanism underlying the transverse ion heating is not yet clear enough. Wave energization is one possibility, with a term to represent the perpendicular energy gain from the "wave-particle interactions (WPI)" in the conic equations [*Gorney et al.* (1985)]: $\mathrm{d}\mathcal{E}_\perp/\mathrm{d}t|_{\mathrm{WPI}}$. This term has been assumed constant (at 1 eV/s) for protons over the altitude range $0.1R_E < h < 1R_E$, and suggested to scale as $m^{\alpha-1}$ for heavy ions (α is a power-law index from the spectral fit)[*Gorney et al.* (1985); *Lund et al.* (1999)].

However, there are some problems with the WPI explanation. When taking a close look at the measurements of ion energy distributions [*Sckopke et al.* (1983); *Klumpar* (1986); *Moore et al.* (1986)], it was found that (1) a one-to-one correspondence between heated ions and any particular type of plasma waves to heat them is not obtained; (2) the energy is not always transferred from wave(s) to ions, or rather, it can flow from ions to the wave(s); and (3) the interaction of ions with small-scale potential structures (a special form of wave-particle interactions) seems closest to being responsible for the transverse ion heating. These potential structures were described as spikelets (or cavitons) [*Chang* (1993); *McFadden et al.* (1999a,b)]. However, the correlation between the ion energization and the pulsative field strengths is still open [*Schuck & Bonnell* (2003)].

The present work can be used to address the transverse ion energization question. First of all, Chapter 2 tell us that after the electric field is switched on, ions start a cyclotron oscillation (ω) about the $\mathbf{E} \times \mathbf{B}$ drift, with a temperature that changes with time (see Fig.2.3 for a reference). If at some point the electric field is switched off, ions will at first have the drift velocity and temperature reached just before the electric field disappears, but now the mean velocity will start to pulsate around the origin. If the electric field continues to be on and off repeatedly, ions could be heated or accelerated continuously to extraordinary levels (*St.-Maurice* 2006: private communication).

Fig.7.1 describes the above process in two cartoons under two simple electric field

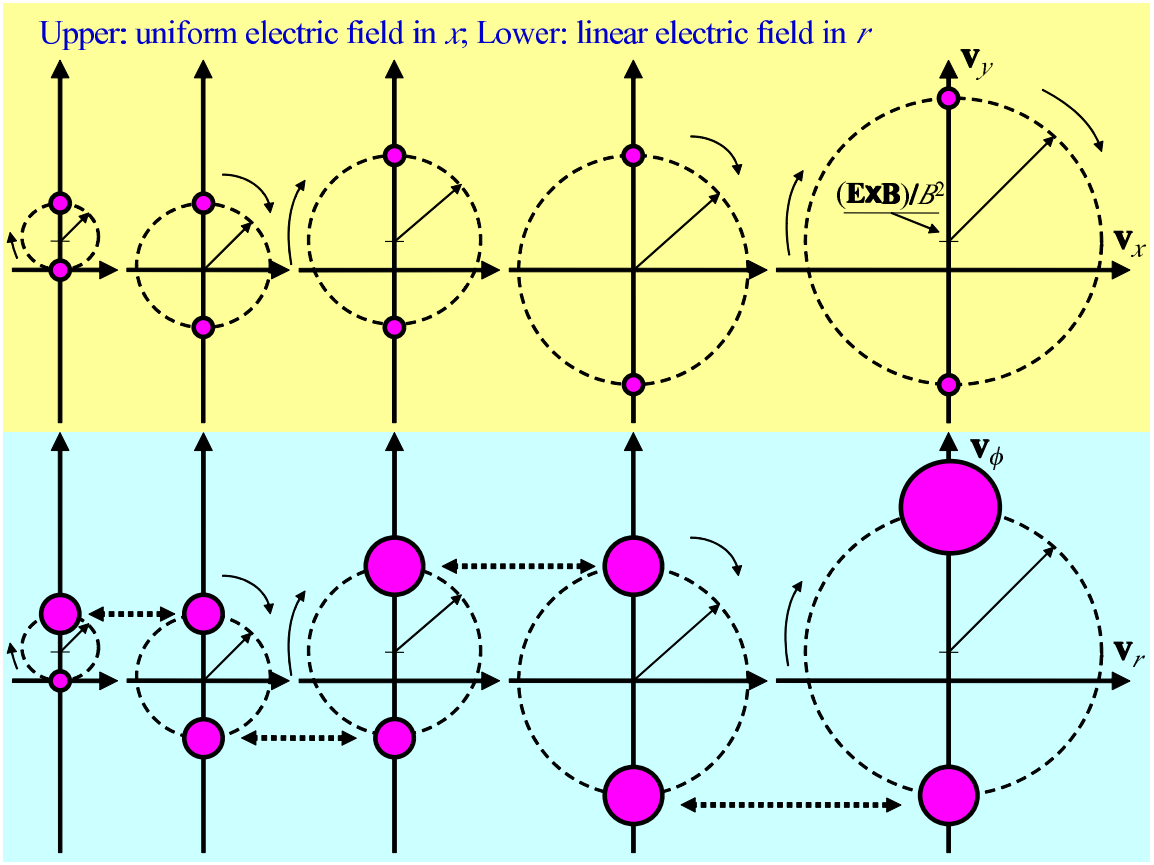

Figure 7.1: Two cartoons showing transverse ion heating by periodically occurring electric fields at frequencies that match the local cyclotron frequency (not a requirement for the heating mechanism, but used to dramatically illustrate the point) (*St.-Maurice* 2006: private communication).

structures taken at the maximum heating efficiency. In the figure, pink-colored areas represent ion distributions. Dotted circles depict the GC orbits around the $\mathbf{E} \times \mathbf{B}$ drift in velocity space. Both pink areas on both sides of the dashed double-head arrows are used to illustrate that at one given moment in time when two different electric field states are formed (on or off). For the uniform electric field case, though the areas are constant (saying both density and temperature are not changing at any stages), the drift velocity increases step by step. So, the kinetic energy goes up. By contrast, under electric field structures that increase linearly with radius, not only

the drift velocity but also the density and temperature of the heated ions become larger and larger. The figure demonstrates that even when the electric field has gone back to zero, we still have cyclotron oscillations but with a new amplitude and a zero mean-velocity. In the process, the mean $\mathbf{v}_\perp$ is never zero (that is, the bulk of the perpendicular flow is not zero).

Of course, we have already seen a more direct alternative mechanism for the formation of conics in Chapter 4 of this thesis, when dealing with electric fields that were not proportional to the radius, particularly near the edge of a negatively charged region. As seen in Fig.4.8, some "halo-core" "halo" populations can be formed and some ions can have very high $\mathbf{v}_\perp$ gains under these conditions. Indeed, many observations of conics see a non-thermal, energetic population outside the colder thermal "core" population [e.g., *Garbe et al.* (1992)].

What was not done in this thesis is a description of the parallel acceleration process under the trigger of strong perpendicular speeds away from the origin in velocity space. The way to tackle this process with kinetic theory is to describe the acceleration produced by small radial component of the magnetic field in situations where the magnetic field is very strong along the z-direction, but nevertheless changes along that direction. From the $\nabla \cdot \mathbf{B} = 0$ condition this means

$$\frac{\partial B_z}{\partial z} = -\frac{1}{r}\frac{\partial}{\partial r}(rB_r) \tag{7.1}$$

For a small $|\partial B_z/\partial z|$, this indicates $|B_r| \ll |B_z|$. The classic mirror force then describes the effect of the B_r field on the perpendicular drift. It is easy to show that the result is an upward expulsion of both ions and electrons if $|B_z|$ is larger at lower altitude.

In mathematical terms, the upward flow is then given by solving the expression

$$\frac{\mathrm{d}v_z^{(1)}}{\mathrm{d}t} = v_\phi^0 \Omega_r \tag{7.2}$$

where superscript "(1)" means perturbation and "(0)" means ambient, and $\Omega_r = |eB_r/m_i| \ll \Omega_z = |eB_z/m_i|$.

It follows from this condition that an ion outflow is triggered during the excitation of a cyclotron wave. More specifically, from Fig.7.1, we know that v_ϕ^0 on average

goes between 0 and $2E_r/B$. Thus, overall, the acceleration is always positive. Nevertheless we could assume to leading order that the region over which the cylindrical electric field is present is not so long that we would need to consider the changes along $\mathbf{B}$ in space. That is to say, $\partial/\partial z$ may not be zero but it is small. Either way, it is reasonable to conclude that ion outflows are triggered by ion cyclotron oscillations. This conclusion is not new, appearing many places in the literature [See the introduction part of *Knudsen et al.* (1998) in details].

Interestingly, even when the applied electric field is off, we have shown that cyclotron oscillations still keep going, but with a new amplitude and a nonzero $\mathbf{v}_\perp$ (yet a zero mean-velocity) as shown by Fig.7.1. In that case, the mirror force can be treated over large distances using the usual adiabatic invariant treatment to describe the "unfolding" of the conics as the upward motion continues.

A related concern is the resolution of observations (with a premise that the sensitivity is sufficiently high) in applying the present work to data analysis. The payloads may be incapable of catching the cyclotron pulsation (except those onboard GEODESIC rocket, FAST and Cluster II satellites). If the resolution is low, the average of data over a period is a better description of what is observed than the instantaneous description we obtained. In this case, it is necessary to obtain the average features of what we have obtained in the thesis so as to provide realistic data-fit modeling.

Let's take the model established in Chapter 2 for example. In that model, the cylinder extends to infinity in the radial direction, and the electric field is proportional to the radius. The ion velocity distribution is given by Eq.(2.16) or Eq.(2.23). We take a time average of the former expression over a full cycle (using $\alpha = \omega t$):

$$\left.\begin{array}{l} \frac{1}{2\pi\omega}\int_0^{2\pi} f_i \mathrm{d}(\omega t) = \frac{1}{2\pi\omega}\int_0^{2\pi} \frac{n_0}{\pi} e^{-(v_r^2+v_\phi^2)} \cdot e^{B_2 \mp B_1 \sin\alpha} \mathrm{d}\alpha = \\ = \frac{n_0}{\pi\omega} e^{B_2-(v_r^2+v_\phi^2)} \cdot I_0(B_1) \end{array}\right\} \tag{7.3}$$

Clearly, this is a horseshoe-shaped distribution in the collision-free case, similar to the result of the collisional part of the ion velocity distribution given in Chapter 3. This time-averaging result tells us that a horseshoe-shaped measurement may indicate that the observed distribution is at the origin of the cyclotron waves.

A further point to extend the thesis work is to elucidate the generation mechanism of the broadband extremely low-frequency (BBELF) oscillations. In Chapter 2 and 6, we have explained the mechanism of the excitation of cyclotron waves under electric field structures which are proportional to radius. Given that outside the center of a charged cylinder where the electric field is not proportional to the radial position, as shown in Chapter 4, we might expect a broad range of frequencies in the vicinity of the (quasi-)cyclotron frequencies. Could this be related to the excitation of BBELF waves?

Of course, there are limitations to what can be done using the approach taken in the present thesis. The most stringent condition imposed in the present work is the lack of time dependence in the driving electric fields. The implicit assumption here is that the electric field is constant over several ion cyclotron oscillations. Also, in the collisional case, the ion (and electron) densities are found to increase exponentially with time because we assume that the mechanism behind the production of a negative space charge induces a fixed potential: in reality the Pedersen currents could well lower the voltage instead of triggering an increase in the local plasma density. Finally, many of the distributions that we have obtained are potentially unstable. Whether or not the distributions that have been calculated in this thesis will survive depends entirely on the growth rate of the instabilities, which has to be compared with the rate at which the distribution functions are shaped by the kinetic processes discussed in this thesis.

Other aspects worth of investigation in the future are the magnetic perturbations produced by the ion motion that we have obtained, particularly in cases for which there is a lot of coherence in the ion motion. The work should also be applied to the laboratory and space-borne data situations.

Bibliography

Akasofu S.-I. (1977), Physics of magnetospheric substorms, Dordrecht, Holland; Boston: D. Reidel.

Akasofu S.-I. (1981a), Energy coupling between the solar wind and the magnetosphere, *Space Sci. Rev.*, *28*(2), 121-190.

Akasofu S.-I. (1981b), The aurora: an electrical discharge phenomenon surrounding the Earth, *Rep. Prog. Phys.*, *44*(10), 1123-1149.

Albert R. (1967), Nearly monoenergetic electron fluxes detected during a visible aurora, *Phys. Rev. Lett.*, *18*, 369C372.

Alexeev I. I., Y. I. Feldstein, R. A. Greenwald (1997), Convection vortex at dayside of high latitude ionosphere, *Phys. Chem. Earth*, *22*(7-8), 691-696.

Alfvén H. (1958), On the theory of magnetic storms and aurorae, *Tellus*, *2*(10), 104-116.

Anastasiadis A., I. A. Daglis, and C. Tsironis (2004), Ion heating in an auroral potential structure, *Astron. Astrophys.*, *419*, 793-799.

Andre M. and T. Chang (1994), Ion heating perpendicular to the magnetic field, *Scientific Rep.* (Center for Space Research, MIT), *2*, 1-37.

Banaszkiewicz M., and W.-H. Ip (1993), The velocity distribution functions of oxygen and sulphur ions in the Io plasma torus, *Adv. Space Res.*, *13*(10), 331-335.

Barakat A. R., and I. A. Barghouthi (1994), The effect of wave-particle interactions on the polar wind O^+, *Geophys. Res. Lett.*, *21*(21), 2279-2282.

Baranoski G. V. G., J. G. Rokne, P. Shirley, et al. (2003), Simulating the aurora, *J. Visual. Comput. Animat.*, *14*, 43-59.

Bernhardt P. A. (2006), Effects of ion composition and velocity distributions on incoherent scatter ion-line spectra, *Polar Aeronomy and Radio Science Summer School*, Fairbanks, Alaska.

Bernhardt P. A., P. J. Erickson, F. D. Lind, et al. (2005), Artificial disturbances of

the ionosphere over the Millstone Hill incoherent scatter radar from dedicated burns of the space shuttle orbital maneuver subsystem engines, *J. Geophys. Res.*, *110*, A05311.

Bernstein I. B. (1964), Kinetic theory of gases, the Fokker-Planck equation, transport coefficients in a plasma, *Lecture Notes*, Princeton University.

Bhatnagar P. L., E. P. Gross, and M. Krook (1954), A model for collision processes in gases, I. Small amplitude processes in charged and neutral one-component systems, *Phys. Rev.*, *94*, 511-525.

Bock B. J. J. (2005), Study of lower-hybrid cavities detected by the GEODESIC and OEDIPUS-C sounding rockets, *M.Sc. Thesis*, University of Calgary.

Burchill J. K., D. J. Knudsen, B. J. J. Bock, et al. (2004), Core ion interactions with BBELF, lower hybrid, and Alfvén waves in the high-latitude topside ionosphere, *J. Geophys. Res.*, *109*, A01219.

Carlson C. W., J. P. McFadden, R. E. Ergun, et al. (1998), FAST observations in the downward auroral current region: Energetic upgoing electron beams, parallel potential drops, and ion heating *Geophys. Rev. Lett.*, *25*, 2017-2020.

Chang T. (1993), Lower-hybrid collapse, caviton turbulence, and charged particle energization in the topside aurora1 ionosphere and magnetosphere, *Phys. Fluids B*, *5*(7), 2646-2656.

Chang T., G. B. Crew, J. M. Retterer, et al. (1989), Ion conics and counterstreaming electrons generated by lower hybrid waves in the Earth's magnetosphere, *IEEE Tran. Plasma Sci.*, *17*(2), 186-195.

Cole K. D. (1971), Atmospheric excitation and ionization by ions in strong auroral and man-made electric fields, *J. Atmo. Terr. Phys.*, *33*, 1241-1249.

Cole K. D. (1976), Effects of crossed magnetic and spatially dependent electric fields on charged particles motion, *Planet. Space Sci.*, *24*, 515-518.

Cranmer S. R. (2002), Solar wind acceleration in coronal holes, in: *ESA SP-508*, Proc. of the SOHO-11 symposium: From solar minimum to solar maximum, Davos, Switzerland, 361-366.

Curtis S. A. (2005), The plasma universe, *Lecture Notes*, International Space University, 2005.

Danielides M. A., and A. Kozlovsky (2001), Aurora vortex structures as a result of disturbed geomagnetic conditions, in *The Outer Heliosphere: The Next Frontiers*,

Eds.: K. Scherer, Horst Fichtner, Hans Jörg Fahr, and Eckart Marsch, *COSPAR* Colloquiua Series, *11*, Amsterdam: Pergamon Press.

Dartevelle S. (2003), Numerical and granulometric approaches to geophysical granular flows, *Ph.D. thesis*, Michigan Technological University.

Date H., and M. Shimozuma (2001), Boltzmann equation description of electron transport in an electric field. with cylindrical or spherical symmetry, *Phys. Rev. E*, *64*, 066410.

Davidson R. C. (2001), Physics of nonneutral plasmas, Imperial College Press, London, and, World Scientific, Singapore.

Drayton R. (2006), Study of SAPS-like flows with the King Salmon SuperDARN radar, *Master Thesis*, University of Saskatchewan.

Dungey J. W. (1961), Interplanetary magnetic field and the auroral zones, *Phys. Rev. Lett.*, *6*, 47-48.

Earle G. D., M. C. Kelley, G. Ganguli (1989), Large velocity shears and associated electrostatic waves and turbulence in the auroral F region, *J. Geophys. Res.*, *94*(1), 15,321-15,333.

Ergun R. (2003), Auroral Particle Acceleration by Strong Double Layers, *45th Annual Meeting of the Division of Plasma Physics*, *Meeting ID: DPP03*, Albuquerque, New Mexico.

Ergun R. E., C. W. Carlson, J. P. McFadden, et al. (2000), Parallel electric fields in discrete arcs, *Geophys. Res. Lett.*, *27*(24), 4053-4056.

Ergun R. E., Y.-J. Su, L. Andersson, et al. (2001), Direct observation of localized parallel electric fields in a space plasma, *Phys. Rev. Lett.*, *87*(4), 045003.

Evans D. S. (1974), Precipitation electron fluxes formed by a magnetic field aligned potential difference, *J. Geophys. Res.*, *79*, 2853-2858.

Frank L. A., and W. R. Paterson (2000), Return to Io by the Galileo spacecraft: plasma observations, *J. Geophys. Res.*, *105*, 25,363-25,378.

Ganguli G., Y. C. Lee, and P. J. Palmadesso (1988), Kinetic theory for electrostatic waves due to transverse velocity shears, *Phys. Fluids*, *31*(4), 823-838.

Garbe G. P., R. L. Arnold, T. E. Moore, et al. (1992), Observations of transverse ion acceleration in the topside auroral ionosphere, *J. Geophys. Res.*, *97*(A2), 1257-1269.

Gartenhaus S. (1964), Elements of plasma physics, Rinehart and Winston Inc., New

York.

Gorney D. J., Y. T. Chiu, and D. R. Croley (1985), Trapping of ion conics by downward parallel electric fields, *J. Geophys. Res.*, *90*, A5, 4205-4210.

Haerendel G., E. Rieger, A. Valenzuela, et al. (1976), First observation of electrostatic acceleration of barium ions into the magnetosphere, in: *European Programmes on sounding-rocket and balloon research in the auroral zone*, 203-211.

Hesse M., J. Birn, and R. A. Hoffman (1997), On the mapping of ionospheric convection into the magnetosphere, *J. Geophys. Res.*, *102*(A5), 9543-9551.

Hoffman R. and D. Evans (1968), Field-aligned electron bursts at high latitudes observed by OGO 4, *J. Geophys. Res.*, *73*, 6201C6214.

Huang C.-S., G. J. Sofko, K. A. McWilliams, et al. (1998), SuperDARN observations of quasi-stationary mesoscale convection vortices in the dayside high-latitude ionosphere, *J. Geophys. Res.*, *103*(A12), 29,239-29,252.

Humphries (Jr.) S. (2002), Charged particle beams: 2. Phase-space description of charged particle beams, John Wiley and Sons.

Israelevich P. L. (2006), Space plasma physics, *Lecture notes*, Department of Geophysics and Planetary Sciences, Tel Aviv University.

Janhunen P., A. Olsson, and H. Laakso (2004), The occurrence frequency of auroral potential structures and electric fields as a function of altitude using Polar/EFI data, *Ann. Geophys.*, *22*(4), 1233-1250.

Kagan L. M., and J.-P. St.-Maurice (2005), Origin of type-2 thermal-ion upflows in the auroral ionosphere, *Ann. Geophys.*, *23*, 13-24.

Kan J. R., and S.-I. Akasofu (1989), Electrodynamics of solar wind-magnetosphere-ionosphere interactions, *IEEE Trans. Plasma Sci.*, *17*(2), 83-108.

Kelley M. C., and R. A. Heelis (1989), The Earth's ionosphere: plasma physics and Electrodynamics, Academic Press, San Diego, California.

Kintner P. M. (1980), On the distinction between electrostatic ion cyclotron waves and ion cyclotron harmonic waves, *Geophys. Res. Lett.*, 7(8), 585-588.

Klumpar D. M. (1986), A digest and comprehensive biblography on transverse auroral ion acceleration, *Geophys.Mono.*, *38*: Ion Acceleration in the Magnetosphere and Ionosphere, Eds.: Tom Chang (Editor-in-Chief), M.K. Hudson, J.R. Jasperse, R.G. Johnson, P.M. Kintner, M. Schulz (Co-Editors), AGU, Washington, D.C., 389-398.

Knudsen D. J., J. H. Clemmons, and J.-E. Wahlund (1998), Correlation between core ion energization, suprathermal electron bursts, and broadband ELF plasma waves, *J. Geophys. Res.*, *103*(A3), 4171-4186.

Knudsen D. J., B. J. J. Bock, S. R. Bounds, et al. (2004), Lower-hybrid cavity density depletions as a result of transverse ion acceleration localized on the gyroradius scale, *J. Geophys. Res.*, *109*, A04212.

Lockwood M., B. J. I. Bromage, R. B. Horne, et al. (1987), Non-Maxwellian ion velocity distributions observed using EISCAT, *Geophys. Res. Lett.*, *14*, 111-114.

Loranc M., and J.-P. St.-Maurice (1994), A time-dependent gyro-kinetic model of thermal ion upflows in the high-latitude F region, *J. Geophys. Res.*, *99*(A9), 17429-17451.

Lund E. J., E. Möbius, R. E. Ergun, et al. (1999), Mass-dependent effects in ion conic production: the role of parallel electric fields, *Geophys. Res. Lett.*, *26*(24), 3593-3596.

Lundin R., and A. Guglielmi (2006), Ponderomotive forces in cosmos, *Space Sci. Rev.*, 10.1007/s11214-006-8314-8, 1-111.

Lyon J. G. (2000), The solar wind-magnetosphere-ionosphere system, *Science*, *288*(16), 1987-1991.

Lysak R. L. (1986), Ion acceleration by wave-particle interaction, in: Ion acceleration in the magnetosphere and ionosphere, *AGU Geophys. Mono.*, *38*, 261-270.

Marklund G., I. Sandahl, and H. Opgenoorth (1982), A study of the dynamics of a discrete auroral arc, *Planet. Space Sci.*, *30*(2), 179-197.

McFadden J. P., C. W. Carlson, and R. E. Ergun (1999a), Microstructure of the auroral acceleration region as observed by FAST, *J. Geophys. Res.*, *104*, 14,453-14,480.

McFadden J. P., C. W. Carlson, R. E. Ergun, et al. (1999b), Ion and electron characteristics in auroral density cavities associated with ion beams: No evidence for cold ionospheric plasma, *J. Geophys. Res.*, *104*(A7), 14671-14682.

McFadden J. P., C. W. Carlson, R. E. Ergun, et al. (2003), FAST observations of ion solitary waves, *J. Geophys. Res.*, *108*(A4), 8018.

McIlwain C.E. (1960), Direct measurement of particles producing visible aurorae, *J. Geophys. Res.*, *65*, 2727-2747.

Meziane K., W. Wilber, A. M. Hamza, et al. (2006), Upstream field-aligned beams:

results from Cluster, in: *ESA SP-598*, Proc. of Cluster and Double Star symposium, 5th Anniversary of Cluster in Space, Noordwijk, Netherlands, 1-5.

Mintzer D. (1965), Generalized orthogonal polynomial solutions of the Boltzmann equation, *Phys. Fluids*, *8*, 1076-1090.

Miyake W., T. Mukai, and N. Kaya (1996), On the origins of the upward shift of elevated (bi-modal) ion conics in velocity space, *J. Geophys. Res.*, *101*, 26,961-26,970.

Mizera P., D. Gorney, and J. Fennell (1982), Experimental verification of an S-shaped potential structure, *J. Geophys. Res.*, *87*, 1535-1539.

Moore T. E., J. H. Waite (Jr.), M. Lockwood, et al. (1986), Observations of coherent transverse ion acceleration, *Geophys.Mono.*, *38*: Ion Acceleration in the Magnetosphere and Ionosphere, Eds.: Tom Chang (Editor-in-Chief), M. K. Hudson, J. R. Jasperse, R. G. Johnson, P. M. Kintner, M. Schulz (Co-Editors), AGU, Washington, D.C., 50-55.

Moore T. E., M. O. Chandler, C. J. Pollock, et al. (1996), Plasma heating and flow in an auroral arc, *J. Geophys. Res.*, *101*(A3), 5279-5298.

Mozer F. S. (1980), On the lowest-altitude S3-3 observations of electrostatic shocks and parallel electric fields, *Geophys. Res. Lett.*, *7*, 1097-1098.

Mozer F., C. Cattell, R. Lysak, et al. (1980), Satellite measurements and theories of low altitude auroral particle acceleration, *Space Sci. Rev.*, *27*, 155-213.

Mozer F. S., and A. Hull (2001), Origin and geometry of upward parallel electric fields in the auroral acceleration region: Insights from the polar spacecraft, *J. Geophys. Res.*, *106*(A4), 5763-5778.

Ott E., and D. T. Farley (1975), Microinstabilities and the production of short-wavelength irregularities in the auroral F region, *J. Geophys. Res.*, *80*, 4599-4602.

Paschmann G., S. Haaland, R. A. Treumann (2003), Auroral plasma physics, Springer.

Pécseli H. L., B. Lybekk, J. Trulsen, et al. (1997), Lower-hybrid wave cavities detected by instrumented spacecrafts, *Plasma Phys. Cont. Fusion*, *39*(5A), A227-236.

Pietrowski D., K. A. Lynch, R. B. Torbert, et al. (1999), Multipoint measurements of large DC electric fields and shears in the auroral zone, *Geophys. Res. Lett.*, *26*(22), 3369-3372.

Raman R. S. V. (1980), Incoherent scattering of radar waves in the auroral ionosphere, *Ph.D. thesis*, University of Michigan.

Raman R. S. V., J.-P. St.-Maurice, and R. S. B. Ong (1981), Incoherent scattering of radar waves in the auroral ionosphere, *J. Geophys. Res.*, *86*, 4751-4762.

Ratcliffe J. A. (1972), An introduction to the ionosphere and magnetosphere, London: Cambridge University Press.

Reiff P. H., and J. L. Burch (1985), IMF B_y-dependent plasma flow and Birkeland currents in the dayside magnetosphere - 2. A global model for northward and southward IMF, *J. Geophys. Res.*, *90*(A2), 1595-1609.

Rich F. J., and M. Hairston (1994), Large-scale convection patterns observed by DMSP, *J. Geophys. Res.*, *99*(A3), 3827-3844.

Roig F. S., and J. E. Schoutens (1986), Remarks on the use of Boltzmann's equation for electrical conduction calculations in metal matrix and in situ composites, *J. Mater. Sci.*, *21*, 2767-2770.

Rothwell P. L., Silevitch M. B., L. P. Block, et al. (1992), Acceleration and stochastic heating of ions drifting through an auroral arc, *J. Geophys. Res.*, *97*, 19,333-19,339.

Rothwell P. L., M. B. Silevitch, L. P. Block, et al. (1995), Particle dynamics in a spatially varying electric field, *J. Geophys. Res.*, *100*, 14,875-14,886.

Ruohoniemi J. M., and R. A. Greenwald (1996), Statistical patterns of high-latitude convection obtained from Goose Bay HF radar observations, *J. Geophys. Res.*, *101*, 21,743-21,763.

Schmidt G. (1979), Physics of high temperature plasmas (second edition), Academic Press, New York.

Schuck P. W., and J. W. Bonnell (2003), Ray trajectories of lower hybrid solitary structures, *J. Geophys. Res.*, *108*(A5), 1175.

Schuck P. W., J. W. Bonnell, and P. M. Kintner (Jr.) (2003), A review of lower hybrid solitary structures, *IEEE Trans. Plasma Sci.*, *31*, 1125-1177.

Schunk R. W., and F. A. Nagy (2000), Ionospheres: physics, plasma physics, and chemistry, *(Cambridge Atmospheric and Space Science Series)*, Cambridge University Press.

Schunk R. W., and J. C. G. Walker (1972), Ion velocity distributions in the auroral ionosphere, *Planet. Space Sci.*, *20*, 2175-2191.

Sckopke N., G. Paschmann, S. J. Bame, et al. (1983), Evolution of ion distributions across the nearly perpendicular bow shock–Specularly and non-specularly reflected-

gyrating ions, *J. Geophys. Res.*, *88*, 6121-6136.

Sckopke N., G. Paschmann, A. L. Brinca, et al. (1990), Ion thermalization in quasi-perpendicular shocks involving reflected ions, *J. Geophys. Res.*, *95*(A5), 6337-6352.

Sharp R. D., R. G. Johnson, and E. G. Shelley (1977), Observations of an ionospheric acceleration mechanism procucing energetic (keV) ions primarily normal to the geomagnetic field direction, *J. Geophys. Res.*, *82*, 3324-3328.

Smirnov B. M. (2007). Plasma processes and plasma kinetics, *Wiley-VCH Verlag GmbH & Co. kGaA*, Weinheim.

Space Physics Group (2006), Space Physics Textbook, *http://www.oulu.fi/∼spaceweb/textbook/*, Oulu, Finland.

Stefflˆ A. J. (2005), The Io plasma torus during the Cassini encounter with Jupiter: temporal, radial and azimuthal variations, *Ph.D. thesis*, University of Colorado.

St.-Maurice J.-P., and R. W. Schunk (1973), Auroral ion velocity distributions using a relaxation model, *Planet. Space Sci.*, *21*, 1115-1130.

St.-Maurice J.-P., and R. W. Schunk (1974), Behavior of ion velocity distributions for a simple collision model, *Planet. Space Sci.*, *21*, 1-18.

St.-Maurice J.-P., W. B. Hanson, and J. C. G. Walker (1976), Retarding potential analyzer measurement of the effect of ion-neutral collisions on the ion velocity distribution in the auroral ionosphere, *J. Geophys. Res.*, *81*(31), 5438-5446.

St.-Maurice J.-P. (1978), On a mechanism for the formation of VLF electrostatic emissions in the high latitude F region, *Planet. Space Sci.*, *26*, 801-816.

St.-Maurice J.-P., and R. W. Schunk (1979), Ion velocity distributions in the high latitude ionosphere, *Rev. Geophys. and Space Phys.*, *17*, 99-134.

St.-Maurice J.-P., E. Winkler, and A. M. Hamza (1994), Ionospheric ion velocity distributions and associated transport properties in the presence of auroral electric field gradients, *J. Geophys. Res.*, *99*, 19,527-19,548.

St.-Maurice J.-P. (1998), Non-Maxwellian ionospheric velocity distributions in large departures from thermodynamic equilibrium, *Phys. in Canada*, *98*, 302-315.

St.-Maurice J.-P. (2006), *private communication.*

Swift D. W. (1975), The effect of electric fields and ion-neutral collisions on Thomson scatter spectra, *J. Geophys. Res.*, *80*(1), 4380-4382.

Takahashi T., K. Morohashi, N. Iwasawa, et al. (2004), Kinetic simulation for infinitely long cylindrical high-beta plasma with field-null surface, *J. Plasma Fusion Res. Series*, *6*, 485-488.

Vandenplas P. E., and R. W. Gould (1964), Equations of a hot inhomogeneous plasma model-I: resonance frequencies of a cylindrical plasma column, *Plasma Phys. (J. Nucl. Energy Part C)*, *6*, 449-458.

Vogelsang H., H. Lühr, H. Voelker, et al. (1993), An ionospheric travelling convection vortex event observed by ground-based magnetometers and by VIKING, *Geophys. Res. Lett.*, *20*, 2343-2346.

Whealton J. H., and S.-B. Woo (1971), Ion velocity distribution of a weakly ionized gas in a uniform electric field of arbitrary strength, *Phys. Res. A*, *6*(6), 2319-2325.

Winkler E., J.-P. St.-Maurice, and A. R. Barakat (1992), Results from improved Monte Carlo calculations of auroral ion velocity distributions, *J. Geophys. Res.*, *97*(A6), 8399-8423.

Wu X.-Y. (2000), Auroral ionospheric ion upflows and outflows: Satellite observations and dynamic fluid-kinetic simulations, *Ph.D. thesis*, University of Alabama (Huntsville).

Wu X.-Y., J. L. Horwitz, and J.-N. Tu (2002), Dynamic fluid kinetic (DyFK) simulation of auroral ion transport: Synergistic effects of parallel potentials, transverse ion heating, and soft electron precipitation, *J. Geophys. Res.*, *107*(A10), 1283.

Yau A. W., W. B. Whalen, W. K. Peterson, et al. (1984), Distribution of upflowing ionospheric ions in the high-altitude polar cap and auroral ionosphere, *J. Geophys. Res.*, *89*, 5507-5522.

Yeh H.-C. B. (1982), Parallel electric field on auroral magnetic field lines, *Ph.D. thesis*, Rice University.

Yermolaev I., A. O. Fedorov, O. L. Vaisberg, et al. (1997), Ion distribution dynamics near the Earth's bow shock: first measurements with the 2D ion energy spectrometer CORALL on the INTERBALL/Tail-probe satellite, *Ann. Geophys.*, *15*(5), 533-541.

Appendix A

Rotating Frame Description

In the absolute (non-inertial) frame of reference, let us express the ion acceleration and velocity using the notation $\mathrm{d}^2\mathbf{r}/\mathrm{d}t^2$ and $\mathrm{d}\mathbf{r}/\mathrm{d}t$, respectively. In this appendix, we choose to express the ion motion instead in a rotating frame that rotates about the axis of the charged cylinder. We apply a constant angular velocity $\vec{\omega}_r$ relative to the absolute frame. In the rotating frame, the ion acceleration and velocity will be denoted by $\ddot{\mathbf{r}}$ and $\dot{\mathbf{r}}$, respectively.

As stated in the text, in the absolute frame of reference, the equation of ion motion (in dimensional form) is given by

$$\frac{\mathrm{d}^2\mathbf{r}}{\mathrm{d}t^2} = -\Omega_i \frac{E_c}{B}\frac{\mathbf{r}}{R_c} + \frac{\mathrm{d}\mathbf{r}}{\mathrm{d}t} \times \mathbf{\Omega}_i \tag{A.1}$$

in which $\mathbf{\Omega}_i = e\mathbf{B}/m_i$ and $\Omega_i = |\mathbf{\Omega}_i|$. In the rotating frame of reference, Eq.(A.1) becomes

$$\ddot{\mathbf{r}} + 2\vec{\omega}_r \times \dot{\mathbf{r}} + \vec{\omega}_r \times (\vec{\omega}_r \times \mathbf{r}) = -\Omega_i \frac{E_c}{B}\frac{\mathbf{r}}{R_c} + (\dot{\mathbf{r}} + \vec{\omega}_r \times \mathbf{r}) \times \mathbf{\Omega}_i \tag{A.2}$$

or

$$\ddot{\mathbf{r}} + (2\vec{\omega}_r + \mathbf{\Omega}_i) \times \dot{\mathbf{r}} = -\vec{\omega}_r \times (\vec{\omega}_r \times \mathbf{r}) - \Omega_i \frac{E_c}{B}\frac{\mathbf{r}}{R_c} + (\vec{\omega}_r \times \mathbf{r}) \times \mathbf{\Omega}_i \tag{A.3}$$

We now choose the direction of $\vec{\omega}_r$ to be along the magnetic field, which means that the rotation is proceeding in the same direction as the $\mathbf{E} \times \mathbf{B}$ direction. Next we choose to adjust that frequency so that the right-hand-side of Eq.(A.3) is equal to zero. Thus, two vector equations are produced. The first one is an equation about ω_r itself (a positive value has to be assumed), coming from the balance on the right-hand-side. For positive ω_r this gives:

$$\left(\omega_r^2 + \Omega_i\omega_r - \Omega_i \frac{E_c}{B}\frac{1}{R_c}\right)\mathbf{r} = 0 \quad \Rightarrow \quad \omega_r = \frac{\Omega_i}{2}\left(\sqrt{1 + 4\frac{E_c/B}{R_c\Omega_i}} - 1\right) \tag{A.4}$$

The meaning of ω_r is made clear once we consider small values of the parameter $(E_c/B)/(R_c\Omega_i)$. It is easy to show in this case that $\omega_r \sim (E_c/B)/R_c$. Thus, the period $2\pi/\omega_r$ is equal to the time it takes for an $\mathbf{E} \times \mathbf{B}$ drifting ion to go around the cylinder. We note that because we assume that all the ions of interest are in a region where the electric field strength increases linearly with the radius, this time is

the same no matter where the initial distance of the particle might be to the center of the cylinder. We also recall that the direction and the sign of $\vec{\omega_r}$ were taken to be such that the rotation was going in the $\mathbf{E} \times \mathbf{B}$ direction.

We obtain a second equation from the fact that the left-hand-side of Eq.(A.3) must also equal 0 when its right-hand-side vanishes. This gives us the balance

$$\ddot{\mathbf{r}} + \vec{\omega} \times \dot{\mathbf{r}} = 0, \text{ or, } \dot{\mathbf{v}} + \vec{\omega} \times \mathbf{v} = 0 \tag{A.5}$$

in which we get, using (A.4),

$$\vec{\omega} = 2\vec{\omega}_r + \mathbf{\Omega}_i = \mathbf{\Omega}_i \sqrt{1 + 4\frac{E_c/B}{R_c \Omega_i}} \tag{A.6}$$

Eq.(A.5) strongly suggests that ω is a generalization of the ion cyclotron frequency since it takes on that value when $(E_c/B)/(R_c\Omega) \ll 1$.

We may thus conclude that the motion described by a rotating frame with a frequency of rotation described by $\vec{\omega}_r$ describes the ion guiding center motion. That motion is a generalization of the usual plasma $\mathbf{E} \times \mathbf{B}$ drift while the motion about the guiding center is described by a circle in velocity space, where the ion oscillates at a frequency which is a generalization of the ion gyrofrequency. Using parameters listed in Section 3, we obtain $\omega = 1.915\Omega_i$ while $(\omega_r R_c)/(E_c/B) = 0.68$. I label ω as the "effective gyrofrequency" in the main text.

Appendix B

Using Complex Variables to Solve for $\{v_r, v_\phi\}$

In Cartesian coordinates $\{x, y, z\}$, Eq.(2.3) can be written as:

$$\ddot{x} = -\frac{E_c}{B}\frac{\Omega_i}{R_c}x + \Omega_i\dot{y} \ , \quad \ddot{y} = -\frac{E_c}{B}\frac{\Omega_i}{R_c}y - \Omega_i\dot{x} \ , \quad \ddot{z} = 0 \tag{B.1}$$

in which $\{\ddot{x}, \ddot{y}, \ddot{z}\} = \{\dot{v}_x, \dot{v}_y, \dot{v}_z\}$ is the ion's acceleration. The position vector is $\mathbf{r} = x\mathbf{i} + y\mathbf{j} + z\mathbf{k}$. The z-component is not coupled to the rest of the problem and can be solved independently. For the acceleration in the plane perpendicular to the magnetic field we use a complex function $Z = x + iy$ with $|Z| = r$. In terms of that function Eq.(B.1) can be written as

$$\frac{\mathrm{d}^2 Z}{\mathrm{d}t^2} + i\Omega_i\frac{\mathrm{d}Z}{\mathrm{d}t} + \frac{E_c}{B}\frac{\Omega_i}{R_c}Z = 0 \tag{B.2}$$

Letting $Z = Z'e^{i\omega_r t}$, the equation becomes

$$\frac{\mathrm{d}^2 Z'}{\mathrm{d}t^2} + i(2\omega_r + \Omega_i)\frac{\mathrm{d}Z'}{\mathrm{d}t} = Z'\left(\omega_r^2 + \omega_r\Omega_i - \frac{E_c}{B}\frac{\Omega_i}{R_c}\right) \tag{B.3}$$

By selecting a frequency ω_r which satisfies $\omega_r^2 + \omega_r\Omega_i - \Omega_i(E_c/B)/R_c = 0$, we obtain

$$\omega_r = \frac{\Omega_i}{2}\left(\sqrt{1 + 4\frac{E_c/B}{R_c\Omega_i}} - 1\right) \tag{B.4}$$

which is the same as Eq.(A.4). As a result, Eq.(B.3) becomes

$$\frac{\mathrm{d}^2 Z'}{\mathrm{d}t^2} + i\omega\frac{\mathrm{d}Z'}{\mathrm{d}t} = 0 \tag{B.5}$$

where ω has also been obtained before, in Eq.(A.6). The integration of Eq.(B.5) gives

$$Z' = Z'_0 - i\frac{V'_0}{\omega}\left(1 - e^{-i\omega t}\right) \tag{B.6}$$

in which $V'_0 = \left(\dfrac{\mathrm{d}Z'}{\mathrm{d}t}\right)_0$.

B.1 Obtaining $\{v_r, v_\phi\}$ from $\{v_x, v_y\}$

Using $Z' = x' + iy'$ and $V_0' = v_{x0}' + iv_{y0}'$, Eq.(B.6) becomes

$$x' = x_0' + \frac{v_{y0}'}{\omega} - A\cos(\omega t + \theta) \ , \quad y' = y_0' - \frac{v_{x0}'}{\omega} + A\sin(\omega t + \theta) \tag{B.7}$$

revealing

$$\left[x' - \left(x_0' + \frac{v_{y0}'}{\omega}\right)\right]^2 + \left[y' - \left(y_0' - \frac{v_{x0}'}{\omega}\right)\right]^2 = A^2 \tag{B.8}$$

in which $A = \sqrt{v_{x0}'^2 + v_{y0}'^2}/\omega$, $\theta = \tan^{-1}(v_{x0}'/v_{y0}')$, and ω_r is the effective gyrofrequency of the ion in the rotating frame.

In terms of the original function Z we have to apply an additional rotation involving $\omega_r t$ to the results posted in Eqs.(B.7,B.8). The new variables are then given respectively by,

$$\left.\begin{aligned} x &= -r_0\sin(\omega_r t - \vartheta) + \frac{B}{\omega}\{\cos[(\omega_r + \Omega_i)t - \vartheta'] - \cos(\omega_r t + \vartheta')\} \\ y &= r_0\cos(\omega_r t - \vartheta) - \frac{B}{\omega}\{\sin[(\omega_r + \Omega_i)t - \vartheta'] + \sin(\omega_r t + \vartheta')\} \end{aligned}\right\} \tag{B.9}$$

and

$$[x + r_0\sin(\omega_r t - \vartheta)]^2 + [y - r_0\cos(\omega_r t - \vartheta)]^2 = 2\left(\frac{B}{\omega}\right)^2(1 - \cos\omega t) \tag{B.10}$$

in which $r_0 = \sqrt{x_0^2 + y_0^2}$, $\vartheta = \tan^{-1}(x_0/y_0)$, $B = \sqrt{(\omega_r x_0 - v_{y0})^2 + (\omega_r y_0 + v_{x0})^2}$, and $\vartheta' = \tan^{-1}[(\omega_r y_0 + v_{x0})/(\omega_r x_0 - v_{y0})]$.

Eqs.(B.7,B.9) provide the following velocity components, respectively:

$$v_x' = \omega A\sin(\omega t + \theta) \ , \quad v_y' = \omega A\cos(\omega t + \theta) \ , \quad v_x'^2 + v_y'^2 = (\omega A)^2 \tag{B.11}$$

and

$$\left.\begin{aligned} &v_x = -\omega_r r_0\cos(\omega_r t - \vartheta) + \frac{B}{\omega}\{-(\omega_r + \Omega_i)\sin[(\omega_r + \Omega_i)t - \vartheta'] + \\ &+\omega_r\sin(\omega_r t + \vartheta')\} \\ &v_y = -\omega_r r_0\sin(\omega_r t - \vartheta) - \frac{B}{\omega}\{(\omega_r + \Omega_i)\cos[(\omega_r + \Omega_i)t - \vartheta'] + \\ &+\omega_r\cos(\omega_r t + \vartheta')\} \\ &[v_x + \omega_r r_0\cos(\omega_r t - \vartheta)]^2 + [v_y + \omega_r r_0\sin(\omega_r t - \vartheta)]^2 = \\ &= B^2\left[\left(\frac{\Omega_i}{\omega}\right)^2 + 2\frac{\omega_r(\omega_r + \Omega_i)}{\omega^2}(1 + \cos\omega t)\right] \end{aligned}\right\} \tag{B.12}$$

which gives

$$v_x^2 + v_y^2 + \frac{E_c}{B} R_c \Omega_i \left(\frac{r^2}{R_c} - \frac{r_0^2}{R_c} \right) = v_{x0}^2 + v_{y0}^2 \tag{B.13}$$

in which Eq.(B.9) is used. This is simply the energy conservation equation.

From Eq.(B.12), we obtain the components of the ion velocity in the cylindrical frame viz

$$v_r = v_x \cos\phi + v_y \sin\phi \ , \quad v_\phi = -v_x \sin\phi + v_y \cos\phi \tag{B.14}$$

in which ϕ is determined by

$$\tan\phi = y/x \tag{B.15}$$

where x and y are given in Eq.(B.9). The explicit form of these expressions, while correct, is rather complicated. A more physically meaningful expression can, however, be derived from Z.

B.2 Obtaining $\{v_r, v_\phi\}$ Directly from Z

From Eq.(B.6), we obtain

$$Z = \left[Z_0 - i \frac{V_0'}{\omega} \left(1 - e^{-i\omega t} \right) \right] e^{i\omega_r t} \tag{B.16}$$

in which $Z_0 = Z_0'$ is used. Thus,

$$V = \frac{\mathrm{d}Z}{\mathrm{d}t} = i\omega_r Z + V_0' e^{i(\omega_r - \omega)t} \tag{B.17}$$

Clearly,

$$V_0' = V_0 - i\omega_r Z_0 \tag{B.18}$$

which gives

$$v_0'^2 = |V_0'|^2 = (v_{x0} + \omega_r y_0)^2 + (v_{y0} - \omega_r x_0)^2 \tag{B.19}$$

The above equations provide velocity components in cylindrical coordinates as follows:

$$\left.\begin{aligned} v_r &= \frac{VZ^* + V^*Z}{2|Z|} = v_0' \cos[(\omega_r - \omega)t + \phi_0] \\ v_\phi &= \frac{VZ^* - V^*Z}{i2|Z|} = \omega_r r + v_0' \sin[(\omega_r - \omega)t + \phi_0] \end{aligned}\right\} \tag{B.20}$$

in which Z^* and V^* are the complex conjugates of Z and V, respectively, and ϕ_0 is determined by

$$e^{i\phi_0} = \frac{V_0' Z^*}{|V_0' Z^*|} \ , \text{ or, } \ \phi_0 = \tan^{-1} \frac{Im(V_0' Z^*)}{Re(V_0' Z^*)} \tag{B.21}$$

The above also implies

$$v_0'^2 = v_{r0}^2 + (v_{\phi 0} - \omega_r r_0)^2 \tag{B.22}$$

Using Eq.(B.16), we can obtain another expression for the velocity components in terms of ω rather than $\omega_r - \omega$:

$$v_r = v_0' \frac{r_0}{r} \cos(\omega t + \phi_0') + \frac{v_0'^2}{\omega r} \sin\omega t \ , \ \ v_\phi = \omega_r r - v_0' \frac{r_0}{r} \sin(\omega t + \phi_0') - \frac{v_0'^2}{\omega r}(1 - \cos\omega t) \tag{B.23}$$

in which ϕ_0' is determined by

$$e^{i\phi_0'} = \frac{V_0'^* Z_0}{|V_0' Z_0^*|} \ , \ \text{or,} \ \ \phi_0' = \tan^{-1} \frac{Im(V_0'^* Z_0)}{Re(V_0'^* Z_0)} \tag{B.24}$$

Eqs.(B.20,B.23) indicate, respectively, that the velocity $\mathbf{v} = \{v_r, v_\phi\}$ can be described in terms of two different circles with different guiding centers and radii:

$$\left.\begin{array}{l} v_r^2 + (v_\phi - \omega_r r)^2 = v_0'^2 \\ \left(v_r - \dfrac{v_0'^2}{\omega r} \sin\omega t\right)^2 + \left[v_\phi + \dfrac{v_0'^2}{\omega r}(1 - \cos\omega t) - \omega_r r\right]^2 = \left(\dfrac{r_0}{r}\right)^2 v_0'^2 \end{array}\right\} \tag{B.25}$$

Appendix C

Hamiltonian mechanics of Ion Motion

Hamiltonian mechanics employs a scalar function, H (the Hamiltonian), and a set of special phase-space coordinates denoted by two vectors, $(\mathbf{r}, \mathbf{p})$. The two vectors are the canonical generalized coordinates, where $\mathbf{r}$ is the position vector, and $\mathbf{p}$ the canonical momentum conjugating to $\mathbf{r}$. They constitute two canonical Hamilton's equations of motion to describe the kinetic characteristics for an arbitrary particle system:

$$\dot{\mathbf{r}} = \frac{\partial H}{\partial \mathbf{p}} = \nabla_{\mathbf{p}} H, \quad \text{and,} \quad \dot{\mathbf{p}} = -\frac{\partial H}{\partial \mathbf{r}} = -\nabla H \tag{C.1}$$

In external electric, magnetic, and gravitational fields $\mathbf{E}$, $\mathbf{B}$, and $\mathbf{g}$, the Lagrangian L of a non-relativistic, charged particle with rest mass m and charge e is

$$L = T - P = \frac{1}{2} m\mathbf{v}^2 - [e(\varphi - \mathbf{v} \cdot \mathbf{A}) + \Psi] \tag{C.2}$$

in which $\mathbf{v} = \dot{\mathbf{r}}$ is the velocity vector where the dot above $\mathbf{r}$ denotes the time derivative, $T = \frac{1}{2} m\mathbf{v}^2$ the kinetic energy, $P = e(\varphi - \mathbf{v} \cdot \mathbf{A}) + \Psi$ the potential energy, and φ, $\mathbf{A}$, and Ψ are vector and scalar potentials defined by

$$\mathbf{E} = -\nabla\varphi - \frac{\partial \mathbf{A}}{\partial t}, \quad \mathbf{B} = \nabla \times \mathbf{A}, \quad \mathbf{g} = -\frac{1}{m}\nabla\Psi \tag{C.3}$$

C.1 Canonical Equation of Motion

Eq.(C.2) produces the canonical momentum $\mathbf{p}$:

$$\mathbf{p} = \nabla_{\mathbf{v}} L = m\mathbf{v} + e\mathbf{A}, \quad \text{or,} \quad \mathbf{v} = \frac{1}{m}(\mathbf{p} - e\mathbf{A}) \tag{C.4}$$

The Hamiltonian $H(\mathbf{r}, \mathbf{p}, t)$ of the particle is then given by

$$H = \mathbf{p} \cdot \mathbf{v} - L = \frac{(\mathbf{p} - e\mathbf{A})^2}{2m} + e\varphi + \Psi \tag{C.5}$$

Applying Eq.(C.5) in the first equality of Eq.(C.1), we obtain

$$\mathbf{p} = m\dot{\mathbf{r}} + e\mathbf{A}\ , \quad \text{or,} \quad \dot{\mathbf{r}} = \frac{1}{m}(\mathbf{p} - e\mathbf{A}) \tag{C.6}$$

which is equivalent to Eq.(C.4). Then,

$$\dot{\mathbf{p}} = m\ddot{\mathbf{r}} + e\dot{\mathbf{A}} = m\ddot{\mathbf{r}} + e\left[\frac{\partial \mathbf{A}}{\partial t} + (\dot{\mathbf{r}} \cdot \nabla)\mathbf{A}\right] \tag{C.7}$$

The other equality in Eq.(C.1) gives

$$\left.\begin{aligned} \dot{\mathbf{p}} = -\frac{1}{m}(\mathbf{p} - e\mathbf{A}) \times [(\mathbf{p} - e\mathbf{A})] - \frac{1}{m}\left[(\mathbf{p} - e\mathbf{A}) \cdot \nabla\right](\mathbf{p} - e\mathbf{A}) - \\ -e\nabla\varphi - \nabla\Psi = e\dot{\mathbf{r}} \times \mathbf{B} + e(\dot{\mathbf{r}} \cdot \nabla)\mathbf{A} + e(\mathbf{E} + \frac{\partial \mathbf{A}}{\partial t}) + m\mathbf{g} \end{aligned}\right\} \tag{C.8}$$

in which a vector identity $(1/2)\nabla\mathbf{F}^2 = \mathbf{F} \times (\nabla \times \mathbf{F}) + (\mathbf{F} \cdot \nabla)\mathbf{F}$ (where $\mathbf{F}$ is an arbitrary vector), and then Eqs.(C.3,C.6) are used successively.

Eqs.(C.7,C.8) jointly produce

$$m\ddot{\mathbf{r}} = e(\mathbf{E} + \dot{\mathbf{r}} \times \mathbf{B}) + m\mathbf{g} \tag{C.9}$$

or, in its popular form,

$$m\frac{\mathrm{d}\mathbf{v}}{\mathrm{d}t} = e(\mathbf{E} + \mathbf{v} \times \mathbf{B}) + m\mathbf{g} \tag{C.10}$$

C.2 Equation of Motion in Cylindrical Frames

In cylindrical coordinates, the kinetic energy T is

$$T = \frac{1}{2}m(\dot{r}^2 + r^2\dot{\phi}^2 + \dot{z}^2) \tag{C.11}$$

in which, and hereafter, we use dimensionless speeds. The unit of speeds is the initial ion thermal speed $v_{th} = \sqrt{2kT_0/m}$ where T_0 is the ion equilibrium temperature, and k the Boltzmann constant.

If the electric field is an arbitrary function of r and constant in time, E_r, while the magnetic field is homogeneous in space and constant in time, B, the potential energy P is

$$P = e\left[\varphi(r) - \mathbf{v} \cdot \mathbf{A}\right] = e\left[\varphi(r) - \frac{1}{2}Br^2\dot{\phi}\right] \tag{C.12}$$

in which the gravitational term is neglected, and

$$\varphi(r) = -\int \mathbf{E} \cdot \mathrm{d}\mathbf{r} = -\int E_r \mathrm{d}r \tag{C.13}$$

For the linear electric field assumed in Chapter 2, $E_r = -E_c(r/R_c)$,

$$\varphi(r) = \frac{1}{2}E_cR_c\left(\frac{r}{R_c}\right)^2 = \frac{m}{2e}\frac{E_c}{B}R_c\Omega_i\left(\frac{r}{R_c}\right)^2 \tag{C.14}$$

The Lagrangian L is

$$L = T - P = \frac{1}{2}m(\dot{r}^2 + r^2\dot{\phi}^2 + \dot{z}^2) - e\left[\varphi(r) - \frac{1}{2}Br^2\dot{\phi}\right] \tag{C.15}$$

which produces the components of the generalized momentum as follows:

$$p_r = \frac{\partial L}{\partial \dot{r}} = m\dot{r}\ , \quad p_\phi = \frac{\partial L}{\partial \dot{\phi}} = mr^2\dot{\phi} + \frac{1}{2}eBr^2\ , \quad p_z = \frac{\partial L}{\partial \dot{z}} = m\dot{z} \tag{C.16}$$

The above two equations give the Hamiltonian:

$$H = p_r\dot{r} + p_\phi\dot{\phi} + p_z\dot{z} - L = \frac{1}{2}mv_r^2 + \frac{1}{2}mv_\phi^2 + \frac{1}{2}mv_z^2 + e\varphi(r) \tag{C.17}$$

Eqs.(C.16,C.17) provide the following equations, respectively:

$$\left.\begin{aligned}
&\frac{\partial H}{\partial p_r} = \frac{p_r}{m} = \dot{r} = v_r \\
&\frac{\partial H}{\partial p_\phi} = \frac{\dfrac{p_\phi}{r} - \dfrac{1}{2}eBr}{m}\frac{1}{r} = \frac{mr\dot{\phi}}{mr} = \dot{\phi} = \frac{v_\phi}{r} \\
&\frac{\partial H}{\partial p_z} = \dot{z} = v_z \\
&\frac{\partial H}{\partial r} = -mr(\dot{\phi}^2 + \Omega_i\dot{\phi}) + e\frac{\partial \varphi}{\partial r} = -mr(\dot{\phi}^2 + \Omega_i\dot{\phi}) - eE_r \\
&\frac{\partial H}{\partial \phi} = 0 \\
&\frac{\partial H}{\partial z} = 0
\end{aligned}\right\} \tag{C.18}$$

in which $\Omega_i = eB/m$ is used, and,

$$\dot{p}_r = m\ddot{r}\ , \quad \dot{p}_\phi = mr\left(r\ddot{\phi} + 2\dot{r}\dot{\phi} + \Omega_i\dot{r}\right)\ , \quad \dot{p}_z = m\ddot{z} \tag{C.19}$$

Using Eq.(C.1), or, $\dot{p}_r = -\partial H/\partial r$, $\dot{p}_\phi = -\partial H/\partial\phi$, and $\dot{p}_z = -\partial H/\partial z$, we obtain

$$\ddot{r} = r(\dot{\phi}^2 + \Omega_i\dot{\phi}) + \frac{e}{m}E_r\ , \quad r\ddot{\phi} = -2\dot{r}\dot{\phi} - \Omega_i\dot{r}\ , \quad \ddot{z} = 0 \tag{C.20}$$

C.3 Constants and Modified Equation of Motion

The ion Hamiltonian shown in Eq.(C.17) does not contain ϕ, z, and time t explicitly. This means that there are three constants of motion: the azimuthal angular

momentum $p_\phi = K$, the axial momentum p_z, and the total energy $\Xi = H$:

$$\left.\begin{aligned} & p_\phi = mr_1 v_{\phi 1} + mr_1^2 \frac{\Omega_i}{2} = mr_2 v_{\phi 2} + mr_2^2 \frac{\Omega_i}{2} = K \\ & p_z = mv_{z1} = mv_{z2} \\ & \Xi = \frac{1}{2} mv_{r1}^2 + \frac{1}{2} mv_{\phi 1}^2 + \frac{1}{2} mv_{z1}^2 + e\varphi(r_1) = \\ & = \frac{1}{2} mv_{r2}^2 + \frac{1}{2} mv_{\phi 2}^2 + \frac{1}{2} mv_{z2}^2 + e\varphi(r_2) \end{aligned}\right\} \tag{C.21}$$

in which $v_r = \dot{r}$ is the radial velocity, $v_\phi = r\dot{\phi}$ the azimuthal velocity, $v_z = \dot{z}$ the axial velocity parallel to $\mathbf{B}$, and $\{r_1, v_{r1}, v_{\phi 1}, v_{z1}\}$ and $\{r_2, v_{r2}, v_{\phi 2}, v_{z2}\}$ the parameters of $\{r, v_r, v_\phi, v_z\}$ at $t = t_1$ and $t = t_2$, respectively.

Eq.(C.21) introduces the following two Hamiltonian's canonical equations:

$$r_1 v_{\phi 1} + r_1^2 \frac{\Omega_i}{2} = r_2 v_{\phi 2} + r_2^2 \frac{\Omega_i}{2} = \frac{K}{m}\,, \text{ and } v_{r1}^2 + v_{\phi 1}^2 + e[\varphi(r_1) - \varphi(r_2)] = v_{r2}^2 + v_{\phi 2}^2 \tag{C.22}$$

the former of which corresponds to the conservation of canonical angular momentum, and the latter to the total energy which can be rewritten as

$$v_{r1}^2 + v_{\phi 1}^2 + (P_1 - P_2) = v_{r2}^2 + v_{\phi 2}^2 \tag{C.23}$$

where $P = e\varphi(r)$ is the potential energy.

Concisely, Eq.(C.22) gives one modified Hamiltonian's canonical equation of motion:

$$v_{r_1}^2 + \left(\frac{\Omega_i r_1}{2}\right)^2 + \left(\frac{K}{mr_1}\right)^2 + e[\varphi(r_1) - \varphi(r_2)] = v_{r_2}^2 + \left(\frac{\Omega_i r_2}{2}\right)^2 + \left(\frac{K}{mr_2}\right)^2 \tag{C.24}$$

or,

$$v_{r_1}^2 + \left(\frac{\Omega_i r_1}{2}\right)^2 + \left(\frac{K}{mr_1}\right)^2 + (P_1 - P_2) = v_{r_2}^2 + \left(\frac{\Omega_i r_2}{2}\right)^2 + \left(\frac{K}{mr_2}\right)^2 \tag{C.25}$$

In the radially linear electric field $E_r = -E_c(r/R_c)$ produced by homogeneous electron space charges, the above two equations become

$$\left.\begin{aligned} & r_1 v_{\phi 1} + r_1^2 \frac{\Omega_i}{2} = r_2 v_{\phi 2} + r_2^2 \frac{\Omega_i}{2} = \frac{K}{m} \\ & v_{r1}^2 + v_{\phi 1}^2 + \frac{E_c}{B} R_c \Omega_i \left[\left(\frac{r_1}{R_c}\right)^2 - \left(\frac{r_2}{R_c}\right)^2\right] = v_{r2}^2 + v_{\phi 2}^2 \end{aligned}\right\} \tag{C.26}$$

and

$$\left.\begin{aligned} & v_{r_1}^2 + \left(\frac{\Omega_i r_1}{2}\right)^2 + \left(\frac{K}{mr_1}\right)^2 + \frac{E_c}{B} R_c \Omega_i \left[\left(\frac{r_1}{R_c}\right)^2 - \left(\frac{r_2}{R_c}\right)^2\right] = \\ & = v_{r_2}^2 + \left(\frac{\Omega_i r_2}{2}\right)^2 + \left(\frac{K}{mr_2}\right)^2 \end{aligned}\right\} \tag{C.27}$$

Taking phase parameters at the final stage $t = t_1$ as $\{r, v_r, v_\phi, v_z\} = \{r_1, v_{r1}, v_{\phi1}, v_{z1}\}$, and those at the initial stage $t = t_2 = t_0 = 0$ as $\{r_0, v_{r0}, v_{\phi0}, v_{z0}\} = \{r_2, v_{r2}, v_{\phi2}, v_{z2}\}$. The above two equations change to

$$\left.\begin{aligned} & rv_\phi + r^2\frac{\Omega_i}{2} = r_0 v_{\phi0} + r_0^2\frac{\Omega_i}{2} = \frac{K}{m} \\ & v_r^2 + v_\phi^2 + \frac{E_c}{B}R_c\Omega_i\left[\left(\frac{r}{R_c}\right)^2 - \left(\frac{r_0}{R_c}\right)^2\right] = v_{r0}^2 + v_{\phi0}^2 \end{aligned}\right\} \tag{C.28}$$

and,

$$\left.\begin{aligned} & v_r^2 + \left(\frac{\Omega_i r}{2}\right)^2 + \left(\frac{K}{mr}\right)^2 + \frac{E_c}{B}R_c\Omega_i \cdot \left[\left(\frac{r}{R_c}\right)^2 - \left(\frac{r_0}{R_c}\right)^2\right] = \\ & = v_{r_0}^2 + \left(\frac{\Omega_i r_0}{2}\right)^2 + \left(\frac{K}{mr_0}\right)^2 \end{aligned}\right\} \tag{C.29}$$

Appendix D

Solution of Ion Equation of Motion, Eq.(2.11)

D.1 Derivations of Results from Eq.(2.12) to Eq.(2.15)

For two arbitrary states $\{\mathbf{r}_1, \mathbf{v}_1\}$ and $\{\mathbf{r}_2, \mathbf{v}_2\}$ in phase space, the canonical equation of motion, Eq.(2.11), or, Eq.(C.27), takes a generalized form as follows:

$$\left.\begin{aligned} &v_{r_1}^2 + \left(\frac{\Omega_i r_1}{2}\right)^2 + \left(\frac{K}{m r_1}\right)^2 + \frac{E_c}{B} R_c \Omega_i \cdot \left[\left(\frac{r_1}{R_c}\right)^2 - \left(\frac{r_2}{R_c}\right)^2\right] = \\ &= v_{r_2}^2 + \left(\frac{\Omega_i r_2}{2}\right)^2 + \left(\frac{K}{m r_2}\right)^2 \end{aligned}\right\} \tag{D.1}$$

Using

$$v_{r_2} = \frac{\mathrm{d}r_2}{\mathrm{d}t_2} \tag{D.2}$$

this expression becomes

$$v_{r_2} = \pm\sqrt{X_1 - \left(\frac{\Omega_i r_2}{2}\right)^2 - \left(\frac{K}{m r_2}\right)^2 + \frac{E_c}{B} R_c \Omega_i \left[\left(\frac{r_1}{R_c}\right)^2 - \left(\frac{r_2}{R_c}\right)^2\right]} \tag{D.3}$$

in which

$$X_1 = v_{r_1}^2 + \left(\frac{\Omega_i r_1}{2}\right)^2 + \left(\frac{K}{m r_1}\right)^2 \tag{D.4}$$

Or,

$$\frac{R_c \mathrm{d}\left(\frac{r_2}{R_c}\right)^2}{\sqrt{-\left(\frac{\Omega_i R_c}{2}\right)^2 \left(\frac{r_2}{R_c}\right)^4 + X_1 \left(\frac{r_2}{R_c}\right)^2 - \left(\frac{K}{m R_c}\right)^2 + X_2 \left(\frac{r_2}{R_c}\right)^2}} = \pm 2 \ \mathrm{d}t_2 \tag{D.5}$$

in which

$$X_2 = \frac{E_c}{B} R_c \Omega_i \left[\left(\frac{r_1}{R_c}\right)^2 - \left(\frac{r_2}{R_c}\right)^2\right] \tag{D.6}$$

In a concise form, we then obtain

$$\frac{\mathrm{d}x_2}{\sqrt{-b_{12}x_2^2+b_{22}x_2-b_{32}}}=\pm\frac{2}{R_c}\mathrm{d}t_2 \tag{D.7}$$

where x_2 is a new radial function, b_{12}, b_{22}, b_{32} are coefficients, shown as follows:

$$\left.\begin{array}{rcl} x_2 & = & \left(\dfrac{r_2}{R_c}\right)^2 \\ b_{12} & = & \left(\dfrac{\Omega_i R_c}{2}\right)^2+\dfrac{E_c}{B}R_c\Omega_i \\ b_{22} & = & b_{12}(\dfrac{r_1}{R_c})^2+v_{r_1}^2+\left(v_{\phi_1}+\dfrac{\Omega_i r_1}{2}\right)^2 \\ b_{32} & = & \left(\dfrac{K}{mR_c}\right)^2=\left(\dfrac{r_1}{R_c}\right)^2\left(v_{\phi_1}+\dfrac{\Omega_i r_1}{2}\right)^2 \end{array}\right\} \tag{D.8}$$

The integration of Eq.(D.7) on both sides gives

$$\left(\frac{r_2}{R_c}\right)^2=A_2\{1+\varepsilon_2\,\sin[\pm\omega(t_2-t_1)+\phi_2]\} \tag{D.9}$$

in which

$$\left.\begin{array}{l} A_2=\dfrac{b_{22}}{2b_{12}} \\ \varepsilon_2=\sqrt{1-4\dfrac{b_{12}b_{32}}{b_{22}^2}} \\ \omega=\Omega_i\sqrt{1+4\dfrac{E_c/B}{R_c\Omega_i}} \\ \phi_2=\sin^{-1}\dfrac{(r_1/R_c)^2/A_2-1}{\varepsilon_2} \end{array}\right\} \tag{D.10}$$

and the sign "$\pm$" before ω takes "$+$" for $v_{r_1}>0$ and "$-$" for $v_{r_1}<0$. Above results are used in Section 2.3.1.

D.2 Derivations of Results from Eq.(2.18) to Eq.(2.21)

To obtain the results presented in Section 2.3.2, we start by re-expressing Eq.(D.9) by moving its non-sine terms on the RHS of to the LHS:

$$\left.\begin{aligned}
&\frac{\left(\frac{r_2}{R_c}\right)^2 / \frac{b_{22}}{2b_{12}} - 1}{\sqrt{1 - \frac{4b_{12}b_{32}}{b_{22}^2}}} = \sin\left[\pm\omega(t_2 - t_1) + \sin^{-1}\frac{\left(\frac{r_1}{R_c}\right)^2 / \frac{b_{22}}{2b_{12}} - 1}{\sqrt{1 - \frac{4b_{12}b_{32}}{b_{22}^2}}}\right] = \\
&= \sin\left[\pm\omega(t_2 - t_1)\right]\cos\left[\sin^{-1}\frac{\left(\frac{r_1}{R_c}\right)^2 / \frac{b_{22}}{2b_{12}} - 1}{\sqrt{1 - \frac{4b_{12}b_{32}}{b_{22}^2}}}\right] + \\
&+\cos\left[\omega(t_2 - t_1)\right]\sin\left[\sin^{-1}\frac{\left(\frac{r_1}{R_c}\right)^2 / \frac{b_{22}}{2b_{12}} - 1}{\sqrt{1 - \frac{4b_{12}b_{32}}{b_{22}^2}}}\right]
\end{aligned}\right\} \quad \text{(D.11)}$$

This means

$$\left.\begin{aligned}
&\frac{\left(\frac{r_2}{R_c}\right)^2 / \frac{b_{22}}{2b_{12}} - 1}{\sqrt{1 - \frac{4b_{12}b_{32}}{b_{22}^2}}} = \\
&= \sin\left[\pm\omega(t_2 - t_1)\right]\sqrt{1 - \sin^2\left[\sin^{-1}\frac{\left(\frac{r_1}{R_c}\right)^2 / \frac{b_{22}}{2b_{12}} - 1}{\sqrt{1 - \frac{4b_{12}b_{32}}{b_{22}^2}}}\right]} + \\
&+\cos\left[\omega(t_2 - t_1)\right]\cdot\frac{\left(\frac{r_1}{R_c}\right)^2 / \frac{b_{22}}{2b_{12}} - 1}{\sqrt{1 - \frac{4b_{12}b_{32}}{b_{22}^2}}} = \\
&= \sin\left[\pm\omega(t_2 - t_1)\right]\frac{\sqrt{2\left(\frac{r_1}{R_c}\right)^2 / \frac{b_{22}}{2b_{12}} - \left[\left(\frac{r_1}{R_c}\right)^2 / \frac{b_{22}}{2b_{12}}\right]^2 - \frac{4b_{12}b_{32}}{b_{22}^2}}}{\sqrt{1 - \frac{4b_{12}b_{32}}{b_{22}^2}}} + \\
&+\cos\left[\omega(t_2 - t_1)\right]\cdot\frac{\left(\frac{r_1}{R_c}\right)^2 / \frac{b_{22}}{2b_{12}} - 1}{\sqrt{1 - \frac{4b_{12}b_{32}}{b_{22}^2}}}
\end{aligned}\right\} \quad \text{(D.12)}$$

which is then converted to

$$\left.\begin{aligned}
&\frac{(r_2/R_c)^2}{b_{22}/(2b_{12})}-1= \\
&=\sin\left[\pm\omega(t_2-t_1)\right]\sqrt{2\frac{(r_1/R_c)^2}{b_{22}/(2b_{12})}-\left[\frac{(r_1/R_c)^2}{b_{22}/(2b_{12})}\right]^2-\frac{4b_{12}b_{32}}{b_{22}^2}}+ \\
&+\cos\left[\omega(t_2-t_1)\right]\cdot\left[\frac{(r_1/R_c)^2}{b_{22}/(2b_{12})}-1\right]= \\
&=\sin\left[\pm\omega(t_2-t_1)\right]2\sqrt{\frac{b_{12}}{b_{22}}}\cdot\sqrt{\left(\frac{r_1}{R_c}\right)^2-\frac{b_{12}}{b_{22}}\left(\frac{r_1}{R_c}\right)^4-\frac{b_{32}}{b_{22}}}+ \\
&+\cos\left[\omega(t_2-t_1)\right]\cdot\left[\frac{(r_1/R_c)^2}{b_{22}/(2b_{12})}-1\right]
\end{aligned}\right\} \tag{D.13}$$

Besides, Eq.(D.10) gives

$$\left.\begin{aligned}
&\left(\frac{r_1}{R_c}\right)^2-\frac{b_{12}}{b_{22}}\left(\frac{r_1}{R_c}\right)^4-\frac{b_{32}}{b_{22}}= \\
&=\left(\frac{r_1}{R_c}\right)^2-\frac{b_{12}\left(\frac{r_1}{R_c}\right)^4+\left(\frac{r_1}{R_c}\right)^2\left(v_{\phi1}+\frac{\Omega_i r_1}{2}\right)^2}{b_{12}(\frac{r_1}{R_c})^2+v_{r1}^2+\left(v_{\phi1}+\frac{\Omega_i r_1}{2}\right)^2}=\left(\frac{r_1}{R_c}\right)^2\frac{v_{r1}^2}{b_{22}}
\end{aligned}\right\} \tag{D.14}$$

or,

$$\sqrt{\left(\frac{r_1}{R_c}\right)^2-\frac{b_{12}}{b_{22}}\left(\frac{r_1}{R_c}\right)^4-\frac{b_{32}}{b_{22}}}=\pm\frac{r_1}{R_c}\frac{v_{r1}}{\sqrt{b_{22}}} \tag{D.15}$$

in which the sign "$\pm$" on the RHS takes "$+$" for $v_{r_1}>0$ and "$-$" for $v_{r_1}<0$.

Substituting Eq.(D.15) into Eq.(D.13) gives

$$\frac{(r_2/R_c)^2}{b_{22}/(2b_{12})}=1+\sin\omega(t_2-t_1)\cdot2\sqrt{\frac{b_{12}}{b_{22}}}\cdot\frac{r_1}{R_c}\frac{v_{r_1}}{\sqrt{b_{22}}}+\cos\omega(t_2-t_1)\cdot\left[\frac{(r_1/R_c)^2}{b_{22}/(2b_{12})}-1\right] \tag{D.16}$$

Thus,

$$\left.\begin{aligned}
&\left(\frac{r_2}{R_c}\right)^2=\frac{b_{22}}{2b_{12}}+\frac{v_{r_1}}{\sqrt{b_{12}}}\frac{r_1}{R_c}\sin\omega(t_2-t_1)+ \\
&+\left[\left(\frac{r_1}{R_c}\right)^2-\frac{b_{22}}{2b_{12}}\right]\cos\omega(t_2-t_1)=\frac{v_{r1}}{\sqrt{b_{12}}}\frac{r_1}{R_c}\sin\omega(t_2-t_1)+ \\
&+\left(\frac{r_1}{R_c}\right)^2\cos\omega(t_2-t_1)+\frac{b_{22}}{2b_{12}}\left[1-\cos\omega(t_2-t_1)\right]= \\
&=\frac{v_{r1}}{\sqrt{b_{12}}}\frac{r_1}{R_c}\sin\omega(t_2-t_1)+\left(\frac{r_1}{R_c}\right)^2\cos\omega(t_2-t_1)+ \\
&+\frac{b_{12}(\frac{r_1}{R_c})^2+v_{r1}^2+\left(v_{\phi1}+\frac{\Omega_i r_1}{2}\right)^2}{2b_{12}}\left[1-\cos\omega(t_2-t_1)\right]
\end{aligned}\right\} \tag{D.17}$$

which gives

$$\left.\begin{aligned}
&\left(\frac{r_2}{R_c}\right)^2 = \frac{1-\cos\omega(t_2-t_1)}{2b_{12}}v_{r1}^2 + \frac{\frac{r_1}{R_c}\sin\omega(t_2-t_1)}{\sqrt{b_{12}}}v_{r1} + \\
&+\frac{1-\cos\omega(t_2-t_1)}{2b_{12}}\left(v_{\phi 1}+\frac{\Omega_i r_1}{2}\right)^2 + \left(\frac{r_1}{R_c}\right)^2\cos\omega(t_2-t_1) + \\
&+\frac{1}{2}\left(\frac{r_1}{R_c}\right)^2[1-\cos\omega(t_2-t_1)] = \frac{1-\cos\omega(t_2-t_1)}{2b_{12}}v_{r1}^2 + \\
&+\frac{\frac{r_1}{R_c}\sin\omega(t_2-t_1)}{\sqrt{b_{12}}}v_{r1} + \frac{1-\cos\omega(t_2-t_1)}{2b_{12}}\left(v_{\phi 1}+\frac{\Omega_i r_1}{2}\right)^2 + \\
&+\frac{1}{2}\left(\frac{r_1}{R_c}\right)^2[1+\cos\omega(t_2-t_1)] = \\
&= \frac{1-a_2}{\frac{E}{B}R_c\Omega_i}\left[\left(v_{r1}+\frac{a_2}{1-a_2}v_{\mathrm{d}r1}\right)^2 + \left(v_{\phi 1}+\frac{a_2}{1-a_2}v_{\mathrm{d}\phi 1}\right)^2\right]
\end{aligned}\right\} \tag{D.18}$$

in which

$$\left.\begin{aligned}
&a_2 = 1 - \frac{\frac{E_c}{B}R_c\Omega_i}{2b_{12}}[1-\cos\omega(t_2-t_1)] = \\
&= 1 - \frac{1}{2}\left[1-\left(\frac{\Omega_i}{\omega}\right)^2\right][1-\cos\omega(t_2-t_1)] \\
&v_{\mathrm{d}r1} = \frac{E_c}{B}R_c\Omega_i\frac{\frac{r_1}{R_c}\sin\omega(t_2-t_1)}{2a_2\sqrt{b_{12}}} = -\frac{1}{a_2}\cdot\frac{1}{2}r_1\frac{\mathrm{d}a_2}{\mathrm{d}t_1} = \\
&= \frac{E_c}{B}\frac{r_1}{R_c}\frac{1}{a_2}\frac{\Omega_i}{\omega}\sin\omega(t_2-t_1) \\
&v_{\mathrm{d}\phi 1} = \frac{E_c}{B}(R_c\Omega_i)^2\frac{\frac{r_1}{R_c}[1-\cos\omega(t_2-t_1)]}{4a_2b_{12}} = \frac{1-a_2}{a_2}\cdot\frac{1}{2}r_1\Omega_i = \\
&= \frac{E_c}{B}\frac{r_1}{R_c}\frac{1}{a_2}\left(\frac{\Omega_i}{\omega}\right)^2[1-\cos\omega(t_2-t_1)]
\end{aligned}\right\} \tag{D.19}$$

where the last two equations provides an important relation:

$$v_{\mathrm{d}r1}^2 + \left(v_{\mathrm{d}\phi 1} - \frac{E_c}{B}\frac{r_1}{R_c}\right)^2 = \left(\frac{E_c}{B}\frac{r_1}{R_c}\right)^2 \tag{D.20}$$

Now let's notice that Eq.(D.18) produces

$$\left.\begin{aligned}
&\left(\frac{r_1}{R_c}\right)^2 - \left(\frac{r_2}{R_c}\right)^2 = \\
&= \left(\frac{r_1}{R_c}\right)^2 - \frac{1-\cos\omega(t_2-t_1)}{2b_{12}}v_{r1}^2 - \frac{\frac{r_1}{R_c}\sin\omega(t_2-t_1)}{\sqrt{b_{12}}}v_{r1} - \\
&-\frac{1-\cos\omega(t_2-t_1)}{2b_{12}}\left(v_{\phi 1}+\frac{\Omega_i r_1}{2}\right)^2 - \frac{1}{2}\left(\frac{r_1}{R_c}\right)^2[1+\cos\omega(t_2-t_1)]
\end{aligned}\right\} \tag{D.21}$$

Applying this expression in the generalized form of the second formula in Eq.(2.10), we have

$$\left.\begin{aligned}
&v_{r2}^2+v_{\phi 2}^2=v_{r1}^2+v_{\phi 1}^2+\frac{E_c}{B}R_c\Omega_i\left[\left(\frac{r_1}{R_c}\right)^2-\left(\frac{r_2}{R_c}\right)^2\right]=\\
&=\left[1-\frac{\frac{E_c}{B}R_c\Omega_i}{2b_{12}}\left(1-\cos\omega(t_2-t_1)\right)\right]v_{r1}^2-\\
&-\frac{E_c}{B}R_c\Omega_i\frac{\frac{r_1}{R_c}\sin\omega(t_2-t_1)}{\sqrt{b_{12}}}v_{r1}+\left[1-\frac{\frac{E_c}{B}R_c\Omega_i}{2b_{12}}\left(1-\cos\omega(t_2-t_1)\right)\right]v_{\phi 1}^2-\\
&-\frac{E_c}{B}(R_c\Omega_i)^2\frac{\frac{r_1}{R_c}\left[1-\cos\omega(t_2-t_1)\right]}{2b_{12}}v_{\phi 1}-\\
&-\frac{E_c}{B}R_c\Omega_i\frac{1-\cos\omega(t_2-t_1)}{2b_{12}}\left(\frac{\Omega_i r_1}{2}\right)^2+\\
&+\frac{1}{2}\frac{E_c}{B}R_c\Omega_i\left(\frac{r_1}{R_c}\right)^2\left[1-\cos\omega(t_2-t_1)\right]=\\
&=a_2\left[v_{r1}^2-\frac{E_c}{B}R_c\Omega_i\frac{\frac{r_1}{R_c}\sin\omega(t_2-t_1)}{a\sqrt{b_{12}}}v_{r1}\right]+\\
&+a_2\left[v_{\phi 1}^2-\frac{E_c}{B}(R_c\Omega_i)^2\frac{\frac{r_1}{R_c}\left[1-\cos\omega(t_2-t_1)\right]}{2a_2b_{12}}v_{\phi 1}\right]+\\
&+\frac{\left(\frac{E_c}{B}R_c\Omega_i\right)^2}{b_{12}}\left(\frac{r_1}{R_c}\right)^2\frac{1-\cos\omega(t_2-t_1)}{2}=\\
&=a_2\left[(v_{r1}-v_{\mathrm{d}r1})^2+(v_{\phi 1}-v_{\mathrm{d}\phi 1})^2\right]+C
\end{aligned}\right\}\tag{D.22}$$

in which

$$C=a_2(v_{\mathrm{d}r1}^2+v_{\mathrm{d}\phi 1}^2)-\frac{\left(\frac{E_c}{B}R_c\Omega_i\right)^2}{b_{12}}\left(\frac{r_1}{R_c}\right)^2\frac{1-\cos\omega(t_2-t_1)}{2}=0\tag{D.23}$$

Therefore, Eqs.(D.18,D.20,D.22) imply

$$\left.\begin{aligned}
&\left(\frac{r_2}{R_c}\right)^2=\frac{1-a_2}{\frac{E}{B}R_c\Omega_i}\left[\left(v_{r1}+\frac{a_2}{1-a_2}v_{\mathrm{d}r1}\right)^2+\left(v_{\phi 1}+\frac{a_2}{1-a_2}v_{\mathrm{d}\phi 1}\right)^2\right]\\
&a_2\left[(v_{r1}-v_{\mathrm{d}r1})^2+(v_{\phi 1}-v_{\mathrm{d}\phi 1})^2\right]=v_{r2}^2+v_{\phi 2}^2\\
&v_{\mathrm{d}r1}^2+\left(v_{\mathrm{d}\phi 1}-\frac{E_c}{B}\frac{r_1}{R_c}\right)^2=\left(\frac{E_c}{B}\frac{r_1}{R_c}\right)^2
\end{aligned}\right\}\tag{D.24}$$

Consequently, with the consideration of the phase parameters at the final stage $t = t_1$ as $\{r, v_r, v_\phi, v_z\} = \{r_1, v_{r1}, v_{\phi 1}, v_{z1}\}$, and those at the initial stage $t = t_2 = t_0 = 0$ as $\{r_0, v_{r0}, v_{\phi 0}, v_{z0}\} = \{r_2, v_{r2}, v_{\phi 2}, v_{z2}\}$ with the sign "$\mp$" being "$-$" for $v_r > 0$ and "$+$" for $v_r < 0$, we then have

$$\left.\begin{aligned}
&\left(\frac{r_0}{R_c}\right)^2 = A_0\{1 + \varepsilon_0 \sin(\mp\omega t + \phi_0)\} = \\
&= \frac{1 - a_0}{\dfrac{E}{B} R_c \Omega_i}\left[\left(v_r + \frac{a_0}{1 - a_0} v_{\mathrm{d}r}\right)^2 + \left(v_\phi + \frac{a_0}{1 - a_0} v_{\mathrm{d}\phi}\right)^2\right] \\
&v_{r0}^2 + v_{\phi 0}^2 = a_0\left[(v_r - v_{\mathrm{d}r})^2 + (v_\phi - v_{\mathrm{d}\phi})^2\right] \quad \text{and} \\
&v_{\mathrm{d}r}^2 + \left(v_{\mathrm{d}\phi} - \frac{E_c}{B}\frac{r}{R_c}\right)^2 = \left(\frac{E_c}{B}\frac{r}{R_c}\right)^2 \\
&A_0 = b_2/(2b_1) \\
&\varepsilon_0 = \sqrt{1 - 4b_1 b_3 / b_2^2} \\
&\omega = \Omega_i \sqrt{1 + 4\frac{E_c/B}{R_c \Omega_i}} \\
&\phi_0 = \sin^{-1}\frac{(r/R_c)^2/A_0 - 1}{\varepsilon_0} \\
&b_1 = \left(\frac{\Omega_i R_c}{2}\right)^2 + \frac{E_c}{B} R_c \Omega_i \\
&b_2 = b_1(\frac{r}{R_c})^2 + v_r^2 + \left(v_\phi + \frac{\Omega_i r}{2}\right)^2 \\
&b_3 = \left(\frac{r}{R_c}\right)^2 \left(v_\phi + \frac{\Omega_i r}{2}\right)^2 \\
&a_0 = 1 - \frac{1}{2}\left[1 - \left(\frac{\Omega_i}{\omega}\right)^2\right](1 - \cos\omega t) \\
&v_{\mathrm{d}r} = \frac{1}{a_0} \cdot \frac{1}{2} r \frac{\mathrm{d}a_0}{\mathrm{d}t} = -\frac{E_c}{B}\frac{r}{R_c}\frac{1}{a_0}\frac{\Omega_i}{\omega}\sin\omega t \\
&v_{\mathrm{d}\phi} = \frac{1 - a_0}{a_0} \cdot \frac{1}{2} r \Omega_i = \frac{E_c}{B}\frac{r}{R_c}\frac{1}{a_0}\left(\frac{\Omega_i}{\omega}\right)^2 (1 - \cos\omega t)
\end{aligned}\right\} \qquad \text{(D.25)}$$

This solution was checked against a numerical integration of the trajectories so as to verify that there were no algebraic mistakes.

Appendix E

Proof of $\mathrm{d}F/\mathrm{d}t = 0$

From

$$\left.\begin{aligned} F = v_r^2 + v_\phi^2 + \frac{E_c}{B} R_c \Omega_i \cdot \\ \cdot \left[\frac{r v_r}{R_c \sqrt{b_1}} \sin\omega t + \frac{\left(\frac{r}{R_c}\right)^2 b_1 - v_r^2 - \left(v_\phi + \frac{r\Omega_i}{2}\right)^2}{2 b_1} (1 - \cos\omega t) \right] \end{aligned}\right\} \tag{E.1}$$

we know that the partial derivatives of F and the terms in $\mathrm{d}F/\mathrm{d}t$ are in following expressions, respectively:

$$\frac{\partial F}{\partial t} = \frac{E_c}{B} R_c \Omega_i \left[\frac{\left(\frac{r}{R_c}\right)^2 b_1 - v_r^2 - \left(v_\phi + \frac{r\Omega_i}{2}\right)^2}{R_c \sqrt{b_1}} \sin\omega t + 2 \frac{r}{R_c^2} v_r \cos\omega t \right] \tag{E.2}$$

$$\left.\begin{aligned} \frac{\partial F}{\partial r} = 2\frac{v_\phi^2}{r} + \frac{E_c}{B} R_c \Omega_i \cdot \\ \cdot \left[\frac{v_r}{R_c \sqrt{b_1}} \sin\omega t + \frac{\left(\frac{r}{R_c^2}\right) b_1 - \left(v_\phi + \frac{r\Omega_i}{2}\right)\left(\frac{v_\phi}{r} + \frac{\Omega_i}{2}\right)}{b_1} (1 - \cos\omega t) \right] \end{aligned}\right\} \tag{E.3}$$

$$\frac{\partial F}{\partial v_r} = 2 v_r + \frac{E_c}{B} R_c \Omega_i \left[\frac{r}{R_c \sqrt{b_1}} \sin\omega t - \frac{v_r}{b_1} (1 - \cos\omega t) \right] \tag{E.4}$$

$$\frac{\partial F}{\partial v_\phi} = 2 v_\phi - \frac{E_c}{B} R_c \Omega_i \frac{v_\phi + \frac{r\Omega_i}{2}}{b_1} (1 - \cos\omega t) \tag{E.5}$$

Then,

$$\left.\begin{aligned} v_r \frac{\partial F}{\partial r} = 2\frac{v_r v_\phi^2}{r} + \frac{E_c}{B} R_c \Omega_i \cdot \\ \cdot \left[\frac{v_r^2}{R_c \sqrt{b_1}} \sin\omega t + \frac{v_r}{r} \frac{\left(\frac{r}{R_c}\right)^2 b_1 - \left(v_\phi + \frac{r\Omega_i}{2}\right)^2}{b_1} (1 - \cos\omega t) \right] \end{aligned}\right\} \tag{E.6}$$

$$\left.\begin{aligned}&\left(\frac{v_\phi^2}{r}+v_\phi\Omega_i-\frac{E_c}{B}R_c\Omega_i\frac{r}{R_c^2}\right)\frac{\partial F}{\partial v_r}=2\frac{v_r v_\phi^2}{r}+2v_r v_\phi\Omega_i-\frac{E_c}{B}R_c\Omega_i\cdot 2\frac{r}{R_c^2}v_r+\\&+\left(\frac{v_\phi^2}{r}+v_\phi\Omega_i-\frac{E_c}{B}R_c\Omega_i\frac{r}{R_c^2}\right)\frac{E_c}{B}R_c\Omega_i\left[\frac{r}{R_c\sqrt{b_1}}\sin\omega t-\frac{v_r}{b_1}(1-\cos\omega t)\right]\end{aligned}\right\}\tag{E.7}$$

$$\left.\begin{aligned}&-\left(2\frac{v_r v_\phi}{r}+v_r\Omega_i\right)\frac{\partial F}{\partial v_\phi}=-4\frac{v_r v_\phi^2}{r}-2v_r v_\phi\Omega_i+\\&+\frac{E_c}{B}R_c\Omega_i\cdot\frac{v_r}{r}\left(2v_\phi+r\Omega_i\right)\frac{v_\phi+\dfrac{r\Omega_i}{2}}{b_1}(1-\cos\omega t)\end{aligned}\right\}\tag{E.8}$$

In above equations, the respective summations of all LHS terms and all RHS terms give

$$\left.\begin{aligned}&\left(\frac{E_c}{B}R_c\Omega_i\right)^{-1}\frac{\mathrm{d}F}{\mathrm{d}t}=\frac{\left(\dfrac{r}{R_c}\right)^2 b_1-v_r^2-\left(v_\phi+\dfrac{r\Omega_i}{2}\right)^2}{R_c\sqrt{b_1}}\sin\omega t+\\&+2\frac{r}{R_c^2}v_r\cos\omega t+\frac{v_r^2}{R_c\sqrt{b_1}}\sin\omega t+\frac{v_r}{r}\frac{\left(\dfrac{r}{R_c}\right)^2 b_1-\left(v_\phi+\dfrac{r\Omega_i}{2}\right)^2}{b_1}\cdot\\&\cdot(1-\cos\omega t)-2\frac{r}{R_c^2}v_r+\left(\frac{v_\phi^2}{r}+v_\phi\Omega_i-\frac{E_c}{B}R_c\Omega_i\frac{r}{R_c^2}\right)\cdot\\&\cdot\left[\frac{r}{R_c\sqrt{b_1}}\sin\omega t-\frac{v_r}{b_1}(1-\cos\omega t)\right]+\frac{v_r}{r}\left(2v_\phi+r\Omega_i\right)\frac{v_\phi+\dfrac{r\Omega_i}{2}}{b_1}(1-\cos\omega t)\end{aligned}\right\}\tag{E.9}$$

which gives

$$\left.\begin{aligned}&\left(\frac{E_c}{B}R_c\Omega_i\right)^{-1}\frac{\mathrm{d}F}{\mathrm{d}t}=\frac{\left(\dfrac{r}{R_c}\right)^2 b_1-\left(v_\phi+\dfrac{r\Omega_i}{2}\right)^2}{R_c\sqrt{b_1}}\sin\omega t-2\frac{r}{R_c^2}v_r(1-\cos\omega t)+\\&+\frac{v_r}{r}\frac{\left(\dfrac{r}{R_c}\right)^2 b_1-\left(v_\phi+\dfrac{r\Omega_i}{2}\right)^2}{b_1}(1-\cos\omega t)+\left(\frac{v_\phi^2}{r}+v_\phi\Omega_i-\frac{E_c}{B}R_c\Omega_i\frac{r}{R_c^2}\right)\cdot\\&\cdot\left[\frac{r}{R_c\sqrt{b_1}}\sin\omega t-\frac{v_r}{b_1}(1-\cos\omega t)\right]+2\frac{v_r}{rb_1}\left(v_\phi+\frac{r\Omega_i}{2}\right)^2(1-\cos\omega t)\end{aligned}\right\}\tag{E.10}$$

or

$$\left.\begin{aligned}
&\left(\frac{E_c}{B}R_c\Omega_i\right)^{-1}\frac{\mathrm{d}F}{\mathrm{d}t}= \\
&=\frac{\left(\frac{r}{R_c}\right)^2 b_1-\left(v_\phi+\frac{r\Omega_i}{2}\right)^2+v_\phi^2+rv_\phi\Omega_i-\frac{E_c}{B}R_c\Omega_i\left(\frac{r}{R_c}\right)^2}{R_c\sqrt{b_1}}\sin\omega t- \\
&-2\frac{r}{R_c^2}v_r(1-\cos\omega t)+\frac{v_r}{r}\frac{\left(\frac{r}{R_c}\right)^2 b_1-\left(v_\phi+\frac{r\Omega_i}{2}\right)^2}{b_1}\cdot \\
&\cdot(1-\cos\omega t)-\left(\frac{v_\phi^2}{r}+v_\phi\Omega_i-\frac{E_c}{B}R_c\Omega_i\frac{r}{R_c^2}\right)\frac{v_r}{b_1}(1-\cos\omega t)+ \\
&+2\frac{v_r}{rb_1}\left(v_\phi+\frac{r\Omega_i}{2}\right)^2(1-\cos\omega t)= \\
&=\frac{\left(\frac{r}{R_c}\right)^2\left(\frac{R_c\Omega_i}{2}\right)^2-\left(v_\phi+\frac{r\Omega_i}{2}\right)^2+v_\phi^2+rv_\phi\Omega_i}{R_c\sqrt{b_1}}\sin\omega t- \\
&-2\frac{r}{R_c^2}v_r(1-\cos\omega t)++\frac{v_r}{rb_1}\cdot \\
&\cdot\left[\left(\frac{r}{R_c}\right)^2 b_1+\left(v_\phi+\frac{r\Omega_i}{2}\right)^2-v_\phi^2-rv_\phi\Omega_i+\frac{E_c}{B}R_c\Omega_i\left(\frac{r}{R_c}\right)^2\right]\cdot \\
&\cdot(1-\cos\omega t)
\end{aligned}\right\} \tag{E.11}$$

which produces

$$\left.\begin{aligned}
&\left(\frac{E_c}{B}R_c\Omega_i\right)^{-1}\frac{\mathrm{d}F}{\mathrm{d}t}=\frac{0}{R_c\sqrt{b_1}}\sin\omega t-2\frac{r}{R_c^2}v_r(1-\cos\omega t)+ \\
&+\frac{v_r}{rb_1}\cdot 2\left(\frac{r}{R_c}\right)^2 b_1(1-\cos\omega t)= \\
&=-2\frac{r}{R_c^2}v_r(1-\cos\omega t)+2\frac{r}{R_c^2}v_r(1-\cos\omega t)=0
\end{aligned}\right\} \tag{E.12}$$

Consequently,

$$\frac{\mathrm{d}F}{\mathrm{d}t}=0 \tag{E.13}$$

Appendix F

Generalized Expressions of N_i and f_i in the collisional case described in Chapter 3

In this appendix we derive an expression for the ion density after a sufficiently large number of gyro-cycles has elapsed in the collisional case described in Chapter 3. While the expression does not apply to earlier times involving only a few gyro-cycles, it proves useful in practice for cases in which collisions have taken over the evolution of the distribution function.

The expression that we need to evaluate is given by Eq.(3.19), which reads

$$N_i = \frac{n_{i0}}{a_0(t)} + n_{i0}\frac{\nu_{in}}{\omega} e^{\frac{\nu_{in}}{\omega}\int_0^{\omega t} \mathrm{d}\alpha'/a_0(\alpha')} \cdot I(\alpha) \tag{F.1}$$

in which

$$I(\alpha) = \int_0^{\omega t} \frac{e^{-\frac{\nu_{in}}{\omega}\int_0^{\omega t'} \mathrm{d}\alpha''/a_0(\alpha'')}}{a_0^2(\alpha')} \mathrm{d}\alpha' \tag{F.2}$$

To simplify the notation, we use $\alpha = \omega t$ and define

$$h(\alpha) = \frac{1}{2\pi}\int_0^{\omega t} \frac{\mathrm{d}\alpha'}{a_0(\alpha')} \tag{F.3}$$

We limit our calculation to the case $\alpha \gg 2\pi$ for simplicity. It is perfectly possible to be more general. However, the algebra becomes unnecessarily tedious in that and little of physical interest in gained by doing so.

Since a_0 is 2π-periodic in $\omega t' = \alpha'$, we can write

$$2\pi h(\alpha) = \int_0^{2\pi} \frac{\mathrm{d}\alpha'}{a_0(\alpha')} + \int_{2\pi}^{4\pi} \frac{\mathrm{d}\alpha'}{a_0(\alpha')} + \cdots + \int_{2\pi(l-1)}^{2\pi l} \frac{\mathrm{d}\alpha'}{a_0(\alpha')} + \int_{2\pi l}^{2\pi l+\varepsilon} \frac{\mathrm{d}\alpha'}{a_0(\alpha')} \tag{F.4}$$

where $l = \mathrm{INT}[\omega t/(2\pi)]$ and ε is the phase left in an incomplete cycle. Our interest is in $\varepsilon \ll 2\pi l$ so that the last term can be ignored and then, $l = \mathrm{INT}[\omega t/(2\pi)] \cong \omega t/(2\pi)$. It follows that

$$2\pi h(\alpha) \cong l\int_0^{2\pi} \frac{\mathrm{d}\alpha'}{a_0(\alpha')} = 2\pi l h_{2\pi} \cong \omega t h_{2\pi} \tag{F.5}$$

where

$$h_{2\pi} = \frac{1}{2\pi}\int_0^{2\pi} \frac{\mathrm{d}\alpha'}{a_0(\alpha')} \tag{F.6}$$

Using the expression of a_0 in Eq.(2.19), we have

$$\int_0^{2\pi} \frac{\mathrm{d}\alpha'}{a_0(\alpha')} = 2\pi\frac{\omega}{\Omega_i} \quad \text{or,} \quad h_{2\pi} = \frac{\omega}{\Omega_i} \tag{F.7}$$

F.1 Evaluation of the first integral

The simplest integral that we have to perform is

$$\frac{\nu_{in}}{\omega}\int_0^{\omega t} \frac{\mathrm{d}\alpha'}{a_0(\alpha')} \cong \frac{\nu_{in}}{\omega}\frac{\omega t}{2\pi}2\pi h_{2\pi} = \nu_{in}t \cdot h_{2\pi} = \frac{\nu_{in}}{\Omega_i}\omega t \tag{F.8}$$

after a large enough number of cycles, in which Eq.(F.7) is used.

F.2 Evaluation of the second integral

We are also required to evaluate the integral $I(\alpha)$ shown in Eq.(F.2). The inner integral inside it is of the same form as that we just evaluated. Therefore,

$$I(\alpha) = \int_0^{\alpha} \frac{e^{-(\nu_{in}/\Omega_i)\alpha'}}{a_0^2(\alpha')}\mathrm{d}\alpha' \tag{F.9}$$

We once again break the integration into 2π integrals and end up with

$$I(\alpha) = \left(1 + e^{-\frac{\nu_{in}}{\Omega_i}2\pi} + e^{-\frac{\nu_{in}}{\Omega_i}2\pi\cdot 2} + \cdots + e^{-\frac{\nu_{in}}{\Omega_i}2\pi\cdot l} + e^{-\frac{\nu_{in}}{\Omega_i}\varepsilon}\right)\int_0^{2\pi} \frac{e^{-(\nu_{in}/\Omega_i)\alpha'}}{a_0^2(\alpha')}\mathrm{d}\alpha' \tag{F.10}$$

We are still interested in $\varepsilon \ll 2\pi l$ so that the last term in the brackets can be ignored. Then, using

$$\sum_{j=0}^{l-1} e^{-2\pi j(\nu_{in}/\Omega_i)} = \frac{1 - e^{-(\nu_{in}/\Omega_i)\omega t}}{1 - e^{-2\pi(\nu_{in}/\Omega_i)}} \tag{F.11}$$

we have

$$I(\alpha) = \frac{1 - e^{-(\nu_{in}/\Omega_i)\omega t}}{1 - e^{-2\pi(\nu_{in}/\Omega_i)}}\int_0^{2\pi} \frac{e^{-(\nu_{in}/\Omega_i)\alpha'}}{a_0^2(\alpha')}\mathrm{d}\alpha' \cong \frac{1 - e^{-(\nu_{in}/\Omega_i)\omega t}}{1 - e^{-2\pi(\nu_{in}/\Omega_i)}}\int_0^{2\pi} \frac{e^{-(\nu_{in}/\Omega_i)\alpha'}}{a_0^2(\alpha')}\mathrm{d}\alpha' \tag{F.12}$$

from Eq.(F.10).

F.3 Expression of N_i

Use Eqs.(F.8,F.12) in Eq.(F.1). We obtain

$$N_i \cong \frac{n_{i0}}{a_0(t)} + n_{i0}\frac{\nu_{in}}{\omega}\frac{e^{(\nu_{in}/\Omega_i)\omega t}-1}{1-e^{-2\pi(\nu_{in}/\Omega_i)}}\int_0^{2\pi}\frac{1}{a_0^2(\alpha')}\mathrm{d}\alpha' \tag{F.13}$$

in which $e^{-(\nu_{in}/\Omega_i)\alpha'} \cong 1$ is used. Because $1-e^{-2\pi(\nu_{in}/\Omega_i)} \cong 2\pi(\nu_{in}/\Omega_i)$, Eq.(F.13) becomes

$$N_i \cong \frac{n_{i0}}{a_0(t)} + n_{i0}\frac{\Omega_i}{\omega}\frac{e^{(\nu_{in}/\Omega_i)\omega t}-1}{2\pi}\int_0^{2\pi}\frac{1}{a_0^2(\alpha')}\mathrm{d}\alpha' \tag{F.14}$$

Using the expression of a_0 in Eq.(2.19) again, we have

$$\int_0^{2\pi}\frac{\mathrm{d}\alpha'}{a_0^2(\alpha')} = 2\pi a_1\frac{\omega}{\Omega_i} \tag{F.15}$$

where $a_1 = 1+2(E_c/B)/(R_c\Omega_i)$. The derivations of this result is shown below in the last section. Therefore,

$$N_i = n_{i0}\left\{\frac{1}{a_0} + a_1\left[e^{(\nu_{in}/\Omega_i)\omega t}-1\right]\right\} \tag{F.16}$$

F.4 Expression of f_i

For the expression of f_i, let's start from substituting Eq.(3.21) directly in Eq.(3.6):

$$f_i = f_{\mathrm{i}1}e^{-\nu_{in}t} + n_{i0}\frac{\nu_{in}}{n_{\mathrm{n}}}e^{-\nu_{in}t}\int_0^t\left\{\frac{1}{a_0} + a_1\left[e^{(\nu_{in}/\Omega_i)\omega t'}-1\right]\right\}f_{\mathrm{n}}(t')\mathrm{d}t' \tag{F.17}$$

Using ωt instead of t and performing similar manipulations as done above for N_i, this equation becomes

$$\left.\begin{array}{l} f_i = f_{\mathrm{i}1}e^{-\nu_{in}t} + \dfrac{n_{i0}}{n_{\mathrm{n}}}\dfrac{\nu_{in}}{\omega}e^{-\nu_{in}t}. \\ \cdot\left\{\int_0^{\omega t}\left(a_0^{-1}-a_1\right)f_{\mathrm{n}}(\alpha')\mathrm{d}\alpha' + \int_0^{\omega t}a_1e^{(\nu_{in}/\Omega_i)\alpha'}f_{\mathrm{n}}(\alpha')\mathrm{d}\alpha'\right\} \end{array}\right\} \tag{F.18}$$

or,

$$\left.\begin{array}{l} f_i = f_{\mathrm{i}1}e^{-\nu_{in}t} + \dfrac{n_{i0}}{n_{\mathrm{n}}}\dfrac{\nu_{in}}{\omega}e^{-\nu_{in}t}. \\ \cdot\left\{\dfrac{\omega t}{2\pi}\int_0^{2\pi}\left(a_0^{-1}-a_1\right)f_{\mathrm{n}}(\alpha')\mathrm{d}\alpha' + a_1\dfrac{1-e^{(\nu_{in}/\Omega_i)\omega t}}{1-e^{2\pi\nu_{in}/\Omega_i}}\int_0^{2\pi}e^{(\nu_{in}/\Omega_i)\alpha'}f_{\mathrm{n}}(\alpha')\mathrm{d}\alpha'\right\} + J_l' \end{array}\right\} \tag{F.19}$$

in which

$$J_l' = \frac{n_{i0}}{n_{\mathrm{n}}}\frac{\nu_{in}}{\omega}e^{-\nu_{in}t}\left\{\int_0^{\epsilon}\left(\frac{1}{a_0}-a_1\right)f_{\mathrm{n}}(\alpha')\mathrm{d}\alpha' + a_1\int_0^{\epsilon}e^{(\nu_{in}/\Omega_i)\alpha'}f_{\mathrm{n}}(\alpha')\mathrm{d}\alpha'\right\} \quad \text{(F.20)}$$

The fact that ν_{in}/Ω_i is very small makes $e^{2\pi\nu_{in}/\Omega_i} \approx 1+2\pi\nu_{in}/\Omega_i$, $e^{(\nu_{in}/\Omega_i)\alpha'} \approx 1$, and $J_l' \to 0$. Thus,

$$\left.\begin{aligned} f_i &= f_{i1}e^{-\nu_{in}t} + \frac{n_{i0}}{n_{\mathrm{n}}}\frac{\nu_{in}}{\omega}e^{-\nu_{in}t}\cdot \\ &\cdot\left[\frac{\omega t}{2\pi}\int_0^{2\pi}\left(\frac{1}{a_0}-a_1\right)f_{\mathrm{n}}(\alpha')\mathrm{d}\alpha' + a_1\frac{e^{(\omega/\Omega_i)\nu_{in}t}-1}{2\pi\nu_{in}/\Omega_i}\int_0^{2\pi}f_{\mathrm{n}}(\alpha')\mathrm{d}\alpha'\right] \end{aligned}\right\} \quad \text{(F.21)}$$

Appendix G

Formulae for Velocity Moments

G.1 Initially homogeneous Ion Density

A series of mathematical formulae must be used in the calculation of velocity momenta. I derived these formulae as follows.

There are four useful formulae,

$$\int_0^{\pi} \frac{\mathrm{d}\alpha}{a_1 \pm a_2 \cos\alpha} = \frac{1}{2}\int_0^{2\pi} \frac{\mathrm{d}\alpha}{a_1 + a_2\cos\alpha} = \frac{\pi}{\sqrt{a_1^2 - a_2^2}} \tag{G.1}$$

$$\int_0^{2\pi} \frac{\sin\alpha \cdot \mathrm{d}\alpha}{(a_1 + a_2\cos\alpha)^3} = 0 \tag{G.2}$$

$$\left.\begin{aligned} &\textstyle\int_0^{\pi} \frac{\mathrm{d}\alpha}{(a_1 + a_2\cos\alpha)^{k+1}} = \\ &= \frac{(2k-1)a_1}{k(a_1^2 - a_2^2)} \textstyle\int_0^{\pi} \frac{\mathrm{d}\alpha}{(a_1 + a_2\cos\alpha)^k} - \frac{k-1}{k(a_1^2 - a_2^2)} \int_0^{\pi} \frac{\mathrm{d}\alpha}{(a_1 + a_2\cos\alpha)^{k-1}} \end{aligned}\right\} \tag{G.3}$$

$$\int_0^{\pi} \frac{\sin^k\alpha \cdot \mathrm{d}\alpha}{(a_1 + a_2\cos\alpha)^{k+1}} = \frac{\sqrt{\pi} \cdot \Gamma\left(\dfrac{k+1}{2}\right)}{(a_1^2 - a_2^2)^{\dfrac{k+1}{2}} \cdot \Gamma\left(\dfrac{k+2}{2}\right)} \tag{G.4}$$

where $a_1^2 > a_2^2$, k is an integer, and $k > -1$ for the upper one, and $k > 0$ for the lower one.

Above equations produce following equalities:

$$\left.\begin{array}{ll}
\int_0^\pi \frac{\mathrm{d}\alpha}{(a_1 \pm a_2\cos\alpha)^2} = \frac{\pi a_1}{\sqrt{(a_1^2-a_2^2)^3}} , & \int_0^\pi \frac{\mathrm{d}\alpha}{(a_1 \pm a_2\cos\alpha)^3} = \frac{\pi(a_1^2+\frac{1}{2}a_2^2)}{\sqrt{(a_1^2-a_2^2)^5}} \\
\int_0^\pi \frac{\mathrm{d}\alpha}{(a_1 \pm a_2\cos\alpha)^4} = \frac{\pi a_1(a_1^2+\frac{3}{2}a_2^2)}{\sqrt{(a_1^2-a_2^2)^7}} , & \int_0^\pi \frac{\cos\alpha\cdot\mathrm{d}\alpha}{(a_1 \pm a_2\cos\alpha)^2} = \mp\frac{\pi a_2}{\sqrt{(a_1^2-a_2^2)^3}} \\
\int_0^\pi \frac{\cos\alpha\cdot\mathrm{d}\alpha}{(a_1 \pm a_2\cos\alpha)^3} = \mp\frac{\frac{3}{2}\pi a_1 a_2}{\sqrt{(a_1^2-a_2^2)^5}} , & \int_0^\pi \frac{\cos^2\alpha\cdot\mathrm{d}\alpha}{(a_1 \pm a_2\cos\alpha)^3} = \frac{\pi(\frac{1}{2}a_1^2+a_2^2)}{\sqrt{(a_1^2-a_2^2)^5}} \\
\int_0^\pi \frac{\cos\alpha\cdot\mathrm{d}\alpha}{(a_1 \pm a_2\cos\alpha)^4} = \mp\frac{\pi a_2(2a_1^2+\frac{1}{2}a_2^2)}{\sqrt{(a_1^2-a_2^2)^7}} , & \int_0^\pi \frac{\cos^2\alpha\cdot\mathrm{d}\alpha}{(a_1 \pm a_2\cos\alpha)^4} = \frac{\pi a_1(\frac{1}{2}a_1^2+2a_2^2)}{\sqrt{(a_1^2-a_2^2)^7}} \\
\int_0^\pi \frac{\cos^3\alpha\cdot\mathrm{d}\alpha}{(a_1 \pm a_2\cos\alpha)^4} = \mp\frac{\pi a_2(\frac{3}{2}a_1^2+a_2^2)}{\sqrt{(a_1^2-a_2^2)^7}} , & \int_0^\pi \frac{\sin\alpha\cdot\mathrm{d}\alpha}{(a_1 \pm a_2\cos\alpha)^2} = \frac{2}{a_1^2-a_2^2} \\
\int_0^\pi \frac{\sin^2\alpha\cdot\mathrm{d}\alpha}{(a_1 \pm a_2\cos\alpha)^3} = \frac{\pi/2}{(a_1^2-a_2^2)^{3/2}} , & \int_0^\pi \frac{\sin^3\alpha\cdot\mathrm{d}\alpha}{(a_1 \pm a_2\cos\alpha)^4} = \frac{4/3}{(a_1^2-a_2^2)^2}
\end{array}\right\} \tag{G.5}$$

Thus,

$$\left.\begin{array}{ll}
\int_0^{2\pi} \frac{\mathrm{d}\alpha}{(a_1 + a_2\cos\alpha)^2} = \frac{2\pi a_1}{\sqrt{(a_1^2-a_2^2)^3}} , & \int_0^{2\pi} \frac{\mathrm{d}\alpha}{(a_1 + a_2\cos\alpha)^3} = \frac{2\pi(a_1^2+\frac{1}{2}a_2^2)}{\sqrt{(a_1^2-a_2^2)^5}} \\
\int_0^{2\pi} \frac{\mathrm{d}\alpha}{(a_1 + a_2\cos\alpha)^4} = \frac{2\pi a_1(a_1^2+\frac{3}{2}a_2^2)}{\sqrt{(a_1^2-a_2^2)^7}} , & \int_0^{2\pi} \frac{\cos\alpha\cdot\mathrm{d}\alpha}{(a_1 + a_2\cos\alpha)^2} = -\frac{2\pi a_2}{\sqrt{(a_1^2-a_2^2)^3}} \\
\int_0^{2\pi} \frac{\cos\alpha\cdot\mathrm{d}\alpha}{(a_1 + a_2\cos\alpha)^3} = -\frac{3\pi a_1 a_2}{\sqrt{(a_1^2-a_2^2)^5}} , & \int_0^{2\pi} \frac{\cos^2\alpha\cdot\mathrm{d}\alpha}{(a_1 + a_2\cos\alpha)^3} = \frac{\pi(a_1^2+2a_2^2)}{\sqrt{(a_1^2-a_2^2)^5}} \\
\int_0^{2\pi} \frac{\cos\alpha\cdot\mathrm{d}\alpha}{(a_1 + a_2\cos\alpha)^4} = -\frac{\pi a_2(4a_1^2+a_2^2)}{\sqrt{(a_1^2-a_2^2)^7}} , & \int_0^{2\pi} \frac{\cos^2\alpha\cdot\mathrm{d}\alpha}{(a_1 + a_2\cos\alpha)^4} = \frac{\pi a_1(a_1^2+4a_2^2)}{\sqrt{(a_1^2-a_2^2)^7}} \\
\int_0^{2\pi} \frac{\cos^3\alpha\cdot\mathrm{d}\alpha}{(a_1 + a_2\cos\alpha)^4} = -\frac{\pi a_2(3a_1^2+2a_2^2)}{\sqrt{(a_1^2-a_2^2)^7}} , & \int_0^{2\pi} \frac{\sin\alpha\cdot\mathrm{d}\alpha}{(a_1 + a_2\cos\alpha)^2} = 0 \\
\int_0^{2\pi} \frac{\sin^2\alpha\cdot\mathrm{d}\alpha}{(a_1 + a_2\cos\alpha)^3} = \frac{\pi}{(a_1^2-a_2^2)^{3/2}} , & \int_0^{2\pi} \frac{\sin^3\alpha\cdot\mathrm{d}\alpha}{(a_1 + a_2\cos\alpha)^4} = 0
\end{array}\right\} \tag{G.6}$$

which produces

$$\left.\begin{array}{l}
\int_0^{2\pi} \frac{1-\cos\alpha}{(a_1 + a_2\cos\alpha)^2}\mathrm{d}\alpha = \frac{2\pi}{\sqrt{(a_1+a_2)(a_1-a_2)^3}} \\
\int_0^{2\pi} \frac{1-\cos\alpha}{(a_1 + a_2\cos\alpha)^3}\mathrm{d}\alpha = \frac{\pi(2a_1+a_2)}{\sqrt{(a_1+a_2)^3(a_1-a_2)^5}} \\
\int_0^{2\pi} \frac{(1-\cos\alpha)^2}{(a_1 + a_2\cos\alpha)^3}\mathrm{d}\alpha = \frac{3\pi}{\sqrt{(a_1+a_2)(a_1-a_2)^5}} \\
\int_0^{2\pi} \frac{(1-\cos\alpha)^3}{(a_1 + a_2\cos\alpha)^4}\mathrm{d}\alpha = \frac{5\pi}{\sqrt{(a_1+a_2)(a_1-a_2)^7}}
\end{array}\right\} \tag{G.7}$$

Above formulae give

$$\int_0^{2\pi} \frac{v'_{\mathrm{d}r}}{a'_0}\mathrm{d}\alpha = \frac{E_c}{B}\frac{r}{R_c}(a_1+a_2)^{3/2}\int_0^{2\pi}\frac{\sin\alpha\cdot\mathrm{d}\alpha}{(a_1+a_2\cos\alpha)^2} = 0 \tag{G.8}$$

$$\left.\begin{aligned}&\int_0^{2\pi}\frac{v'_{\mathrm{d}\phi}}{a'_0}\mathrm{d}\alpha = \frac{E_c}{B}\frac{r}{R_c}(a_1+a_2)\int_0^{2\pi}\frac{1-\cos\alpha}{(a_1+a_2\cos\alpha)^2}\mathrm{d}\alpha = \\ &= \frac{E_c}{B}\frac{r}{R_c}(a_1+a_2)\frac{2\pi}{\sqrt{(a_1+a_2)(a_1-a_2)^3}} = 2\pi\frac{E_c}{B}\frac{r}{R_c}\sqrt{\frac{a_1+a_2}{(a_1-a_2)^3}}\end{aligned}\right\} \tag{G.9}$$

$$\left.\begin{aligned}&\int_0^{2\pi}\frac{v'^2_{\mathrm{d}r}}{a'_0}\mathrm{d}\alpha = \left(\frac{E_c}{B}\frac{r}{R_c}\right)^2(a_1+a_2)^2\int_0^{2\pi}\frac{\sin^2\alpha}{(a_1+a_2\cos\alpha)^3}\mathrm{d}\alpha = \\ &= \left(\frac{E_c}{B}\frac{r}{R_c}\right)^2(a_1+a_2)^2\frac{\pi}{(a_1^2-a_2^2)^{3/2}} = \pi\left(\frac{E_c}{B}\frac{r}{R_c}\right)^2\sqrt{\frac{a_1+a_2}{(a_1-a_2)^3}}\end{aligned}\right\} \tag{G.10}$$

$$\left.\begin{aligned}&\int_0^{2\pi}\frac{v'^2_{\mathrm{d}\phi}}{a'_0}\mathrm{d}\alpha = \left(\frac{E_c}{B}\frac{r}{R_c}\right)^2(a_1+a_2)\int_0^{2\pi}\frac{(1-\cos\alpha)^2}{(a_1+a_2\cos\alpha)^3}\mathrm{d}\alpha = \\ &= \left(\frac{E_c}{B}\frac{r}{R_c}\right)^2(a_1+a_2)\frac{3\pi}{\sqrt{(a_1+a_2)(a_1-a_2)^5}} = 3\pi\left(\frac{E_c}{B}\frac{r}{R_c}\right)^2\sqrt{\frac{a_1+a_2}{(a_1-a_2)^5}}\end{aligned}\right\} \tag{G.11}$$

$$\left.\begin{aligned}&\int_0^{2\pi}\frac{1}{a'^2_0}\mathrm{d}\alpha = (a_1+a_2)^2\int_0^{2\pi}\frac{\mathrm{d}\alpha}{(a_1+a_2\cos\alpha)^2} = (a_1+a_2)^2\frac{2\pi a_1}{\sqrt{(a_1^2-a_2^2)^3}} = \\ &= 2\pi a_1\sqrt{\frac{a_1+a_2}{(a_1-a_2)^3}}\end{aligned}\right\} \tag{G.12}$$

$$\left.\begin{aligned}&\int_0^{2\pi}\frac{v'^3_{\mathrm{d}r}}{a'_0}\mathrm{d}\alpha = \left(\frac{E_c}{B}\frac{r}{R_c}\right)^3(a_1+a_2)^{5/2}\int_0^{2\pi}\frac{\sin^3\alpha}{(a_1+a_2\cos\alpha)^4}\mathrm{d}\alpha = \\ &= \left(\frac{E_c}{B}\frac{r}{R_c}\right)^3(a_1+a_2)^{5/2}\cdot 0 = 0\end{aligned}\right\} \tag{G.13}$$

$$\left.\begin{aligned}&\int_0^{2\pi}\frac{v'^3_{\mathrm{d}\phi}}{a'_0}\mathrm{d}\alpha = \left(\frac{E_c}{B}\frac{r}{R_c}\right)^3(a_1+a_2)\int_0^{2\pi}\frac{(1-\cos\alpha)^3}{(a_1+a_2\cos\alpha)^4}\mathrm{d}\alpha = \\ &= \left(\frac{E_c}{B}\frac{r}{R_c}\right)^3(a_1+a_2)\frac{5\pi}{\sqrt{(a_1+a_2)(a_1-a_2)^7}} = 5\pi\left(\frac{E_c}{B}\frac{r}{R_c}\right)^3\sqrt{\frac{a_1+a_2}{(a_1-a_2)^7}}\end{aligned}\right\} \tag{G.14}$$

$$\int_0^{2\pi}\frac{v'_{\mathrm{d}r}}{a'^2_0}\mathrm{d}\alpha = \frac{E_c}{B}\frac{r}{R_c}(a_1+a_2)^{5/2}\int_0^{2\pi}\frac{\sin\alpha}{(a_1+a_2\cos\alpha)^3}\mathrm{d}\alpha = 0 \tag{G.15}$$

$$\left.\begin{aligned}&\int_0^{2\pi}\frac{v'_{\mathrm{d}\phi}}{a'^2_0}\mathrm{d}\alpha = \frac{E_c}{B}\frac{r}{R_c}(a_1+a_2)^2\int_0^{2\pi}\frac{1-\cos\alpha}{(a_1+a_2\cos\alpha)^3}\mathrm{d}\alpha = \\ &= \frac{E_c}{B}\frac{r}{R_c}(a_1+a_2)^2\frac{\pi(2a_1+a_2)}{\sqrt{(a_1+a_2)^3(a_1-a_2)^5}} = \pi\frac{E_c}{B}\frac{r}{R_c}(2a_1+a_2)\sqrt{\frac{a_1+a_2}{(a_1-a_2)^5}}\end{aligned}\right\} \tag{G.16}$$

Therefore,

$$\left.\begin{aligned}
&\int_0^{2\pi}\left(\frac{v_{\mathrm{d}r}'^2}{a_0'}+\frac{k_bT_\mathrm{n}}{m_\mathrm{n}}\frac{1}{a_0'^2}\right)\mathrm{d}\alpha=\pi\left(\frac{E_c}{B}\frac{r}{R_c}\right)^2\sqrt{\frac{a_1+a_2}{(a_1-a_2)^3}}+\\
&+\frac{k_bT_\mathrm{n}}{m_\mathrm{n}}\cdot 2\pi a_1\sqrt{\frac{a_1+a_2}{(a_1-a_2)^3}}=\pi\left[\left(\frac{E_c}{B}\frac{r}{R_c}\right)^2+\frac{2k_bT_\mathrm{n}}{m_\mathrm{n}}a_1\right]\sqrt{\frac{a_1+a_2}{(a_1-a_2)^3}}\ ,\\
&\int_0^{2\pi}\left(\frac{v_{\mathrm{d}\phi}'^2}{a_0'}+\frac{k_bT_\mathrm{n}}{m_\mathrm{n}}\frac{1}{a_0'^2}\right)\mathrm{d}\alpha=3\pi\left(\frac{E_c}{B}\frac{r}{R_c}\right)^2\sqrt{\frac{a_1+a_2}{(a_1-a_2)^5}}+\\
&+\frac{k_bT_\mathrm{n}}{m_\mathrm{n}}\cdot 2\pi a_1\sqrt{\frac{a_1+a_2}{(a_1-a_2)^3}}=\pi\left[3\left(\frac{E_c}{B}\frac{r}{R_c}\right)^2+\frac{2k_bT_\mathrm{n}}{m_\mathrm{n}}a_1\right]\sqrt{\frac{a_1+a_2}{(a_1-a_2)^3}}\ ,\\
&\int_0^{2\pi}\left(\frac{v_{\mathrm{d}r}'^3}{a_0'}+\frac{3k_bT_\mathrm{n}}{m_\mathrm{n}}\frac{v_{\mathrm{d}r}'}{a_0'^2}\right)\mathrm{d}\alpha=0\ ,\\
&\int_0^{2\pi}\left(\frac{v_{\mathrm{d}\phi}'^3}{a_0'}+\frac{3k_bT_\mathrm{n}}{m_\mathrm{n}}\frac{v_{\mathrm{d}\phi}'}{a_0'^2}\right)\mathrm{d}\alpha=5\pi\left(\frac{E_c}{B}\frac{r}{R_c}\right)^3\sqrt{\frac{a_1+a_2}{(a_1-a_2)^7}}+\\
&+\frac{3k_bT_\mathrm{n}}{m_\mathrm{n}}\cdot\pi\frac{E_c}{B}\frac{r}{R_c}(2a_1+a_2)\sqrt{\frac{a_1+a_2}{(a_1-a_2)^5}}=\\
&=\pi\frac{E_c}{B}\frac{r}{R_c}\sqrt{\frac{a_1+a_2}{(a_1-a_2)^5}}\left[\frac{5}{a_1-a_2}\left(\frac{E_c}{B}\frac{r}{R_c}\right)^2+(2a_1+a_2)\frac{3k_bT_\mathrm{n}}{m_\mathrm{n}}\right]
\end{aligned}\right\}\qquad(\mathrm{G}.17)$$

Considering

$$\left.\begin{aligned}
&a_1=1+2\frac{E_c/B}{R_c\Omega_i}\ ,\quad a_2=2\frac{E_c/B}{R_c\Omega_i}\\
&a_1+a_2=1+4\frac{E_c/B}{R_c\Omega_i}=\left(\frac{\omega}{\Omega_i}\right)^2\ ,\quad a_1-a_2=1
\end{aligned}\right\}\qquad(\mathrm{G}.18)$$

there exist following relations:

$$\left.\begin{aligned}
&\int_0^{2\pi}\frac{v_{\mathrm{d}r}'}{a_0'}\mathrm{d}\alpha=0\\
&\int_0^{2\pi}\frac{v_{\mathrm{d}\phi}'}{a_0'}\mathrm{d}\alpha=2\pi\frac{\omega}{\Omega_i}\frac{E_c}{B}\frac{r}{R_c}\\
&\int_0^{2\pi}\left(\frac{v_{\mathrm{d}r}'^2}{a_0'}+\frac{k_bT_\mathrm{n}}{m_\mathrm{n}}\frac{1}{a_0'^2}\right)\mathrm{d}\alpha=2\pi\frac{\omega}{\Omega_i}\left[\frac{1}{2}\left(\frac{E_c}{B}\frac{r}{R_c}\right)^2+a_1\frac{k_bT_\mathrm{n}}{m_\mathrm{n}}\right]\\
&\int_0^{2\pi}\left(\frac{v_{\mathrm{d}\phi}'^2}{a_0'}+\frac{k_bT_\mathrm{n}}{m_\mathrm{n}}\frac{1}{a_0'^2}\right)\mathrm{d}\alpha=2\pi\frac{\omega}{\Omega_i}\left[\frac{3}{2}\left(\frac{E_c}{B}\frac{r}{R_c}\right)^2+a_1\frac{k_bT_\mathrm{n}}{m_\mathrm{n}}\right]\\
&\int_0^{2\pi}\left(\frac{v_{\mathrm{d}r}'^3}{a_0'}+\frac{3k_bT_\mathrm{n}}{m_\mathrm{n}}\frac{v_{\mathrm{d}r}'}{a_0'^2}\right)\mathrm{d}\alpha=0\\
&\int_0^{2\pi}\left(\frac{v_{\mathrm{d}\phi}'^3}{a_0'}+\frac{3k_bT_\mathrm{n}}{m_\mathrm{n}}\frac{v_{\mathrm{d}\phi}'}{a_0'^2}\right)\mathrm{d}\alpha=\\
&=2\pi\frac{\omega}{\Omega_i}\frac{E_c}{B}\frac{r}{R_c}\left\{\frac{5}{2}\left(\frac{E_c}{B}\frac{r}{R_c}\right)^2+\left[\left(\frac{\omega}{\Omega_i}\right)^2-\frac{E_c/B_0}{R_c\Omega_i}\right]\frac{3k_bT_\mathrm{n}}{m_\mathrm{n}}\right\}
\end{aligned}\right\}\qquad(\mathrm{G}.19)$$

G.2 Initially Inhomogeneous Ion Density

A general class of Gaussian integrals has a form of

$$I_n(\lambda)=\int_0^\infty x^n e^{-\lambda x^2}\mathrm{d}x=\begin{cases}\dfrac{(n-1)!!}{2^{n/2+1}\lambda^{n/2}}\sqrt{\dfrac{\pi}{\lambda}} & \text{for } \ n=0,2,4,\cdots\\ \dfrac{\left(\dfrac{n-1}{2}\right)!}{2\lambda^{(n+1)/2}} & \text{for } \ n=1,3,5,\cdots\end{cases} \tag{G.20}$$

which are convenient in applications. For example, for $n=6$, we have

$$I_6(\lambda)=\int_0^\infty x^6 e^{-\lambda x^2}\mathrm{d}x=\frac{5!!}{2^4\lambda^3}\sqrt{\frac{\pi}{\lambda}}=\frac{15}{16}\frac{\sqrt{\pi}}{\lambda^{7/2}} \tag{G.21}$$

A series of expressions are used in the thesis. They are given as follows:

$$\left.\begin{array}{l}
\frac{1}{\sqrt{\pi}}\int_{-\infty}^{\infty} e^{-\lambda v_x^2}\mathrm{d}v_x=\frac{1}{\sqrt{\lambda}}\\
\frac{1}{\sqrt{\pi}}\int_{-\infty}^{\infty} e^{-\lambda(v_x-v_{\mathrm{d}x})^2}\mathrm{d}v_x=\frac{1}{\sqrt{\lambda}}\\
\frac{1}{\sqrt{\pi}}\int_{-\infty}^{\infty} v_x e^{-\lambda v_x^2}\mathrm{d}v_x=0\\
\frac{1}{\sqrt{\pi}}\int_{-\infty}^{\infty} v_x e^{-\lambda(v_x-v_{\mathrm{d}x})^2}\mathrm{d}v_x=\frac{v_{\mathrm{d}x}}{\sqrt{\lambda}}\\
\frac{1}{\sqrt{\pi}}\int_{-\infty}^{\infty} v_x^2 e^{-\lambda v_x^2}\mathrm{d}v_x=\frac{1}{2\lambda^{3/2}}\\
\frac{1}{\sqrt{\pi}}\int_{-\infty}^{\infty} v_x^2 e^{-\lambda(v_x-v_{\mathrm{d}x})^2}\mathrm{d}v_x=\frac{1}{\sqrt{\lambda}}\left(v_{\mathrm{d}x}^2+\frac{1}{2\lambda}\right)\\
\frac{1}{\sqrt{\pi}}\int_{-\infty}^{\infty} v_x^3 e^{-\lambda v_x^2}\mathrm{d}v_x=0\\
\frac{1}{\sqrt{\pi}}\int_{-\infty}^{\infty} v_x^3 e^{-\lambda(v_x-v_{\mathrm{d}x})^2}\mathrm{d}v_x=\frac{v_{\mathrm{d}x}}{\sqrt{\lambda}}\left(v_{\mathrm{d}x}^2+\frac{3}{2\lambda}\right)\\
\frac{1}{\sqrt{\pi}}\int_{-\infty}^{\infty} v_x^4 e^{-\lambda v_x^2}\mathrm{d}v_x=\frac{3}{4\lambda^{5/2}}\\
\frac{1}{\sqrt{\pi}}\int_{-\infty}^{\infty} v_x^4 e^{-\lambda(v_x-v_{\mathrm{d}x})^2}\mathrm{d}v_x=\frac{1}{\sqrt{\lambda}}\left(v_{\mathrm{d}x}^4+\frac{3v_{\mathrm{d}x}^2}{\lambda}+\frac{3}{4\lambda^2}\right)\\
\frac{1}{\sqrt{\pi}}\int_{-\infty}^{\infty} v_x^5 e^{-\lambda v_x^2}\mathrm{d}v_x=0\\
\frac{1}{\sqrt{\pi}}\int_{-\infty}^{\infty} v_x^5 e^{-\lambda(v_x-v_{\mathrm{d}x})^2}\mathrm{d}v_x=\frac{v_{\mathrm{d}x}}{\sqrt{\lambda}}\left(v_{\mathrm{d}x}^4+\frac{5v_{\mathrm{d}x}^2}{\lambda}+\frac{15}{4\lambda^2}\right)
\end{array}\right\} \tag{G.22}$$

where following polynomial identities are used:

$$\left.\begin{array}{l}
(a+b)^2=a^2+2ab+b^2\\
(a+b)^3=a^3+3a^2b+3ab^2+b^3\\
(a+b)^4=a^4+4a^3b+6a^2b^2+4ab^3+b^4\\
(a+b)^5=a^5+5a^4b+10a^3b^2+10a^2b^3+5ab^4+b^5
\end{array}\right\} \tag{G.23}$$

In addition,

$$\left.\begin{aligned} I_{001} &= \frac{1}{\pi}\int v_r e^{-a_0(\mathbf{v}-\mathbf{v}_\mathrm{d})^2}\mathrm{d}\mathbf{v} = \frac{v_{\mathrm{d}r}}{a_0} \\ I'_{001} &= \frac{1}{\pi}\int v_r e^{-(\alpha_{0c}+a_0)(\mathbf{v}-\beta_2\mathbf{v}_\mathrm{d})^2}\mathrm{d}\mathbf{v} = \frac{\beta_2 v_{\mathrm{d}r}}{\alpha_{0c}+a_0} \end{aligned}\right\} \tag{G.24}$$

$$\left.\begin{aligned} I_{002} &= \frac{1}{\pi}\int v_\phi e^{-a_0(\mathbf{v}-\mathbf{v}_\mathrm{d})^2}\mathrm{d}\mathbf{v} = \frac{v_{\mathrm{d}\phi}}{a_0} \\ I'_{002} &= \frac{1}{\pi}\int v_\phi e^{-(\alpha_{0c}+a_0)(\mathbf{v}-\beta_2\mathbf{v}_\mathrm{d})^2}\mathrm{d}\mathbf{v} = \frac{\beta_2 v_{\mathrm{d}\phi}}{\alpha_{0c}+a_0} \end{aligned}\right\} \tag{G.25}$$

$$\left.\begin{aligned} I_{003} &= \frac{1}{\pi}\int v_r^2 e^{-a_0(\mathbf{v}-\mathbf{v}_\mathrm{d})^2}\mathrm{d}\mathbf{v} = \frac{1}{a_0}\left(v_{\mathrm{d}r}^2 + \frac{1}{2a_0}\right) \\ I'_{003} &= \frac{1}{\pi}\int v_r^2 e^{-(\alpha_{0c}+a_0)(\mathbf{v}-\beta_2\mathbf{v}_\mathrm{d})^2}\mathrm{d}\mathbf{v} = \frac{\beta_2^2 v_{\mathrm{d}r}^2}{\alpha_{0c}+a_0} + \frac{1}{2(\alpha_{0c}+a_0)^2} \end{aligned}\right\} \tag{G.26}$$

$$\left.\begin{aligned} I_{004} &= \frac{1}{\pi}\int v_\phi^2 e^{-a_0(\mathbf{v}-\mathbf{v}_\mathrm{d})^2}\mathrm{d}\mathbf{v} = \frac{1}{a_0}\left(v_{\mathrm{d}\phi}^2 + \frac{1}{2a_0}\right) \\ I'_{004} &= \frac{1}{\pi}\int v_\phi^2 e^{-(\alpha_{0c}+a_0)(\mathbf{v}-\beta_2\mathbf{v}_\mathrm{d})^2}\mathrm{d}\mathbf{v} = \frac{\beta_2^2 v_{\mathrm{d}\phi}^2}{\alpha_{0c}+a_0} + \frac{1}{2(\alpha_{0c}+a_0)^2} \end{aligned}\right\} \tag{G.27}$$

$$\left.\begin{aligned} I_{005} &= \frac{1}{\pi}\int v_r^3 e^{-a_0(\mathbf{v}-\mathbf{v}_\mathrm{d})^2}\mathrm{d}\mathbf{v} = \frac{v_{\mathrm{d}r}}{a_0}\left(v_{\mathrm{d}r}^2 + \frac{3}{2a_0}\right) \\ I'_{005} &= \frac{1}{\pi}\int v_r^3 e^{-(\alpha_{0c}+a_0)(\mathbf{v}-\beta_2\mathbf{v}_\mathrm{d})^2}\mathrm{d}\mathbf{v} = \frac{\beta_2 v_{\mathrm{d}r}}{\alpha_{0c}+a_0}\left(\beta_2^2 v_{\mathrm{d}r}^2 + \frac{3}{2(\alpha_{0c}+a_0)}\right) \end{aligned}\right\} \tag{G.28}$$

$$\left.\begin{aligned} I_{006} &= \frac{1}{\pi}\int v_\phi^3 e^{-a_0(\mathbf{v}-\mathbf{v}_\mathrm{d})^2}\mathrm{d}\mathbf{v} = \frac{v_{\mathrm{d}\phi}}{a_0}\left(v_{\mathrm{d}\phi}^2 + \frac{3}{2a_0}\right) \\ I'_{006} &= \frac{1}{\pi}\int v_\phi^3 e^{-(\alpha_{0c}+a_0)(\mathbf{v}-\beta_2\mathbf{v}_\mathrm{d})^2}\mathrm{d}\mathbf{v} = \frac{\beta_2 v_{\mathrm{d}\phi}}{\alpha_{0c}+a_0}\left(\beta_2^2 v_{\mathrm{d}\phi}^2 + \frac{3}{2(\alpha_{0c}+a_0)}\right) \end{aligned}\right\} \tag{G.29}$$

$$\left.\begin{aligned} I_{007} &= \frac{1}{\pi}\int v_r^4 e^{-a_0(\mathbf{v}-\mathbf{v}_\mathrm{d})^2}\mathrm{d}\mathbf{v} = \frac{1}{a_0}\left(v_{\mathrm{d}r}^4 + \frac{3v_{\mathrm{d}r}^2}{a_0} + \frac{3}{4a_0^2}\right) \\ I'_{007} &= \frac{1}{\pi}\int v_r^4 e^{-(\alpha_{0c}+a_0)(\mathbf{v}-\beta_2\mathbf{v}_\mathrm{d})^2}\mathrm{d}\mathbf{v} = \\ &= \frac{1}{\alpha_{0c}+a_0}\left(\beta_2^4 v_{\mathrm{d}r}^4 + \frac{3\beta_2^2 v_{\mathrm{d}r}^2}{\alpha_{0c}+a_0} + \frac{3}{4(\alpha_{0c}+a_0)^2}\right) \end{aligned}\right\} \tag{G.30}$$

$$\left.\begin{aligned} I_{008} &= \frac{1}{\pi}\int v_\phi^4 e^{-a_0(\mathbf{v}-\mathbf{v}_\mathrm{d})^2}\mathrm{d}\mathbf{v} = \frac{1}{a_0}\left(v_{\mathrm{d}\phi}^4 + \frac{3v_{\mathrm{d}\phi}^2}{a_0} + \frac{3}{4a_0^2}\right) \\ I'_{008} &= \frac{1}{\pi}\int v_\phi^4 e^{-(\alpha_{0c}+a_0)(\mathbf{v}-\beta_2\mathbf{v}_\mathrm{d})^2}\mathrm{d}\mathbf{v} = \\ &= \frac{1}{\alpha_{0c}+a_0}\left(\beta_2^4 v_{\mathrm{d}\phi}^4 + \frac{3\beta_2^2 v_{\mathrm{d}\phi}^2}{\alpha_{0c}+a_0} + \frac{3}{4(\alpha_{0c}+a_0)^2}\right) \end{aligned}\right\} \tag{G.31}$$

$$\left.\begin{aligned} I_{009} &= \frac{1}{\pi}\int v_r^5 e^{-a_0(\mathbf{v}-\mathbf{v}_\mathrm{d})^2}\mathrm{d}\mathbf{v} = \frac{v_{\mathrm{d}r}}{a_0}\left(v_{\mathrm{d}r}^4 + 5\frac{v_{\mathrm{d}r}^2}{a_0} + \frac{15}{4a_0^2}\right) \\ I'_{009} &= \frac{1}{\pi}\int v_r^5 e^{-(\alpha_{0c}+a_0)(\mathbf{v}-\beta_2\mathbf{v}_\mathrm{d})^2}\mathrm{d}\mathbf{v} = \\ &= \frac{\beta_2 v_{\mathrm{d}r}}{\alpha_{0c}+a_0}\left(\beta_2^4 v_{\mathrm{d}r}^4 + 5\frac{\beta_2^2 v_{\mathrm{d}r}^2}{\alpha_{0c}+a_0} + \frac{15}{4(\alpha_{0c}+a_0)^2}\right) \end{aligned}\right\} \tag{G.32}$$

$$\left.\begin{aligned} I_{010} &= \frac{1}{\pi}\int v_\phi^5 e^{-a_0(\mathbf{v}-\mathbf{v}_\mathrm{d})^2}\mathrm{d}\mathbf{v} = \frac{v_{\mathrm{d}\phi}}{a_0}\left(v_{\mathrm{d}\phi}^4 + 5\frac{v_{\mathrm{d}\phi}^2}{a_0} + \frac{15}{4a_0^2}\right) \\ I'_{010} &= \frac{1}{\pi}\int v_\phi^5 e^{-(\alpha_{0c}+a_0)(\mathbf{v}-\beta_2\mathbf{v}_\mathrm{d})^2}\mathrm{d}\mathbf{v} = \\ &= \frac{\beta_2 v_{\mathrm{d}\phi}}{\alpha_{0c}+a_0}\left(\beta_2^4 v_{\mathrm{d}\phi}^4 + 5\frac{\beta_2^2 v_{\mathrm{d}\phi}^2}{\alpha_{0c}+a_0} + \frac{15}{4(\alpha_{0c}+a_0)^2}\right) \end{aligned}\right\} \tag{G.33}$$

$$\left.\begin{aligned} I_{011} &= \frac{1}{\pi}\int v_r v_\phi e^{-a_0(\mathbf{v}-\mathbf{v}_\mathrm{d})^2}\mathrm{d}\mathbf{v} = \frac{v_{\mathrm{d}r} v_{\mathrm{d}\phi}}{a_0} \\ I'_{011} &= \frac{1}{\pi}\int v_r v_\phi e^{-(\alpha_{0c}+a_0)(\mathbf{v}-\beta_2\mathbf{v}_\mathrm{d})^2}\mathrm{d}\mathbf{v} = \frac{\beta_2^2 v_{\mathrm{d}r} v_{\mathrm{d}\phi}}{\alpha_{0c}+a_0} \end{aligned}\right\} \tag{G.34}$$

$$\left.\begin{aligned} I_{012} &= \frac{1}{\pi}\int v_r^2 v_\phi^2 e^{-a_0(\mathbf{v}-\mathbf{v}_\mathrm{d})^2}\mathrm{d}\mathbf{v} = \frac{1}{a_0}\left(v_{\mathrm{d}r}^2 + \frac{1}{2a_0}\right)\left(v_{\mathrm{d}\phi}^2 + \frac{1}{2a_0}\right) \\ I'_{012} &= \frac{1}{\pi}\int v_r^2 v_\phi^2 e^{-(\alpha_{0c}+a_0)(\mathbf{v}-\beta_2\mathbf{v}_\mathrm{d})^2}\mathrm{d}\mathbf{v} = \\ &= \frac{1}{\alpha_{0c}+a_0}\left(\beta_2^2 v_{\mathrm{d}r}^2 + \frac{1}{2(\alpha_{0c}+a_0)}\right)\left(\beta_2^2 v_{\mathrm{d}\phi}^2 + \frac{1}{2(\alpha_{0c}+a_0)}\right) \end{aligned}\right\} \tag{G.35}$$

$$\left.\begin{aligned} I_{013} &= \frac{1}{\pi}\int v_r v_\phi^2 e^{-a_0(\mathbf{v}-\mathbf{v}_\mathrm{d})^2}\mathrm{d}\mathbf{v} = \frac{v_{\mathrm{d}r}}{a_0}\left(v_{\mathrm{d}\phi}^2 + \frac{1}{2a_0}\right) \\ I'_{013} &= \frac{1}{\pi}\int v_r v_\phi^2 e^{-(\alpha_{0c}+a_0)(\mathbf{v}-\beta_2\mathbf{v}_\mathrm{d})^2}\mathrm{d}\mathbf{v} = \frac{\beta_2 v_{\mathrm{d}r}}{\alpha_{0c}+a_0}\left(\beta_2^2 v_{\mathrm{d}\phi}^2 + \frac{1}{2(\alpha_{0c}+a_0)}\right) \end{aligned}\right\} \tag{G.36}$$

$$\left.\begin{aligned} I_{014} &= \frac{1}{\pi}\int v_r^2 v_\phi e^{-a_0(\mathbf{v}-\mathbf{v}_\mathrm{d})^2}\mathrm{d}\mathbf{v} = \frac{v_{\mathrm{d}\phi}}{a_0}\left(v_{\mathrm{d}r}^2 + \frac{1}{2a_0}\right) \\ I'_{014} &= \frac{1}{\pi}\int v_r^2 v_\phi e^{-(\alpha_{0c}+a_0)(\mathbf{v}-\beta_2\mathbf{v}_\mathrm{d})^2}\mathrm{d}\mathbf{v} = \frac{\beta_2 v_{\mathrm{d}\phi}}{\alpha_{0c}+a_0}\left(\beta_2^2 v_{\mathrm{d}r}^2 + \frac{1}{2(\alpha_{0c}+a_0)}\right) \end{aligned}\right\} \tag{G.37}$$

$$\left.\begin{aligned} I_{015} &= \frac{1}{\pi}\int v_r^3 v_\phi e^{-a_0(\mathbf{v}-\mathbf{v}_\mathrm{d})^2}\mathrm{d}\mathbf{v} = \frac{v_{\mathrm{d}r} v_{\mathrm{d}\phi}}{a_0}\left(v_{\mathrm{d}r}^2 + \frac{3}{2a_0}\right) \\ I'_{015} &= \frac{1}{\pi}\int v_r^3 v_\phi e^{-(\alpha_{0c}+a_0)(\mathbf{v}-\beta_2\mathbf{v}_\mathrm{d})^2}\mathrm{d}\mathbf{v} = \frac{\beta_2^2 v_{\mathrm{d}r} v_{\mathrm{d}\phi}}{\alpha_{0c}+a_0}\left(\beta_2^2 v_{\mathrm{d}r}^2 + \frac{3}{2(\alpha_{0c}+a_0)}\right) \end{aligned}\right\} \tag{G.38}$$

$$\left.\begin{aligned} I_{016} &= \frac{1}{\pi}\int v_r v_\phi^3 e^{-a_0(\mathbf{v}-\mathbf{v}_\mathrm{d})^2}\mathrm{d}\mathbf{v} = \frac{v_{\mathrm{d}r} v_{\mathrm{d}\phi}}{a_0}\left(v_{\mathrm{d}\phi}^2 + \frac{3}{2a_0}\right) \\ I'_{016} &= \frac{1}{\pi}\int v_r v_\phi^3 e^{-(\alpha_{0c}+a_0)(\mathbf{v}-\beta_2\mathbf{v}_\mathrm{d})^2}\mathrm{d}\mathbf{v} = \frac{\beta_2^2 v_{\mathrm{d}r} v_{\mathrm{d}\phi}}{\alpha_{0c}+a_0}\left(\beta_2^2 v_{\mathrm{d}\phi}^2 + \frac{3}{2(\alpha_{0c}+a_0)}\right) \end{aligned}\right\} \tag{G.39}$$

$$\left.\begin{aligned} I_{017} &= \frac{1}{\pi}\int v_r^3 v_\phi^2 e^{-a_0(\mathbf{v}-\mathbf{v}_\mathrm{d})^2}\mathrm{d}\mathbf{v} = \frac{v_{\mathrm{d}r}}{a_0}\left(v_{\mathrm{d}r}^2 + \frac{3}{2a_0}\right)\left(v_{\mathrm{d}\phi}^2 + \frac{1}{2a_0}\right) \\ I'_{017} &= \frac{1}{\pi}\int v_r^3 v_\phi^2 e^{-(\alpha_{0c}+a_0)(\mathbf{v}-\beta_2\mathbf{v}_\mathrm{d})^2}\mathrm{d}\mathbf{v} = \\ &= \frac{\beta_2 v_{\mathrm{d}r}}{\alpha_{0c}+a_0}\left(\beta_2^2 v_{\mathrm{d}r}^2 + \frac{3}{2(\alpha_{0c}+a_0)}\right)\left(\beta_2^2 v_{\mathrm{d}\phi}^2 + \frac{1}{2(\alpha_{0c}+a_0)}\right) \end{aligned}\right\} \tag{G.40}$$

$$\left.\begin{aligned} I_{018} &= \frac{1}{\pi}\int v_r^2 v_\phi^3 e^{-a_0(\mathbf{v}-\mathbf{v}_\mathrm{d})^2}\mathrm{d}\mathbf{v} = \frac{v_{\mathrm{d}\phi}}{a_0}\left(v_{\mathrm{d}r}^2 + \frac{1}{2a_0}\right)\left(v_{\mathrm{d}\phi}^2 + \frac{3}{2a_0}\right) \\ I'_{018} &= \frac{1}{\pi}\int v_r^2 v_\phi^3 e^{-(\alpha_{0c}+a_0)(\mathbf{v}-\beta_2\mathbf{v}_\mathrm{d})^2}\mathrm{d}\mathbf{v} = \\ &= \frac{\beta_2 v_{\mathrm{d}\phi}}{\alpha_{0c}+a_0}\left(\beta_2^2 v_{\mathrm{d}r}^2 + \frac{1}{2(\alpha_{0c}+a_0)}\right)\left(\beta_2^2 v_{\mathrm{d}\phi}^2 + \frac{3}{2(\alpha_{0c}+a_0)}\right) \end{aligned}\right\} \tag{G.41}$$

Using above expressions, we have

$$\left.\begin{aligned}
&I_1 = \int_{-\infty}^{\infty} v_r f_i(\mathbf{r},\mathbf{v},t)\mathrm{d}\mathbf{v} = \frac{n_0}{\pi}\int_{-\infty}^{\infty} v_r e^{-a_0\left[(v_r-v_{\mathrm{d}r})^2+(v_\phi-v_{\mathrm{d}\phi})^2\right]}\mathrm{d}\mathbf{v}+\\
&+\frac{n_{0r}}{\pi}\alpha_{0c}\int_{-\infty}^{\infty} v_r\left[v_r^2+v_\phi^2+\beta_1^2\mathbf{v}_{\mathrm{d}}^2-2\beta_1\left(v_{\mathrm{d}r}v_r+v_{\mathrm{d}\phi}v_\phi\right)\right]\cdot\\
&\cdot e^{-(\alpha_{0c}+a_0)\left[(v_r-\beta_2 v_{\mathrm{d}r})^2+\left(v_\phi-\beta_2 v_{\mathrm{d}\phi}\right)^2\right]}\mathrm{d}\mathbf{v} =\\
&= n_0\frac{v_{\mathrm{d}r}}{a_0}+\frac{n_{0r}}{\pi}\alpha_{0c}\int_{-\infty}^{\infty}\left[v_r^3+v_rv_\phi^2+\beta_1^2\mathbf{v}_{\mathrm{d}}^2v_r-2\beta_1\left(v_{\mathrm{d}r}v_r^2+v_{\mathrm{d}\phi}v_rv_\phi\right)\right]\cdot\\
&\cdot e^{-(\alpha_{0c}+a_0)\left[(v_r-\beta_2 v_{\mathrm{d}r})^2+\left(v_\phi-\beta_2 v_{\mathrm{d}\phi}\right)^2\right]}\mathrm{d}\mathbf{v} =\\
&= n_0\frac{v_{\mathrm{d}r}}{a_0}+n_{0r}\alpha_{0c}\cdot\\
&\cdot\left[I'_{005}+I'_{013}+\beta_1^2\left(v_{\mathrm{d}r}^2+v_{\mathrm{d}\phi}^2\right)I'_{001}-2\beta_1\left(v_{\mathrm{d}r}I'_{003}+v_{\mathrm{d}\phi}I'_{011}\right)\right]
\end{aligned}\right\} \quad (G.42)$$

$$\left.\begin{aligned}
&I_2 = \int_{-\infty}^{\infty} v_\phi f_i(\mathbf{r},\mathbf{v},t)\mathrm{d}\mathbf{v} = \frac{n_0}{\pi}\int_{-\infty}^{\infty} v_\phi e^{-a_0\left[(v_r-v_{\mathrm{d}r})^2+(v_\phi-v_{\mathrm{d}\phi})^2\right]}\mathrm{d}\mathbf{v}+\\
&+\frac{n_{0r}}{\pi}\alpha_{0c}\int_{-\infty}^{\infty} v_\phi\left[v_r^2+v_\phi^2+\beta_1^2\mathbf{v}_{\mathrm{d}}^2-2\beta_1\left(v_{\mathrm{d}r}v_r+v_{\mathrm{d}\phi}v_\phi\right)\right]\cdot\\
&\cdot e^{-(\alpha_{0c}+a_0)\left[(v_r-\beta_2 v_{\mathrm{d}r})^2+\left(v_\phi-\beta_2 v_{\mathrm{d}\phi}\right)^2\right]}\mathrm{d}\mathbf{v} =\\
&= n_0\frac{v_{\mathrm{d}\phi}}{a_0}+\frac{n_{0r}}{\pi}\alpha_{0c}\int_{-\infty}^{\infty}\left[v_\phi^3+v_r^2v_\phi+\beta_1^2\mathbf{v}_{\mathrm{d}}^2v_\phi-2\beta_1\left(v_{\mathrm{d}\phi}v_\phi^2+v_{\mathrm{d}r}v_rv_\phi\right)\right]\cdot\\
&\cdot e^{-(\alpha_{0c}+a_0)\left[(v_r-\beta_2 v_{\mathrm{d}r})^2+\left(v_\phi-\beta_2 v_{\mathrm{d}\phi}\right)^2\right]}\mathrm{d}\mathbf{v} =\\
&= n_0\frac{v_{\mathrm{d}r}}{a_0}+n_{0r}\alpha_{0c}\cdot\\
&\cdot\left[I'_{006}+I'_{014}+\beta_1^2\left(v_{\mathrm{d}r}^2+v_{\mathrm{d}\phi}^2\right)I'_{002}-2\beta_1\left(v_{\mathrm{d}\phi}I'_{004}+v_{\mathrm{d}r}I'_{011}\right)\right]
\end{aligned}\right\} \quad (G.43)$$

$$\left.\begin{aligned}
&I_3 = \int_{-\infty}^{\infty} v_r^2 f_i(\mathbf{r},\mathbf{v},t)\mathrm{d}\mathbf{v} = \frac{n_0}{\pi}\int_{-\infty}^{\infty} v_r^2 e^{-a_0\left[(v_r-v_{\mathrm{d}r})^2+(v_\phi-v_{\mathrm{d}\phi})^2\right]}\mathrm{d}\mathbf{v}+\\
&+\frac{n_{0r}}{\pi}\alpha_{0c}\int_{-\infty}^{\infty} v_r^2\left[v_r^2+v_\phi^2+\beta_1^2\mathbf{v}_{\mathrm{d}}^2-2\beta_1\left(v_{\mathrm{d}r}v_r+v_{\mathrm{d}\phi}v_\phi\right)\right]\cdot\\
&\cdot e^{-(\alpha_{0c}+a_0)\left[(v_r-\beta_2 v_{\mathrm{d}r})^2+\left(v_\phi-\beta_2 v_{\mathrm{d}\phi}\right)^2\right]}\mathrm{d}\mathbf{v} = n_0\left(\frac{v_{\mathrm{d}r}^2}{a_0}+\frac{1}{2a_0^2}\right)+\\
&+\frac{n_{0r}}{\pi}\alpha_{0c}\int_{-\infty}^{\infty}\left[v_r^4+v_r^2v_\phi^2+\beta_1^2\mathbf{v}_{\mathrm{d}}^2v_r^2-2\beta_1\left(v_{\mathrm{d}r}v_r^3+v_{\mathrm{d}\phi}v_r^2v_\phi\right)\right]\cdot\\
&\cdot e^{-(\alpha_{0c}+a_0)\left[(v_r-\beta_2 v_{\mathrm{d}r})^2+\left(v_\phi-\beta_2 v_{\mathrm{d}\phi}\right)^2\right]}\mathrm{d}\mathbf{v} =\\
&= n_0\frac{v_{\mathrm{d}r}}{a_0}+n_{0r}\alpha_{0c}\cdot\\
&\cdot\left[I'_{007}+I'_{012}+\beta_1^2\left(v_{\mathrm{d}r}^2+v_{\mathrm{d}\phi}^2\right)I'_{003}-2\beta_1\left(v_{\mathrm{d}r}I'_{005}+v_{\mathrm{d}\phi}I'_{014}\right)\right]
\end{aligned}\right\} \quad (G.44)$$

$$\left.\begin{aligned}
&I_4 = \int_{-\infty}^{\infty} v_\phi^2 f_i(\mathbf{r},\mathbf{v},t)\mathrm{d}\mathbf{v} = \frac{n_0}{\pi}\int_{-\infty}^{\infty} v_\phi^2 e^{-a_0\left[(v_r-v_{\mathrm{d}r})^2+(v_\phi-v_{\mathrm{d}\phi})^2\right]}\mathrm{d}\mathbf{v}+\\
&+\frac{n_{0r}}{\pi}\alpha_{0c}\int_{-\infty}^{\infty} v_\phi^2\left[v_r^2+v_\phi^2+\beta_1^2\mathbf{v}_{\mathrm{d}}^2-2\beta_1\left(v_{\mathrm{d}r}v_r+v_{\mathrm{d}\phi}v_\phi\right)\right]\cdot\\
&\cdot e^{-(\alpha_{0c}+a_0)\left[(v_r-\beta_2 v_{\mathrm{d}r})^2+\left(v_\phi-\beta_2 v_{\mathrm{d}\phi}\right)^2\right]}\mathrm{d}\mathbf{v} = n_0\left(\frac{v_{\mathrm{d}\phi}^2}{a_0}+\frac{1}{2a_0^2}\right)+\\
&+\frac{n_{0r}}{\pi}\alpha_{0c}\int_{-\infty}^{\infty}\left[v_\phi^4+v_r^2v_\phi^2+\beta_1^2\mathbf{v}_{\mathrm{d}}^2v_\phi^2-2\beta_1\left(v_{\mathrm{d}\phi}v_\phi^3+v_{\mathrm{d}r}v_rv_\phi^2\right)\right]\cdot\\
&\cdot e^{-(\alpha_{0c}+a_0)\left[(v_r-\beta_2 v_{\mathrm{d}r})^2+\left(v_\phi-\beta_2 v_{\mathrm{d}\phi}\right)^2\right]}\mathrm{d}\mathbf{v} =\\
&= n_0\frac{v_{\mathrm{d}r}}{a_0}+n_{0r}\alpha_{0c}\cdot\\
&\cdot\left[I'_{008}+I'_{012}+\beta_1^2\left(v_{\mathrm{d}r}^2+v_{\mathrm{d}\phi}^2\right)I'_{004}-2\beta_1\left(v_{\mathrm{d}\phi}I'_{006}+v_{\mathrm{d}r}I'_{013}\right)\right]
\end{aligned}\right\} \quad (G.45)$$

$$
\left.
\begin{aligned}
&I_5 = \int_{-\infty}^{\infty} v_r^3 f_i(\mathbf{r},\mathbf{v},t)\mathrm{d}\mathbf{v} = \frac{n_0}{\pi}\int_{-\infty}^{\infty} v_r^3 e^{-a_0\left[(v_r-v_{\mathrm{d}r})^2+(v_\phi-v_{\mathrm{d}\phi})^2\right]}\mathrm{d}\mathbf{v}+\\
&+\frac{n_{0r}}{\pi}\alpha_{0c}\int_{-\infty}^{\infty} v_r^3\left[v_r^2+v_\phi^2+\beta_1^2\mathbf{v}_{\mathrm{d}}^2-2\beta_1\left(v_{\mathrm{d}r}v_r+v_{\mathrm{d}\phi}v_\phi\right)\right]\cdot\\
&\cdot e^{-(\alpha_{0c}+a_0)\left[(v_r-\beta_2 v_{\mathrm{d}r})^2+\left(v_\phi-\beta_2 v_{\mathrm{d}\phi}\right)^2\right]}\mathrm{d}\mathbf{v} = n_0\left(\frac{v_{\mathrm{d}r}^2}{a_0}+\frac{3}{2a_0^2}\right)+\\
&+\frac{n_{0r}}{\pi}\alpha_{0c}\int_{-\infty}^{\infty}\left[v_r^5+v_r^3v_\phi^2+\beta_1^2\mathbf{v}_{\mathrm{d}}^2v_r^3-2\beta_1\left(v_{\mathrm{d}r}v_r^4+v_{\mathrm{d}\phi}v_r^3v_\phi\right)\right]\cdot\\
&\cdot e^{-(\alpha_{0c}+a_0)\left[(v_r-\beta_2 v_{\mathrm{d}r})^2+\left(v_\phi-\beta_2 v_{\mathrm{d}\phi}\right)^2\right]}\mathrm{d}\mathbf{v} =\\
&= n_0\frac{v_{\mathrm{d}r}}{a_0}+n_{0r}\alpha_{0c}\cdot\\
&\cdot\left[I'_{009}+I'_{017}+\beta_1^2\left(v_{\mathrm{d}r}^2+v_{\mathrm{d}\phi}^2\right)I'_{005}-2\beta_1\left(v_{\mathrm{d}r}I'_{007}+v_{\mathrm{d}\phi}I'_{015}\right)\right]
\end{aligned}
\right\} \quad \text{(G.46)}
$$

$$
\left.
\begin{aligned}
&I_6 = \int_{-\infty}^{\infty} v_\phi^3 f_i(\mathbf{r},\mathbf{v},t)\mathrm{d}\mathbf{v} = \frac{n_0}{\pi}\int_{-\infty}^{\infty} v_\phi^3 e^{-a_0\left[(v_r-v_{\mathrm{d}r})^2+(v_\phi-v_{\mathrm{d}\phi})^2\right]}\mathrm{d}\mathbf{v}+\\
&+\frac{n_{0r}}{\pi}\alpha_{0c}\int_{-\infty}^{\infty} v_\phi^3\left[v_r^2+v_\phi^2+\beta_1^2\mathbf{v}_{\mathrm{d}}^2-2\beta_1\left(v_{\mathrm{d}r}v_r+v_{\mathrm{d}\phi}v_\phi\right)\right]\cdot\\
&\cdot e^{-(\alpha_{0c}+a_0)\left[(v_r-\beta_2 v_{\mathrm{d}r})^2+\left(v_\phi-\beta_2 v_{\mathrm{d}\phi}\right)^2\right]}\mathrm{d}\mathbf{v} = n_0\left(\frac{v_{\mathrm{d}\phi}^2}{a_0}+\frac{3}{2a_0^2}\right)+\\
&+\frac{n_{0r}}{\pi}\alpha_{0c}\int_{-\infty}^{\infty}\left[v_\phi^5+v_r^2v_\phi^3+\beta_1^2\mathbf{v}_{\mathrm{d}}^2v_\phi^3-2\beta_1\left(v_{\mathrm{d}\phi}v_\phi^4+v_{\mathrm{d}r}v_rv_\phi^3\right)\right]\cdot\\
&\cdot e^{-(\alpha_{0c}+a_0)\left[(v_r-\beta_2 v_{\mathrm{d}r})^2+\left(v_\phi-\beta_2 v_{\mathrm{d}\phi}\right)^2\right]}\mathrm{d}\mathbf{v} =\\
&= n_0\frac{v_{\mathrm{d}r}}{a_0}+n_{0r}\alpha_{0c}\cdot\\
&\cdot\left[I'_{010}+I'_{018}+\beta_1^2\left(v_{\mathrm{d}r}^2+v_{\mathrm{d}\phi}^2\right)I'_{006}-2\beta_1\left(v_{\mathrm{d}\phi}I'_{008}+v_{\mathrm{d}r}I'_{016}\right)\right]
\end{aligned}
\right\} \quad \text{(G.47)}
$$

Appendix H

Meetings and Publications during Ph.D Study (2005.06-2008.12)

H.1 Meetings

Ma J. Z. G., and J.-P. St-Maurice (2008), *37th COSPAR Scientific Assembly*, Montréal, Canada, 1860: ***Ion velocity distributions in the presence of cylindrically symmetric electric field perturbations: the collision-free case*** (oral).

Ma J. Z. G., and J.-P. St-Maurice (2007), *Fall meeting, American Geophysical Union*, San Francisco, USA, SM51A-0281: ***Ion distribution functions in response to cylindrically symmetric electric fields that change linearly with radius*** (poster).

Ma J. Z. G., and J.-P. St-Maurice (2007), *2007 CAP*, Saskatoon, Canada, MO-P10-9: ***Auroral ion velocity distributions in inhomogeneous cylindrical electric field geometries*** (oral).

H.2 Publications

Ma J. Z. G., and A. Hirose (2009), *Phys. Scr.*, *79*, in press: ***Parallel Propagation of Ion Solitons in Magnetic Flux Tubes***.

Ma J. Z. G., and A. Hirose (2009),*Phys. Scr.*, *79*, in press: ***High-frequency electrostatic lower-hybrid waves in magnetic flux tubes***.

Ma J. Z. G., and J.-P. St.-Maurice (2008), *J. Geophys. Res.*, *113*, A05312, doi:10.1029/2007JA012815: ***Ion distribution functions in cylindrically symmetric electric fields in the auroral ionosphere: The collision-free case in a uniformly charged configuration***.

Ni W.-T., Y. Bao, H. Dittus, T. Huang, C. Lammerzahl, G. Li, J. Luo, Z. G. Ma, J. F. Mangin, Y.-X. Nie, A. Peters, A. Rudiger, E. Samain, S. Schiller, S. Shiomi, T. Sumner, C.-J. Tang, J. Tao, P. Touboul, H. Wang, A. Wicht, X.-J. Wu, Y. Xiong, C. Xu, J. Yan, D.-Z. Yao, H.-C. Yeh, S.-L. Zhang, Y.-Z. Zhang, Z.-B. Zhou (2006), *Acta Astronautica*, *59*, 598-607: ***ASTROD-I: Mission concept and Venus flybys***.